

Electrocatalysis in Solid Acid Fuel Cell Electrodes

Thesis by
Vanessa Evoen

In Partial Fulfillment of the Requirements for
the Degree of
Doctor of Philosophy

The logo for the California Institute of Technology (Caltech), featuring the word "Caltech" in a bold, orange, sans-serif font.

CALIFORNIA INSTITUTE OF TECHNOLOGY
Pasadena, California

2016
(Defended May 25, 2016)

© 2016

Vanessa Evoen
ORCID: 0000-0003-2824-1896

ACKNOWLEDGEMENTS

This work would not have been possible without financial support from the National Science Foundation (NSF), Gordon and Betty Moore foundation (via the Caltech Center for the Science and Engineering of Materials), and the Advanced Research Projects Agency-Energy (ARPA-E). In addition, I am thankful to the NSF Graduate Research Fellowship Program (GRFP) for three years of support.

I am forever grateful to my thesis advisor Professor Sossina Haile, who has been an inimitable advisor. She is great at identifying the best experiment to do next, which makes for exciting scientific discoveries. I am grateful for all of her personal and professional insight, and for her guidance through my graduate school career. She is a great role model for women in science, and I am thankful for the opportunity to work with her. I am also grateful to have met her wonderful kids Alem and Hanu, who have been a joy to get to know.

I would like to acknowledge Professor Robert Hicks for being a great mentor while I was an undergraduate at UCLA. He encouraged me to pursue a PhD, and wrote me great letters of recommendation for graduate school and graduate fellowships. His infinite enthusiasm for science was encouraging and inspiring. I am grateful for all his support, and I am thankful that he encouraged me at a very early stage to tackle graduate-level scientific research.

I am thankful to Professor Sarah Tolbert at UCLA and Professor Paula Hammond at MIT for giving me the opportunity as an undergraduate, to work with graduate students in their research groups. These opportunities exposed me to a variety of research fields and expanded my skill set in the laboratory. Most importantly, these experiences shaped a solid foundation for my graduate research career. Finally, I am grateful for their recommendation letters for graduate school applications and graduate fellowships.

I thank my thesis committee chair Professor Kostas Giapis for his support. I learned a great deal about instrumentation from him. With his help, I was able to build a working electrospray setup in my second year at Caltech. I am also grateful to Professor George Rossman for serving on my thesis committee and for teaching me the basics of Raman Spectroscopy. He was always available to answer questions, even on weekends! I am also very grateful that I had free access to his laboratory. I would

also like to thank Professor Harry Atwater for serving on my thesis committee and granting me access to his group's COMSOL license. Finally, I would like to thank Professor Rick Flagan for serving on my candidacy committee. His insight into my PhD work was very helpful in shaping the direction of my research.

There are many individuals to whom I owe my gratitude for various contributions to my progress at Caltech. I am grateful to Calum Chisholm for fruitful discussions about solid acids and for granting access to test stations at SAFCell. I am grateful to Mandy Abbott and Fernando Campos for providing samples for research purposes and for answering questions regarding solid acid fuel cell (SAFC) test station construction. I would like to thank the supportive staff at Caltech, Dr. Felicia Hunt, Natalie Gilmore and Teresita Legaspi for the countless work they do to support students every day.

I have worked with a lot of researchers at Caltech that I have learned a great deal from. I am grateful to Aron Varga for teaching me how to electrospray. I am thankful to Moritz Pfohl for showing me how to use the chemical vapor deposition (CVD) setup. His recommendations for improving the setup were helpful in generating reproducible results. I am thankful to Jaemin Kim for teaching me how to take impedance measurements. I would like to acknowledge Hadi Tavassol, who helped with polarization curve measurements and stability studies. He was an encouraging partner on the solid acid team. I would also like to thank Tim Davenport who taught me how to do mass spectrometry measurements and thermal stability studies. Tim is one of the most helpful people I have worked with at Caltech. I would like to acknowledge Nick Brunelli who helped with synthesizing nickel nanoparticles used for all of the in-house grown carbon nanotubes studied in this work. Finally, I would like to thank Mike Ignatowich, whose thermochemical test station I used for reactivity studies at Northwestern university.

I have had the pleasure of collaborating and mentoring exceptional students during my graduate school career. I am grateful to Max Fischer for our collaboration on plasma CVD of carbon nanosheets. I am especially grateful to Phillip Donaubaueer for working with me on carbon nanostructures for SAFC cathodes. We made extraordinary progress during his short visit to Caltech. I would like to acknowledge Dong-gyu Lee for collaborating with me on aqueous electrochemistry studies of carbon nanotubes. I would like to thank Nobert Radasci for collaborations on electrospray scale up. Finally, I would like to thank my undergraduate students; Mike Bauer, Jinho Kim and Yung Yao, who excelled in the various projects assigned to them.

It has been a great pleasure being in the Haile group. I would like to thank Haemin Paik for being a great collaborator and friend in the solid acid team. I would like to acknowledge recent additions to the solid acid team, Sheel Sanghvi and Shobhit Pandey. It has been great to work with them, as they effectively start their graduate research. I would like to acknowledge friends I have made in the Haile/Snyder group like Chirranjeevi Balaji Gopal (BG), Moureen Kemei, Philipp Simons, Yinglu Tang, Carolyn Richmonds, Jenny Schmidt, Tristan Day, and Hyunsik Kim. At any point, I could rely on any of them for support and encouragement on the third floor of Steele Labs, and I am grateful.

I forged lifelong bonds with people I met during my first year in chemical engineering at Caltech. I would like to thank Marilena Dimotsantou for being a great friend and roommate. We had so much fun together and saw each other through some tough times. I would like to thank Charlie Slominski, Ricardo Bermejo-Deval and Kate Fountaine for being great friends and roommates. Finally, Kat Fang for being the best study partner. I was fortunate to meet other amazing friends in other departments like Eyrun Eyjolfsdottir, Steve Demers, Ryan Henning, Jean Pierre-Voropaieff, Georgia Papadakis, and Marius Lemm. I had so much fun getting to know you all.

I have had many supportive friends outside of graduate school who have made this journey so much better. I would like to thank Jennifer Guerrerro and Basak Kilic, who have been my best friends since my undergraduate days at UCLA. I would like to acknowledge Amaka Liz James for being a great friend and always providing a necessary break from academia from time to time. Thank you to all my supportive friends over the years like Kehinde and Taiwo Osuntola and Eleanor Okubor.

I would like to acknowledge Joanna and Don Gwinn, who opened up their home to me in Evanston, Illinois. You made the transition from Caltech to Northwestern so much easier when I moved in with you. Thank you for giving me a home away from home.

Finally, I would like to thank my family. I would like to thank my mum for all the support she has given me. I cannot say thank you enough for the sacrifices she made to ensure I got to this point. I would also like to thank my father for all of his support. He worked tirelessly to provide for my sister and I, as kids. I would like to thank my uncle Ade for all of his support. He gave me a home in California and provided support for whatever I needed. I would like to thank my grandmother, Aunty Morenike and Aunty Moji for all of their support and encouragement. To my sisters/cousins; Valerie, Tope, Tolu, Sade, Elizabeth, Olivia and Blessing, thank you for inspiring me. I love you all, in perpetuity.

ABSTRACT

Fuel cells are appealing alternatives to combustion engines for efficient conversion of chemical energy to electrical energy, with the potential to meet substantial energy demands with a small carbon footprint. Intermediate temperature fuel cells (200–300°C) combine the kinetic benefits and fuel flexibility of higher operating temperatures along with the flexibility in material choices that lower operating temperatures allow. Solid acid fuel cells (SAFCs) offer the unique benefit amongst intermediate temperature fuel cells of a truly solid electrolyte, specifically, CsH_2PO_4 , which in turn, provides significant system simplifications relative to phosphoric acid or alkaline fuel cells^{9, 10} However, the power output of even the most advanced SAFCs has not yet reached levels typical of conventional polymer electrolyte or solid oxide fuel cells. This is largely due to poor activity of the cathodes. That is, while it has been possible to limit electrolyte voltage losses in SAFCs through fabrication of thin-membrane fuel cells (with electrolyte thicknesses of 25–50 μm), it has not been possible to attain high activity cathodes or to limit Pt loadings to competitive levels.¹ In this thesis, the efficacy of non-precious metal catalysts in the solid acid electrochemical system is evaluated. In addition, an attractive synthesis route (specifically, the electrospray method) to fabricating high surface area electrodes with high catalyst utilization is presented.

Elimination of Pt was pursued by the evaluation of carbon nanostructures as potential oxygen reduction reaction (ORR) catalysts in the solid acid electrochemical system. Multi-walled carbon nanotubes were the most consistently catalytically active in comparison with nano-graphite. It is demonstrated that the a) precursor partial pressure, b) seed catalyst size, c) growth temperature and d) chemical functionalization can be used to control the defect density and atomic composition of multi-walled carbon nanotubes (MWCNTs), all of which play a significant role on the measured ORR activity. Increasing the precursor partial pressure, decreasing the seed catalyst size, and decreasing the growth temperature increases the density of ORR active defects. In addition, the oxygen reduction

reaction (ORR) electrochemical activity evaluated by symmetric cell AC impedance spectroscopy and fuel cell measurements, were significantly enhanced by chemical functionalization with oxygen containing functional groups. Area normalized impedance responses as low as $7 \Omega \text{ cm}^2$ were measured on symmetric MWCNT/ CsH_2PO_4 cells. However, it was discovered that these reactive MWCNTs also catalyze and are slightly consumed by steam reforming. Moreover, the orders of magnitude improvement with functionalization measured in impedance measurements is not replicated in fuel cell power output as a result of a decrease in open circuit voltage relative to standard cells. It is proposed that the loss in voltage results from hydrogen production at the cathode via the steam reforming reaction, although formation of hydrogen peroxide rather than water as the oxygen reduction product cannot be ruled out. This work has a significant contribution to catalysis, it demonstrates how carbon nanostructures can be designed by synthesis routes and chemical functionalization processes, to create active precious-metal-free ORR catalysts. It is also important that we have demonstrated potential ORR catalysts in acidic media. These catalysts have potential applications in phosphoric acid fuel cells and PEMFCs.

In addition to the study of carbon nanostructures, oxides were evaluated as potential ORR catalysts. Specifically, TiO_x nanoparticles were studied. Analysis shows that the activity is controlled by the oxidation state of Ti. The active site seems to be on or near slightly reduced Ti sites. In this study we have outlined synthesis routes to tune the oxidation state of Ti and enhance ORR activity in the solid acid fuel cell.

Finally, the fundamentals of the electrospray process are explored to understand how the particle size ultimately resulting from electrospray synthesis depends on both solution properties and process parameters. This analysis presents a systematic way to control the fabrication of high surface area SAFC electrodes with increased throughput, catalyst utilization and consequently power density.

TABLE OF CONTENTS

ACKNOWLEDGEMENTS	iii
ABSTRACT.....	vi
TABLE OF CONTENTS	viii
LIST OF FIGURES	x
NOMENCLATURE.....	xvii
CHAPTER 1. Introduction.....	1
1.1 Overview.....	1
1.2 Fuel cells.....	1
1.3 Solid Acid Fuel cells	5
1.3.1 Solid Acid compounds.....	5
1.3.2 Solid acid fuel cells (SAFCs); basics, challenges and current status.....	9
1.4 Objectives of this thesis.....	15
CHAPTER 2. Experimental methods.....	16
2.1 Characterization techniques	16
2.1.1 Electrochemical characterization (<i>in situ</i>)	16
2.1.2 <i>Ex situ</i> characterization	26
2.2 Synthesis methods	29
2.2.1 Electrospray deposition.....	29
CHAPTER 3. Electrochemistry as a tool for evaluating the reactivity of carbon	35
Section 3.1 Accessing the efficacy of MWCNTs in SAFCs.....	35
3.1.1. Introduction.....	35
3.1.2. Experimental	37
3.1.3. Results and discussion	39
3.1.4. Conclusion	54
Section 3.1. Supplemental material.....	56
Section 3.2. Parametric Study on MWCNT oxygen reduction reaction activity (ORR)	62
3.2.1. Overview	62
3.2.2. Results and discussion	66
3.2.3. Conclusion	71
CHAPTER 4. Tuning the reactivity of carbon nanostructures by growth parameters	72
4.1. Abstract	72
4.2. Introduction.....	72

4.3. Experimental	76
4.4. Results and discussion	79
4.5. Conclusion	97
4.6. Acknowledgement	98
CHAPTER 5. Oxygen reduction by TiO_x overlayers	99
5.1. Introduction.....	99
5.2. Experimental	99
5.3. Results and discussion	100
5.4. Conclusion	111
CHAPTER 6. Electro spray of nano-sized CsH₂PO₄ for SAFC electrodes	112
Section 6.1. <i>In situ</i> characterization of electro sprayed CsH ₂ PO ₄ solid acid nanoparticles	112
6.1.1. Abstract	112
6.1.2. Introduction.....	112
6.1.3. Electro spray background	114
6.1.4. Experimental procedures	117
6.1.5. Results.....	122
6.1.6. Discussion	130
6.1.7. Conclusions.....	133
Section 6.1. Supplementary material	135
Solvent evaporation of a single μm sized droplet	135
Section 6.2. Electro spray throughput.....	140
6.2.1. Experimental details.....	141
6.2.2. Results and discussion	145
6.2.3. Conclusion	160
IMPACTS AND INSIGHTS	162
BIBLIOGRAPHY	163

LIST OF FIGURES

Chapter 1

- Figure 1.1.** Schematic of a fuel cell polarization curve, with contributions of various overpotentials indicated by the shaded regions, and explained on the right. The power density (dotted line) is the product of the cell voltage and current density.....3
- Figure 1.2.** Schematic of a typical porous composite electrode showing a proton conducting electrolyte, electron conducting catalyst, and gas phase species (O_2), that comprise a triple phase boundary (TBP) point.4
- Figure 1.3.** Arrhenius plot of proton conductivity, σ_H , of a few solid acid compounds that exhibit a super-protonic phase transition.²⁰⁻³6
- Figure 1.4.** Super-protonic phase transition in CsH_2PO_4 . (a) Arrhenius plot of proton conductivity (σ), in humidified N_2 . (b) Unit cells of monoclinic and cubic phases.^{2,3}7
- Figure 1.5.** Phase stability regions of CsH_2PO_4 adapted from Taninouchi et al.⁵ and Chisholm et al.⁹8
- Figure 1.6.** Schematic of a fuel cell depicting the anode and cathode half reactions.⁴9
- Figure 1.7.** (a) IR corrected solid acid fuel cell polarization plot showing small ohmic losses in comparison to other sources of overpotential loss.⁴ (b) Cathode and anode contributions to the overpotential of a SAFC.²⁹10
- Figure 1.8.** Comparison of IR-free polarization curves of SAFCs incorporating different sized CsH_2PO_4 in the cathode. Scanning electron micrographs are shown below.¹11
- Figure 1.9.** (a) SEM micrographs of composite electrode nanostructures comprising CsH_2PO_4 , Pt-black and poly-vinylpyrrolidone (PVP). (b) Impedance spectra of representative CsH_2PO_4 + Pt/ CsH_2PO_4 / CsH_2PO_4 + Pt symmetric, electrochemical cells with electrosprayed electrodes on carbon and a Pt loading of 0.3 ± 0.2 mg/cm²; data collected under humidified hydrogen with $pH_2O = 0.4$ atm at 240 °C.⁷12
- Figure 1.10.** Impedance spectra of four CsH_2PO_4 + Pt +PVP composite electrodes electrosprayed onto CNTs, and one without CNTs but otherwise identical.⁶13
- Figure 1.11.** (a) Synthetic approach for Pt decorated CNTs. (b) Electrospray deposition strategy of Pt-CNT + CsH_2PO_4 composites. (c) Symmetric cell impedance measurements of 30 wt % Pt-CNT based electrodes. Measurements performed in humidified H_2 ($pH_2O = 0.4$ atm) and Pt loading is 5.1 E-3 mg/cm². Inset is equivalent circuit used for fitting.⁸13

Chapter 2

- Figure 2.1.** (a) The j - η representation of a hypothetical electrochemical reaction. The Tafel approximation deviates from Butler-Volmer kinetics at low overpotentials.¹⁰ (b) Effect of overpotential on fuel cell performance.18
- Figure 2.2.** (a) Application of a small signal perturbation confines the impedance measurement to a pseudo-linear portion of a fuel cell's I-V curve (b) A sinusoidal voltage perturbation and resulting current response with a phase shift (θ).....19
- Figure 2.3.** (a) Nyquist plot of a hypothetical fuel cell. Regions marked correspond to ohmic, anode activation and cathode activation losses, respectively. (b) Schematic of a fuel cell with cathode and anode half reactions.....20
- Figure 2.4.** (a) An illustration of the movement of a proton under electric field perturbation at varying frequencies. (b) Physical representation of an electrochemical interface. (c) Proposed equivalent circuit model of an electrochemical reaction interface.21

Figure 2.5. (a) Simulated impedance spectrum of a symmetric cell showing the grain boundary and bulk arcs at mid-range and high frequency. Half-cell reactions for a symmetric (b) cathode cell and (c) anode cell.....	22
Figure 2.6. (a) Schematic of Stokes, Rayleigh and anti-Stokes scattering. (b) Scattered Raman spectrum intensities plotted against relative wave numbers.	27
Figure 2.7. First and second-order Raman spectra of a carbon nanotube material. Background corrected spectrum is shown in black, fitted peaks in green dashed lines and cumulative fit peak is shown in red.....	28
Figure 2.8. A schematic of electrospray ionization, the effluent leaves the Taylor cone as charged droplets that undergo columbic explosions at the Rayleigh limit.	30
Figure 2.9. Four types of film morphologies obtained by electrospray. I, dense film; II, dense film with incorporated particles; III, porous top layer with dense bottom layer; IV, fractal-like porous structure, according to Chen et al. ⁶⁰	31
Figure 2.10. Initial droplet velocity of the emitted droplet of varying solid acid concentration.	33

Chapter 3

Figure 3.1. (a) Fourier-Transform infrared (FTIR) spectra of hollow CNTs, CNT-NH ₂ and CNT-COOH. Dashed lines identify peaks corresponding to labelled functional groups. (b) First order Raman spectra of the CNTs, CNT-NH ₂ and CNT-COOH. The dashed lines specify the peak position of the D band, G band and D' band. The defect density characterized as the ratio of the D band intensity to the G band intensity is shown inset.....	41
Figure 3.2. Deconvolution of the XPS (a) C1s, the (b) N1s and (c) O1s spectra of the CNTs, CNT-NH ₂ and CNT-COOH.	42
Figure 3.3. TGA profiles for hollow MWCNTs, MWCNT-NH ₂ and MWCNT-COOH measured under flowing air at a heating rate of 2 °C/min.	44
Figure 3.4. (a) Ion current ratio of H ₂ to H ₂ O for 400 mg of hollow CNT, hollow CNT-NH ₂ and hollow CNT-COOH at p _{H₂O} = 0.2 atm and 800°C. (b) Ion current ratio of H ₂ to H ₂ O for 400 mg of hollow CNT and hollow CNT-COOH with varying p _{H₂O}	45
Figure 3.5. Arrhenius plot of H ₂ ion current versus inverse temperature of the cool down and heat up between 800°C to 600°C of 200 mg of CNT-COOH (ramp rate is 100 °C/ hour).....	46
Figure 3.6. a) SEM images of Hollow MWCNTs 15 ± 5 nm in outer diameter, 5-20 μm in length. Cross-sectional SEM images of symmetric pellets with 600mg of CsH ₂ PO ₄ electrolyte sandwiched between 50mg 1:1 MWCNT: CsH ₂ PO ₄ composite electrodes of b) Hollow MWCNTs, c) Hollow MWCNTs-NH ₂ , d) Hollow MWCNTs-COOH.	47
Figure 3.7. Measurements performed at 250 °C under humidified O ₂ and H ₂ gases (p _{H₂O} = 0.4 atm) at a flow rate of 40 sccm. (a) Four H ₂ /O ₂ polarization curves (IR corrected) measured consecutively between 0.0V and 0.95 V on 50mg 1:1 CNT: CsH ₂ PO ₄ composite cathode and 25 mg 1:3 Pt/C : CsH ₂ PO ₄ anode. Fuel cell polarization curve recorded at 2.5mv/s for CNTs, CNT-NH ₂ and CNT-COOH electrodes. Inset is the open circuit potential (OCP). (b) Impedance measurements on the fuel cell, at equilibrium in the frequency range of 10 mHz to 0.2 MHz. Inset is the impedance model fit which is a finite length Warburg element (W _s) and a resistor in series with a resistor (R) and constant phase element (CPE) in parallel. Impedance measurements were taken on the cell before the polarization curves were measured. (c) Open circuit potential versus area normalized impedance from impedance curve fits. (d) Summary of impedance curve fitting.....	48
Figure 3.8. Measurements performed at 250 °C under humidified oxygen (p _{H₂O} = 0.4atm) flowing at 40 sccm. (a) Comparison of Symmetric cell impedance measurements of 50mg 1:1 CNT: CsH ₂ PO ₄ composite electrodes of MWCNTs, MWCNTs-NH ₂ and MWCNTs-COOH in humidified O ₂ in a Nyquist representation (ω=10 KHz – 5 mHz). Inset is the impedance model fit which is a finite length Warburg element (W _s) and a resistor in series with a resistor (R) and constant phase element (CPE) in parallel. (b) Semi-log plot of average normalized impedance for the CNT electrodes (~10 samples	

- each) from curve fitting. The error bar is the standard deviation in fit results. (c) Summary of impedance fitting values showing Warburg resistance (W_s), constant phase element resistance (R_{CPE}) and the total resistance (R_{TOT}). 49
- Figure 3.9.** Long term degradation behavior of MWCNTs. (a) Symmetric impedance measurements in humidified O_2 ($p_{H_2O} = 0.4\text{atm}$). R_{rel} is the electrochemical resistance of 50 mg 1:1 CNT : CsH_2PO_4 composite electrodes at time (t) divided by electrochemical resistance measured 10 min after O_2 is flowed to the cell. Inset is an SEM image of MWCNT over-grown carbon paper used as a current collector to improve electrode stability. (b) Comparison of symmetric cell impedance measurements of 50mg 1:1 CNT: CsH_2PO_4 composite electrodes of hollow MWCNTs, hollow MWCNT after 12-hour treatment in air and hollow MWCNT after 12-hour treatment in humidified O_2 . Measurements performed at $250^\circ C$ under humidified O_2 gas flowing at 40 sccm ($\omega=10\text{ KHz} - 5\text{ mHz}$). 51
- Figure 3.10.** (a) Forward and reverse hydrogen oxidation and oxygen reduction half reactions at the anode and cathode, respectively, in fuel cell configuration. (b) The oxygen reduction reaction and the steam reforming reaction at the electrodes in symmetric cell configuration. The proposed carbon corrosion reaction is highlighted in blue and the oxygen reduction reaction is highlighted in red. 53
- Figure 3.11.** (a) First scan of the I-V curve measured in Figure 3.6. Inset shows that the cathodic branch of the I-V curve has a higher OCP than the anodic branch of the fuel cell I-V curve. (b) The average OCP value (where the I-V curve crosses the zero current density line) for the cathodic and anodic branch of the I-V curve versus the average slope at zero current 54
- Figure 3.S.1.** Comparison of electrode responses for 50 mg 1:1 CNT : CsH_2PO_4 composite electrodes in humidified ($p_{H_2O} = 0.4\text{atm}$) under Ar at the cathode and H_2 at the anode. 56
- Figure 3.S.2.** (a) Comparison of electrode responses for 50 mg 1:1 CNT : CsH_2PO_4 composite electrodes in humidified ($p_{H_2O} = 0.4\text{atm}$) under symmetric argon. (b) Log-log plot of $|z(\omega)^2|$ versus $1/\omega$, where the offset is $(R_0)^2/\tau$ 57
- Figure 3.S.3.** Symmetric impedance measurements in humidified O_2 ($p_{H_2O} = 0.4\text{atm}$). R_{rel} is the electrochemical resistance of 25 mg 1:1 CNT : CsH_2PO_4 composite electrodes at time (t) divided by electrochemical resistance measured 10 min after O_2 is flowed to the cell 57
- Figure 3.S.4.** (a) Symmetric cell AC impedance measurements of 1:1 hollow CNT-COOH: CsH_2PO_4 composite electrodes in humidified O_2 ($p_{H_2O}=0.4\text{ atm}$). Electrode loading was 25mg, 50mg and 100mg, respectively. (b) Plot of average area specific resistance (ASR) from fitting impedance data versus mass of 1:1 hollow CNT-COOH : CsH_2PO_4 composite electrodes. The error bars correspond to the standard deviation in ASR over the number of samples measured (in set). 58
- Figure 3.S.5.** (a) Comparison of symmetric cell impedance measurements of 50mg 1:1 CNT: $CsHSO_4$ composite electrodes of Hollow MWCNTs-COOH. Measurements performed at $165^\circ C$ in symmetric 60 sccm O_2 and varying p_{H_2O} . (b) Electrode resistance from impedance fitting with varying p_{H_2O} . (c) Electrode impedance from R ($\omega=0.005\text{ Hz}$) - R ($\omega=1000\text{ Hz}$) with varying p_{H_2O} 59
- Figure 3.S.6.** RDE polarization curves for Hollow MWCNTs and Hollow MWCNTs-COOH. 5 mg of Hollow MWCNT and 10 mg of hollow MWCNT-COOH were suspended respectively, in 450 μ L of ethanol, 450 μ L of isopropanol and 100 μ L of Nafion. 5 μ l of the resulting carbon nanotube ink was deposited on the glassy carbon electrode. In a) polarization curves in acidic media are shown for 0.1 M $HClO_4$, 0.1 M phosphate buffer, and 0.1 M acetate buffer. (b) Polarization curves in 0.1 M KOH are shown for MWCNTs in comparison with Pt/C. In c) the onset voltage at $-1\text{mA}/\text{cm}^2$ is summarized for all MWCNTs in acidic and basic media. 60
- Figure 3.S.7.** Average area specific resistance (ASR) or area normalized impedance (from symmetric cell AC impedance measurements in humidified O_2) versus the mass loading of the CNT electrodes. This shows that the 1:1 mass ratio loading had the highest ORR activity, hence was used for all measurements. 61
- Figure 3.2.1.** SEM image and schematic of (a) hollow MWCNTs and (b) bamboo MWCNTs. 62

Figure 3.2.2. First order Raman spectra of hollow MWCNTs and bamboo MWCNTs. Inset is the integrated peak ratio of the D peak to the G peak (I_D/I_G). Hollow MWCNTs (OD is 15 ± 5 nm and length is 5– 10 μ m) and bamboo MWCNTs (OD is 30 ± 5 nm and length is 1–5 μ m).	63
Figure 3.2.3. Measurements performed at 250°C under humidified oxygen ($p_{H_2O} = 0.4$ atm) flowing at 40 sccm. Comparison of symmetric cell impedance measurements of 50mg 1:1 CNT: CsH_2PO_4 composite electrodes in a Nyquist representation ($\omega=10$ KHz – 5 mHz).	63
Figure 3.2.4. a) First order Raman spectra of hollow and bamboo MWCNTs. The dashed lines specify the peak position of the D band, G band and D' band. The defect density characterized as the ratio of the D band intensity to the G band intensity is shown inset. b) Fourier-transform infrared (FTIR) spectra of hollow and bamboo MWCNTs. Dashed lines identify peaks corresponding to labelled functional groups.	64
Figure 3.2.5. Plot of average area specific resistance (ASR) from fitting impedance data versus type of CNT used in 50 mg 1:1 mass ratio CNT : CsH_2PO_4 composite electrodes. The error bars correspond to the standard deviation in ASR.	65
Figure 3.2.6. Area normalized impedance from impedance measurements versus outer diameter (OD) and length (L) of hollow and bamboo variation MWCNTs.	66
Figure 3.2.7. I_D/I_G (from Raman measurements) for all varying hollow and bamboo MWCNTs characterized, versus area normalized impedance values (from symmetric cell AC impedance measurements in humidified O_2). Brackets indicate that the shorter MWCNTs of both variations have higher measured I_D/I_G	67
Figure 3.2.8. BET surface area for all varying hollow and bamboo MWCNTs characterized, versus area normalized impedance values (from symmetric cell AC impedance measurements in humidified O_2).	68
Figure 3.2.9. Area normalized impedance from symmetric AC impedance measurements in humidified O_2 versus the relative concentration of the carbonyl (C=O) functional group in the hollow/bamboo MWCNT.	70

Chapter 4

Figure 4.1. (a) Schematic diagram of tip growth model at different time steps. (b) The MWCNT in the tip growth scheme depicting the (i) catalyst particle, (ii) embryo and (iii) full grown MWCNT (Reproduced from Hembram et al.). ⁸¹	74
Figure 4.2. SEM micrographs of MWCNTs grown with 80 nm Ni seed catalyst and growth temperature 800 °C in; (a) $PC_{2H_2} = 0.016$ atm: 16 sccm C_2H_2 , 750 sccm Ar, 250 sccm H_2 and (b) $PC_{2H_2} = 0.060$ atm: 16 sccm C_2H_2 , 250 sccm H_2 . Inset is higher magnification.	79
Figure 4.3. STEM images of MWCNTs grown with 80 nm Ni seed catalyst and growth temperature 800 °C in (a) $PC_{2H_2} = 0.016$ atm. Dashed lines show the 'bamboo' like structure of the MWCNTs. (b) $PC_{2H_2} = 0.060$ atm. Dark spots are amorphous carbon deposits.	80
Figure 4.4. First order Raman spectra measured for MWCNTs grown with $PC_{2H_2} = 0.016$ atm (top) and $PC_{2H_2} = 0.060$ atm (bottom). (a) 80 nm Ni seed catalyst. (b) 40 nm Ni seed catalyst. The dashed lines indicate the peak position of the D band, G band and D' band. The defect density characterized as the ratio of the D band intensity to the G band intensity is shown inset. In all cases, the growth temperature is 800 °C.	82
Figure 4.5. a) Comparison of symmetric cell impedance measurements of 50mg 1:1 CNT: CsH_2PO_4 composite electrodes (varied parameters shown inset and growth temperature is 800 °C) in a Nyquist representation ($\omega=10$ KHz – 5 mHz). Measurements collected at 250°C under humidified O_2 ($p_{H_2O} = 0.4$ atm) flowing at 40 sccm. (b) Area normalized impedance versus I_D/I_G ratios from Raman characterization.	83
Figure 4.6. STEM microscopy images of MWCNTs grown at $PC_{2H_2} = 0.060$ atm, growth temperature = 800 °C, and 80 nm Ni seed catalyst in (a) scanning mode and (b) transmission mode.	84

Figure 4.7. Normalized relative transmittance FTIR spectra of MWCNTs grown at 800 °C with 80 nm Ni seed catalyst. Solid lines indicate peaks corresponding to labelled functional groups.	85
Figure 4.8. Deconvolution of the XPS C1s peak for MWCNTs grown at PC2H2 = 0.060 atm,	85
Figure 4.9. First order Raman spectra measured for MWCNTs grown with PC2H2 = 0.60 atm and 80 nm Ni seed, at 800 °C; (a) HNO ₃ treated and (b) untreated MWCNTs. The dashed lines specify the peak position of the D band, G band and D' band. I _D /I _G and I _D /I _G is shown inset.....	87
Figure 4.10. Comparison of symmetric cell impedance measurements of 50mg 1:1 MWCNT: CsH ₂ PO ₄ composite electrodes in a Nyquist representation for untreated and HNO ₃ treated MWCNTs. Measurements were collected at 250°C under humidified O ₂ (pH ₂ O = 0.4atm) flowing at 40 sccm in the 5mHz to 10KHz frequency range. Inset is higher magnification. MWCNTs grown in PC2H2 = 0.060 atm, growth temperature = 800 °C, and 80 nm Ni seed catalyst.	88
Figure 4. 11. SEM images of MWCNTs grown in PC2H2 = 0.060 atm with 80 nm Ni particles at 600 °C, 650 °C, 700 °C, and 800 °C. Inset is higher magnification	89
Figure 4.12. First order Raman spectra measured for HNO ₃ -treated MWCNTs grown with PC2H2 = 0.060 atm and 80 nm Ni seed catalyst; (a) fit with D band, G band and D' band (b) D band, G band D' band, and T ₂ band. Growth temperature is inset.	90
Figure 4.13. FWHM of the 'D' peak in Raman measurements versus growth temperature.	91
Figure 4.14. Deconvolution of the XPS C1s peak for MWCNTs grown at PC2H2 = 0.060 atm with 80 nm Ni seed catalyst at a growth temperature of (a) 600 °C, (b) 650 °C, (c) 700 °C, and (d) 800 °C	92
Figure 4.15. Deconvolution of the XPS C1s peak for HNO ₃ treated MWCNTs grown at PC2H2 = 0.060 atm with 80 nm Ni seed catalyst at a growth temperature of (a) 600 °C, (b) 650 °C, (c) 700 °C, and (d) 800 °C.	93
Figure 4.16. Deconvolution of the XPS N1s peak for MWCNTs grown at PC2H2 = 0.060 atm with 80 nm Ni seed catalyst at a growth temperature of (a) 600 °C, (b) 650 °C, (c) 700 °C, and (d) 800 °C (CPS refers to counts per second).....	94
Figure 4.17. Comparison of symmetric cell impedance measurements of 50mg 1:1 MWCNT: CsH ₂ PO ₄ composite electrodes in a Nyquist representation for HNO ₃ treated MWCNTs. Measurements were collected at 250°C under humidified O ₂ (pH ₂ O = 0.4atm) flowing at 40 sccm in the 5mHz to 10KHz frequency range. MWCNTs grown in PC2H2 = 0.060 atm with 80 nm Ni seed catalyst. The growth temperature is inset.....	96
Figure 4.18. Average area normalized impedance values versus the % Oxygen from XPS analysis of HNO ₃ treated MWCNTs grown with PC2H2 = 0.16 atm and 80 nm Ni seed catalyst.....	97

Chapter 5

Figure 5.1. (a) Polarization behavior and (b) phase fraction of the as-received TiO ₂ micropowders of rutile (R) and anatase (A).....	102
Figure 5.2. (a) Phase fraction of rutile and anatase TiO ₂ in the oxide layers grown on Ti metal powders. (b) Polarization response of different Ti-based cathodes, and comparison with a Pt on carbon black cathode. R and A represents as received rutile and anatase micro-powders. Polarization curves represented are from Titanium micro-powders treated at shown temperatures for 30 min under 0.7% O ₂ (Ar balance). (c) Cell voltage of the titania cathodes shown in part b at 5 mA cm ⁻² of current. ..	104
Figure 5.3. Cell voltage with cathodes made from titanium micropowders annealed at 600 °C, under 0.7% O ₂ (balance Ar) for different growth times. Voltage is compared at 5 mA cm ⁻² of current. Gray bars represent the cathodes following five electrochemical cycles between 0.95 V and 0V at a scan rate of 2.5 mV s ⁻¹	105
Figure 5.4. Samples prepared from titanium metal micropowder (a) before annealing; and after annealing at 600 °C in 0.7% O ₂ (balance Ar) for (b) 15 min, (c) 30 min and (d) 60 min.....	106
Figure 5.5. Rutile and anatase phase fractions of the powder samples following annealing at 600 °C for different times.	108

Figure 5.6. XPS spectra of (a) Ti 2P and (b) O 1S regions acquired from the different powder samples prepared.....	109
Figure 5.7. Raman spectra of the titanium metal powder (Ti, Bg), titanium powders following annealing at 600 °C under Ar for 30 min, and under 0,7% O ₂ (balance Ar) for 15, 30 and 60 min, and at 700, 800 and 900 °C. For comparison, Raman spectra of as received TiO ₂ rutile (R) and anatase (A) micropowders are also shown.	111

Chapter 6

Figure 6.1. Schematic of the electrospray and differential mobility analyzer	117
Figure 6.2. Scanning electron micrograph of deposited CsH ₂ PO ₄ structure for feature size measurement.	119
Figure 6.3. Example of particle size measurements and data analysis. (a) Counts (cm ⁻³ s ⁻¹) as a function of particle diameter, multiple measurements, as detected at discrete particle sizes; and (b) averaged values and fit to a log-normal distribution.	121
Figure 6.4. Solubility limit of CsH ₂ PO ₄ in water-methanol mixtures	122
Figure 6.5. (a) Surface tension of precursor solutions with 16 wt %, 33 wt %, 50 wt%, and 60 wt% methanol in water vs. CsH ₂ PO ₄ concentration. Inset is surface tension of precursor solutions vs. methanol concentration (3 g/L CsH ₂ PO ₄ and no CsH ₂ PO ₄ , respectively). (b) Conductivity of precursor solutions with 16 wt %, 33 wt %, 50 wt%, and 60 wt% methanol in water vs. CsH ₂ PO ₄ concentration. Inset is conductivity versus methanol concentration.	124
Figure 6.6. Influence of electrospray voltage on (a) mean particle size in the CDP aerosol, and (b) detected current, with and without the Po neutralizer. Solution and process parameters as given in Table 6.1 (default values), with CDP concentration of 10 g/L.	126
Figure 6.7. Expected variation in initial droplet size and corresponding expected variation in solid volume according to Eq. (6.1) as a result of varying solution and process parameters: (a) varied methanol concentration, (b) varied CsH ₂ PO ₄ concentration, and (c) varied liquid flow rate. Where not varied, methanol content is 50 mol% (46 wt%), CDP is 10 g/L, and liquid flow is 0.5 mL/h.	127
Figure 6.8. Mean particle size of aerosol vs. (a) MeOH concentration, (b) CsH ₂ PO ₄ concentration, and (c) liquid flow rate through electrospray capillary with standard deviation of the distributions indicated.	129
Figure 6.9. Mean particle size of aerosol vs. (a) PVP concentration, (b) electrospray chamber temperature, and (c) sheath nitrogen flow rate through electrospray capillary with standard deviation of the distributions indicated.	130
Figure 6.S.1. Evolution of a single 1µm droplet to 100nm dry CsH ₂ PO ₄ particle in 20-99% relative humidity and ambient temperature of (a) 25°C and (b) 100°C.	138
Figure 6.S.2. For $\alpha_T = \alpha_C$ ranging from 0.05-1, the evolution of a single droplet of initial droplet size 1µm at 40% relative humidity and T=100 °C.	139
Figure 6.2.1. Electric field map showing top view and side view, to the right is the scale bar depicting red as the highest electric field value. A schematic of Taylor cone formation shown at bottom left. (a) Flat capillary (b) Frustum shaped capillary.	143
Figure 6.2.2. Plot of electric field versus the capillary tip angle.....	144

Figure 6.2.3. SEM micrograph of porous interconnected CsH_2PO_4 obtained by electrospray. (a) Published work by Varga et al. ⁷ (b) This work.	146
Figure 6.2.4. Schematic of symmetric cell assembly used for electrochemical characterization. (B) Picture of compression holder that holds the symmetric cell in the testing chamber.....	147
Figure 6.2.5. Impedance spectra of a representative CsH_2PO_4 (CDP) : platinum : platinum on carbon symmetric cell collected under humidified hydrogen with a water partial pressure of 0.4 atm at 248°C.	148
Figure 6.2.6. a) SEM micrographs of the cross section of an electrosprayed CsH_2PO_4 sample on carbon paper. (b) Picture showing the top view of CsH_2PO_4	149
Figure 6.2.7. Side view of the electric field map, the electric field scale bar is on the right. The highest value of electric field (at the top right corner) corresponds to the electric field at the capillary tip (not visible). (a) Single capillary biased at 5kV. (b) Single capillary surrounded by a ring 1.9 cm in diameter. (c) Single capillary surrounded by a ring 2.8 cm in diameter. (d) Single capillary surrounded by a ring 5.7 cm in diameter.....	150
Figure 6.2.8. Side view of the electric field map, the electric field scale bar is on the right. The highest value of electric field (at the top right corner) corresponds to the electric field at the capillary tip (not visible). (a) Single capillary biased at 5kV. (b) Single capillary surrounded by a ring 1.9 cm in diameter with no bias. (c) Single capillary surrounded by a ring 1.9 cm in diameter with a bias of -0.5 kV. (d) Single capillary surrounded by a ring 1.9 cm in diameter with a bias of -3 kV.....	150
Figure 6.2.9. Plot of film diameter (in inches) versus the bias on the negative bias on the ring surrounding the capillary (-kV). Increasing the bias increases the defocusing effect.....	151
Figure 6.2.10. Plot of deposited film diameter (in inches) versus the internal diameter of the metal ring (in inches). Decreasing shield radius increases the defocusing effect.	152
Figure 6.2.11. SEM micrographs of the cross section of an electrosprayed CsH_2PO_4 sample with a defocusing ring on carbon paper.....	153
Figure 6.2.12. Impedance spectra for electrosprayed 2:1:1 CsH_2PO_4 :Pt : Pt/C of equal area with and without a defocusing ring.	153
Figure 6.2.13. (a) Top view of the capillary arrangement. (b) Side view showing the central emitting capillaries and the dummy capillaries lower in height. (c) Picture of the capillaries used in the experiment.....	154
Figure 6.2.14. First row is the electric field map (red -highest electric field, blue-lowest), second row is the electric field range at the capillary tip, and the third row is the experimental result. (a) 3 capillaries only. (b) 3 capillaries surrounded by dummy capillaries half the height of the emitting capillaries in the center. (c) 3 capillaries surrounded by dummy capillaries three quarters their height. (d) 3 capillaries surrounded by dummy capillaries of the same height.....	156
Figure 6.2.15. a) Schematic of the seven-capillary system with a metal ring. (b) Picture of apparatus. ...	156
Figure 6.2.16. First row is the electric field map at the capillary tips, to the right is the electric field scale bar. Second row is a picture of the capillary arrangement. Third row is the CsH_2PO_4 deposition profile. (a) All seven capillaries are the same height. (b) The central capillary is ~0.3cm above the surrounding capillaries.....	157
Figure 6.2.17. First row is COMSOL simulation showing the electric field lines and the potential vector plot. Second row is the picture of the apparatus. Third row is the resulting CsH_2PO_4 profile. (a) Two capillaries 1.3cm apart. (b) Two capillaries each surrounded by metal rings 2.8 cm in diameter biased at -3kV. (c) Three capillaries equidistant from each other surrounded by rings 2.8cm in diameter.	159
Figure 6.2.18. Schematic of proposed multi-capillary apparatus.	160
Figure 6.2.19. COMSOL simulations comparing the electric field lines and the potential gradient vector plot for a seven-capillary system (a) with a defocusing plate (b) without a defocusing plate.	160

NOMENCLATURE

ORR oxygen reduction reaction

HOR hydrogen oxidation reaction

ACIS alternating current impedance spectroscopy

AFC alkali fuel cell

CDP cesium dihydrogen phosphate, CsH_2PO_4

CV cyclic voltammetry

FRA frequency response analyzer

FTIR Fourier-transform infrared

MCFC molten carbonate fuel cell

OCP open circuit potential

PAFC phosphoric acid fuel cell

SAFC solid acid fuel cell

PEMFC polymer electrolyte membrane or proton exchange membrane fuel cell

SEM scanning electron microscopy

SOFC solid oxide fuel cell

XPS X-ray-photoelectron spectroscopy

CNT carbon nanotube

MWCNT multi-walled carbon nanotubes

CHAPTER 1

Introduction

1.1. Overview

In this chapter, we present a brief introduction to fuel cells with an emphasis on SAFCs. The basics of electro-catalysis in SAFCs and the current challenges facing solid acid electrochemical systems will be presented.

1.2. Fuel cells

Of the various technology routes being studied to combat the energy crisis, fuel cells have the potential to play a significant role in any renewable energy cycle design. Fuel cells can be refueled like a combustion engine and can directly convert chemical energy to electrical energy like a battery. In addition, they are not limited by the Carnot efficiency as is the case in combustion engines. This results in a technology with a host of advantages, which is poised to make an impact in both stationary and mobile power generation.

A fuel cell consists of an anode and a cathode separated by an electrolyte membrane. With hydrogen as the fuel and oxygen as the oxidant, the overall reaction is



which is a spontaneous reaction driven by the Gibbs free energy conversion. In a fuel cell, the direct reaction is inhibited by separating the electrodes with an electrolyte membrane. In general, the fuel cells are classified by electrolyte composition.¹⁰

A fuel cell is a galvanic cell and the standard Gibbs free energy of formation (ΔG_0) of **Reaction 1.1** can be converted into the standard electrical potential E^0 or Nernst potential (at standard pressure $p^0=101.325$ kPa) via the equation:

$$E^0(T) = -\frac{\Delta G_0(T)}{nF}, \quad (1.1)$$

where n is the number of electrons transferred in the overall reaction and F is the Faraday constant (96,485 C/mol). ΔG_0 (Temperature = 298K) = -237 kJ/mol; from Equation (1), $E^0 = 1.23V$. To compute the theoretical Nernst potential at more realistic conditions:

$$E_{eq}(T) = E^0(T) - \frac{RT}{nF} \ln \left(\frac{P_{H_2O}^{(cathode)}}{P_{H_2}^{(anode)} (P_{O_2}^{(cathode)})^{0.5}} \right), \quad (1.2)$$

where E_{eq} is the theoretical equilibrium current density at zero current density ($j = 0$) and p_x is the partial pressure of species x at the anode or cathode. The voltage across the cell during operation is less than predicted by the Nernst potential as a result of irreversible losses as current is drawn from the cell. The overpotential η is defined as the drop in voltage from equilibrium to drive a particular process. In fuel cell operation, the goal is to maximize the power (current * voltage) density, minimizing the overall overpotential losses. The losses in fuel cell operation are depicted schematically and explained in **Figure 1.1**.

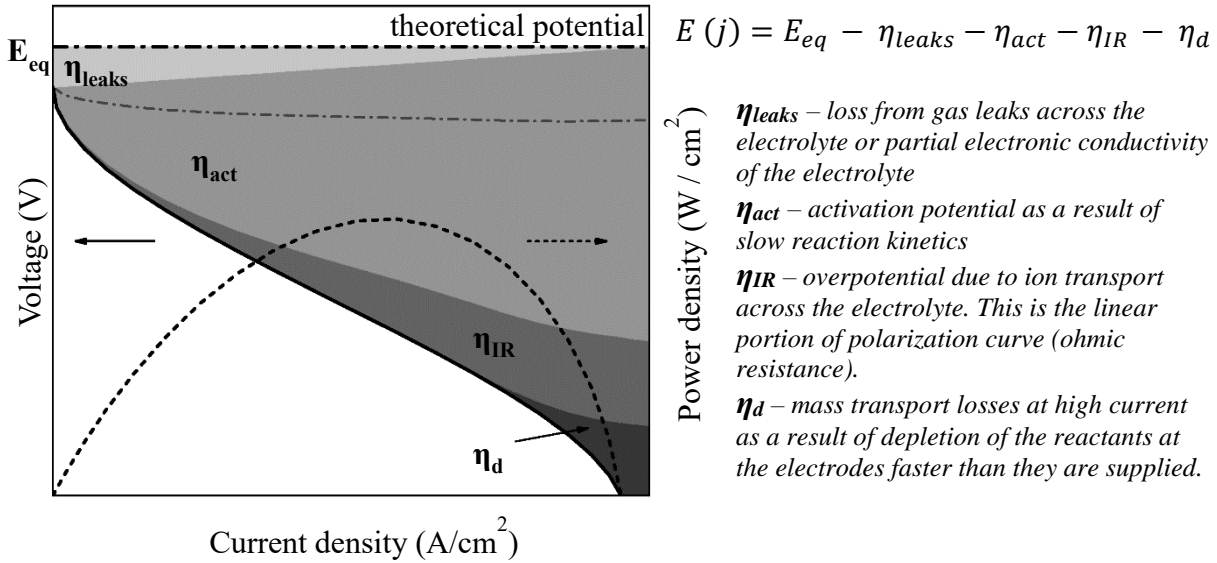


Figure 1.1. Schematic of a fuel cell polarization curve, with contributions of various overpotentials indicated by the shaded regions, and explained on the right. The power density (dotted line) is the product of the cell voltage and current density

It is evident from **Figure 1.1**, that the largest source of overpotential loss is as a result of slow kinetics at the electrodes (η_{act}). η_{leaks} can be minimized by proper sealing of the electrodes and choosing an electrolyte that is a pure ion conductor with high density and low porosity. η_{IR} can be calculated as;

$$\eta_{IR} = jR = j \frac{L}{\sigma}, \quad (1.3)$$

where L is the electrolyte thickness, σ is the proton conductivity and j is the current density. Hence, ohmic losses can be minimized by fabricating electrodes that are as thin as possible and preventing leakage. The activation potential (η_{act}) is related to the rate at which half-cell reactions can occur at the electrodes and is often expressed as

$$\eta_{act} = \frac{RT}{\alpha nF} \ln \left[\frac{j}{j_0} \right], \quad (1.4)$$

where j_0 is the exchange current density that flows under zero overpotential and α is the exchange coefficient, an indicator of the electrochemical activity under non-equilibrium conditions.³ From

Equation 1.4, it is clear that to lower η_{act} and improve electrode activity, larger values of α and j_0 are desirable. If the electrode activity is high, lower overpotentials are required to attain sufficient current densities. To increase the exchange current density (j_0), the number of active sites per electrode area can be increased or the intrinsic activity of the electrode improved. On the other hand, the exchange coefficient (α) is not dependent on electrode geometry and can only be modified by changing inherent material properties.

The requirements for electrodes are obviously more arduous to meet than other fuel cell components. To minimize η_{act} , electrodes must be catalytically active, readily transport electrons and ions to and from reaction sites, and have sufficient porosity, enabling easy gas access, to minimize diffusion losses (η_d). Typically, an electrode is a porous composite of electrolyte (pure ion conductor) and catalyst (electron conductor) particles. The electrocatalytic reaction is limited to the triple-phase boundaries (TPBs) at which the electrolyte, catalyst and the gas phase are in contact as illustrated in **Figure 1.2**. An ideal electrode must have a well interconnected structure to ensure continuous pathways for ion, electron and gas phase transport, since any isolated catalyst site will not contribute to the total measured power density.

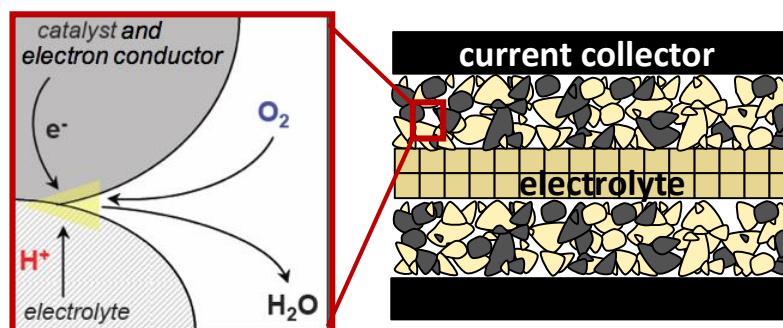


Figure 1.2. Schematic of a typical porous composite electrode showing a proton conducting electrolyte, electron conducting catalyst, and gas phase species (O_2), that comprise a triple phase boundary (TPB) point.

Fuel cells are classified by the type of electrolyte in the cell. **Table 1.1** shows the major types of fuel cells and their characteristics. Low temperature (70-200 °C) fuel cells have the advantage of rapid thermal cycling, making them a convenient option for portable/mobile applications. However, operation with sufficient power density requires high catalyst loading. Generally, high operating temperatures (500-1000 °C) increase the electrode reaction kinetics, allowing for lower catalyst loading and fuel flexibility in terms of tolerance to impurities like

carbon monoxide. However, higher operating temperatures put stringent constraints on the choices for support components and the portability of the fuel cells. Consequently, there is a significant amount of research in lowering the operating temperature of solid oxide fuel cells (SOFCs) and increasing the operating temperature of polymer electrolyte fuel cells (PEMFCs).^{11, 12} Of all the intermediate temperature fuel cells available, solid acid fuel cells have a truly solid electrolyte as opposed to the corrosive liquid electrolyte in phosphoric acid fuel cells. This allows the added benefit of ease of cell stack fabrication and flexibility in support components.

Fuel cell type	Common electrolyte	Operating temperature range (°C)	Transport ion	Fuel
PEMFC polymer electrolyte membrane fuel cell	Nafion™	70 - 110	(H ₂ O) _n H ⁺	H ₂ , CH ₃ OH
AFC alkaline fuel cell	KOH _(aq)	100 - 250	OH ⁻	H ₂
PAFC phosphoric acid fuel cell	H ₃ PO ₄	150 - 250	H ⁺	H ₂
SAFC solid acid fuel cell	CsH ₂ PO ₄	230 - 280	H ⁺	H ₂
MCFC molten carbonate fuel cell	(Na/K) ₂ CO ₃	500 - 700	CO ₃ ²⁻	Hydrocarbons, CO
SOFC solid oxide fuel cell	(Zr/Y)O _{2-δ}	700 - 1000	O ²⁻	Hydrocarbons, CO

Table 1.1. Major fuel cell types and their characteristics.^{3, 10, 13}

1.3. Solid Acid Fuel cells

1.3.1. Solid Acid compounds

Solid acids are compounds whose chemical properties lie between those of an acid such as H₂SO₄ and a salt such as K₂SO₄. Solid acid compounds have a structure typically in the form of MHXO₄, MH₂XO₄ or M₃H(XO₄)₂, where M can be an alkali metal or an ammonium ion and X = P, A, S, Se. In these structures oxyanions XO₄^{2-/3-} are linked by hydrogen bonds and charge balanced by large cations M⁺. A few of these compounds undergo a structural polymorphic superprotonic phase transition.¹⁴ Through this transition, the conductivity jumps by several orders of magnitude to 10⁻² S/cm, which approaches the value of state of the art aqueous proton

conducting electrolytes.^{9, 15} Superprotonic transition behavior has been confirmed for various compounds like CsHSeO_4 and CsHSO_4 ,¹⁶ $\text{Cs}_3\text{H}(\text{SeO}_4)_2$ and $\text{Rb}_3\text{H}(\text{SeO}_4)_2$,¹⁷ CsH_2PO_4 ,¹⁵ $(\text{NH}_4)_3\text{H}(\text{SO}_4)_2$ ¹⁸ and other mixed Cesium sulfate-phosphates.¹⁹ The proton conductivity σ_H as a function of temperature for several solid acids is plotted in **Figure 1.3**.

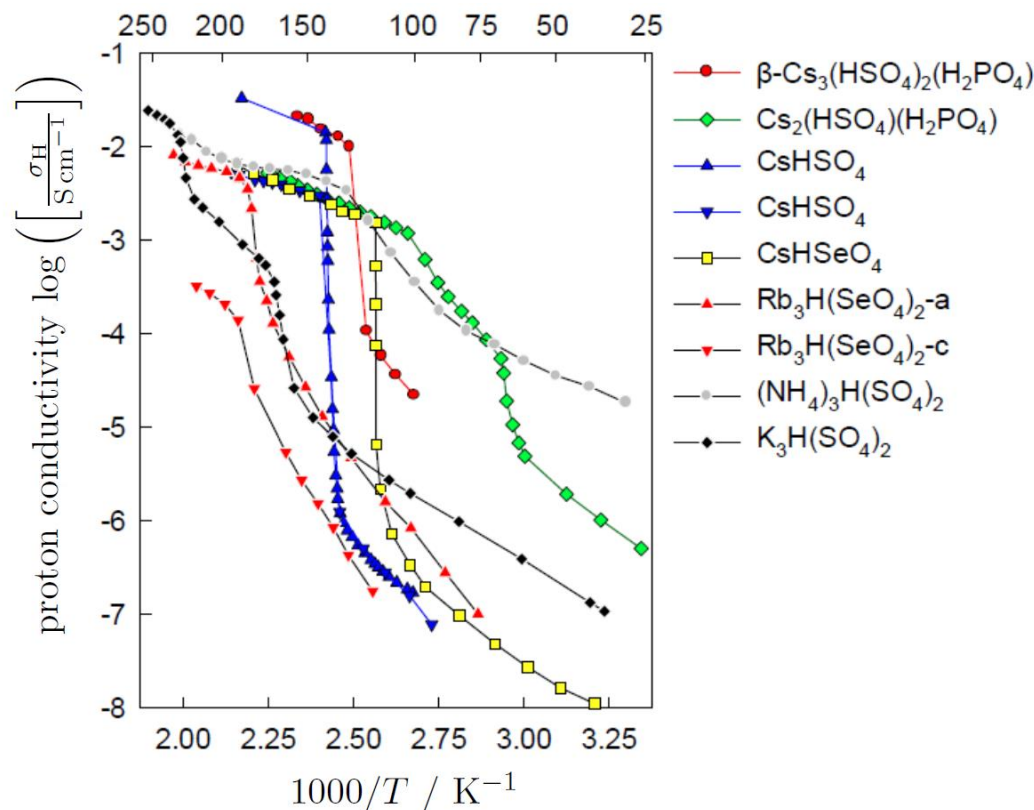


Figure 1.3. Arrhenius plot of proton conductivity, σ_H , of a few solid acid compounds that exhibit a super-protonic phase transition.^{20, 3}

Typical transition temperatures are between 50 °C – 250 °C and the rate of that transition depends on the type of solid acid. For now, cesium di-hydrogen phosphate (CsH_2PO_4) is the most viable solid acid fuel cell electrolyte of the solid acids studied.²¹ Although other solid acids have sufficiently high proton conductivity, studies of selenates and acid sulfates reveal instability of S and Se containing oxyanions in the presence of hydrogen to form H_2S and H_2Se , respectively.²² These by-products are poisonous to precious metal catalysts used in fuel cell operation, hence, S and Se containing electrolytes are considered unsuitable for SAFC operation. CsH_2PO_4 exhibits high proton conductivity of 10^{-2} S/cm upon heating to temperatures above the superprotonic

transition at 230°C¹⁴. CsH₂PO₄ undergoes a polymorphic phase transition from a low symmetry monoclinic phase to a high symmetry cubic phase²⁰. **Figure 1.4a** shows the Arrhenius behavior of CsH₂PO₄ proton conductivity first reported by Baranov *et al.* and confirmed by Haile *et al.* **Figure 1.4a** shows hysteresis behavior of the superprotonic conductivity which is due to the structural incompatibility of the high temperature and low temperature phases.¹⁴ CsH₂PO₄ undergoes a monoclinic to cubic phase transition illustrated in **Figure 1.4b**. The monoclinic structure is comprised of phosphate groups linked in chains by double minima hydrogen bonds, charge balanced by Cs cations. The high temperature structure is a cubic CsCl type structure with a phosphate group in the center and Cs cations at the corners.

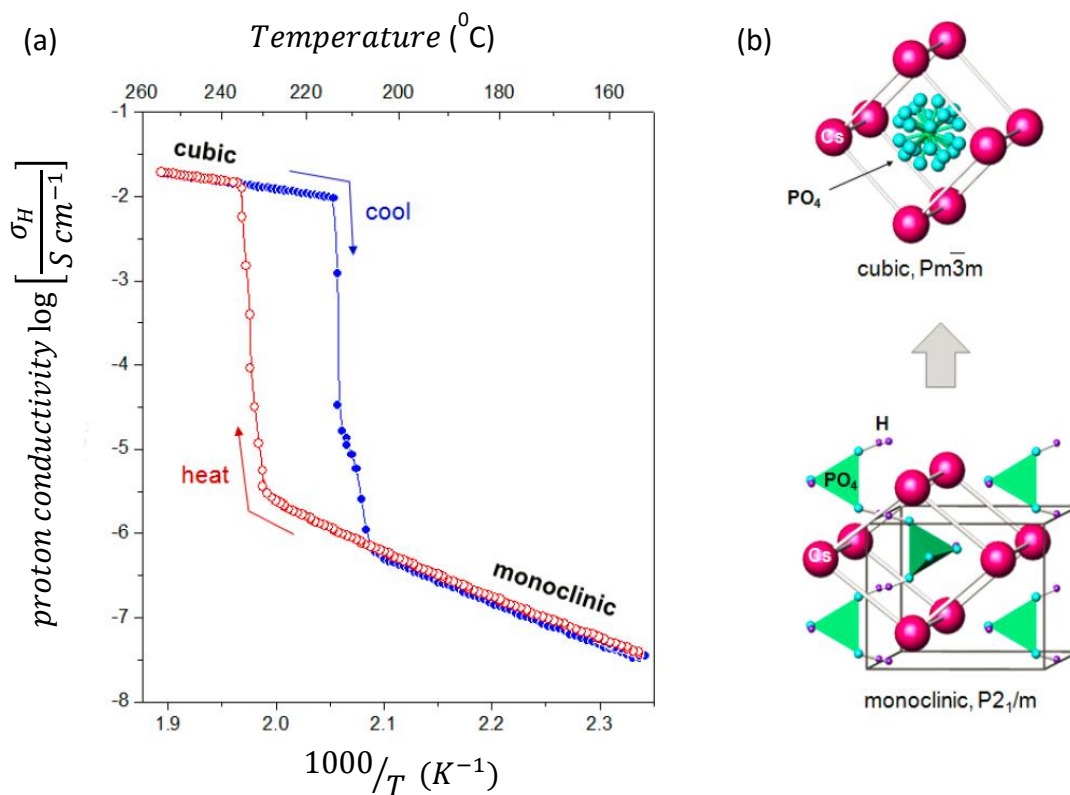
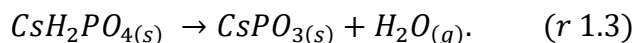


Figure 1.4. Super-protonic phase transition in CsH₂PO₄. (a) Arrhenius plot of proton conductivity (σ), in humidified N₂. (b) Unit cells of monoclinic and cubic phases.^{2, 3}

A major challenge with CsH_2PO_4 is that it is subject to thermodynamic driving forces favoring dehydration at high temperatures. As illustrated in the phase diagram in **Figure 1.5**, when CsH_2PO_4 is heated to superprotonic temperatures the following dehydration reaction takes place:



Above 260 °C a stable conductive liquid phase $\text{CsH}_{2(1-x)}\text{PO}_{4(1-x)}$ is formed.²³ Under application of a suitable partial pressure of H_2O the dehydration reaction can be suppressed.

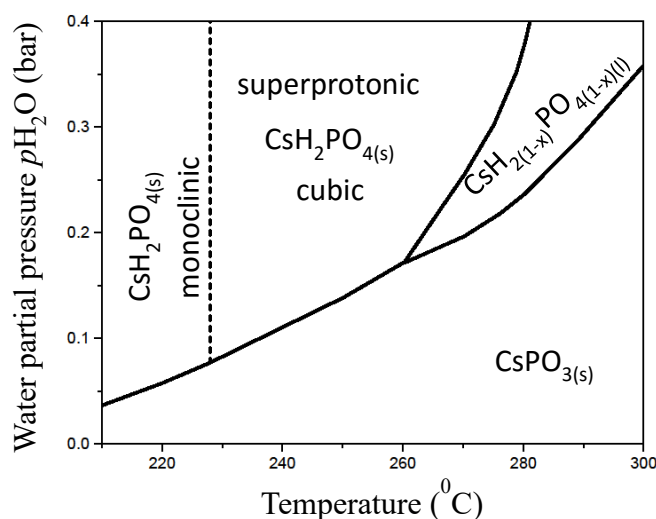


Figure 1.5. Phase stability regions of CsH_2PO_4 adapted from Taninouchi et al.⁵ and Chisholm et al.⁹

While solid acid compounds have a tendency to dehydrate at elevated temperatures, they are soluble in water. This is not a cause for concern as operating temperatures are well above 100 °C and humid reactant/product gases are purged out of the system during on-off cycling. Another challenge in working with CsH_2PO_4 is its high ductility in the superprotonic phase. This is quite undesirable in fuel cell operation but can be easily remedied with the addition of 10 wt% SiO_2 . On the other hand, there is a small loss of about 20% in super-protonic conductivity⁹.

Despite challenges associated with CsH_2PO_4 as a fuel cell electrolyte, CsH_2PO_4 is for now the ideal solid acid. Nevertheless, this is not cause to relax the search for other applicable solid acids. Solid acid compounds are a relatively unexplored class of materials and the full potential is

yet to be exploited. The possibility of having a solid acid that has lower transition temperature and smaller hysteresis in super-protonic conductivity, with similar or better proton conductivity than CsH_2PO_4 , could ease the burden on thermal cycling in SAFC electrolytes. CsHPO_3H has a relatively low transition temperature ($\sim 140^\circ\text{C}$) but has not been pursued as it is expected to be unstable at oxidizing conditions, although related compounds have shown promise as good electrolytes.^{3, 24, 25} In addition, solid acids with sulfur and selenates could be potential solid acid electrolytes after all, if precious metal catalysts are completely eliminated from the fuel cell.

1.3.2. Solid acid fuel cells (SAFCs); basics, challenges and current status

In a solid acid fuel cell (SAFC) the electrolyte is a proton conducting solid acid. The electrolyte between the cathode and anode serves as a barrier to gas diffusion that would otherwise result because of the chemical driving force for oxygen and hydrogen to react to form water. However, the electrolyte permits the transport of hydrogen protons across it. A schematic of a SAFC and the anode and cathode half reactions are presented in **Figure 1.6**.

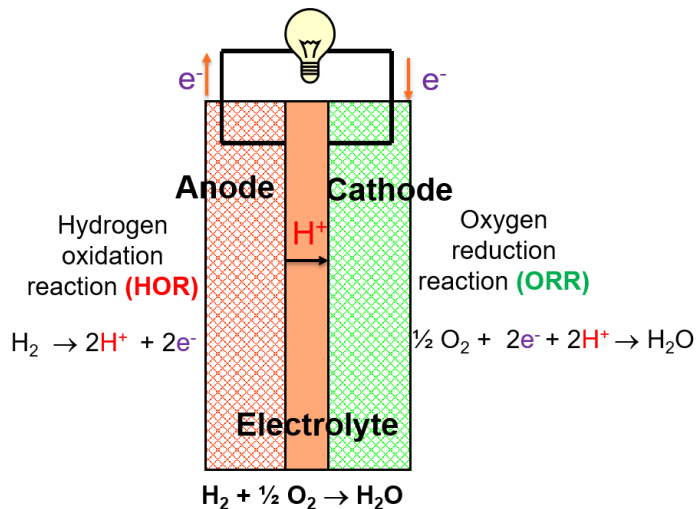


Figure 1.6. Schematic of a fuel cell depicting the anode and cathode half reactions.⁴

Results to date have proven the viability of solid acid fuel cells^{20, 26}, with peak power outputs of 415 mW/cm^2 at 248°C and 8 mg/cm^2 Pt loading²⁷. Power densities of 200 mW/cm^2 have been demonstrated to be scalable to 20 cell stacks, with each cell having a total electrode Pt loading of

4 mg cm² (50 μm CsH₂PO₄ membrane). In addition, SAFCs have shown potential fuel flexibility by demonstrating tolerance to 100ppm H₂S, 100 ppm NH₃, 5% CH₃OH, 5% CH₄, 3% C₃H₈, and 20% CO.

SAFC peak power output is not yet competitive with state of the art polymer electrolyte membrane fuel cells (PEMFCs) or solid oxide fuel cells^{14, 28} Pt loadings of 4-8 mg/cm² are over an order of magnitude higher than competitive loadings (0.1mg/cm² for PEMFCs). A major limitation is the high over-potential loss at the electrodes¹⁴. In **Figure 1.7a**, the electrolyte area specific resistance (calculated from the electrode thickness) is subtracted from the raw polarization curve data. It is clear that ohmic losses from the electrode thickness have a small effect on polarization losses in comparison to slow electro-catalysis¹⁴. The contribution from the anode and cathode is shown in **Figure 1.7b**. It is evident that activation polarization at the cathode is dominant over the anode (~ 2 orders of magnitude larger).

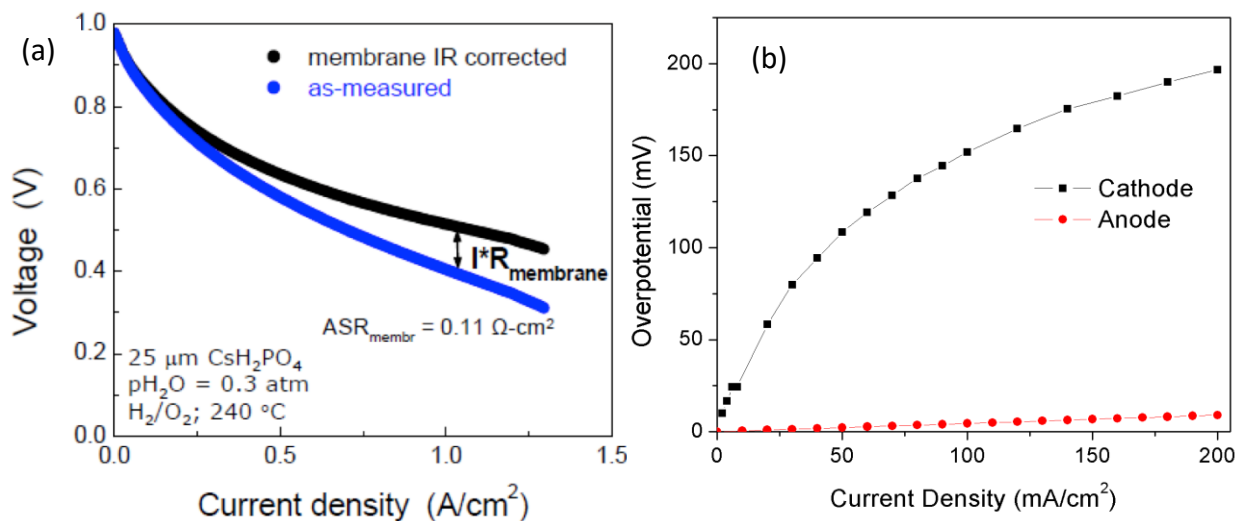


Figure 1.7. (a) IR corrected solid acid fuel cell polarization plot showing small ohmic losses in comparison to other sources of overpotential loss.⁴ (b) Cathode and anode contributions to the overpotential of a SAFC.²⁹

Another major challenge to SAFCs is cost. At present the precious metal loading in SAFCs is about 22 mg Pt/W (Pt costs ~\$1800 per oz), exceeding the target for commercialization by two to three times (\$1000/kW)⁹. With this knowledge, there is tremendous focus on the improvement of SAFC electrodes to increase structural stability, minimize Pt loading and maintain catalytic activity.

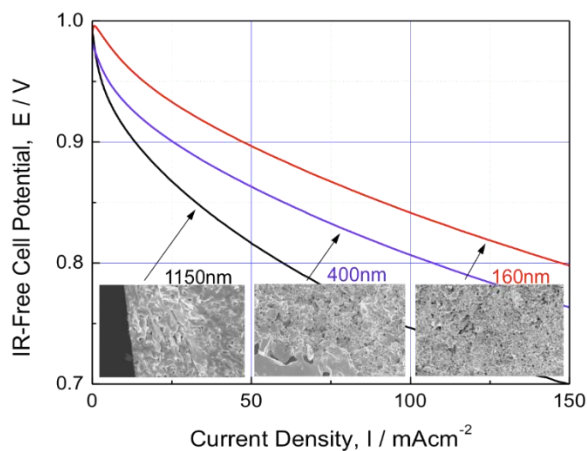


Figure 1.8. Comparison of IR-free polarization curves of SAFCs incorporating different sized CsH_2PO_4 in the cathode. Scanning electron micrographs are shown below.¹

Typical fuel cell electrode fabrication tools include crude techniques like mechanical mixing, slurry deposition and cold pressing. These methods lead to non-ideal CsH_2PO_4 microstructures⁷. Hence, it is nearly impossible to get a high density of TPBs with micron sized CsH_2PO_4 and nanoparticle Pt. Recent successes in incorporating CsH_2PO_4 in SAFCs suggest that intimate mixing of nanoparticles of platinum (Pt) and CsH_2PO_4 dramatically enhances the contact area between the two phases⁹. **Figure 1.8** shows the polarization curve for different CsH_2PO_4 particle sizes. The overpotential losses as a result of the effective charge transfer resistance, has a square root dependence on average particle size, and decreases with decreasing CsH_2PO_4 particle size⁹. Since the activity is inversely dependent on the charge transfer resistance, further reductions in the nanoscale will increase the TPB per unit - projected area, increasing electrocatalytic activity. Accordingly, the goal is to have an interconnected, porous 3D composite. Electro spray deposition has been demonstrated as a suitable method to fabricate this ideal structure.⁷ **Figure 1.9a** shows SEM micrographs of composite anode nanostructures composed of CsH_2PO_4 , Pt-black and polyvinylpyrrolidone (PVP). The anode is a three-dimensional, porous, interconnected CsH_2PO_4 and Pt nanostructure with an average feature size of 100 nm. Impedance spectra of representative $\text{CsH}_2\text{PO}_4 + \text{Pt}|\text{CsH}_2\text{PO}_4|\text{CsH}_2\text{PO}_4 + \text{Pt}$ symmetric, electrochemical cells with electro sprayed electrodes on carbon and a Pt loading of $0.3 \pm 0.2 \text{ mg/cm}^2$ are presented in **Figure 1.9b**. Data was collected under humidified hydrogen with $p_{\text{H}_2\text{O}} = 0.4 \text{ atm}$ at 240°C . The interfacial impedance is $\sim 1.5 \Omega \text{ cm}^2$ for hydrogen electro-oxidation. In comparison to mechanically milled electrodes of Pt

black and CsH_2PO_4 with similar composition, the electrochemical activity is maintained despite a ~ 30 -fold reduction in Pt loading.⁷ This result indicates that electrospray deposition can dramatically increase Pt utilization in SAFC electrodes relative to cruder fabrication methods, however, the specific combination of activity and Pt loading reported here is not sufficient to meet the standard for commercialization.

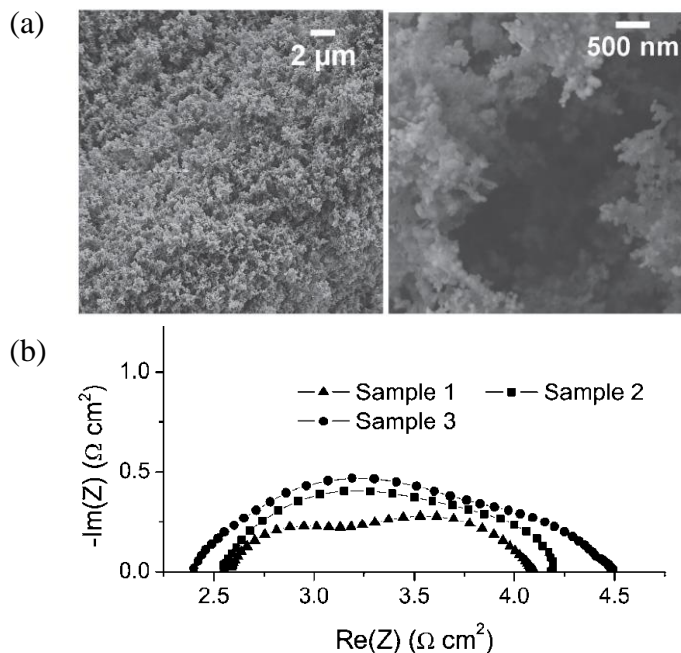


Figure 1.9. (a) SEM micrographs of composite electrode nanostructures comprising CsH_2PO_4 , Pt-black and poly-vinylpyrrolidone (PVP). (b) Impedance spectra of representative $\text{CsH}_2\text{PO}_4 + \text{Pt} | \text{CsH}_2\text{PO}_4 / \text{CsH}_2\text{PO}_4 + \text{Pt}$ symmetric, electrochemical cells with electrosprayed electrodes on carbon and a Pt loading of $0.3 \pm 0.2 \text{ mg/cm}^2$; data collected under humidified hydrogen with $p_{\text{H}_2\text{O}} = 0.4 \text{ atm}$ at 240°C .⁷

To improve current collection in the electrosprayed nanostructures, and consequently the Pt utilization, carbon nanotubes (CNTs) have been explored as interconnects in SAFC anodes to improve the link between nanoscale Pt catalyst and macroscale current collectors. **Figure 1.10** shows the impedance spectra of composites (similar to the composites shown in **Figure 1.9**) electrosprayed onto carbon nanotube overgrown current collectors. Results show about a five-fold improvement in impedance over previous work as a result of improved interconnectivity. This corresponds to a three times improvement in Pt utilization for the same Pt loading.

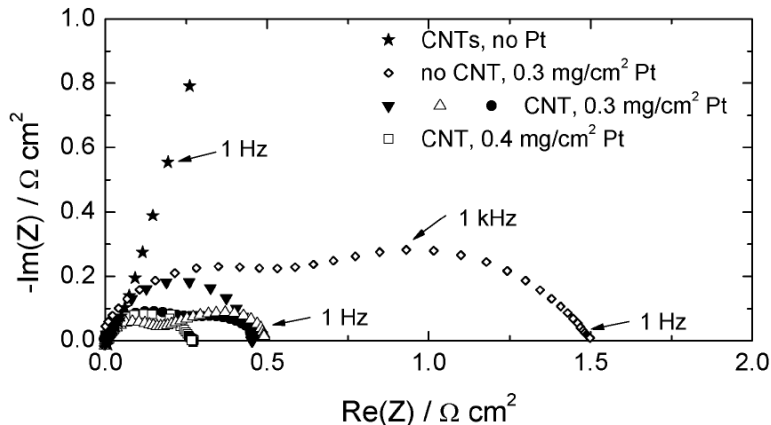


Figure 1.10. Impedance spectra of four $\text{CsH}_2\text{PO}_4 + \text{Pt} + \text{PVP}$ composite electrodes electrospayed onto CNTs, and one without CNTs but otherwise identical.⁶

Further improvements on Pt utilization have been made in solid acid anodes by using Pt decorated carbon nanotubes for hydrogen oxidation.⁸ **Figure 1.11a** details the synthesis approach to decorating the CNTs with Pt. **Figure 1.11b** shows a route to making a symmetric cell with two porous interconnected Pt decorated CNT + CsH_2PO_4 composite electrodes. Impedance

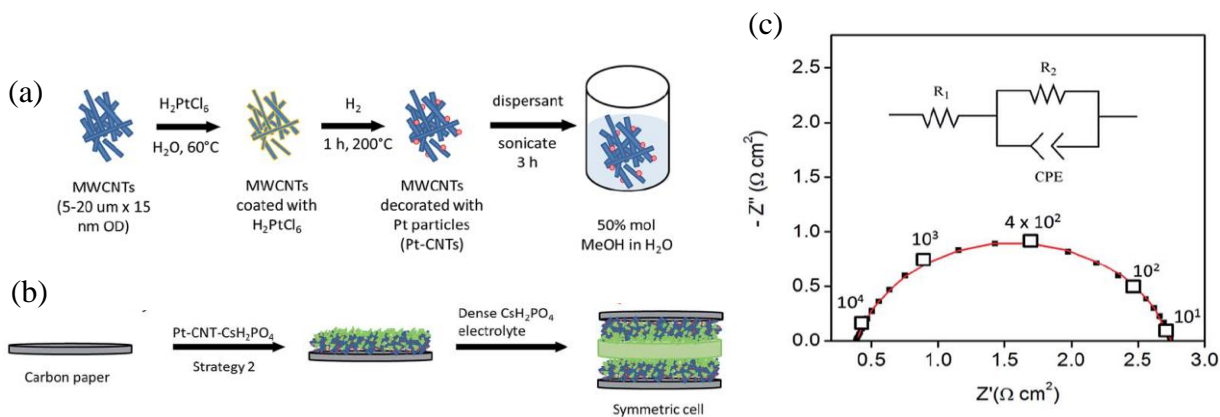


Figure 1.11. (a) Synthetic approach for Pt decorated CNTs. (b) Electro spray deposition strategy of Pt-CNT + CsH_2PO_4 composites. (c) Symmetric cell impedance measurements of 30 wt % Pt-CNT based electrodes. Measurements performed in humidified H_2 ($p_{\text{H}_2\text{O}} = 0.4 \text{ atm}$) and Pt loading is $5.1 \text{ E-}3 \text{ mg/cm}^2$. Inset is equivalent circuit used for fitting.⁸

characterization is shown in **Figure 1.11c**. For a platinum loading of $5.1 \text{ E-}3 \text{ mg/cm}^2$, the electrode area normalized impedance is $\sim 1.5 \text{ } \Omega \text{ cm}^2$. This corresponds to an order of magnitude improvement in Pt utilization over previous work.⁸ Direct growth of Pt nanoparticles onto carbon nanotube

ensures minimal catalyst particle isolation and electro spraying the Pt decorated CNTs + CsH₂PO₄ composites result in uniformly distributed porous nanostructures. **Table 1.2** details the progress of SAFC anodes in terms of performance, Pt loading and Pt utilization thus far.

Anode	Area normalized impedance ($\Omega \text{ cm}^2$)	Pt loading (mg/cm^2)	Pt utilization (S/mg)
Pt + CsH₂PO₄ + Pt/C (3:3:1) mechanically milled ^{26,30}	0.06	7.1	2.2
Pt 7.5 nm sputtered Pt film ³¹	3.1	17E-3	19
Pt + Pt/C + CsH₂PO₄ ⁹ SAFCCell Inc.	0.06	0.8	21
Pt + CsH₂PO₄ (1:2) electro sprayed on carbon paper ⁷	1.5	0.3	2.2
Pt + CsH₂PO₄ + Pt/C (3:3:1) electro sprayed on CNT overgrown carbon paper ⁶	0.5	0.3	6.6
30 wt% Pt-CNT + CsH₂PO₄ electro sprayed on carbon paper ⁸	2.0-3.0	4.9-5.7 ($\times 10^{-3}$)	64-81
40 wt% Pt-CNT + CsH₂PO₄ electro sprayed on carbon paper ⁸	1.6-1.9	6.3-11 ($\times 10^{-3}$)	45-94
46 wt% Pt-CNT + CsH₂PO₄ electro sprayed on carbon paper ⁸	1.2-1.3	10-14 ($\times 10^{-3}$)	61-78

Table 1.2. Progress of Pt-CNT-CsH₂PO₄ SAFC anodes thus far

It is evident that substantial progress has been made in improving Pt utilization in SAFC anodes, however, there is still room for improvement with the Pt decorated CNTs' electrode nanostructure. In addition, as discussed previously, cathode overpotential losses are dominant over anode losses (**Figure 1.7b**). Cathodes require almost an order of magnitude higher catalyst loading than anodes. Therefore, considerable effort is required to increase catalyst utilization in the cathode structures as well. However, further reduction of catalyst loading at the anode gives more leeway for cathode catalyst loading. Hence, SAFCs stand to gain by improving the performance and decreasing the cost of both the anode and the cathode.

1.4. Objectives of this thesis

Alternative cathode catalysts- The oxygen reduction reaction (ORR) at the cathode is the dominant contributor to the overpotential in fuel cell systems, and is therefore the focus of tremendous electrocatalysis research. Generally, the cathode requires higher catalyst loading in various energy conversion processes and the allure of replacing precious metal catalysts with alternatives to precious metal catalysts has garnered attention. This dissertation aims to assess the efficacy of carbon nanostructures and oxides as oxygen reduction (ORR) reaction catalysts in solid acid fuel cells (SAFCs) cathodes.

Enhancing catalyst utilization in SAFC electrodes - The electrospray method has been demonstrated as an electrode fabrication method that can reduce the electrolyte size and increase triple phase boundary density and Pt utilization. In this dissertation, the fundamentals of the electrospray process are explored to understand how the particle size ultimately resulting from electrospray synthesis depends on both solution properties and process parameters.

CHAPTER 2

Experimental methods

In this chapter, we introduce the underlying principles of the characterization techniques and the synthesis methods used in this work.

2.1. Characterization techniques

We can divide characterization techniques into two types: (a) Electrochemical characterization (*in situ*) and (b) *ex situ* characterization. *In situ* techniques use the electrochemical variables of voltage, current and time to characterize the performance of fuel cell under operating conditions. (b) *Ex situ* techniques characterize the structure or chemical properties of fuel cell components employing methods such as Raman spectroscopy, x-ray photoelectron spectroscopy (XPS), and infrared spectroscopy. In this section, Raman spectroscopy is discussed.

2.1.1. Electrochemical characterization (*in situ*)

The most common fuel cell characterization technique is a current-voltage measurement.¹⁰ It provides an overall quantitative evaluation of fuel cell performance and power density. There are two main methods used; in the potentiostatic technique, the voltage of the system is controlled and the resulting current is measured, whereas in the Galvanostatic technique, the current of the system is controlled and the resulting voltage is measured. Either approach can be steady state, where the current/voltage is constant in time, or dynamic, where the current/voltage is varying with time. At steady state, it does not matter whether a potentiostatic or galvanostatic measurement is used to record the *j*-V curve, both methods will yield the same result. Under non-steady-state conditions, potentiostatic and galvanostatic measurements may differ from one another if the system has not had time to 'relax' to its steady state condition. Study of these slow relaxation processes can give better insight to fuel cell performance. Hence, sophisticated dynamic techniques like current interrupt measurement, cyclic voltammetry and impedance spectroscopy are often combined with the steady state *j*-V curve to give a complete picture of fuel cell behavior.

2.1.1.1 Current voltage (*j*-*V*) measurement

In the steady state *j*-*V* measurement, the current/voltage is held fixed in time and the steady state value of the fuel cell voltage/current is recorded after a long equilibration time. A high performance fuel cell will exhibit higher voltage for a given current load. By slowly stepping the current demand, the entire *j*-*V* response of the fuel cell can be recorded. For small fuel cell systems, a slow scan *j*-*V* curve can be recorded where the current demanded is gradually scanned in time from zero to a set limit and the voltage is recorded as it steadily drops. Alternatively, the voltage applied can be scanned in a predetermined range and the resulting current measured. To determine the suitable scan rate, a series of *j*-*V* curves at different scan rates should be measured first. If the scan rate is too fast, the *j*-*V* will be artificially high. The point at which the decreasing the scan speed no longer affects the *j*-*V* curve significantly is usually a good indication of a suitable scan rate.¹⁰

At low current densities as illustrated in **Figure 1.1**, ohmic losses can be calculated from Equation 1.3 and subtracted, and the approximate activation loss can be calculated from the data. If the *j*-*V* curve is plotted on a log scale, the low current density region shows linear behavior. In low-temperature fuel cells, reaction kinetics are slow and large activation potentials are required at both electrodes. Data analysis of the *j*-*V* curve by the Tafel equation allows approximate activation losses to be isolated. The Tafel equation can be written¹⁰

$$\eta_{act} = \frac{RT}{n\alpha F} \ln(j_0) - \frac{RT}{n\alpha F} \ln(j), \quad (2.1)$$

where *n* is the number of electrons transferred in the redox reaction, *j*₀ is the exchange current density, and *α* is the transfer coefficient. Experimental data plotted in the form *η* versus ln(*j*) can be fit with a line that yields a slope of *α* and intercept ln(*j*₀) as illustrated in **Figure 2.1a**. From the Tafel equation, it is evident that to lower *η*_{act}, larger values of *α* and *j*₀ are desirable. To increase the exchange current density (*j*₀), the intrinsic activity of the catalyst needs to be improved or the density of active sites increased. On the other hand, the exchange coefficient (*α*) is not dependent on electrode geometry and can only be modified by changing inherent material properties. **Figure 2.1b** shows the effect of activation potential on fuel cell performance.

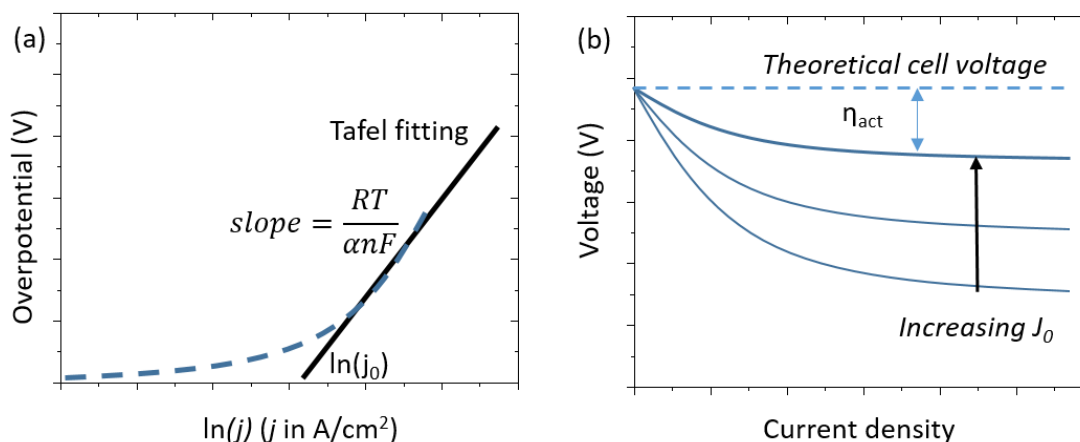


Figure 2.1. (a) The j - η representation of a hypothetical electrochemical reaction. The Tafel approximation deviates from Butler-Volmer kinetics at low overpotentials.¹⁰ (b) Effect of overpotential on fuel cell performance.

2.1.1.2. AC Impedance spectroscopy

Alternating current impedance spectroscopy is the study of microscopic processes simulated by an electric field. It is a widely used technique for fuel cell electrochemistry because it gives insight into material properties, transport processes and electrode | electrolyte interfacial processes.^{10, 32, 33} In an impedance measurement, a low sinusoidal voltage $V(t)$ of varying frequency is applied to the system and the resulting current is measured. The current response will have the same frequency as the voltage perturbation but will generally have a phase shift as illustrated in **Figure 2.2a**. The frequency variation in voltage gives insight into different electrochemical processes in the system with a characteristic timescale. In comparison to a fuel cell measurement, a small signal voltage perturbation confines the impedance measurement to a pseudo-linear portion of a fuel cell's I-V curve as shown in **Figure 2.2b**.¹⁰

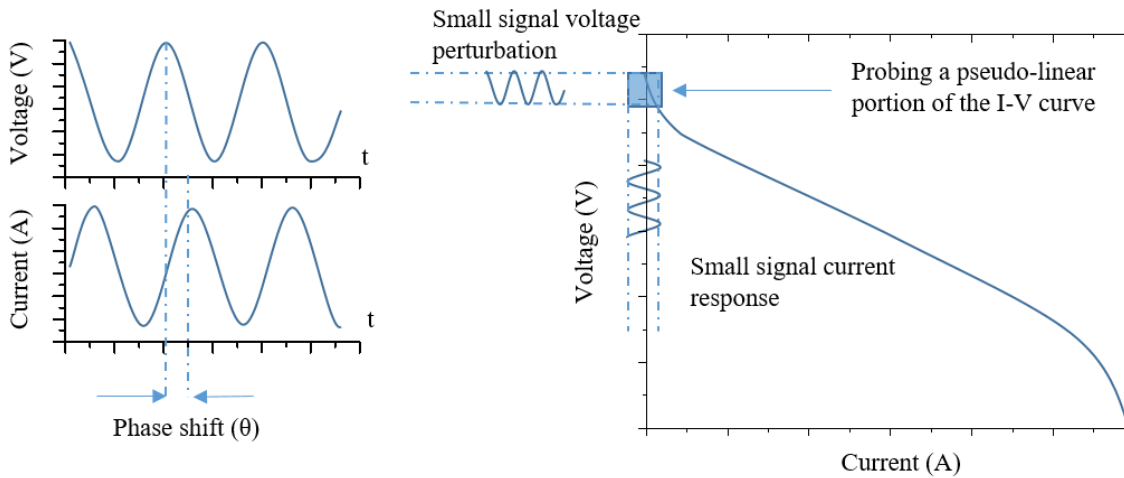


Figure 2.2. (a) Application of a small signal perturbation confines the impedance measurement to a pseudo-linear portion of a fuel cell's I-V curve (b) A sinusoidal voltage perturbation and resulting current response with a phase shift (θ)

The input signal is a complex time-dependent wave function of the form

$$V(t) = V_0 \cdot e^{j\omega t}, \quad (2.2)$$

where V_0 is the amplitude voltage, the angular frequency $\omega = 2\pi f$ and j is the complex index. For a small voltage perturbation, this input potential generates a current output;

$$I(t) = I_0 \cdot e^{j(\omega t + \theta)}, \quad (2.3)$$

where θ is the phase shift. The respective impedance Z is calculated as

$$Z(\omega) = \frac{V(t)}{I(t)} = |Z|e^{-j\theta} = |Z| \cos(\theta) - j|Z| \sin(\theta) = Z_{Re} - jZ_{Im}, \quad (2.4)$$

where Z_{Re} is the real and Z_{Im} is the imaginary part of the impedance and $|Z|$ is the impedance modulus.^{32, 33}

An AC impedance analyzer is able to measure the current output and calculate the frequency dependent impedance response of the system. In a Nyquist plot (Z_{Im} vs. Z_{Re}),

electrochemical processes with sufficiently different characteristic timescales (at least two orders of magnitude apart) can be distinguished as separate arcs along the real axis. Another common representation is the Bode-Bode plot, which is a plot of $|Z|(\omega)$ versus $\theta(\omega)$, where $|Z|$ and θ are

$$|Z| = Z(\omega) = \sqrt{Z_R^2 + Z_I^2}, \quad (2.5)$$

$$\theta = \tan^{-1}\left(\frac{Z_I}{Z_R}\right). \quad (2.6)$$

Figure 2.3a shows the Nyquist plot of a hypothetical fuel cell. For the hypothetical fuel cell, the size of these two semicircles, Z_A and Z_C , can be attributed to the magnitude of the anode and cathode activation losses, respectively. The anode and cathode half reactions are shown in **Figure 2.3b**. Z_Ω corresponds to ohmic losses across the electrolyte. In this hypothetical fuel cell, cathode activation losses dominate fuel cell performance while anode activation and ohmic losses are small. This is the case for many fuel cell types.^{9, 10, 13, 34}

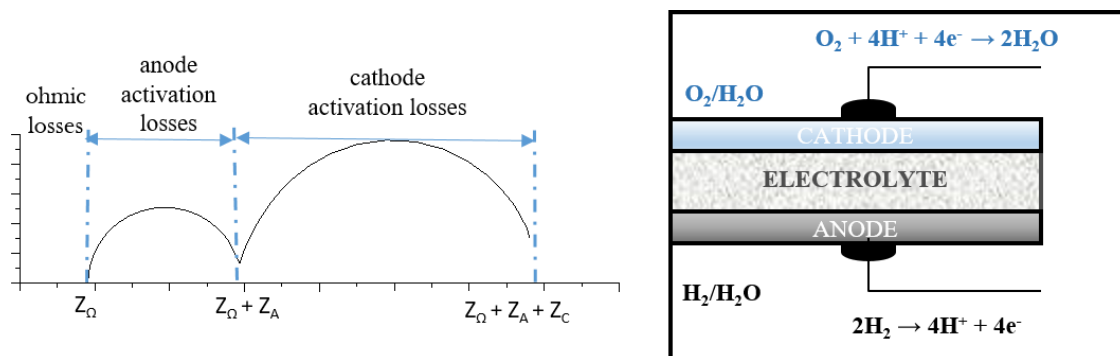


Figure 2.3. (a) Nyquist plot of a hypothetical fuel cell. Regions marked correspond to ohmic, anode activation and cathode activation losses, respectively. (b) Schematic of a fuel cell with cathode and anode half reactions.

The phase shift between the input voltage and output current is as a result of the time-dependent nature of the capacitive processes occurring in the system, such as the charging of the interfaces as depicted in **Figure 2.4b**. The movement of the charged species sampled is a consequence of the perturbation frequency. As depicted in **Figure 2.4a**, at infinitely large frequencies, the charged species samples an infinitely small distance in the bulk of the electrolyte. Hence the resistance to this flow is zero. At a high and finite frequency, the charged species can interact with the bulk

lattice and have a finite impedance. At lower frequencies the interaction of the charged species with grain boundaries can be sampled, and at even lower frequencies the electrode | electrolyte interface can be sampled. The impedance of each of these electrochemical processes can be modelled as a resistor and capacitor in parallel as shown in **Figure 2.4c**. The capacitor describes the charge separation between ions and electrons across the interface. The resistor describes the kinetic resistance to the electrochemical reaction process.¹⁰ At infinitely low frequencies, the impedance measured correspond to the resistance of all the processes in the system. Bulk processes typically have higher characteristic frequencies than electrode processes, hence yield arcs that are well separated from electrode arcs.³

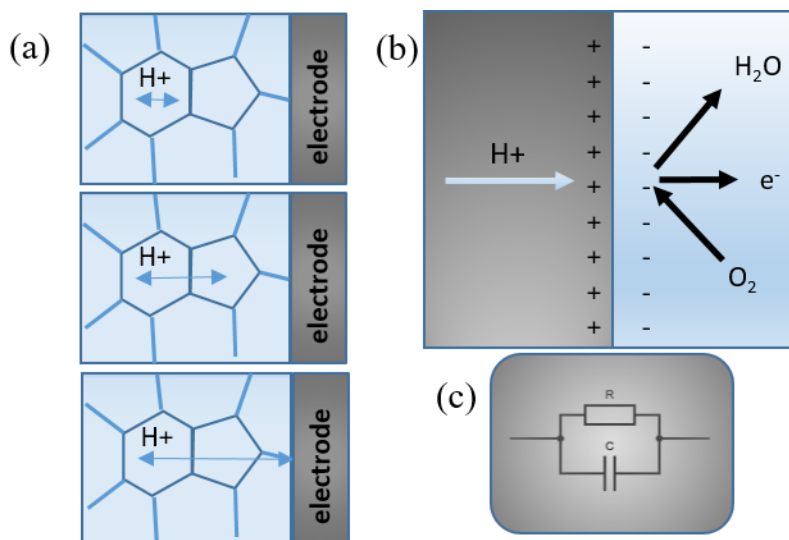


Figure 2.4. (a) An illustration of the movement of a proton under electric field perturbation at varying frequencies. (b) Physical representation of an electrochemical interface. (c) Proposed equivalent circuit model of an electrochemical reaction interface.

Fuel cell testing requires sealing of respective oxidant and fuel gas, hence, symmetric cell AC impedance measurements are common to study individual electrodes. **Figure 2.5a** shows a simulated impedance spectrum of a symmetric cell showing the grain boundary and bulk arcs at mid-range and high frequency. **Figure 2.5b** and **2.5c** show the half-cell reactions for a symmetric cathode cell and anode cell, respectively.

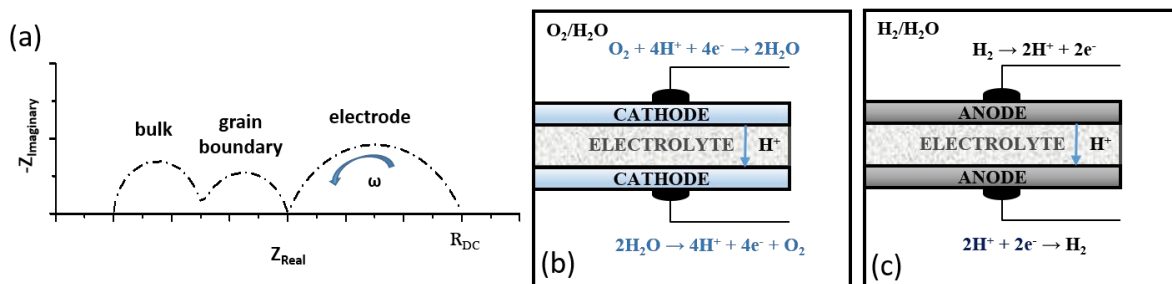


Figure 2.5. (a) Simulated impedance spectrum of a symmetric cell showing the grain boundary and bulk arcs at mid-range and high frequency. Half-cell reactions for a symmetric (b) cathode cell and (c) anode cell.

In this thesis, bulk and grain boundary interactions are not studied in detail, so the frequency range of measurement is selected to study the electrode arc. In addition, in the symmetric configuration, both the forward and reverse half reactions are probed at both electrodes and the forward and reverse reaction kinetics are assumed to have equal activation potential. Hence, the electrode arc measured is divided by two to get the impedance of the cathode or anode.

The modelling of real electrochemical systems can lead to complex equivalent circuits since systems involve both ionic and electronic transport in addition to multiple electrochemical reactions. To analyze electrochemical data, an equivalent circuit model comprised of a combination of discrete circuit elements. An in depth look into equivalent circuit modelling can be found in the literature.^{32, 33} **Table 2.1** shows a summary of the impedance and Nyquist plot of frequently encountered circuit elements. It is noteworthy that only the ohmic resistance (R) is independent of frequency. The inductance is represented as L and the capacitance as C . The constant phase element, Q , is an empirical circuit element introduced to account for deviations from purely capacitive behavior. The constant phase element is purely capacitive when $n=1$ and purely resistive when $n=0$. The Warburg elements (W_s and W_0) are used to describe diffusion phenomena of uncharged reactant species, which undergo a charge transfer reaction. Warburg impedance is derived from a solution to Fick's second law, specifying an unsteady diffusion of the species.³² For reversible diffusion with fast charge transfer and fast supply of the uncharged species at the site where the electrochemical step occurs, the result is a finite-length Warburg circuit element (W_s). For reversible diffusion and slow supply of the uncharged species at the electrochemical step, the result is the blocked Warburg solution (W_0). The solution of the diffusion problem yields $n=0.5$, but n is allowed to vary freely. Thus, n acts as an indicator for non-ideality.³²

Table 2.2 shows the impedance response of several common sub circuits. As shown in **Figure 2.4**, an electrochemical interface can be modelled as a resistor and capacitor in parallel, which generates a perfect semi-circle. There are indications that surface roughness or spatial heterogeneities at the electrochemical interface result in the dispersion of characteristic frequencies of a process and thus can cause a depression of the resulting arc.³⁵ To capture this dispersion, the constant phase element (Q) is used in parallel with a resistor to fit a depressed impedance arc.

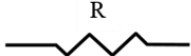
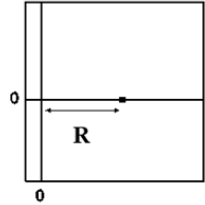
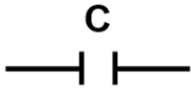
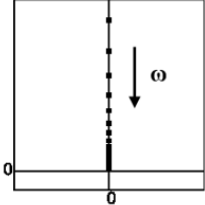
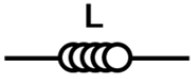
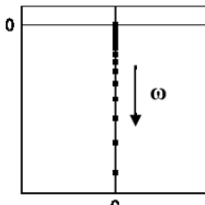
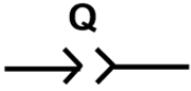
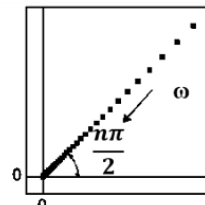
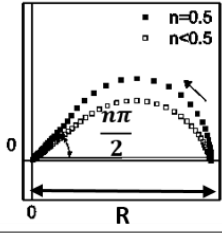
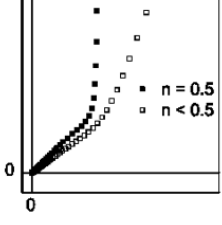
	Impedance $Z(\omega)$	Nyquist plot
resistor 	R	
capacitor 	$\frac{1}{j\omega C}$	
inductor 	$j\omega L$	
constant phase element 	$\frac{1}{Y(j\omega)^n}$	
finite-length Warburg 	$R \frac{\tanh[(j\omega\tau)^n]}{(j\omega\tau)^n}$	
Blocked Warburg 	$R \frac{\coth[(j\omega\tau)^n]}{(j\omega\tau)^n}$	

Table 2.1. Impedance of common circuit elements

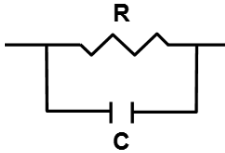
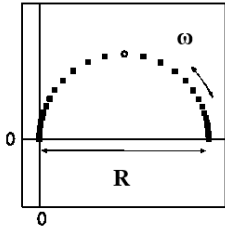
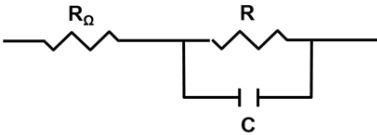
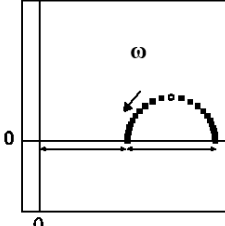
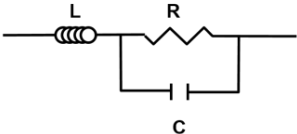
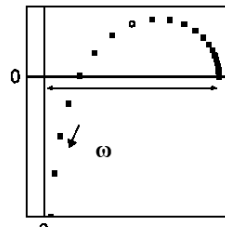
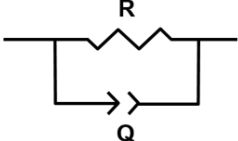
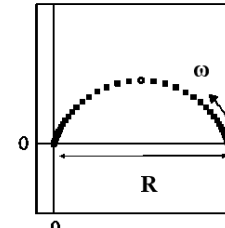
	Impedance $Z(\omega)$	Nyquist plot
	$\frac{R}{1 + \omega^2 C^2 R^2} - j \frac{\omega C R^2}{1 + \omega^2 C^2 R^2}$	
	$R_\Omega \frac{R}{1 + \omega^2 C^2 R^2} - j \frac{\omega C R^2}{1 + \omega^2 C^2 R^2}$	
	$\frac{R}{1 + \omega^2 C^2 R^2} - j \omega \frac{C R^2 - \omega^2 C^2 R^2 L - L}{1 + \omega^2 C^2 R^2}$	
	$\left(\frac{1}{R} + Y(j\omega)^n \right)^{-1}$	

Table 2.2. Impedance response of frequently encountered sub-circuits. The open circle corresponds to the characteristic frequency, ω_0 .

It is important to note, that in analyzing experimental data, choosing a particular circuit element or sub-circuit should be supported with additional evidence about the electrochemical processes being studied. In general, impedance spectra can be fit with several different circuit elements or sub-circuits with similar fidelities. For example, observance of a teardrop shape arc could suggest that the process is rate-limited by diffusion and the spectra could be fit with a finite length Warburg circuit element. However, two or more electrode processes with similar characteristic frequencies can manifest themselves as a single arc with a half teardrop shape.

2.1.2. *Ex situ* characterization

2.1.2.1. Raman spectroscopy

Raman spectroscopy is a two photon inelastic light scattering event where the incident photon is of much greater quantum energy, and loses part of its energy to the molecular vibrations³⁶ thereby emitting a quanta of energy $h \cdot c \cdot (\tilde{\nu}_0 \pm \tilde{\nu}_{vib})$, with the remaining energy scattered as a photon with reduced frequency. Light scattering in terms of electromagnetic radiation (EM) is produced by oscillating dipoles induced in the molecule by the EM fields of the incident radiation. Induced dipole moment occurs as a result of the molecular polarizability, α , where the polarizability is the deformability of the electron cloud about the molecule by an external electric field. The principle of Raman scattering is shown in **Figure 2.6**.

There are two photon processes involving scattering of incident light from a virtual state: Stokes and anti-Stokes. Stokes scattering describes the excitation of a molecule from the ground state by the incident photon with energy, $hc\tilde{\nu}_0$. A new photon is created and scattered with energy $hc(\tilde{\nu}_0 - \tilde{\nu}_{vib})$, leaving the molecule in an excited vibrational state. Depending on the absolute temperature of the sample, according to Boltzmann's distribution some molecules are already excited, hence can perform the reverse scattering process, the so-called anti-Stokes. Both processes lead to second order scattering, resulting in a jump of two vibrational levels. Rayleigh scattering is elastic scattering, hence there is no change in energy.

The intensity ratio of the Stokes relative to the anti-Stokes Raman bands is governed by absolute temperature of the sample and energy difference between ground and excited state. Figure (b) depicts the relative intensities and illustrates the low level of anti-Stokes scattering at ambient temperatures. Therefore, in common Raman spectroscopy only Stokes scattering is detected and anti-Stokes is negligible. In addition, Raman scattering is less probable in comparison to Rayleigh scattering. Hence, high energy lasers are used in addition to a filter that removes Rayleigh scattered photons to get measurable Raman effect.³⁷ Raman spectrometry is best for symmetric vibrations of non-polar groups. Certain functional groups show characteristic frequencies. Only molecular vibrations that cause a change in the polarizability are Raman active.³⁶ In this work, Raman spectra was used for the characterization of carbon materials. First and second-order scattered photons can be detected, as shown in **Figure 2.7**.

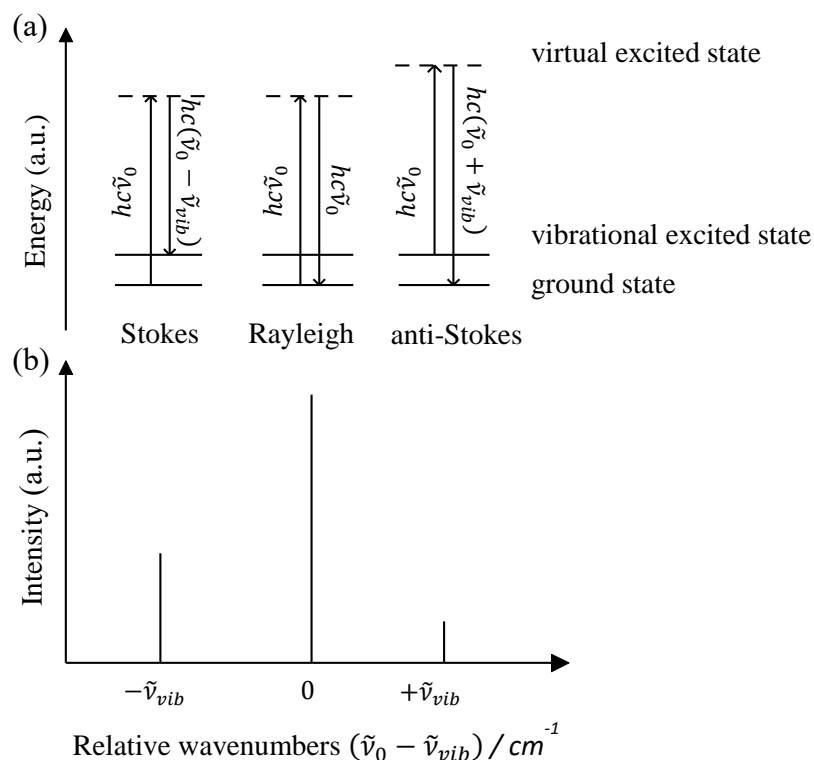


Figure 2.6. (a) Schematic of Stokes, Rayleigh and anti-Stokes scattering. (b) Scattered Raman spectrum intensities plotted against relative wave numbers.

Carbon materials (that are not single crystal) have a variety of bands.^{38, 39} The G band ($\sim 1580 \text{ cm}^{-1}$) is the Raman active mode of graphitic materials. It is relatively constant despite excitation wavelength. The intensities of the D and D' band are defect dependent and these bands are dispersive with incident wavelength.³⁸ These disorders cause a symmetry break of the graphene sheets as a result of impurities, point vacancies, or five/seven member rings.^{40, 41} The D band is also a measure of the density of edge plane exposures.⁴² According to double resonance theory,⁴³ the crystal defects scatter the excited electrons resulting in the wave vector condition that explains the D band appearance. The D and D' bands are a result of elastic phonon scattering, close to the K and Γ points of the Brillouin zone, respectively. The overtone of the D-band is called the G'-band, which is a result of an inelastic phonon emission process, and occurs usually around 2700 cm^{-1} .⁴⁴ Observations indicate that there is a correlation between defect density and I_D/I_G ratio,⁴⁵⁻⁵¹ but there is some influence on structural arrangement on the enhancement of the D band.⁵² Relative

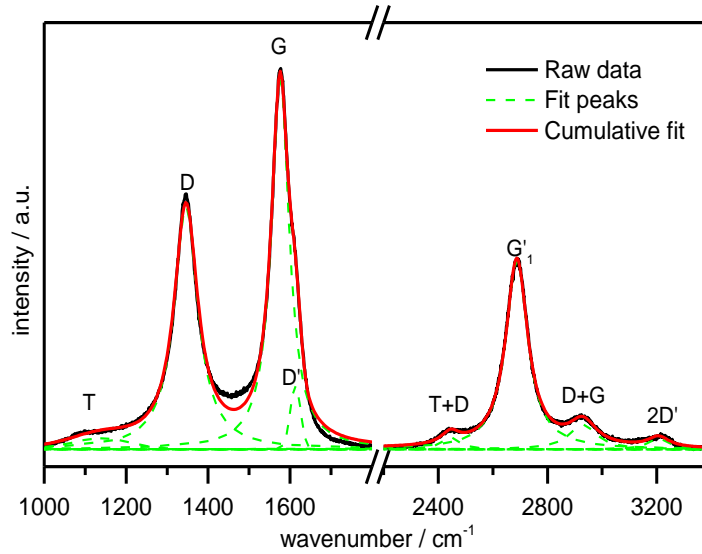


Figure 2.7. First and second-order Raman spectra of a carbon nanotube material. Background corrected spectrum is shown in black, fitted peaks in green dashed lines and cumulative fit peak is shown in red.

intensities of the G+D band follow the same trend as I_D/I_G . T is a band that appears $\sim 1080 \text{ cm}^{-1}$. The T and T+D bands have negative dispersion, that is, they shift to larger wavenumber with increasing incident wavelength. However, these modes are not well studied in the literature and were excluded from the characterization study in this work.

As proposed by Mennella et al and shown in **Figure 2.7**, the black spectrum is deconvoluted and fitted by green Lorentz shaped peaks, with exception of the D' band which is fitted with a Gaussian. This is the best fitting strategy to capture the non-dispersive behavior of the G band and the dispersive behavior of the defect dependent bands.⁵³

The Lorentz shaped peaks used for the fitting of Raman spectroscopy can be expressed as

$$y(x) = y_0 + \frac{2A}{\pi} \cdot \frac{w}{4(x-x_c)^2 + w^2}, \quad (2.7)$$

where A is the integrated intensity and y_0 and x_c are the y-offset and the peak center, respectively. The parameter w describes the peak broadening and can be attributed to the full-width-half-maximum FWHM by

$$FWHM = \sqrt{2 \cdot \ln(2)} \cdot w. \quad (2.8)$$

The Gaussian peak shape used for the fitting of Raman spectroscopy can be expressed as

$$y(x) = y_0 + \frac{A}{w \cdot \sqrt{\frac{\pi}{2}}} \cdot e^{-2\left(\frac{x-x_c}{w}\right)^2}. \quad (2.9)$$

In this thesis, Raman spectra were collected with a Renishaw M1000 Micro Raman Spectrometer System, using a green laser at 514.5 nm. Measurements were made at room temperature, in air, using a depolarized light-source in a wave-number range from 1150-1800 cm^{-1} at 20 s exposure time and a maximum laser power of 6mW on the sample surface. Samples were prepared by dispersing the carbon nanotube in a volatile organic solvent and drying an aliquot of the suspension onto a slide.

2.2. Synthesis methods

The synthesis method discussed is electrospray deposition. The principles guiding the synthesis of electrolyte nanoparticles via electrospray deposition are explained and considered in relation to this work.

2.2.1. Electrospray deposition

Electrospray deposition is a well-established technique for aerosolizing liquids⁵⁴⁻⁵⁸. It has also recently gained attention for thin film fabrication of ceramics, battery electrodes and fuel cell electrodes^{7, 59-69}. It relies on electrostatic forces to expel micron-sized droplets from a charged liquid. Liquid is pumped through a capillary and a counter balance of surface tension on the liquid meniscus and electrostatic forces causes the liquid to emerge in a shape called a Taylor cone⁷⁰. This is called cone-jet mode; at the cone tip a concentrated strong electric field induces the emission of a fine spray of charged droplets. Evaporation occurs as the droplets are accelerated towards the grounded substrate. This results in a charge concentration that induces the columbic breakup of the droplet at the Rayleigh limit as illustrated in **Figure 2.8** and the ultimate deposition of sub-micron to nanoscale particles on the substrate⁵⁷. The electric field required to overcome the surface tension of a liquid and establish a Taylor cone is given as⁷¹

$$E_s = \left(\frac{2\gamma \cos\theta}{\varepsilon_0 r_c} \right)^{\frac{1}{2}}, \quad (2.10)$$

where r_c is the capillary radius, γ is the gas-liquid surface tension, θ is the cone semi vertex angle, and ε_0 is the permittivity of free space.

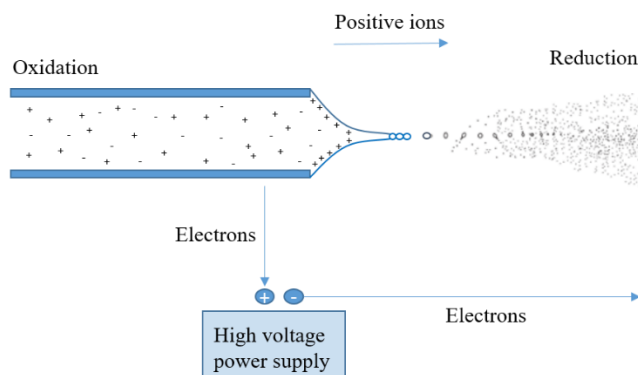


Figure 2.8. A schematic of electro spray ionization, the effluent leaves the Taylor cone as charged droplets that undergo coulombic explosions at the Rayleigh limit.

The equilibrium cone semi-vertex is 49.3° , ignoring space charge effects⁷¹. The onset capillary voltage required to establish this electric field at the capillary tip is

$$V_s = 0.667 \left(\frac{2\gamma r_c \cos\theta}{\varepsilon_0} \right)^{\frac{1}{2}} \ln \left(\frac{4h}{r_c} \right), \quad (2.11)$$

where h is the distance between the capillary tip and the grounded substrate. The greater the distance between the capillary tip and substrate, the higher the voltage required to establish a Taylor cone. Parameters like solvent composition, solution concentration (affecting solution conductivity, surface tension and viscosity), temperature, gas flow rate, and spray geometry (e.g. tip-to-substrate path length, spraying direction) can be varied to tune the characteristics of the resultant structure⁵⁹. Under the appropriate set of conditions, the cone-jet mode of the electro spray method has been employed to obtain porous composite electrode structures of solid acid electrolyte and catalyst with increased triple phase boundaries (TPB) per unit-projected area and reduced Pt loading⁷.

2.2.1.1 Film morphology

Chen *et al.* observed four types of film morphologies from electro spray in the cone-jet regime: dense, dense with incorporated particles, porous top layer with dense bottom layer and fractal-like porous, as shown schematically in **Figure 2.9**.^{60, 64}:

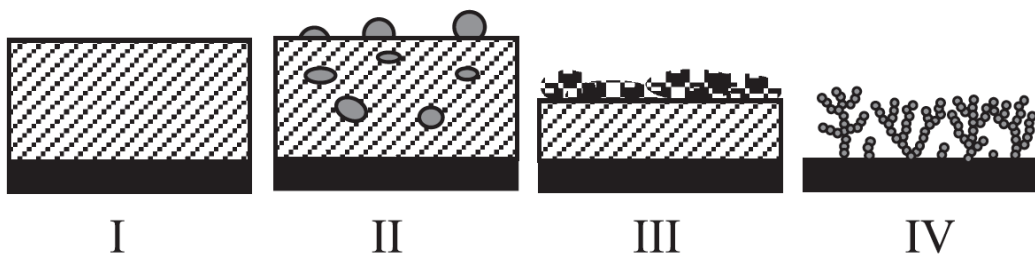


Figure 2.9. Four types of film morphologies obtained by electro spray. I, dense film; II, dense film with incorporated particles; III, porous top layer with dense bottom layer; IV, fractal-like porous structure, according to Chen *et al.*⁶⁰

The authors concluded that the main parameter that determines the film morphology is the substrate temperature, and the concentration of the precursor solution also had an effect. They suggested that the spreading behavior of droplets on the substrate determines the resultant morphology and this behavior is determined by the surface tension of the droplet and the roughness of the coated substrate. They showed that films with low porosity were produced using a solvent with a high boiling point and dense films were produced with a solvent with a lower boiling point⁷². This is a result of slower evaporation of the solvent during the droplet transport and spreading on the substrate causing slower precipitation. Therefore, the morphology of the film can also be tailored by using additives to the precursor solution⁶⁴. Varga *et al.* demonstrated that thin electrolyte films can be deposited as opposed to fractal porous structures by controlling the concentration of the precursor solution and the substrate temperature.⁷

2.2.1.2 Droplet formation and size

A study by Ganan-Calvo presents an integrated analysis that unifies previous observations of different scaling laws under different experimental regimes.⁷³ Under conditions relevant to the

present work ((i) inertial forces dominate the jet development over surface tension and viscous forces, and (ii) electrostatic suction dominates over polarization forces in cone-jet necking), the diameter of the jet is given as⁷³

$$d_j = \left(\frac{\rho \varepsilon_0}{\gamma K} \right)^{\frac{1}{6}} Q^{\frac{1}{2}}. \quad (2.12)$$

where Q is the volumetric flow rate through the capillary. K is the electrical conductivity of the solution. This relation suggests that the size of the droplet decreases with a decrease in flow rate and an increase in conductivity of the solution. Significantly, the viscosity of the liquid and its dielectric constant do not appear to influence the system behavior. The minimal influence of viscosity in this parametric regime, moreover, results in emitted droplets having diameters, d_d , comparable to those of the jet, and thus d_j can be evaluated as a proxy for d_d .⁷⁴ Since the initial droplet size emitted from the cone tip determines the size of the particles deposited, to deposit nanoparticle CsH_2PO_4 for an ideal SAFC electrode the droplet size must be minimized. This puts a large constraint on the flow rate and the throughput of the process.

2.2.1.3 Droplet velocity and travel time

At the cone jet tip, the surface tension forces on the liquid meniscus are counter balanced by the electrostatic forces as

$$F_{\text{surface tension}} = F_{\text{electrostatic}}, \quad (2.13)$$

$$2\pi\gamma d_j = \frac{q^2}{\pi\varepsilon_0 d_j^2}. \quad (2.14)$$

The electric charge of the liquid, q, can be derived as

$$q = \sqrt{2\pi^2 \varepsilon_0 \gamma d_j^3}. \quad (2.15)$$

A force balance on the emitted droplet can be written as

$$F_{electric\ field} = F_{drag} + F_{gravity}, \quad (2.16)$$

$$qE = \frac{\pi C_D \rho d_d^2 u^2}{8 C_c} + m_p g, \quad (2.17)$$

where the drag coefficient, $C_D = \frac{24}{Re}$ in the Stokes regime and the C_c is the Cunningham correction factor or slip factor. The Cunningham correction factor C_c accounts for the “slip” between the particle and the surrounding gas that develops in the transition from continuum to non-continuum flow.^{75, 76} For micron-sized droplets in the continuum range, where $d_d \gg$ mean free path of the sheath gas molecules ($\lambda=60-75$ nm), $C_c = 1 + 1.257 \frac{2\lambda}{d_d} \approx 1$. However, for droplets and or nanoparticles in the free molecular/non-continuum regime, where $\lambda \gg d_d$, $C_c = 1 + 1.657 \frac{2\lambda}{d_d}$. In

Figure 2.10, the velocity of the emitted droplet calculated from the force balance above is plotted for varying liquid CsH_2PO_4 concentration. It is evident that the velocity increases with increasing solute (in this case CsH_2PO_4/CDP). After emission, the electric field gradient (normally also the direction of gas flow) drives the droplets toward the substrate. In addition to the electrostatic force, during travel the droplets experience aerodynamic drag and rapidly approach a quasi-steady-state migration velocity

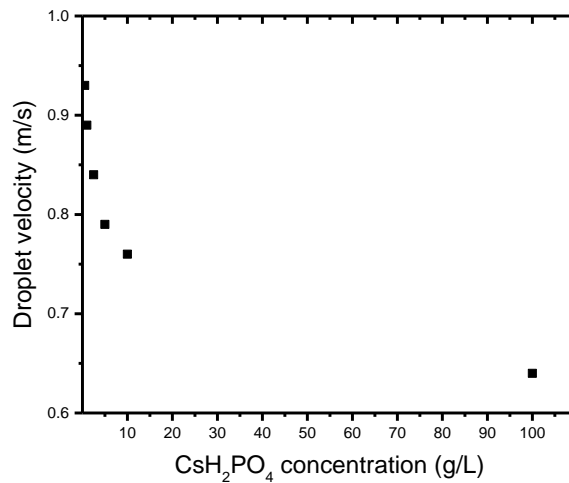


Figure 2.10. Initial droplet velocity of the emitted droplet of varying solid acid concentration.

The characteristic time required to establish this steady-state is the aerodynamic relaxation time, given as⁷⁵

$$\tau = \frac{\rho d_d^2 C_c}{18\eta}, \quad (2.18)$$

where η is the liquid viscosity. These parameters allow informed design of the electrospray setup for desired nanoparticle deposition.

In this thesis, two generations of electrospray stations were fabricated. The first generation electrospray is a single emitter spray station modeled according to specifications in Varga *et al.*⁷ The second is a bi-functional, multi-capillary setup.

CHAPTER 3

Electrochemistry as a tool for evaluating the reactivity of carbon

Section 3.1. Accessing the efficacy of MWCNTs in SAFCs

3.1.1. Introduction

Multi-walled CNTs have been proposed as catalyst support because of their mechanical stability and high thermal and electrical conductivity.^{77, 78} Depending on the chiral symmetry, CNTs can either be metallic or semiconducting. These changes in electronic properties suggest that CNTs can promote electron transfer with an active species in solution.⁷⁹ It has been shown that electrodes modified with CNTs exhibit higher electrochemical response.⁸⁰ Pure CNTs are electrochemically inert. However, during synthesis, electroactive structural and chemical defects can be introduced into the CNT structure.⁸¹ In addition, CNTs can be modified by chemical oxidation or doping to enhance chemical reactivity. Of late, there is much interest in using doped multiwall CNTs as oxygen reduction catalysts in the low to intermediate temperature fuel cell community.

The oxygen reduction reaction (ORR) at the cathode is the dominant contributor to the overpotential in fuel cell systems, and is therefore the focus of tremendous electrocatalysis research. Generally, the cathode requires higher catalyst loading in various energy conversion processes and the allure of replacing precious metal catalysts with fabricated carbon nanostructures has garnered attention.^{82, 83} Gong *et al.* demonstrated nitrogen doped CNT based electrodes exhibit higher power densities than Pt/C electrodes in alkaline fuel cells.⁸⁴ Li *et al.* demonstrated that a nitrogen doped mesoporous CNT nanostructure has higher catalytic activity and better tolerance to methanol cross-over than a comparable Pt/C catalyst.⁸⁵ However, most studies of ORR on carbon nanostructure electrodes are in alkaline media,⁸⁶⁻⁹³ as opposed to acidic media,⁹⁴⁻⁹⁷ because carbon nanostructures are more active at high pH. In general, it is accepted that in alkaline and acidic media, ORR on carbon-based electrodes involves the formation of hydrogen peroxide which is an unwanted by-product in polymer electrolyte fuel cells.^{94, 98}

Most electrochemical characterization of CNT nanostructures is done by cyclic voltammetry (CV) and rotating ring disk electrode (RRDE). This serves as a facile screening method of catalysis and gives insight into kinetics of heterogeneous electron-transfer reactions and coupled chemical reactions. However, it is important to consider the activity of the carbon nanostructure in a composite fuel cell electrode in comparison to platinum. Tang *et al.* showed that cathode stability and fuel cell performance are dramatically degraded due to corrosion of the carbon support in a polymer electrolyte fuel cell (PEMFC) as a result of air leakage into the anode.⁹⁹ Maas *et al.* studied this carbon corrosion mechanism and found that dynamic operation of the PEMFC leads to higher carbon corrosion rates than constant-potential operation, and that carbon oxidation showed strong positive correlation with humidity and temperature.¹⁰⁰

The goal of this study is to assess the efficacy of multiwall CNTs as oxygen reduction (ORR) reaction catalysts in solid acid fuel cell (SAFC) cathodes. SAFCs are intermediate temperature fuel cells in which the electrolyte is a solid acid (cesium di-hydrogen phosphate, CsH_2PO_4 , was used in this study).¹⁵ SAFCs combine kinetic benefits of higher operating temperatures, with the flexibility in fuel and material choices that lower operating temperatures permit. In a previous study, it has been demonstrated that the use of CNTs as platinum supports in SAFC anodes increases current collection and platinum utilization.^{6, 8} In these studies, characterization of the SAFC anodes was done by symmetric cell alternating current (AC) impedance spectroscopy. AC impedance spectroscopy is a powerful facile technique for characterizing a variety of solid state electrochemical systems with the potential to distinguish between electrochemical processes with sufficiently different timescales and determine the contribution of each process to the overpotential losses.^{10, 32} Symmetric cell measurements give information about the resistance of the reaction of interest at equilibrium, (slope of the polarization curve at zero current). The main disadvantage of the symmetric cell AC impedance technique is the inability to probe the catalytic activity at non-equilibrium conditions. In addition, the forward and the reverse half reactions are probed simultaneously and it is not straightforward to isolate the electrochemical behavior in the direction of interest. On the other hand, a current-voltage measurement during fuel cell operation gives quantitative performance of the electrode reaction in the direction of interest. In this work, the ORR activity of bare multiwall CNTs, and CNTs with carboxylic acid and amine functionalization, were studied by AC impedance spectroscopy and current-voltage measurements in gas environments relevant to SAFC operating conditions.

Typically, SAFCs operated at high levels of humidity ($p_{\text{H}_2\text{O}} > 0.2\text{atm}$) are required to inhibit a thermodynamically favored dehydration reaction of CsH_2PO_4 to CsPO_3 at operating temperatures.^{14,15} In this study, we found that at non-equilibrium conditions, the more active CNTs (as characterized by AC impedance spectroscopy) undergo corrosion reactions with steam that degrade fuel cell performance. The reactivity of the CNTs with steam is studied by mass spectroscopy and the corresponding impact on fuel cell performance is investigated.

3.1.2. Experimental

Materials- Commercial multi-walled CNTs and CNTs with carboxylic acid (CNT-COOH) and amine (CNT-NH₂) functionalizations (15 ± 5 nm diameter, 1–5 μm length) were purchased from Nanolab, Inc. CsH_2PO_4 was synthesized in-house by dissolving stoichiometric amounts of Cs_2CO_3 (Alfa Aesar, 99% metal basis, Stk# 12 887)) and H_3PO_4 (Mallinckrodt Chemicals, 85%, Stk#2788-14) in deionized water. The mixture was pipetted into a vat of methanol to induce precipitation of a CsH_2PO_4 powder. The resulting precipitate was dried at 120°C for 6 hours. To increase triple phase boundary density in the electrode layer, fine CsH_2PO_4 was synthesized by precipitating a saturated solution of CsH_2PO_4 in deionized water (100 mg CsH_2PO_4 : 85 mL DI water) through a fine needle (26G1/2) into excess anhydrous methanol (J.T. Baker, #9093-03). The resulting surface area was measured to be $\sim 2\text{--}2.5$ m^2/g by the BET method. Toray carbon paper (TGP-H-120, Fuel Cell Earth, LLC.) was used as the current collector in symmetric cells and fuel cells. Porous stainless steel (McMaster-Carr, Type 316, mesh size 100×100) served as a gas-diffusion layer and mechanical support for the cell.

Cell Fabrication – For electrochemical testing, symmetric cells were configured as: SS | carbon paper | CNT/ CsH_2PO_4 cathode | CsH_2PO_4 electrolyte | CNT/ CsH_2PO_4 cathode | carbon paper | SS. The fuel cell is configured as SS | carbon paper | CNT/ CsH_2PO_4 cathode | CsH_2PO_4 electrolyte | Pt/ CsH_2PO_4 anode | carbon paper | SS. The CNT/ CsH_2PO_4 cathode was prepared by milling a mixture of the multiwall CNTs and fine CsH_2PO_4 . Unless otherwise stated, the CNT/ CsH_2PO_4 electrode is 50 mg in a 1:1 mass ratio. The anode in all cases is 25 mg of a CsH_2PO_4 and Pt on carbon black (40% Pt/Carbon black, Sigma Aldrich) mixture in a 3:1 mass ratio. Cells were fabricated by sequentially depositing the electrode, electrolyte and counter electrode powders into a stainless steel die. The cells were assembled by pressing the cathode and anode composites (in

symmetric configuration it is cathode versus cathode) against *ca.* 700 mg of CsH_2PO_4 powder in a 19 mm die at 69 MPa for 20 min. The thickness of the CsH_2PO_4 solid electrolyte was *ca.* 0.7 mm with *ca.* 90% of the theoretical density. The current collector and the stainless steel gas diffusion layers were placed on either side of the cells. The fuel cells were wrapped in Teflon tape to ensure proper sealing before placing in the custom-built stainless steel anode and cathode cell compartments. Symmetric cell pellets were 1.9 cm diameter and 3 mm thick and fuel cell pellets were 1.9 cm in diameter and ~1 mm thick.

Characterization- CNT defect density was characterized by Raman spectroscopy with a M-1000 Renishaw Ramanscope (514.3 nm) at 20 s exposure time and a maximum laser power of 5.0 mW. Qualitative characterization of polar functional groups was done by Fourier-transform infrared (FTIR) on a Nicolet 6700 FTIR with a deuterated tri-glycine sulfate (DTGS) detector and a potassium bromide beamsplitter (KBr). The morphological features of the CNTs and the cells were characterized using a scanning electron microscope (Zeiss 1550VP field emission SEM) equipped with a secondary electron detector. X-ray photoelectron spectroscopy (XPS) experiments were carried out in an ultrahigh vacuum system (Thermo Scientific ESCALAB 250Xi) equipped with a 180° hemispherical electron analyzer. A monochromatic Al $K\alpha$ X-ray source (1486.7 eV; anode operating at 14.6 kV and 4.35 mA) was used as incident radiation in all XPS measurements. Charging effects were compensated by using a flooding electron gun and Ar ion gun. The XPS core level spectra were analyzed with a CASAXPS fitting routine, which can deconvolute each spectrum into mixed Lorentzian-Gaussian peaks after a Shirley background subtraction. The binding energies were calibrated based on the graphite C 1s peak at 284.4 eV. The standard deviation in XPS core level peak positions is $\sim \pm 0.06$ eV. Thermochemical studies were performed in a tube furnace (Lindberg/Blue M #STF54434C) held at 800 °C, with the CNTs placed in an alumina crucible at the center of the furnace. The sheath gas (argon) was humidified by passing the gas through a bubbler upstream of the furnace and dehydrated by passing through a condenser (held at 1 °C) downstream of the furnace. The exhaust was sampled by a quadrupole mass spectrometer (Pfeiffer ThermoStar GSD301T2) every 0.44 sec. Quantification of the mass spectrometry data was achieved by a six-point calibration with known compositions of hydrogen and oxygen in Ar. The Arrhenius dependence of hydrogen current was collected by cooling the sample down from 800 °C to 600 °C and allowing it to equilibrate for 4 hours and then heating the

sample up from 600 °C to 800 °C and the resulting ion current measured. Thermo-gravimetric analysis (TGA) of the CNTs was conducted in air at 280 °C (heating rate of 2 °C/min) by a Netzsch Model STA 449C Jupiter.

AC impedance spectra on the symmetric cells were collected using a Solartron 1260 Impedance/Gain-Phase Analyzer. The perturbation voltage was 40 mV and the frequency range was 5 mHz to 10 kHz. The cell was initially heated to 140 °C at 2 °C/min in air, then heated up to 250 °C under Ar humidified through a water bubbler held at 80 °C (saturation $p_{\text{H}_2\text{O}} = 0.4$ atm). At each condition, the cells were equilibrated for 10 minutes before collecting the impedance spectra. Polarization curves were measured with an AutoLab PGSTAT20N instrument, the cells were cycled between 0.95 V and 0.0 V at a scan rate of 2.5 mV s⁻¹. Impedance measurements on fuel cells were collected using the same Autolab instrument. The perturbation voltage was 40 mV and the frequency range was 10 mHz to 0.2 MHz. Impedance data was fitted with was fitted with a blocked Warburg circuit element with Zview (Scribner Associates).

3.1.3. Results and discussion

Surface characterization- Fourier transform infrared (FTIR) spectroscopy can identify organic functional groups on the MWCNT surface by measuring characteristic vibrational modes. Surface functional groups of the as-received CNTs were characterized by Fourier transform infrared (FTIR) spectroscopy. As shown in **Figure 3.1a** CNTs with carboxylic acid functionalization (CNT-COOH) have characteristic carbonyl ($w = 1730$ cm⁻¹), hydroxyl ($w = 1575$ cm⁻¹), and carboxylic acid groups ($w = 1150$ cm⁻¹). CNTs with amine functionalization (CNT-NH₂) have the characteristic amide ($w = 1700$ cm⁻¹) and amine ($w = 3290$ cm⁻¹) peaks. Both sets of peaks are consistent with the literature.¹⁰¹⁻¹⁰³ The structural quality of the MWCNTs can be characterized quantitatively by Raman spectroscopy. Characteristic D ($w = 1350$ cm⁻¹), G ($w = 1585$ cm⁻¹), and D' ($w = 1619$ cm⁻¹) peaks appear in the wavenumber region of 1150-2250 cm⁻¹ as first order Raman modes.³⁸ The G band is as a result of tangential in-plane stretching of C-C bonds in graphene sheets.^{50, 104} The D and D' bands are a double resonance Raman mode and can be attributed to CNT defects.³⁹ Raman spectra of the as-received CNTs are presented in **Figure 3.1b**. As proposed by Mennella *et al.*, the D and G bands were fitted with Lorentzian curves and the D' band was

fitted with a Gaussian (shown inset).⁵³ The integrated intensity ratio (I_D/I_G) is a measure of defect density.^{39, 105} CNT-COOH and CNT-NH₂ have higher defect densities than un-functionalized CNTs. The defects are attributed to bends, kinks in the graphite planes and missing carbon atoms in the hexagonal ring. In addition, acid refluxing can shorten the CNTs, increasing the density of edge plane sites and consequently the measured structural defect density.^{50, 106} XPS C 1s, N 1s, and O 1s peaks of the as-received CNTs are presented in **Figure 3.2** and curve fitting results (Casa XPS) are summarized in **Table 3.1**. In general, CNT and CNT-COOH samples have no nitrogen content and CNT-NH₂ samples have 5% nitrogen content. CNT-COOH has the highest oxygen content (22%) followed by CNT-NH₂ (7%) and CNT (3%), respectively. The carbon to oxygen ratio for each sample is calculated as $C/O_{\text{CNT}} = 32$, $C/O_{\text{CNT-NH}_2} = 13$, and $C/O_{\text{CNT-COOH}} = 3.5$. CNT-NH₂ is made by reacting CNT-COOH powder with ethylene diamine, hence it follows that there is residual oxygen. The appearance of the N 1s peak at 399 eV indicates presence of pyridinic nitrogen on the CNT surface.^{103, 107} The appearance of the O1s peak at 532.2 eV is assigned to oxygen in a double bond with carbon atoms (C=O or O-C=O).¹⁰⁸ Deconvolution of the CNT, CNT-NH₂, CNT-COOH C1s spectra has a characteristic peak at 284.4 eV and ~291 eV attributed to sp² hybridized graphitic carbon atoms and the characteristic shakeup line of carbon in aromatic compounds (π - π^* transition loss), respectively.^{77, 109} The most intense peak in the C 1s scan appears at ~285.8 - 285.9 eV. This peak is likely a sum of contributions from sp³ hybridized carbon atoms that are a result of structural defects at the surface of the graphitic sheet (amorphous carbon atoms in another state to typical graphitic sp² carbon atoms), typically present at 285.5 eV, and C-OH species, typically present at 286 eV.¹⁰⁸⁻¹¹¹ There isn't a significant difference between the CNT and the CNT-NH₂ C 1s scans. The CNT C 1s scan has a peak at 287 eV assigned to carbon atoms in a double bond with oxygen (C=O bonds in quinones, ketones and aldehydes).⁷⁷ This peak is slightly shifted to 286.9 eV in the CNT-NH₂ C 1s scan. According to literature, the presence of C-N shifts the characteristic C=O peak to a lower binding energy of 286.5 eV.^{103, 107} As the nitrogen content is about 5% as indicated in **Table 3.1**, there isn't a significant peak shift. The CNT-COOH C 1s scan has a peak at 288 eV that originates from the COOH species, absent from the CNT and CNT-NH₂ spectra.^{77, 108}

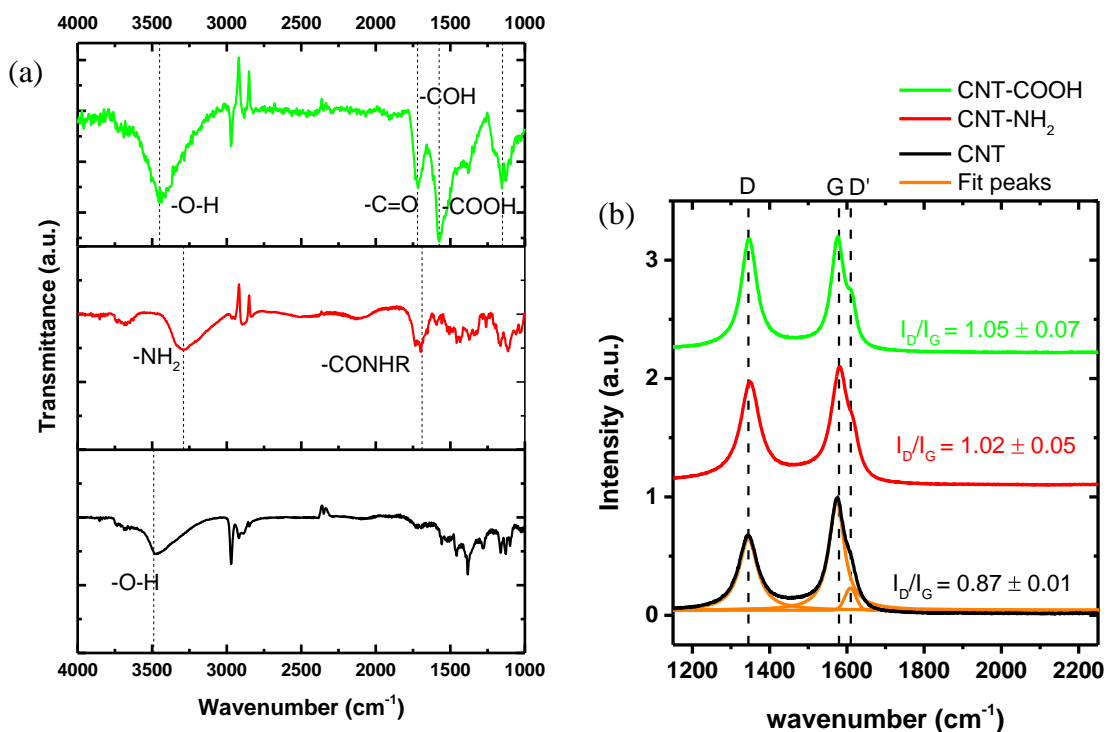


Figure 3.1. (a) Fourier-Transform infrared (FTIR) spectra of hollow CNTs, CNT-NH₂ and CNT-COOH. Dashed lines identify peaks corresponding to labelled functional groups. (b) First order Raman spectra of the CNTs, CNT-NH₂ and CNT-COOH. The dashed lines specify the peak position of the D band, G band and D' band. The defect density characterized as the ratio of the D band intensity to the G band intensity is shown inset.

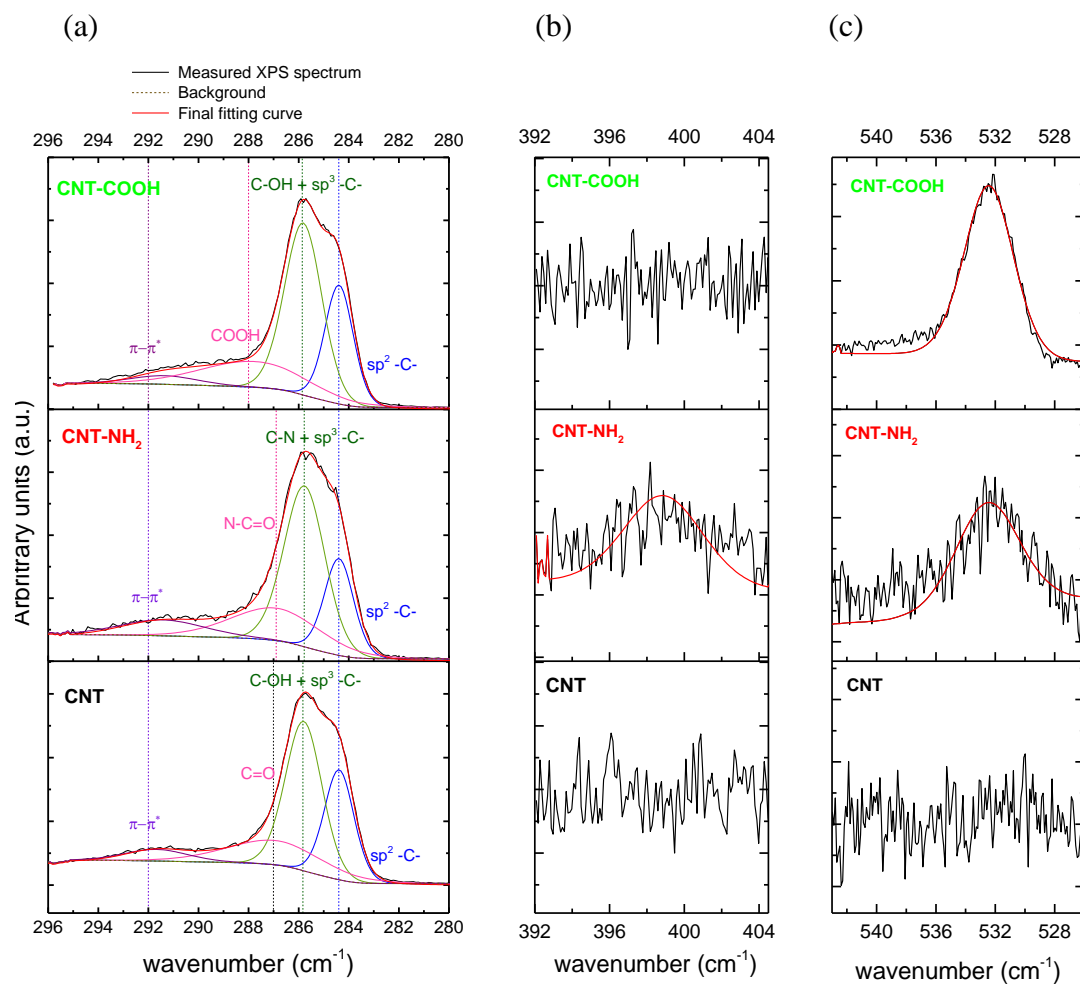


Figure 3.2. Deconvolution of the XPS (a) C1s, the (b) N1s and (c) O1s spectra of the CNTs, CNT-NH₂ and CNT-COOH.

	Binding energy (eV)				Total		Total	C/O
					C1 %	N1 %	O1 %	
CNT	291.7 π - π^*	286.9 C=O	285.9 C-OH + sp ³ -C-	284.4 sp ² -C-	97	-	532.2	32
	3	10	71	13				
CNT-NH ₂	291.4 π - π^*	286.8 N-C=O	285.8 C-OH + sp ³ -C-	284.4 sp ² -C-	88	5	399	532.2
	4	10	65	9				
CNT-COOH	291.4 π - π^*	287.8 COOH	285.9 C-OH + sp ³ -C-	284.4 sp ² -C-	78	-	532.2	3.5
	2	8	58	10				

Table 3.1. Integrated atomic concentrations of MWCNTs, MWCNT-NH₂, and MWCNT-COOH from XPS characterization

Thermal stability in air- Thermal stability of the varying CNTs was characterized by thermogravimetric analysis (TGA). Thermo-gravimetric analysis (TGA) profiles for the CNTs in dry air is presented in **Figure 3.3**. Functionalized CNT samples exhibit weight loss at 280 °C (~8% for CNT-COOH and ~3% for CNT-NH₂) while the plain CNTs have negligible weight loss in air. The trend in mass loss suggests that there are reactive functional groups present in CNT-COOH, and less so in CNT-NH₂, that are evolved at 280 °C. The elemental composition of the CNT-COOH powders was quantitatively characterized by XPS, before and after TGA analysis. Curve fitting results from the C 1s and O 1s scans are summarized in **Table 3.2**. The oxygen content is decreased in the post-TGA CNT-COOH powders, hence, the C/O atomic ratio increases with oxidation in air from 3.5 to 5.2. However, there is an increase in the relative concentration of the –COOH species (from 8% - 10%), and structural defects (sp³ –C-) with oxidation in air.

Thermal stability in humidified atmosphere- Mass spectroscopy analysis reveals hydrogen evolution upon heating in humidified argon (pH₂O = 0.2 atm). **Figure 3.4a** shows the ion current of ratio of H₂ to H₂O of 400mg of the varying multi-walled CNTs at pH₂O = 0.2 atm and 800 °C. The temperature and humidity levels were chosen to maximize signal above the mass spectrometer

detection limit. There is a correlation between the water signal and the hydrogen signal, giving excess to the hydrogen mass. Hence, the ratio of $H_2 : H_2O$ ion current is reported as the metric for hydrogen production comparison between samples. In **Figure 3.4a**, the hydrogen production of CNT-COOH is greater than CNT-NH₂ and CNT. **Figure 3.4b**, shows that at 800 °C, hydrogen production decreases with decreasing humidity for CNT-COOH and CNT. **Figure 3.5** shows the Arrhenius behavior of hydrogen production from a CNT-COOH sample in humidified argon. The hydrogen detection limit of the mass spectrometer is reached at ~600 °C. To estimate the amount of hydrogen produced in CNT-COOH electrodes at 250 °C, the high temperature behavior (linear region) is extrapolated to 250 °C. The hydrogen concentration estimated from the data collected during the cool down measurement is 3E-15 atm, and the hydrogen concentration estimated from data collected during the heat up measurement is 4E-15 atm. It is important to note that this measurement was taken on a 200 mg of CNT-COOH sample in 250 sccm of argon and $p_{H_2O} = 0.2$ atm. At SAFC testing conditions, 50 mg of CNT-COOH is at the cathode, at a gas flow rate of 40 sccm and $p_{H_2O} = 0.4$ atm. However, it is clear that the functionalized CNTs have higher reactivity with steam than the un-functionalized CNTs.

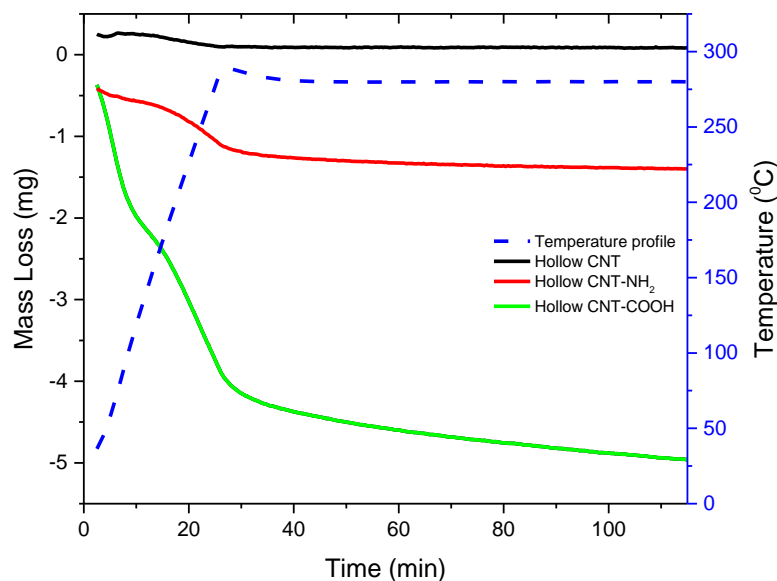


Figure 3.3. TGA profiles for hollow MWCNTs, MWCNT-NH₂ and MWCNT-COOH measured under flowing air at a heating rate of 2 °C/min.

						Total C1 %	Total O1 %	C/O
Binding energy (eV)	291.4	287.8	286	285.5	284.4		532	
	$\pi-\pi^*$	COOH	C-OH	sp^3 -C-	sp^2 -C-			
CNT- COOH	2	8	19	39	10	78	22	3.5
CNT- COOH (post TGA)	1.5	10	21	42	10	84	16	5.2

Table 3.2. Integrated atomic concentrations of hollow CNTs and hollow CNTs after 12 hours in oxidizing atmosphere at 250 °C

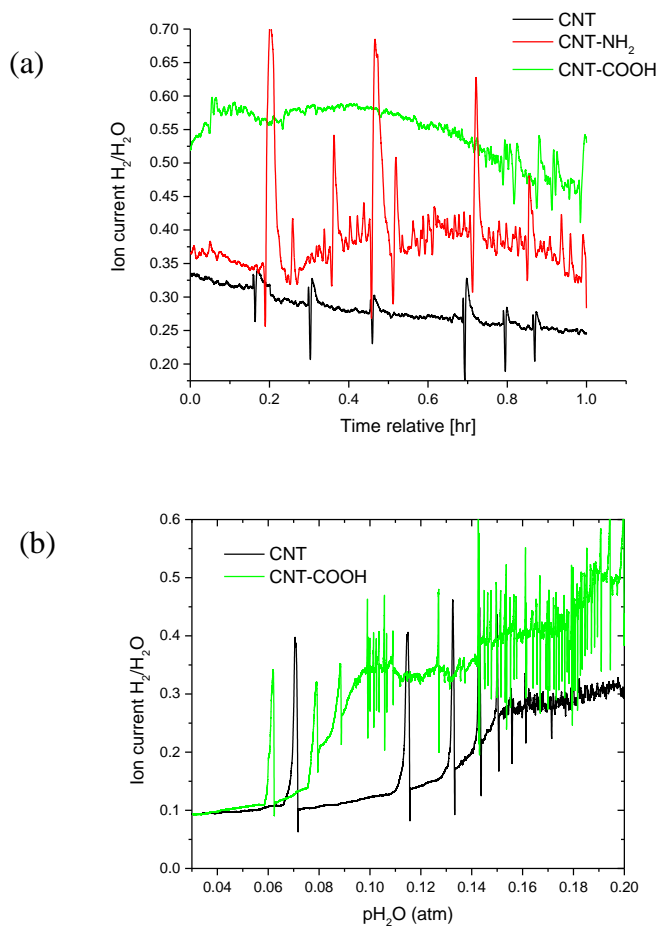


Figure 3.4. (a) Ion current ratio of H₂ to H₂O for 400 mg of hollow CNT, hollow CNT-NH₂ and hollow CNT-COOH at pH₂O = 0.2 atm and 800°C. (b) Ion current ratio of H₂ to H₂O for 400 mg of hollow CNT and hollow CNT-COOH with varying pH₂O.

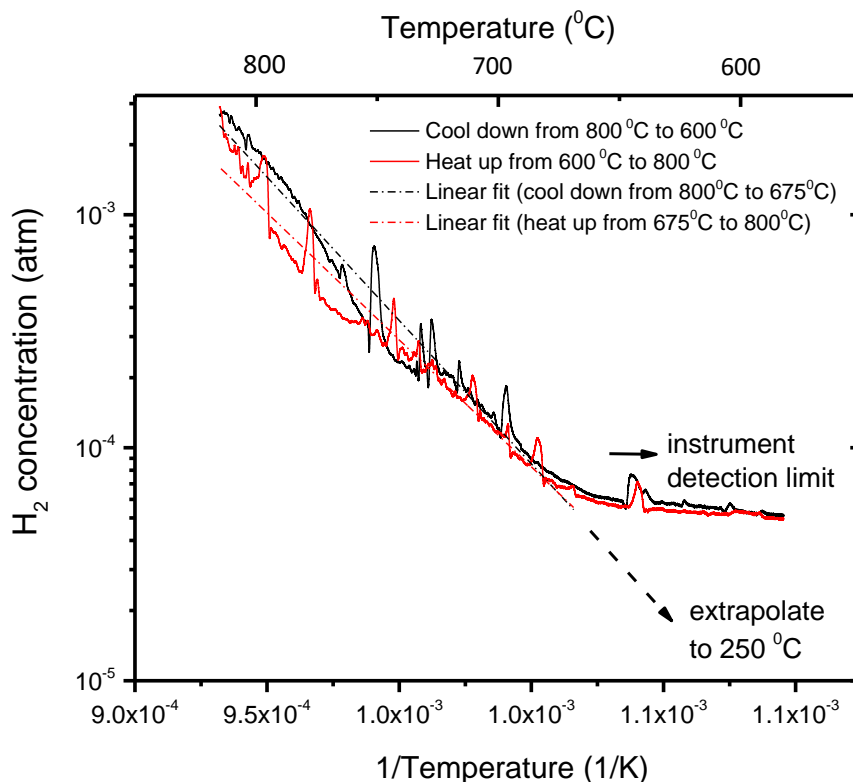


Figure 3.5. Arrhenius plot of H_2 ion current versus inverse temperature of the cool down and heat up between 800°C to 600°C of 200 mg of CNT-COOH (ramp rate is $100^\circ\text{C}/\text{hour}$).

Morphology characterization- The CNTs are ‘hollow’ multi-walled CNTs that are of 15 ± 5 nm diameter and 1–5 μm length. The cross section of the electrode | electrolyte interface of the CNT, CNT-NH₂, CNT-COOH symmetric pellets after impedance testing is shown in **Figure 3.6a**, **3.6b**, and **3.6c**, respectively. It appears that the electrolyte/catalyst mixing improves with functionalization. For equal electrode mass, electrode thickness decreases as CNT > CNT-NH₂ > CNT-COOH. It has been shown in the literature that oxygen functionalities increase hydrophilicity of CNTs.¹¹² Therefore, it is likely that interconnectivity between hydrophobic CNT powders and hydrophilic CsH₂PO₄ during electrode fabrication improves with increasing oxygen content. Impedance spectra collected on CNT symmetric cells in humidified argon and on fuel cells in H₂ | N₂ atmosphere show a decrease in diffusion resistance with a decrease in electrode layer thickness (see **Figure 3.S.1** in Supplemental Information). However, it is unclear whether surface functionalities directly enhance proton transport through the electrode, or if the decrease in

electrode thickness (as a result of improved mixing) is the reason for decrease in diffusion resistance.

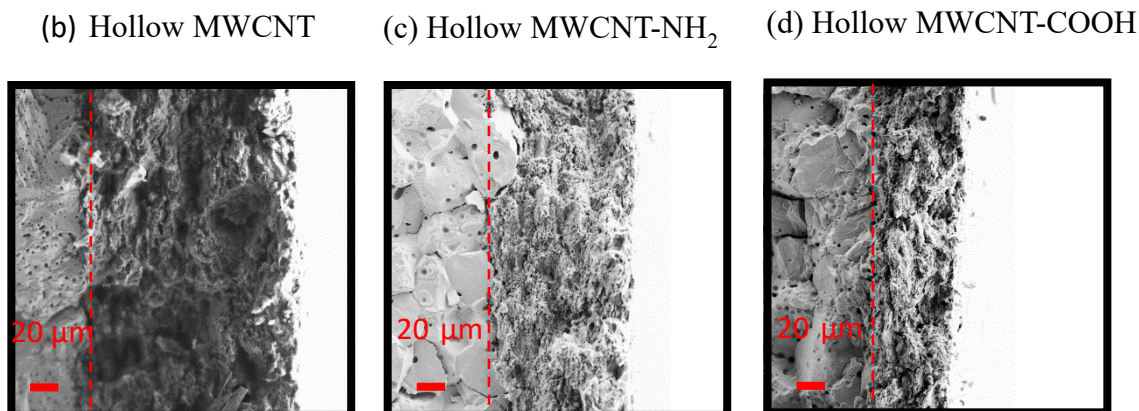


Figure 3.6. a) SEM images of Hollow MWCNTs 15 ± 5 nm in outer diameter, 5-20 μ m in length. Cross-sectional SEM images of symmetric pellets with 600mg of CsH_2PO_4 electrolyte sandwiched between 50mg 1:1 MWCNT: CsH_2PO_4 composite electrodes of b) Hollow MWCNTs, c) Hollow MWCNTs-NH₂, d) Hollow MWCNTs-COOH.

Electrochemical characterization- Polarization curves measured on fuel cells with Pt based anodes and CNT, CNT-NH₂ and CNT-COOH cathodes are presented in **Figure 3.7a**. Four cycles between 0.0V and 0.95 V were measured consecutively for each electrode. Impedance measurements taken on each fuel cell, at equilibrium (before polarization curve measurements) are presented in **Figure 3.7b**. The impedance is the resistance of the hydrogen oxidation reaction and the oxygen reduction reaction at equilibrium (slope of the polarization curve at zero current). **Figure 3.7a** and **Figure 3.7b** show that the CNT-COOH electrodes are more active towards ORR than the CNT-NH₂ and CNT electrodes. From the summary of impedance fitting results in **Figure 3.7d**, the total area normalized impedance values are $R_{\text{CNT}} = 1868 \Omega \text{ cm}^2$, $R_{\text{CNT-NH}_2} = 101 \Omega \text{ cm}^2$, and $R_{\text{CNT-COOH}} = 33 \Omega \text{ cm}^2$. In SAFCs, the anode impedance is on the order of $1 \Omega \text{ cm}^2$,³⁴ therefore, we can attribute the total impedance measured to the cathode. The electrode overpotential (η) at higher current densities follows the trend in activity measured in impedance ($\eta_{\text{CNT-COOH}} < \eta_{\text{CNT-NH}_2} < \eta_{\text{CNT}}$). However, there is a surprising anti-correlation between open circuit potential (OCP) and electrode impedance (**Figure 3.7**). The CNT-COOH electrodes with the lowest impedance values and lowest overpotentials have the lowest OCP. The presence of an oxidation current below the equilibrium Nernst voltage (1.13V) suggests the presence of a species at the cathode that lowers the Nernst voltage from the expected value of 1.13V.

Impedance spectra collected on CNT symmetric cells in humidified oxygen are presented in **Figure 3.8a**. As measured in the fuel cell configuration, there is a two order of magnitude improvement with functionalization (**Figure 3.8b**). The CNT-COOH electrodes are most active, followed by the CNT-NH₂ electrodes. For ~10 samples each, the average area normalized impedance for the oxygen reduction reaction from curve fitting are $R_{CNT} = 858 \pm 87 \Omega \text{ cm}^2$, $R_{CNT-NH_2} = 150 \pm 30 \Omega \text{ cm}^2$, and $R_{CNT-COOH} = 33 \pm 3 \Omega \text{ cm}^2$, summarized in **Figure 3.8c**. In addition, the ORR area normalized impedance values are reproducible in the symmetric cell and fuel cell configuration.

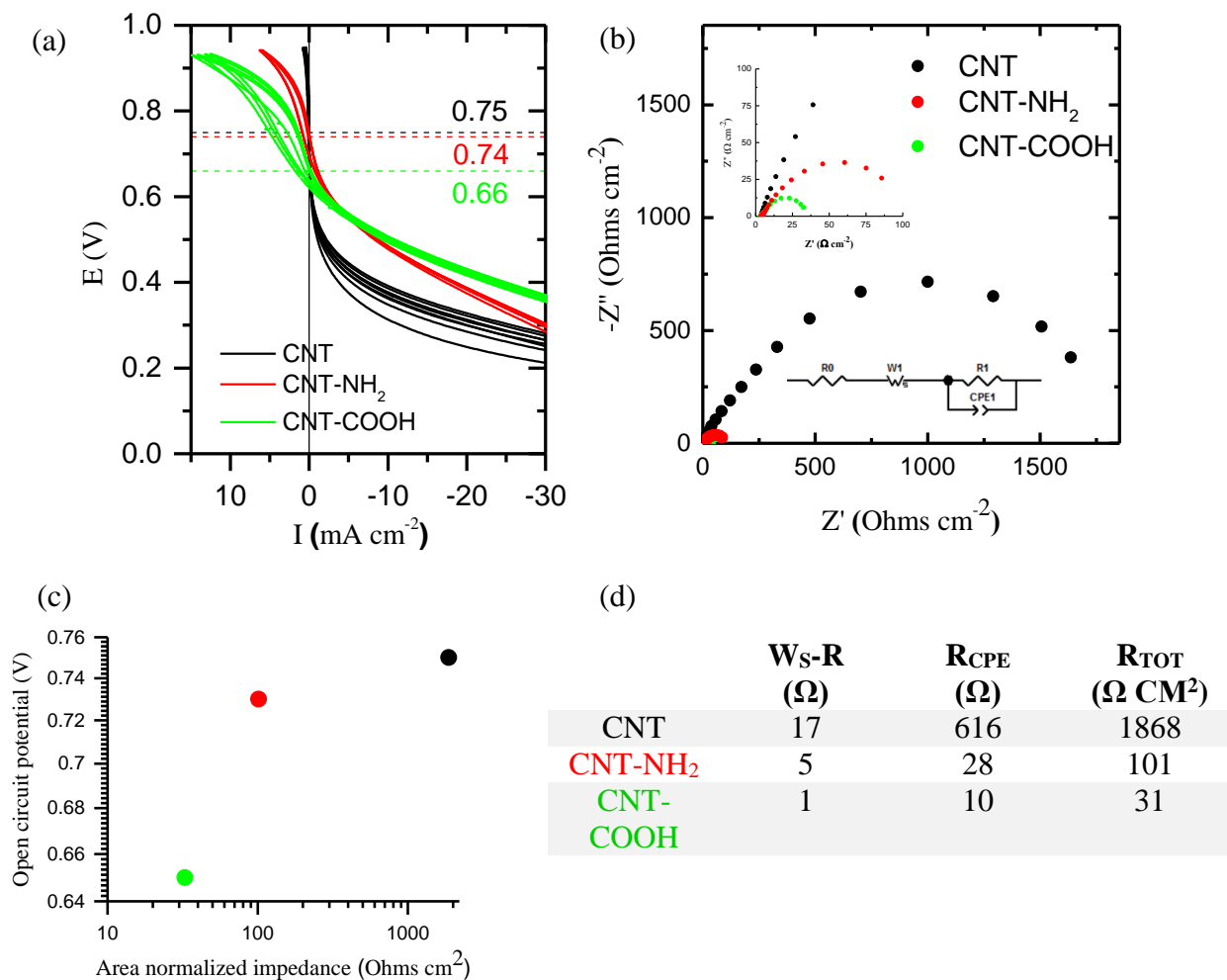


Figure 3.7. Measurements performed at 250 °C under humidified O₂ and H₂ gases ($p_{H_2O} = 0.4 \text{ atm}$) at a flow rate of 40 sccm. (a) Four H₂/O₂ polarization curves (IR corrected) measured consecutively between 0.0V and 0.95 V on 50mg 1:1 CNT: CsH₂PO₄ composite cathode and 25

mg 1:3 Pt/C : CsH₂PO₄ anode. Fuel cell polarization curve recorded at 2.5mv/s for CNTs, CNT-NH₂ and CNT-COOH electrodes. Inset is the open circuit potential (OCP). (b) Impedance measurements on the fuel cell, at equilibrium in the frequency range of 10 mHz to 0.2 MHz. Inset is the impedance model fit which is a finite length Warburg element (W_s) and a resistor in series with a resistor (R) and constant phase element (CPE) in parallel. Impedance measurements were taken on the cell before the polarization curves were measured. (c) Open circuit potential versus area normalized impedance from impedance curve fits. (d) Summary of impedance curve fitting.

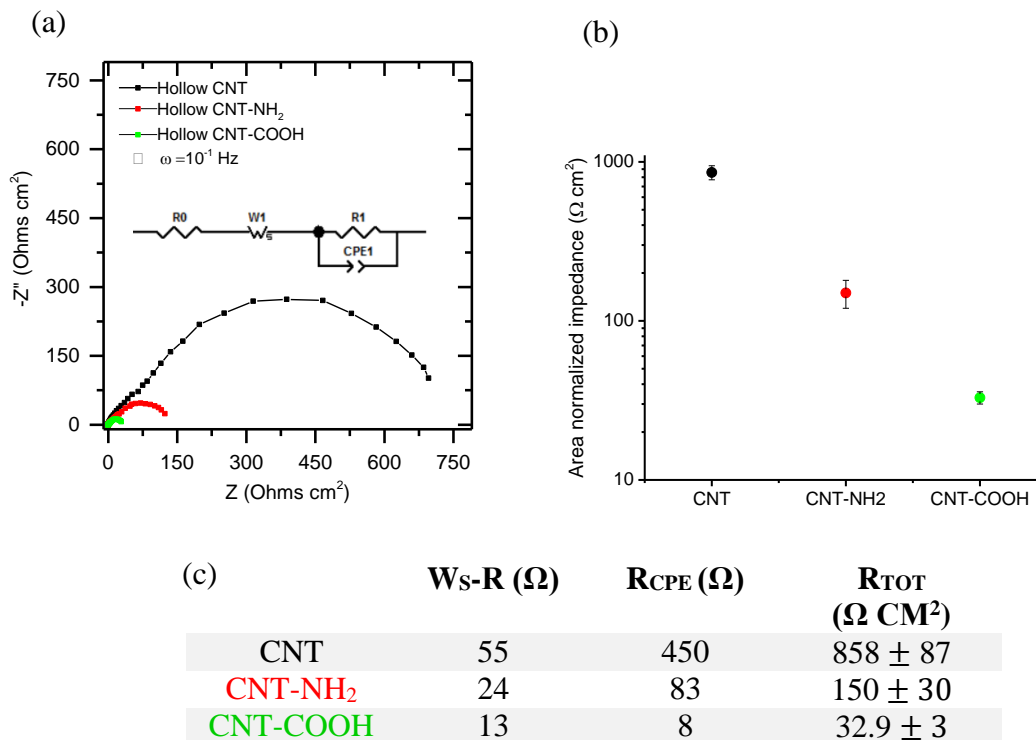


Figure 3.8. Measurements performed at 250 °C under humidified oxygen ($p_{H_2O} = 0.4\text{atm}$) flowing at 40 sccm. (a) Comparison of Symmetric cell impedance measurements of 50mg 1:1 CNT: CsH₂PO₄ composite electrodes of MWCNTs, MWCNTs-NH₂ and MWCNTs-COOH in humidified O₂ in a Nyquist representation ($\omega=10$ KHz – 5 mHz). Inset is the impedance model fit which is a finite length Warburg element (W_s) and a resistor in series with a resistor (R) and constant phase element (CPE) in parallel. (b) Semi-log plot of average normalized impedance for the CNT electrodes (~10 samples each) from curve fitting. The error bar is the standard deviation in fit results. (c) Summary of impedance fitting values showing Warburg resistance (W_s), constant phase element resistance (R_{CPE}) and the total resistance (R_{TOT}).

Electrochemical stability- To quantify the degradation in ORR impedance, the measurements were repeated at intervals of 25 min for 1000 min (shown in **Figure 3.9a**). R_{rel} is the electrochemical resistance of 50 mg 1:1 CNT : CsH₂PO₄ composite electrodes at time (t)

normalized by the area normalized impedance measured after 10 minute equilibration in humidified O_2 (impedance measurement in **Figure 3.8a**). Therefore, the steepness of R_{rel} versus time is a measure of degradation rate of the symmetric cell impedance. The degradation rates of CNT-COOH electrodes are higher than those of CNT-NH₂ and CNT electrodes. However, when a similar electrode is tested with CNT over-grown carbon paper (in-house grown by CVD) as the current collector rather than plain carbon paper, the degradation rate is similar to the CNT and CNT-NH₂ electrodes. This result suggests that although the mixing of the electrode is improved with carboxylic acid functionalization, the thinner electrode needs to be mechanically stabilized during testing. It has been shown CsH₂PO₄ exhibits ductile behavior in the super-protonic state. In general, composite membranes can be stabilized with oxides.⁹ In this case, the in-house CNT overgrown-mesh is chemically inert and provides mechanical stability to the electrode. In addition, using an organic poreformer (naphthalene) in the CNT-COOH electrodes stabilizes the electrode impedance over 1000 min (see **Figure 3.S.2** in Supplemental Material).

To probe if the reactivity in air significantly affects the density of active sites, the impedance of CNT-COOH electrodes made from post-TGA CNT-COOH powders, and CNT-COOH powders that had been oxidized in humidified oxygen (40 sccm, p_{H₂O} = 0.4 atm) at 250 °C for 12 hours, were measured (**Figure 3.9b**). The electrodes made from pre-treated CNT-COOH powders have lower impedance values from $30 \pm 3 \Omega \text{ cm}^2$ to $21 \pm 1 \Omega \text{ cm}^2$ (12 hours in air) and $17 \pm 1 \Omega \text{ cm}^2$ (12 hours in humidified oxygen). This suggests that the mass loss does not affect the density of active sites, and it is likely that active functional groups are created and consumed in the oxidation process. From the elemental composition analysis from XPS of the post-TGA sample (summarized in **Table 3.2**), there isn't a significant change in the surface chemistry of the MWCNTs with oxidation. Therefore, the MWCNTs appear to be electrochemically stable at SAFC test conditions.

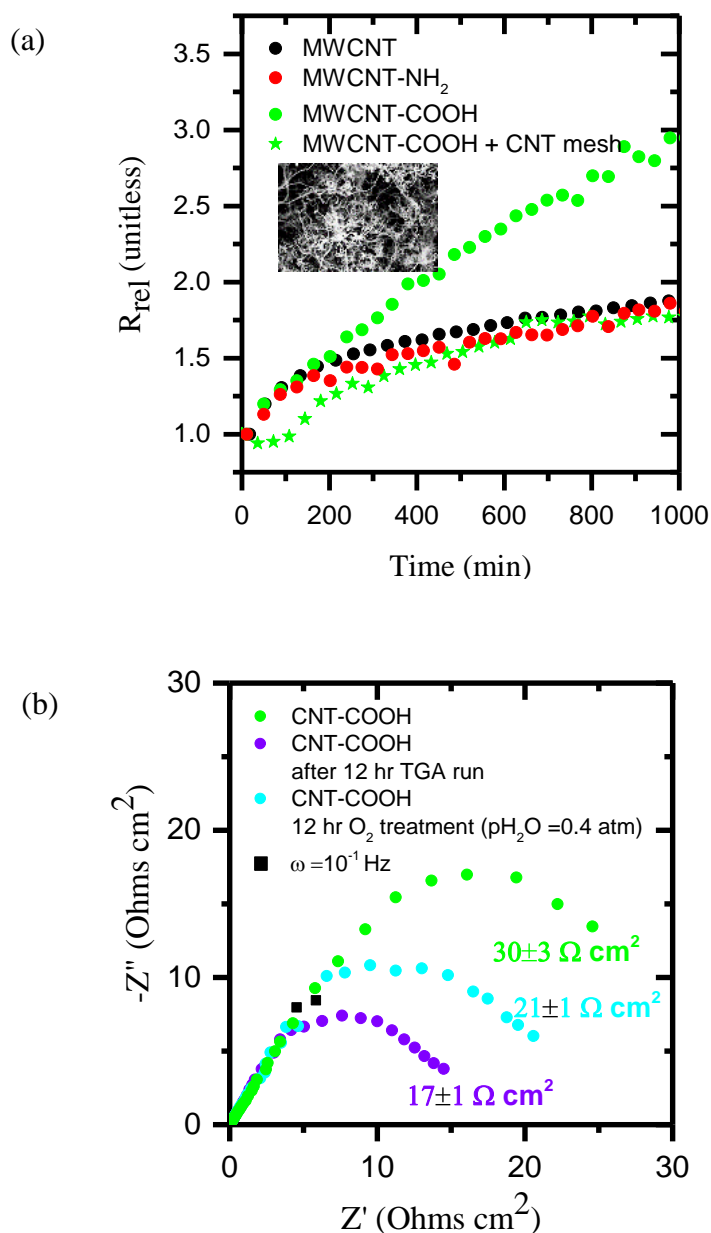


Figure 3.9. Long term degradation behavior of MWCNTs. (a) Symmetric impedance measurements in humidified O₂ (pH₂O = 0.4 atm). R_{rel} is the electrochemical resistance of 50 mg 1:1 CNT : CsH₂PO₄ composite electrodes at time (t) divided by electrochemical resistance measured 10 min after O₂ is flowed to the cell. Inset is an SEM image of MWCNT over-grown carbon paper used as a current collector to improve electrode stability. (b) Comparison of symmetric cell impedance measurements of 50mg 1:1 CNT: CsH₂PO₄ composite electrodes of hollow MWCNTs, hollow MWCNT after 12-hour treatment in air and hollow MWCNT after 12-hour treatment in humidified O₂. Measurements performed at 250°C under humidified O₂ gas flowing at 40 sccm ($\omega=10$ KHz – 5 mHz).

ORR electrochemical activity- Impedance measurements at OCP in fuel cell mode and symmetric cell mode show that the CNT-COOH electrodes are more active than the CNT-NH₂ electrodes, followed by the CNT electrodes. However, polarization curve results suggest a side reaction that reduces the concentration of the oxygen at the cathode or hydrogen at the anode. We propose a corrosion reaction of carbon with steam at the cathode. **Figure 3.10a** shows a schematic of the hydrogen oxidation reaction and the ORR at the anode and cathode, respectively, in the fuel cell configuration. At the CNT/CsH₂PO₄ cathode in the forward direction, we propose a carbon corrosion reaction, $C + H_2O \rightarrow CO + H_2$, where steam oxidation of carbon generates hydrogen at the cathode, lowering the OCP from the expected value based on input H₂O and O₂ partial pressures at the cathode. In the reverse direction, $C + H_2O \rightarrow CO + 2H^+ + 2e^-$, where the proton generated also lowers the voltage. **Figure 3.10b** shows the oxygen reduction reaction and the counter steam reforming reaction at the acting anode in symmetric cell configuration. In the symmetric cell configuration, the CNT electrode in the forward direction catalyzes the oxygen reduction reaction (ORR), and in reverse the electrode could either catalyze the steam reforming reaction or the carbon corrosion reaction. Either reaction will drive the formation of protons and electrons that complete the electron pathway. We can estimate the resistance to proton diffusion from the length of the linear portion of the impedance response under H₂ at the anode and Ar at the cathode (**Figure 3.S.1a** in Supplementary Material). These results show that the resistance to proton diffusion is lower for the CNT-COOH cathodes in comparison to the CNT-NH₂ cathodes, and the CNT cathodes. This likely drives the carbon-steam reforming reaction at the fuel cell cathode that lowers the Nernst potential.

Ignoring all other sources of voltage loss, the expected Nernst voltage is 1.1 V. From Equation 1, the P_{H_2} at the cathode required to decrease the OCP to 0.65 V (measured for CNT-COOH electrode) is 10^{-14} atm at 250 °C and 0.4 atm.

$$V = \frac{RT}{nF} \ln \left(\frac{P_{H_2}(cathode)}{P_{H_2}(anode)} \right) \quad (3.1)$$

From linear extrapolation of the Arrhenius behavior of CNT-COOH H₂ production (**Figure 3.5**), at 250 °C and 0.2 atm, a value of $\sim 10^{-15}$ atm is estimated for hydrogen production from 200 mg of CNT-COOH. Although this is not a direct comparison, the estimated value of P_{H_2} (cathode)

calculated from Equation 3.1 does not consider losses as a result of leaks and crossover, hence is possibly an over-estimation of the amount of H_2 required to lower OCP to values measured. In addition, the comparison between the H_2 production of the varying CNTs shows that the more active CNT-COOH electrode for ORR is the more reactive carbon material with steam (**Figure 3.4a**). The cathodic branch of the I-V curve crosses the zero current line at a higher OCP than the anodic branch of the I-V curve, demonstrated with the CNT electrode I-V curve in **Figure 3.11a**. A plot of the average OCP (for all four polarization curves in **Figure 3.7a**) versus the average slope of the polarization curve at zero current is presented in **Figure 3.11b**. The slope at zero current corresponds to the electrode impedance at OCP. From **Figure 3.11b**, the OCP of each electrode decreases with a decrease in the slope at zero current (electrode impedance). This substantiates the hypothesis that with increase in electrocatalytic activity for the ORR, there is an increase in catalytic activity for the steam reforming reaction with carbon. This hydrogen production in fuel mode at the cathode lowers the theoretical Nernst voltage and the measured OCP, impacting fuel cell power output.

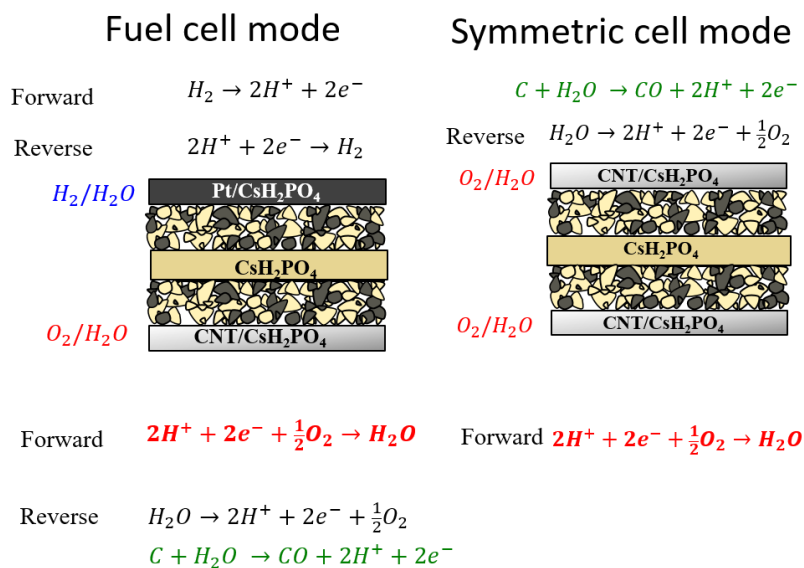


Figure 3.10. (a) Forward and reverse hydrogen oxidation and oxygen reduction half reactions at the anode and cathode, respectively, in fuel cell configuration. (b) The oxygen reduction reaction and the steam reforming reaction at the electrodes in symmetric cell configuration. The proposed carbon corrosion reaction is highlighted in blue and the oxygen reduction reaction is highlighted in red.

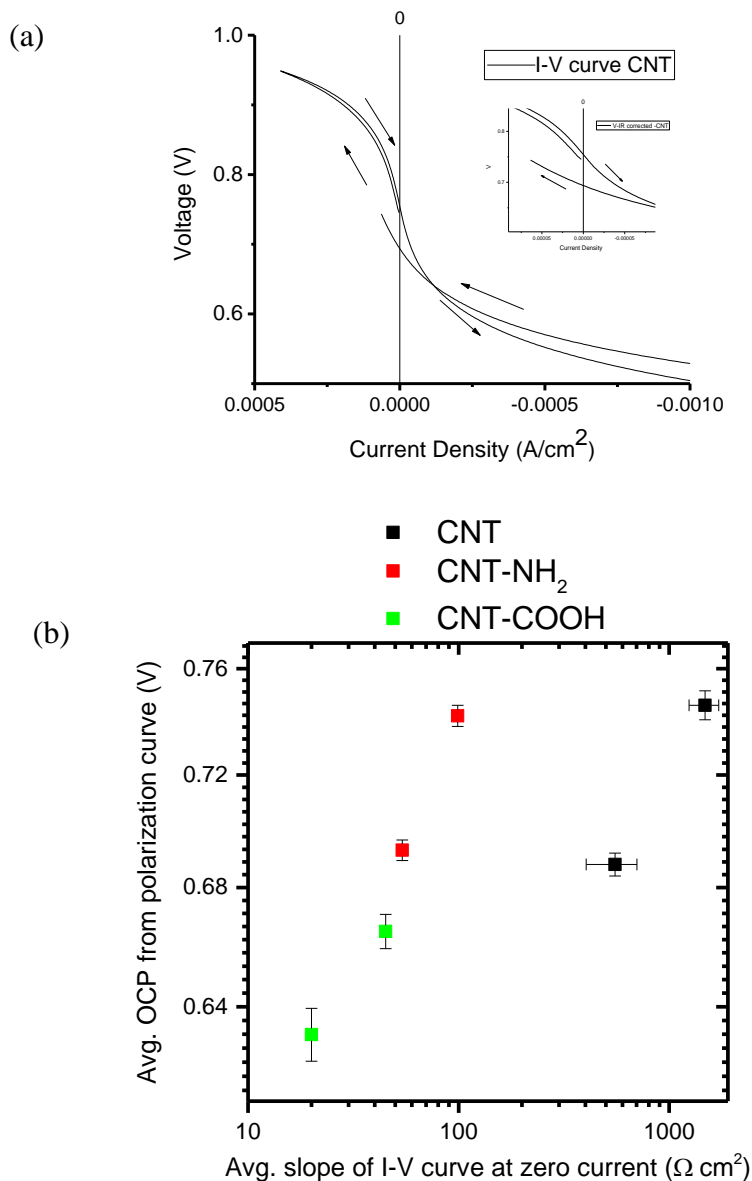


Figure 3.11. (a) First scan of the I-V curve measured in Figure 3.6. Inset shows that the cathodic branch of the I-V curve has a higher OCP than the anodic branch of the fuel cell I-V curve. (b) The average OCP value (where the I-V curve crosses the zero current density line) for the cathodic and anodic branch of the I-V curve versus the average slope at zero current

3.1.4. Conclusion

In conclusion, we have demonstrated catalytic activity of hollow tube multi-walled CNTs in the solid acid electrochemical system. CNTs with carboxylic acid functionalization have decreased proton transport resistance and higher activity towards ORR than CNTs with NH₂

functionalization and untreated MWCNTs. This activity was characterized by two orders of magnitude decrease in symmetric cell impedance in humidified oxygen, and fuel cell impedance in H_2/O_2 . However, the orders of magnitude improvement in impedance was not replicated in the decrease in overpotential in H_2/O_2 fuel cell measurements. In fact, the measured OCP was anti-correlated with the electrode impedance measured in fuel cell mode and symmetric cell mode. A carbon reaction with steam producing hydrogen at the cathode was proposed as the suspect for reducing the theoretical Nernst voltage and impacting the fuel cell performance. This suggests that hydrogen production at the cathode, as a result of oxidation of carbon with water, is a major setback to CNT performance in the SAFC cathode. However, in the symmetric cell configuration, at equilibrium, the carbon corrosion reaction is not detrimental to the performance of the catalysts studied. Hence, CNTs with COOH functionalization have the potential to be used as ORR catalysts in solid acid fuel cells if the requirement for high humidity is circumvented.

Section 3.1. Supplemental material

Figure 3.S.1 and **Figure 3.S.2a** are the impedance measured on the varying CNT electrodes under humidified hydrogen at the anode and humidified argon at the cathode and symmetric humidified argon, respectively. The resistance of the linear region in each curve (indicated for the CNT electrode as a dashed line) is a multiple of the resistance to proton diffusion. The length of the linear region is the resistance to proton diffusion divided by three.¹¹³ The resistance to proton clearly decreases with functionalization in fuel cell and symmetric mode.

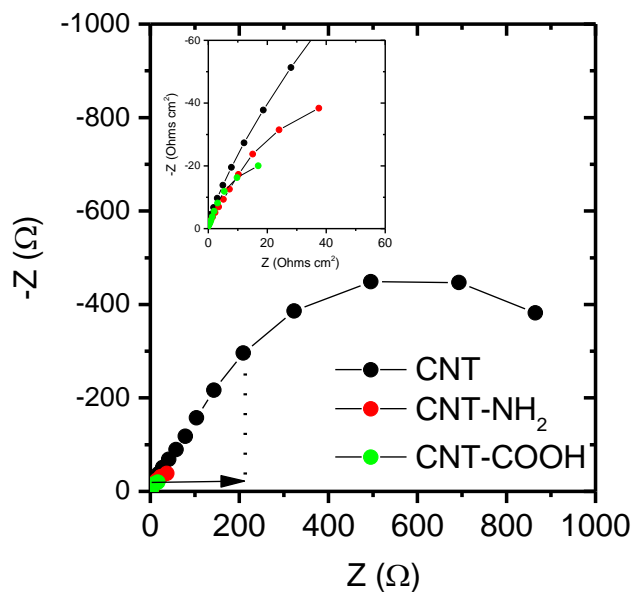


Figure 3.S.1. Comparison of electrode responses for 50 mg 1:1 CNT : CsH₂PO₄ composite electrodes in humidified ($p_{\text{H}_2\text{O}} = 0.4\text{atm}$) under Ar at the cathode and H₂ at the anode.

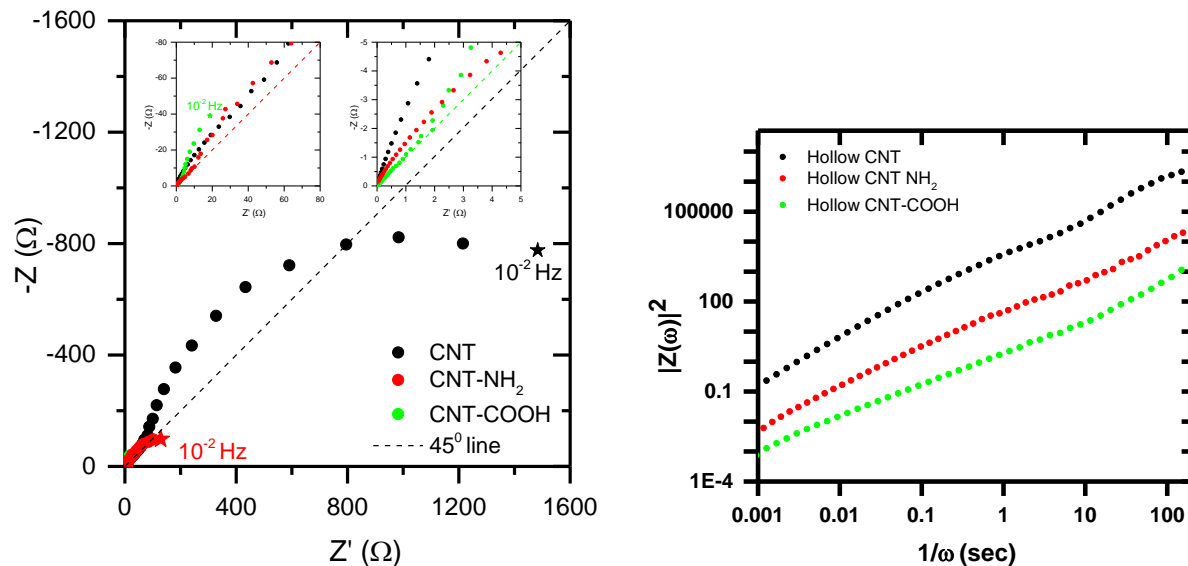


Figure 3.S.2. (a) Comparison of electrode responses for 50 mg 1:1 CNT : CsH₂PO₄ composite electrodes in humidified ($p_{\text{H}_2\text{O}} = 0.4\text{atm}$) under symmetric argon. (b) Log-log plot of $|z(\omega)|^2$ versus $1/\omega$, where the offset is $(R_0)^2/\tau$.

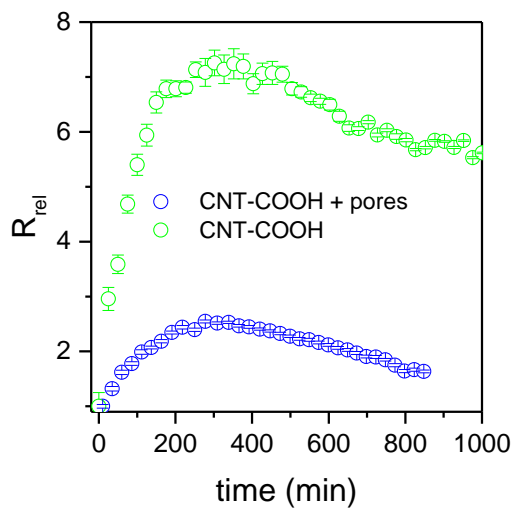


Figure 3.S.3. Symmetric impedance measurements in humidified O₂ ($p_{\text{H}_2\text{O}} = 0.4\text{atm}$). R_{rel} is the electrochemical resistance of 25 mg 1:1 CNT : CsH₂PO₄ composite electrodes at time (t) divided by electrochemical resistance measured 10 min after O₂ is flowed to the cell

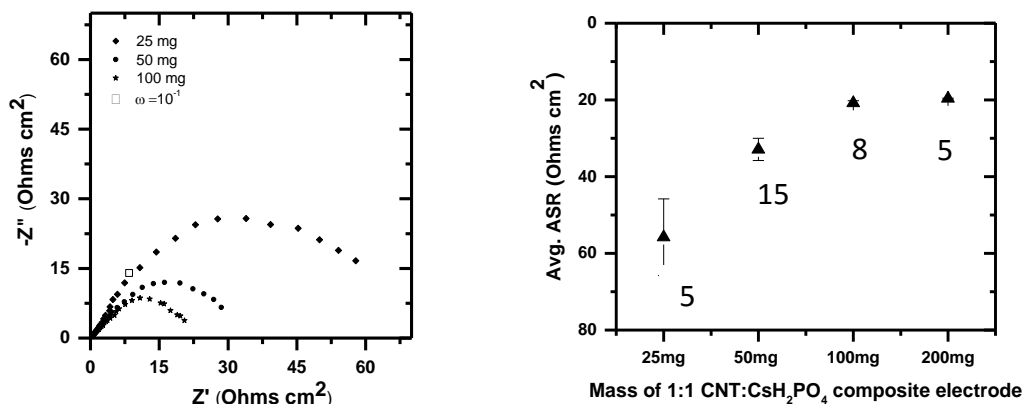


Figure 3.S.4. (a) Symmetric cell AC impedance measurements of 1:1 hollow CNT-COOH: CsH_2PO_4 composite electrodes in humidified O_2 ($p_{\text{H}_2\text{O}}=0.4 \text{ atm}$). Electrode loading was 25mg, 50mg and 100mg, respectively. (b) Plot of average area specific resistance (ASR) from fitting impedance data versus mass of 1:1 hollow CNT-COOH : CsH_2PO_4 composite electrodes. The error bars correspond to the standard deviation in ASR over the number of samples measured (in set).

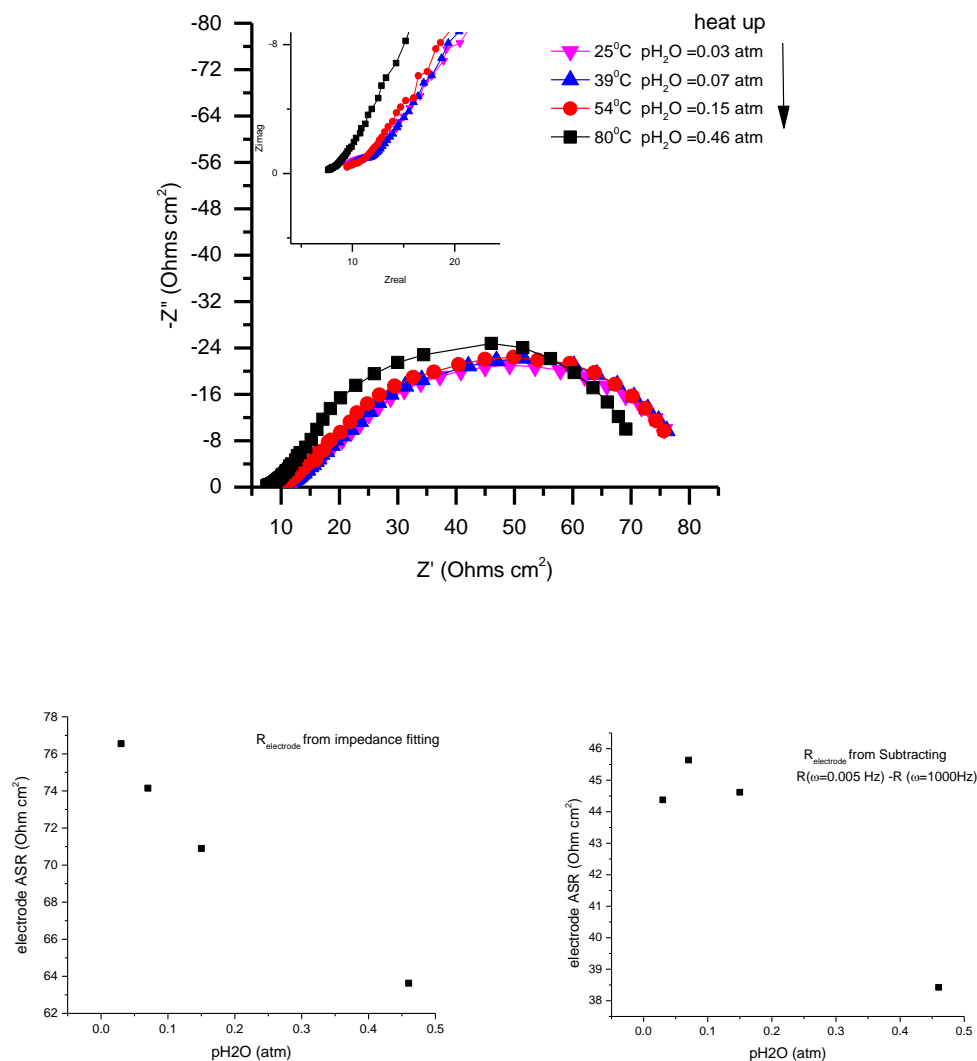


Figure 3.S.5. (a) Comparison of symmetric cell impedance measurements of 50mg 1:1 CNT: CsHSO₄ composite electrodes of Hollow MWCNTs-COOH. Measurements performed at 165°C in symmetric 60 sccm O₂ and varying p_{H₂O}. (b) Electrode resistance from impedance fitting with varying p_{H₂O}. (c) Electrode impedance from $R(\omega=0.005 \text{ Hz}) - R(\omega=1000 \text{ Hz})$ with varying p_{H₂O}.

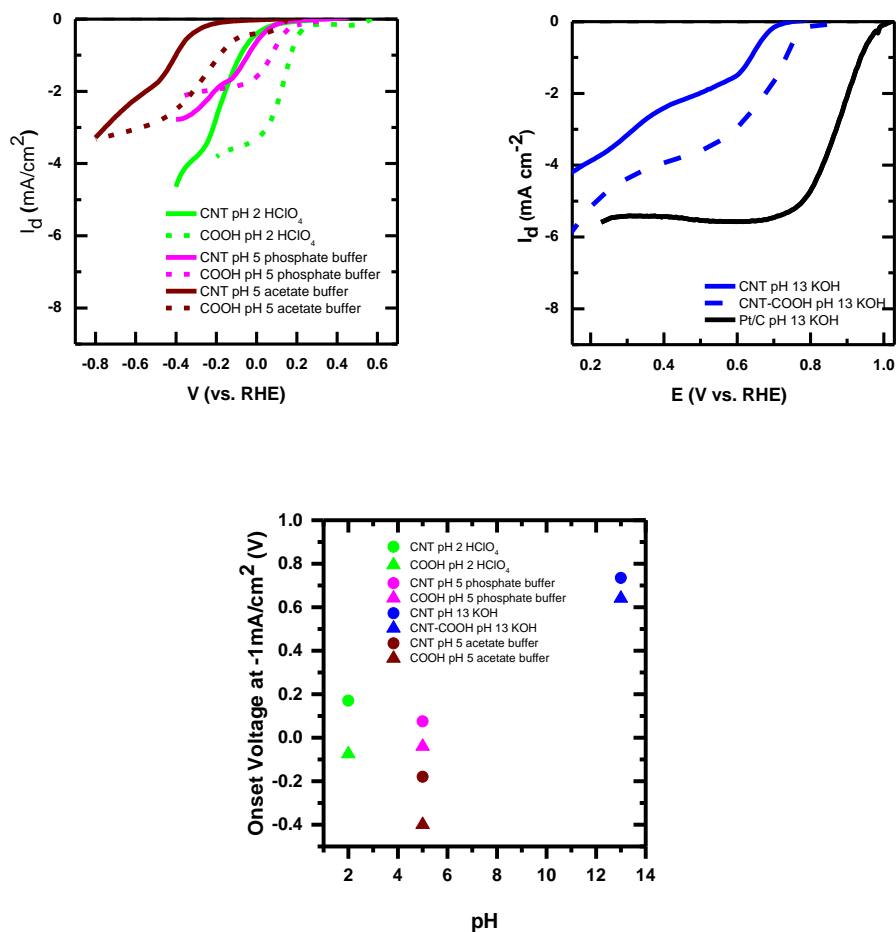


Figure 3.S.6. RDE polarization curves for Hollow MWCNTs and Hollow MWCNTs-COOH. 5 mg of Hollow MWCNT and 10 mg of hollow MWCNT-COOH were suspended respectively, in 450 μ L of ethanol, 450 μ L of isopropanol and 100 μ L of Nafion. 5 μ l of the resulting carbon nanotube ink was deposited on the glassy carbon electrode. In a) polarization curves in acidic media are shown for 0.1 M HClO₄, 0.1 M phosphate buffer, and 0.1 M acetate buffer. (b) Polarization curves in 0.1 M KOH are shown for MWCNTs in comparison with Pt/C. In c) the onset voltage at -1 mA/cm² is summarized for all MWCNTs in acidic and basic media.

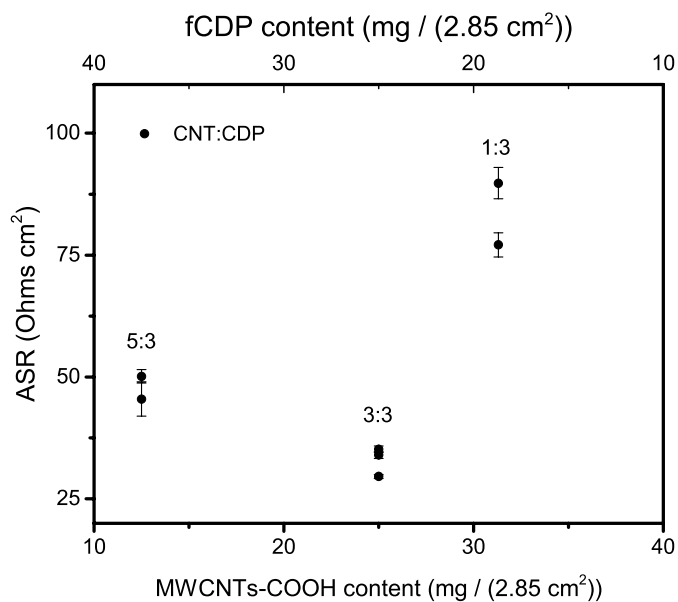


Figure 3.S.7. Average area specific resistance (ASR) or area normalized impedance (from symmetric cell AC impedance measurements in humidified O₂) versus the mass loading of the CNT electrodes. This shows that the 1:1 mass ratio loading had the highest ORR activity, hence was used for all measurements.

Section 3.2. Parametric Study on MWCNT oxygen reduction reaction activity (ORR)

3.2.1. Overview

The MWCNTs introduced in Section 3.1 are ‘hollow’ tube MWCNTs with concentric graphite tubes. In this section we introduce bamboo MWCNTs. These are MWCNTs with graphite planes at an angle from the tube axis as illustrated in the schematic¹¹⁴ in **Figure 3.2.1**. As a result, bamboo MWCNTs have a higher density of edge plane sites than the traditional hollow MWCNTs. **Figure**

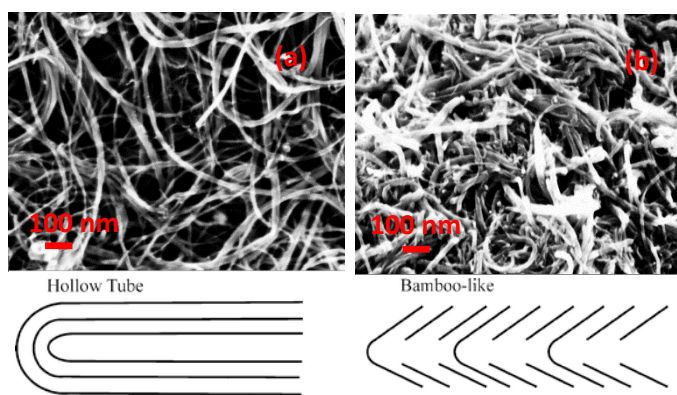


Figure 3.2.1. SEM image and schematic of (a) hollow MWCNTs and (b) bamboo MWCNTs.

3.2.1a shows an SEM image of hollow MWCNTs that are 15 ± 5 nm in diameter (OD) and 5 – 10 μm in length (L). **Figure 3.2.1b** shows bamboo MWCNTs that are 30 ± 5 nm in diameter (OD) and 1-5 μm in length (L).

The defects in the structure can be characterized by Raman spectroscopy in terms of an increase in I_D/I_G , shown in **Figure 3.2.2**.

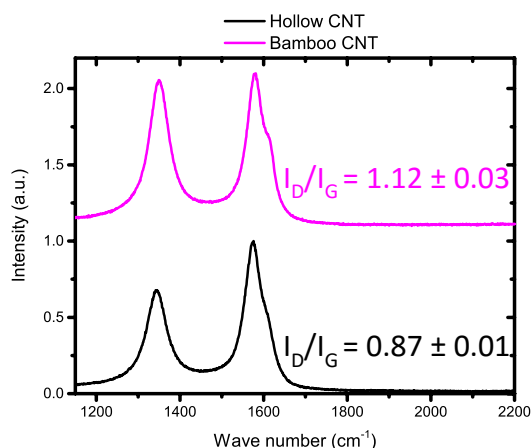


Figure 3.2.2. First order Raman spectra of hollow MWCNTs and bamboo MWCNTs. Inset is the integrated peak ratio of the D peak to the G peak (I_D/I_G). Hollow MWCNTs (OD is 15 ± 5 nm and length is 5–10 μm) and bamboo MWCNTs (OD is 30 ± 5 nm and length is 1–5 μm).

From symmetric AC impedance measurements, we find that this increase in structural defects enhances the oxygen reduction reaction (ORR) activity, characterized by a decrease in area normalized impedance (**Figure 3.2.3**).

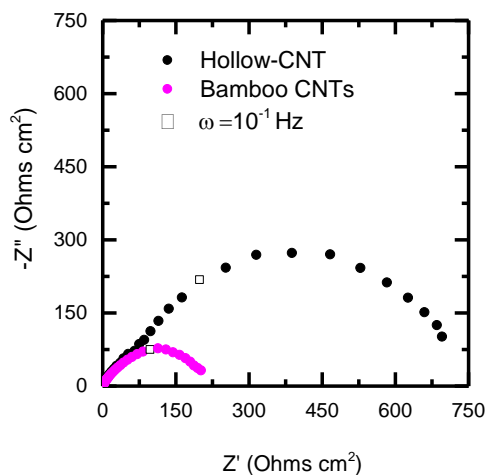


Figure 3.2.3. Measurements performed at 250°C under humidified oxygen ($p_{\text{H}_2\text{O}} = 0.4\text{atm}$) flowing at 40 sccm. Comparison of symmetric cell impedance measurements of 50mg 1:1 CNT: CsH_2PO_4 composite electrodes in a Nyquist representation ($\omega = 10\text{ KHz} - 5\text{ mHz}$).

Additional electroactive sites can be added to the bamboo variation MWCNTs by carboxylic acid functionalization as shown in Section 3.1. Raman characterization of the as-received MWCNTs in **Figure 3.2.4a** shows that the structural defect density (characterized by the I_D/I_G) increases with functionalization with $-NH_2$ and $-COOH$ functionalization. Surface functional groups of the as-received CNTs were characterized by Fourier transform infrared (FTIR) spectroscopy. As shown in **Figure 3.2.4b**, CNTs with carboxylic acid functionalization (CNT-COOH) have characteristic carbonyl ($w = 1730\text{ cm}^{-1}$), hydroxyl ($w = 1575\text{ cm}^{-1}$), and carboxylic acid groups ($w = 1150\text{ cm}^{-1}$). CNTs with amine functionalization (CNT-NH₂) have the characteristic amide ($w = 1700\text{ cm}^{-1}$) and amine ($w = 3290\text{ cm}^{-1}$) peaks. Both sets of peaks are consistent with the literature.¹⁰¹⁻¹⁰³ **Figure 3.2.5** is a summary of the electrochemical activity of select hollow and bamboo CNTs, with and without functionalization.

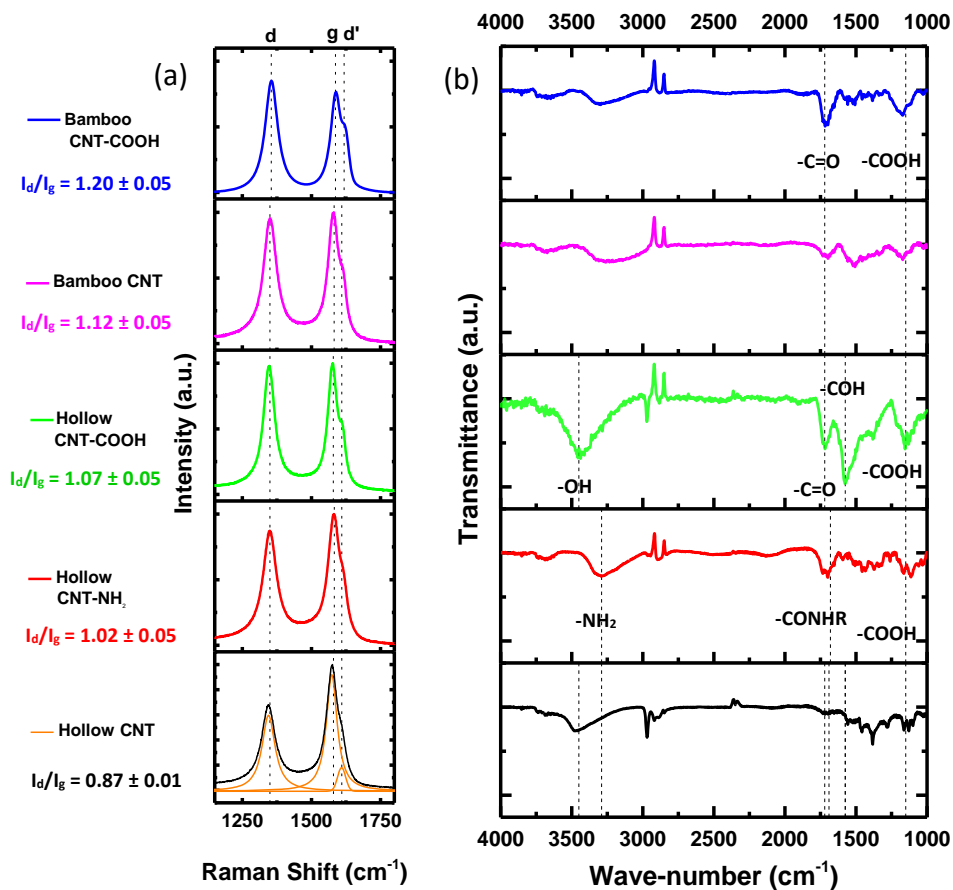


Figure 3.2.4. a) First order Raman spectra of hollow and bamboo MWCNTs. The dashed lines specify the peak position of the D band, G band and D' band. The defect density characterized as the ratio of the D band intensity to the G band intensity is shown inset. b) Fourier-transform

infrared (FTIR) spectra of hollow and bamboo MWCNTs. Dashed lines identify peaks corresponding to labelled functional groups.

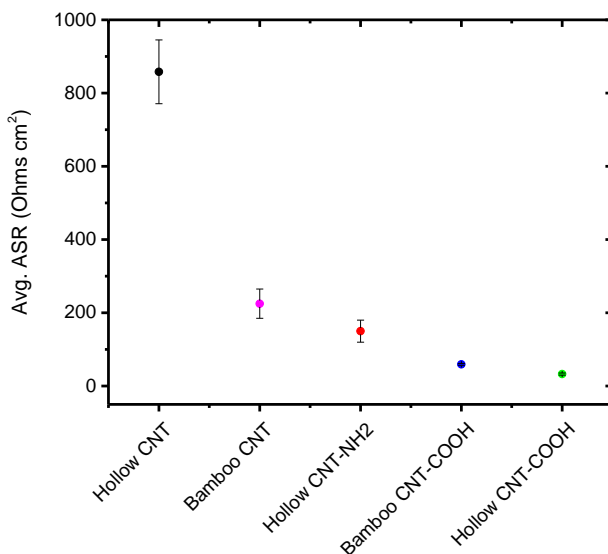


Figure 3.2.5. Plot of average area specific resistance (ASR) from fitting impedance data versus type of CNT used in 50 mg 1:1 mass ratio CNT : CsH₂PO₄ composite electrodes. The error bars correspond to the standard deviation in ASR.

From **Figure 3.2.5**, it is evident that –COOH functionalized MWCNTs have the lowest area normalized impedance, and consequently the highest ORR activity.

In this section we evaluate the electrochemical activity of –COOH functionalized hollow MWCNTs and bamboo MWCNTs of varying length and diameter, and characterize all the samples by Raman spectroscopy, BET surface area measurements and XPS. ORR electrochemical activity was assessed by symmetric cell AC impedance spectroscopy in humidified O₂ (as described in Section 3.1). The aim is to conduct a parametric study of structural defect density (characterized by Raman spectroscopy), surface area (characterized by BET measurements), and elemental composition (characterized by XPS) on the measured ORR electrochemical activity. Four variations in length (L) and outer diameter (OD) of hollow MWCNTs were studied with given dimensions; (i) OD= 15 nm, L= 1-5 μm, (ii) OD- 15 nm, L= 5- 20 μm, (iii) OD= 30 nm, L=1-5 μm, and (iv) OD= 30 nm, L=5- 20 μm. Two variations of bamboo MWCNTs were studied with dimensions; (i) OD= 30 nm, L= 1-5 μm, and (ii) OD = 30 nm L= 5- 20 μm.

3.2.2. Results and discussion

Length and diameter (aspect ratio) of MWCNT- The lengths (L) and diameter s(OD) of the hollow MWCNTs and bamboo variation MWCNTs are plotted versus the area normalized impedance and the defect density (I_D/I_G from Raman spectroscopy measurements) are presented in **Figure 3.2.6** The I_D/I_G ratio does not discriminate active defects for hollow MWCNTs. That is, the higher defect density measured by Raman spectroscopy does not correlate with lower area normalized impedance (higher ORR activity). On the other hand, the I_D/I_G ratio does discriminate active defects in the case of the bamboo variation MWCNTs. For the two lengths tested, the shorter MWCNTs (1-5 μm) had the higher defect densities and the lower measured area normalized impedances. Raman spectroscopy is more sensitive to the graphene structures along the tube axis, because an in-plane polarization of the electric field is necessary for these optical transitions. Since the graphite planes are along the tube axis for bamboo MWCNTs, and the edges are likely to be the location of the electroactive sites, Raman spectroscopy is better at discriminating active structural defects for bamboo MWCNTs than hollow MWCNTs.

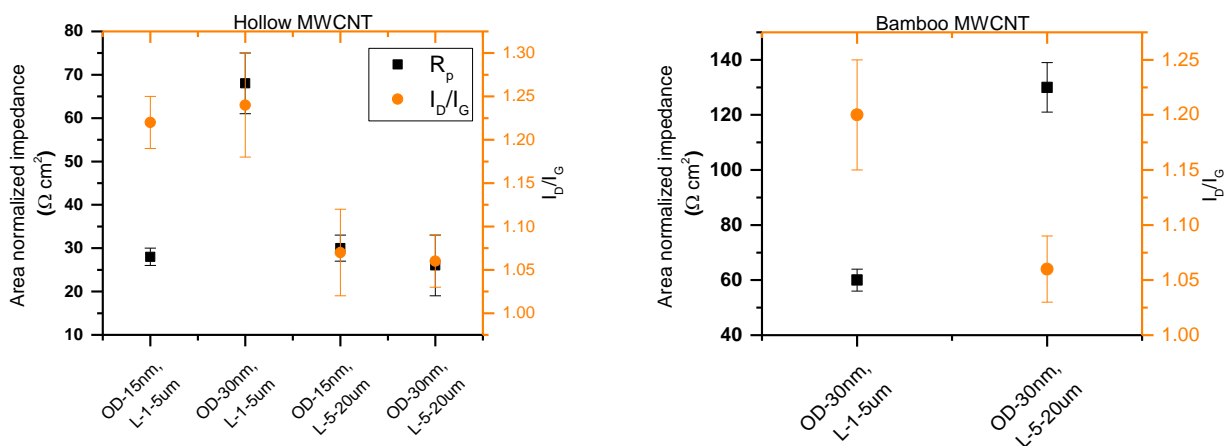


Figure 3.2.6. Area normalized impedance from impedance measurements versus outer diameter (OD) and length (L) of hollow and bamboo variation MWCNTs.

However, in both cases, the I_D/I_G is sensitive to length (summarized in **Table 3.2.1**). The shorter MWCNTs have higher densities of edge sites and that corresponds to increased intensity of the D band. The diameter variation (hollow CNTs only) does not affect the I_D/I_G . This agrees

with previous reports on sensitivity of I_D/I_G to diameter variation. If the top of the hollow MWCNTs is not aligned to the incident radiation, the I_D/I_G is insensitive to diameter variation.⁵² Another interesting observation in **Figure 3.2.6** is that for the same dimension (OD, L) the bamboo variation MWCNTs do not necessarily have higher defect densities than equivalent hollow tubes.

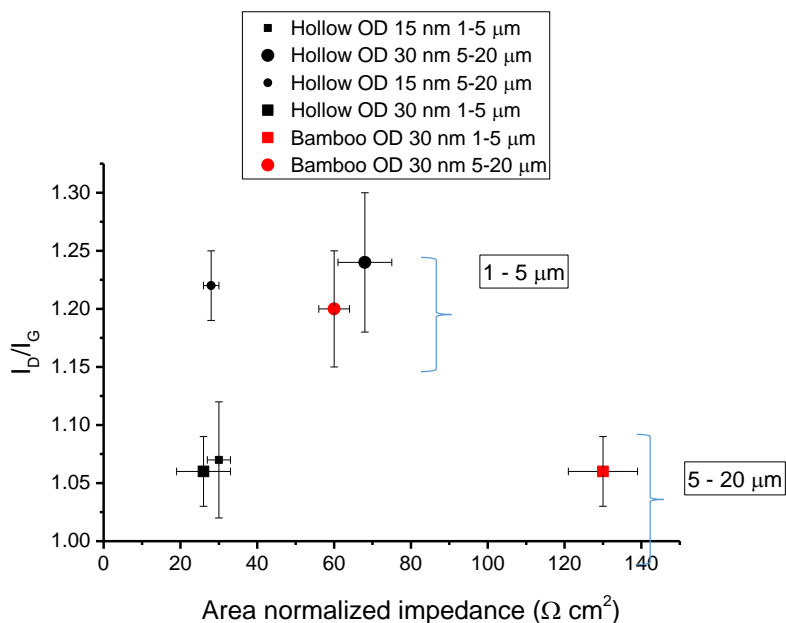


Figure 3.2.7. I_D/I_G (from Raman measurements) for all varying hollow and bamboo MWCNTs characterized, versus area normalized impedance values (from symmetric cell AC impedance measurements in humidified O_2). Brackets indicate that the shorter MWCNTs of both variations have higher measured I_D/I_G .

BET surface area- The surface area measured by BET for all MWCNTs is summarized in **Figure 3.2.8**. Surprisingly, there appears to be no correlation between impedance and CNT dimension for the hollow MWCNTs measured. In addition, it appears that decreasing surface area corresponds to decreasing area normalized impedance, which is counter-intuitive. On the other hand, the shorter bamboo MWCNTs have higher BET surface areas and lower area normalized impedances (higher ORR activity). The counter-intuitive trend observed for the hollow MWCNTs suggest that the BET method is perhaps not the best method for accurate measurement of nanotube surface area. A summary of the data in **Figure 3.2.7** and **Figure 3.2.8** is presented in **Table 3.2.1**.

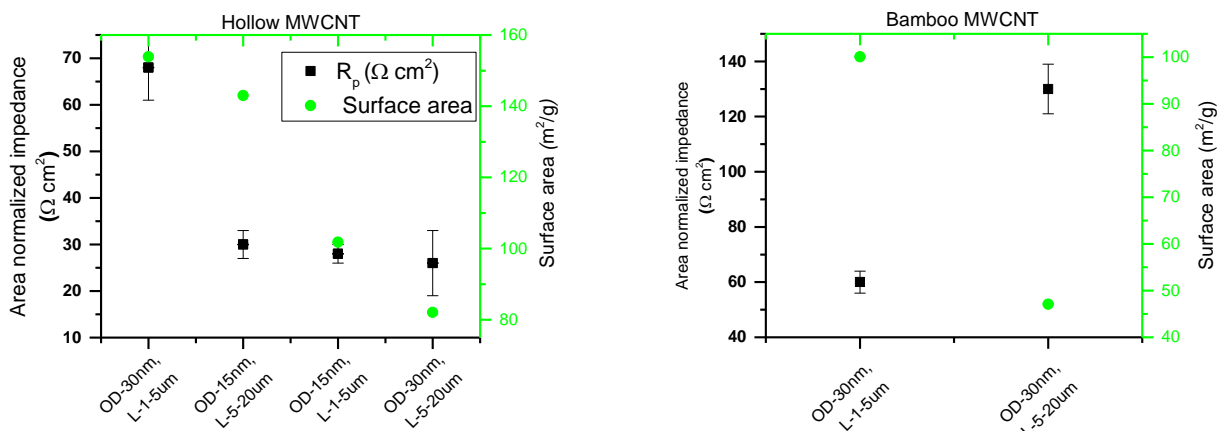


Figure 3.2.8. BET surface area for all varying hollow and bamboo MWCNTs characterized, versus area normalized impedance values (from symmetric cell AC impedance measurements in humidified O_2).

MWCNT structure	Outer diameter (nm)	Length (μm)	Area normalized impedance (Ohms cm^2)	Defect density (I_D/I_G)	BET surface area (m^2/g)
Hollow CNT-COOH	15	5-20	30 \pm 3	1.05 \pm 0.07	143.0 \pm 0.7
Hollow CNT-COOH	15	1-5	28 \pm 2	1.22 \pm 0.03	101.8 \pm 0.1
Hollow CNT-COOH	30	5-20	26 \pm 7	1.06 \pm 0.03	82.1 \pm 1.1
Hollow CNT-COOH	30	1-5	68 \pm 7	1.24 \pm 0.06	153.9 \pm 0.4
Bamboo CNT-COOH	30	5-20	130 \pm 9	1.06 \pm 0.03	47.1 \pm 0.2
Bamboo CNT-COOH	30	1-5	60 \pm 3	1.20 \pm 0.05	100.1 \pm 0.1

Table 3.2.1. MWCNT dimension and corresponding area normalized impedance, I_D/I_G and BET surface area.

Elemental composition- The elemental composition of the near surface region of the as-received –COOH functionalized MWCNTs was quantitatively analyzed by XPS. Curve fitting results are summarized in **Table 3.2.2**. C 1s peak assignments are as explained in Section 3.1. For the hollow MWCNTs, the 30 nm tubes have increased oxygen content in comparison to the 15 nm tubes of equal length. This suggests that oxygen incorporation is dominant at the edges of the hollow tube CNTs. This is in agreement with literature reports that carbon atoms at the tube edges are more reactive than carbon atoms on the side wall.¹¹⁴ This is also consistent with the observation that shorter hollow and bamboo MWCNTs (especially for OD = 30 nm, L = 1-5 μm) have higher oxygen content because of the higher density of tube edges exposed than longer tubes have (5-20 μm).

<i>Outer diameter (nm)</i>	<i>Length (μm)</i>	<i>Binding energy (eV)</i>				<i>Total C1 %</i>	<i>Total O1 %</i>	<i>C/O</i>
Hollow CNT-COOH		290.5 π - π^*	287.8 COOH	285.8 C-OH + sp^3 -C-	284.4 C-C			
15	5-20	2.76	7.86	57.4	9.74	78	22	3.5
15	1-5	5.54	7.94	55.5	9.02	78	22	3.5
30	5-20	4.48	8.05	55.2	7.77	76	24	3.2
30	1-5	5.89	7.37	50.1	9.06	72	28	2.6
Bamboo CNT-COOH		290.5 π - π^*	287.8 COOH	285.8 C-OH + sp^3 -C-	284.4 C-C			
30	5-20	5.45	7.21	54.9	10.3	78	22	3.5
30	1-5	3.87	8.40	42.4	7.02	65	35	1.9

Table 3.2.2. Integrated atomic concentrations of hollow and bamboo MWCNTs of varying outer diameter and length.

The effect of elemental composition on ORR activity is summarized in **Figure 3.2.9**. In general, the MWCNTs with higher relative concentration of carboxylic acid functional group have decreased area normalized impedance and consequently higher ORR activity. The catalytic ORR activity of carbon materials is generally attributed to quinone (C=O) groups.¹¹⁵ Although the trendline is not equivalent for the different variations in MWCNT structure, in each case, the MWCNT with higher carbonyl content has higher ORR activity. This gives experimental evidence that the proposed mechanism on carbon nanostructures extends to MWCNTs.

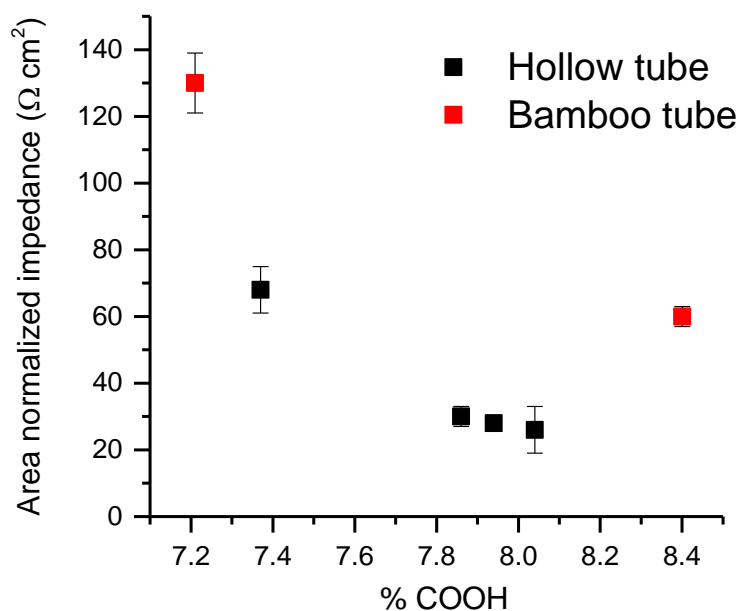


Figure 3.2.9. Area normalized impedance from symmetric AC impedance measurements in humidified O₂ versus the relative concentration of the carbonyl (C=O) functional group in the hollow/bamboo MWCNT.

Although unfunctionalized bamboo MWCNTs have higher electrochemical activity than unfunctionalized hollow MWCNTs (**Figure 3.2.3**), it is unclear why equivalent –COOH functionalized bamboo MWCNTs have lower electrochemical activity than the –COOH hollow MWCNTs. This is not in agreement with a previous report on the ORR electrochemical activity of bamboo MWCNTs versus hollow MWCNTs measured by cyclic voltammetry in aqueous 0.1 M HClO₄.⁹⁶ The hollow and bamboo MWCNTs used in that study were purchased from the same source as this study (Nanolab Inc.) and the –COOH functionalized was done in-house by the

authors. For this study, pretreated -COOH functionalized MWCNTs were purchased from Nanolab.

3.2.3. Conclusion

In conclusion, we have found that the I_D/I_G ratio is a unique descriptor of active defects for bamboo variation MWCNTs and not hollow MWCNTs. In addition, the BET surface area can be used to parametrize bamboo MWCNTs but not hollow MWCNTs. We have also found that the elemental composition is the most important parameter in determining ORR activity. The higher the relative concentration of the -COOH group, the higher the ORR activity. This is because the quinone (C=O) group is considered the active center for the ORR on carbon surfaces. Finally, we found in this parametric study that although bamboo MWCNTs have higher density of edge sites, -COOH functionalized bamboo MWCNTs do not have higher ORR activity than hollow MWCNTs of equivalent size.

CHAPTER 4

Tuning the reactivity of carbon nanostructures by growth parameters

4.1. Abstract

This work focuses on the synthesis and characterization of highly defective multi-walled CNTs as potential precious metal free ORR catalysts. CNTs were grown by chemical vapor deposition (CVD) onto silicon using nickel nanoparticles as the seed catalyst and acetylene as the carbon source. It was found that increasing the precursor partial pressure, decreasing the Ni catalyst size, and decreasing the growth temperature increases the density of ORR active defects evaluated by symmetric AC impedance spectroscopy. In addition, the oxygen reduction reaction (ORR) electrochemical activity was significantly enhanced by chemical functionalization with oxygen containing functional groups. Area normalized impedance as low as 200 ohms cm^2 has been measured for MWCNT/CsH₂PO₄ composite electrodes. In addition, HNO₃ functionalization decreased the area normalized impedance by two orders of magnitude, corresponding to a decrease in impedance to ~ 7 ohms cm^2 . We have demonstrated that the relative concentration of carbonyl functional groups in the form of quinones can be correlated to the ORR activity. This gives substantial experimental evidence for the ORR mechanism on carbon surfaces proposed by Yeager in 1970.¹¹⁵

4.2. Introduction

There is growing interest in carbon nanostructures for oxygen reduction reaction (ORR) catalysis and catalyst support in aqueous electrochemistry systems and in polymer electrolyte membrane fuel cells.^{84, 95, 96, 116} Multi-walled carbon nanotubes (MWCNTs) have high mechanical stability and high thermal and electrical conductivity.^{77, 78} Depending on the chiral symmetry, MWCNTs can either be metallic or semiconducting. These changes in electronic properties can promote electron transfer with an active species in solution.⁷⁹ It has been shown that electrodes modified with MWCNTs exhibit higher electrochemical activity.⁸⁰ In low to intermediate temperature fuel cells, the cathode has been identified as the dominant source of activation losses.

Generally, catalyst loading is higher at the cathode, and in various energy conversion processes the allure of replacing precious metal catalysts with fabricated carbon nanostructures has garnered attention.^{82, 83} Most studies of the ORR on MWCNT electrodes are in alkaline media,⁸⁶⁻⁹³ as opposed to acidic media,⁹⁴⁻⁹⁶ because carbon nanostructures are more active at high pH.

It has been shown in the literature that the ORR activity of a graphite edge plane is higher than that of a basal plane in alkaline solutions.¹¹⁷ This catalytic activity difference is attributed to the presence of electro-active surface moieties on the edge plane as opposed to the basal plane. Ideal MWCNTs are electrochemically inert concentric graphene layers. However, during synthesis, electroactive structural and chemical defects can be introduced into the MWCNT structure.⁸¹

MWCNTs generally have two areas with active sites: the fullerene-like tube ends and the less reactive hexagonal cylindrical tube walls.⁵⁰ The possible types of structural defects are (i) rehybridization, (electronic state between sp^2 and sp^3) (ii) incomplete bonding defects (vacancies, dislocations), and (iii) topological defects (non-hexagonal rings).¹¹⁸ A schematic growth model for MWCNT tip growth is depicted in **Figure 4.1a**.⁸¹ At time t_0 , the seed catalyst is on the substrate in the reactive atmosphere. At time t_1 , the volume of the CNT is v_1 , with pressure p_1 . The pressure in the growth chamber is p_c . Assuming walls are hardly permeable to sheath gases, at a particular time, t_1 , the pressure inside the CNT is less than the pressure in the chamber ($p_1 < p_c$). At a later time, t_2 , as the CNT grows, the volume of the CNT increases, $v_2 > v_1$, and the pressure in the CNT, p_2 , is less than the pressure in the chamber ($p_2 < p_c$). It follows that $p_2 < p_1$, or in general the pressure inside the MWCNT continuously decreases, and the pressure gradient across the side walls continuously increases causing defects in the side wall structure. The weakest part of the CNT is the 'embryo', where the catalyst and CNT side wall are joined, and this is thought to buckle during growth as a result of the axial load, causing additional bends and kinks in MWCNT structure.⁸¹ In **Figure 4.1b**, the growth rate (dL/dt) depends on the rate of diffusion (dN_c/dt) of active carbon species through the catalyst, which depends on the amount of carbon flux on the catalyst particle and the specific temperature of the catalyst.¹¹⁹

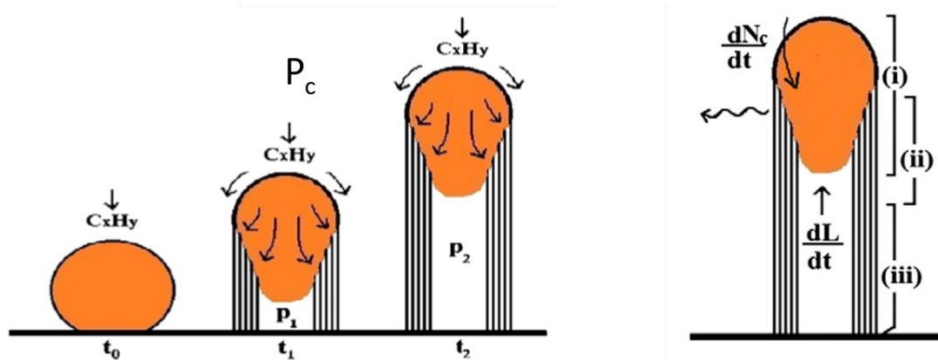


Figure 4.1. (a) Schematic diagram of tip growth model at different time steps. (b) The MWCNT in the tip growth scheme depicting the (i) catalyst particle, (ii) embryo and (iii) full grown MWCNT (Reproduced from Hembram *et al.*).⁸¹

The structural quality and defect density of MWCNTs is commonly studied through Raman spectroscopy. This is especially useful to optimize the growth recipe, and to investigate the impact of growth parameters on the resulting MWCNT morphology and crystal structure. This was demonstrated by Hembram *et al.* where MWCNTs grown at a heating rate of 20 °C/min had higher defect densities from Raman studies than MWCNTs grown at 5 °C/min.⁸¹ The authors cited these results as experimental justification for the tip growth defect formation model in **Figure 4.1**. In addition, Matsubara *et al.* have shown that for two types of carbon nanotubes, the MWCNTs with the higher defect density from Raman studies had higher electrochemical activity measured by RRDE experiments in alkaline media.⁹⁶ However, the influence of growth parameters on the MWCNT structure, and the synthesis routes to incorporate electro-active defects were not studied.

Carbon materials (that are not single crystal) have a variety of Raman bands.^{38, 39} The G band ($\sim 1580\text{ cm}^{-1}$) is the Raman active mode of graphitic materials. It is relatively constant despite excitation wavelength. The intensity of the D ($\sim 1350\text{ cm}^{-1}$) and D' ($\sim 1620\text{ cm}^{-1}$) band is defect dependent and these bands are dispersive with incident wavelength.³⁸ These disorders cause a symmetry break of the graphene sheets as a result of impurities, point vacancies, or five/seven member rings.^{40, 41} The D band is also measure of the density of edge plane exposures.⁴² According to double resonance theory,⁴³ the crystal defects scatter the excited electrons resulting in the wave vector condition that explains the D band appearance. The D and D' band are as a result of elastic phonon scattering close to the K and Γ point of the Brillouin zone, respectively. The overtone of the D-band is called G'-band, which is a result of an inelastic phonon emission process, and occurs usually around 2700 cm^{-1} .⁴⁴ In general, hollow and bamboo variation MWCNTs the ratio of the

integrated intensity of the D band to the G band (I_D/I_G) is considered a quantitative measure of the density of defects in the MWCNT structure. However, for low crystalline quality carbon nanostructures like herringbone CNTs or carbon nanofibers, an additional T_2 band appears at $\sim 1500\text{ cm}^{-1}$ in the Raman spectra. This band increases I_D/I_G with increasing crystallinity, rendering it an incorrect estimate of the defect density. Few reports have looked at empirical correlations of crystallinity with Raman spectra parameters, there are indications that the FWHM of the D band decreases with increasing crystallinity for low quality carbon nanostructures.¹²⁰ Another report recommends the ratio of I_G/I_G , which shows an increase with increasing crystallinity.¹²¹ Unfortunately, fitting of second order bands is difficult for low quality samples as they appear as modulation only. In this work the FWHM (D) was looked at for low crystalline quality CNTs grown. Finally, these Raman parameters are dependent on the excitation laser wavelength, substrate and MWCNT alignment, therefore it is crucial that these parameters be equivalent for quantitatively fair defect density comparison between samples.

MWCNTs can be modified by chemical oxidation,^{122, 123} and doping^{84, 91, 93} to enhance oxygen reduction reaction activity. Common oxidizing treatments include high concentration acids, plasma techniques, and UV/ozone oxidants. Oxygen containing functional groups like carboxyls, carbonyls, esters, ether, and aldehyde can be incorporated into the MWCNT structure. The type and the degree of oxygen functional groups present in the MWCNT structure after oxidation depends on the oxidizing agent and synthesis/processing technique. It is not clearly understood why pre-treatment of MWCNTs improves the ORR catalytic activity, but it is understood that pre-treatment creates more surface functional groups and exposes fresh carbon edges and defects along the MWCNT wall.^{124, 125} X-ray photoelectron spectroscopy (XPS) and Fourier transform infrared (FTIR) spectroscopy can give information about the functional groups present on the surface of the MWCNT structure. XPS has the advantage over FTIR in that it gives quantitative information about the oxygen content. In addition, XPS spectra yield relative percentages of different oxygen containing functional groups in the MWCNT structure.^{126, 127}

The overarching goal of this work is to investigate the efficacy of MWCNTs as ORR electrocatalysts in SAFCs. SAFCs are intermediate temperature fuel cells in which the electrolyte is a solid acid (cesium di-hydrogen phosphate, CsH_2PO_4 , was used in this case). Specifically, we performed a parametric study of the effect of a) precursor partial pressure, b) seed catalyst size, c) growth temperature and d) chemical functionalization on the defect density and elemental

composition of MWCNTs. The defect structure and elemental composition were studied by Raman spectroscopy and X-ray photoelectron spectroscopy, respectively. The ORR activity was quantified by symmetric cell AC impedance spectroscopy under conditions relevant for operation of SAFCs

4.3. Experimental

CsH₂PO₄ synthesis: CsH₂PO₄ was synthesized in-house by dissolving stoichiometric amounts of Cs₂CO₃ (Alfa Aesar, 99% metal basis, Stk# 12 887)) and H₃PO₄ (Mallinckrodt Chemicals, 85%, Stk#2788-14) in deionized water. The mixture was pipetted into a vat of methanol to induce precipitation of a CsH₂PO₄ powder. The resulting precipitate was dried at 120 °C for 6 hours. To increase triple phase boundary density in the electrode layer, fine CsH₂PO₄ was synthesized by precipitating a saturated solution of CsH₂PO₄ in deionized water (100 mg CsH₂PO₄: 85 mL DI water) through a fine needle (26G1/2) into excess anhydrous methanol (J.T. Baker, #9093-03). The resulting surface area of the CsH₂PO₄ particles was measured to be ~2-2.5 m²/g by the BET method.

Carbon nanotube synthesis: Nickel nanoparticles served as the seed catalyst and the precursor gas was acetylene. The nickel nanoparticles were synthesized according to the procedure by Metin *et al.*¹²⁸ Typical particle sizes obtained by this method are 40 ± 8 nm and 80 ± 10 nm. The resulting oleylamine-capped particles were re-dispersed in hexane for substrate coating. To prepare the substrate, the catalyst suspension was subjected to ultra-sonication for 10 min to break up agglomerates, then a silicon wafer was dip-coated in the catalyst suspension. The catalyst loaded substrate was placed in the center of a quartz tube (1" diameter, 25" length) that was loaded into a tube furnace (Lindberg/Blue M Mini Mite). The silicon substrate was placed such that it was on top of a K-type thermocouple and mass flow controllers. The growth steps and conditions are detailed in **Table 4.1**. After the sample is loaded into the reactor, the nickel nanoparticles are passivated in a mixture of argon and acetylene for 10 min. Then the oven was ramped up at 50 °C/min to the growth temperature which was varied in this study from 600 °C – 800 °C in argon only. This was followed by a 10 min Ar/H₂ anneal to remove the oleyl-amine ligands on the nickel nanoparticles. Then Ar/H₂/C₂H₂ were introduced in the desired ratio for carbon nanotube growth

for 10 min. After growth, the oven was rapidly cooled down to allow additional defects to be incorporated into the structure.

Step	Passivation	Ramp up	Ni anneal	Growth	Cool down
Time (min)	10	20		10	120
Temp (°C)	25	600-800	600-800	600-800	25
Ramp rate (°C/min)	-	50	-	-	-
Ar flow rate (sccm)	750	750	750	750/0	750
H ₂ flow rate (sccm)	0	0	250	250	0
C ₂ H ₂ flow rate /sccm)	16	0	0	16	0

Table 4.1. Growth conditions for multi-walled CNTs by chemical vapor deposition

Chemical vapor deposition is sensitive to growth temperature, so care was taken to place substrate in the oven in the region with uniform temperature distribution. Unfortunately, that limits the sample loading per growth cycle, resulting in low yields of ~5 mg per growth. After growth, the MWCNTs were extracted from the silicon substrate by ultra-sonication in methanol. This suspension was dried in an oven at 80 °C for 6 hours. The MWCNTs disperse well in methanol, making it difficult to collect the MWCNTs for electrode processing. To collect the MWCNTs, the MWCNTs were re-dispersed in toluene in an ultrasonic bath. The resulting suspension was centrifuged and decanted. The collected MWCNTs were dried in an oven at 100 °C for 6 hours.

MWCNT functionalization: Procedure was adapted from experiments detailed in Tsang *et al.*¹²⁹ MWCNTs were functionalized by refluxing 100 mg MWCNTs in 50 mL HNO₃ for 12 hours at 135 °C. Functionalization was quenched by pouring 50 mL de-ionized water into the flask after 12 hours. The suspension was centrifuged and decanted, then rinsed with deionized water. This washing step was repeated three to four times to remove excess acid. The collected MWCNTs were dried in an oven at 150 °C for 12 hours.

Cell Fabrication – For electrochemical testing, symmetric cells were configured as: SS | carbon paper | CNT/ CsH₂PO₄ cathode | CsH₂PO₄ electrolyte | CNT/ CsH₂PO₄ cathode | carbon paper | SS. The CNT/ CsH₂PO₄ cathode was prepared by milling a mixture of the multiwall CNTs and fine CsH₂PO₄. Unless otherwise stated, the CNT/ CsH₂PO₄ electrode is 50 mg in a 1:1 mass ratio. Cells were fabricated by sequentially depositing the electrode, electrolyte and counter electrode powders into a stainless steel die. The cells were assembled by pressing the cathode and anode composites (in symmetric configuration it is cathode versus cathode) against *ca.* 700 mg of CsH₂PO₄ powder in a 19 mm die at 69 MPa for 20 min. The thickness of the CsH₂PO₄ solid electrolyte was *ca.* 1-1.5 mm with *ca.* 90% of the theoretical density. Toray carbon paper (TGP-H-120, Fuel Cell Earth, LLC.) was used as the current collector. Two stainless steel gas diffusion layers (McMaster-Carr, Type 316, mesh size 100 × 100) were placed on either side of the cells and served as a gas-diffusion layer and mechanical support for the structure. Symmetric cell pellets were 1.9 cm diameter and 2 mm thick.

MWCNT characterization- MWCNT defect density was characterized by Raman spectroscopy with a M-1000 Renishaw Ramanscope (514.3 nm) at 20s exposure time and a maximum laser power of 5.0 mW. Qualitative characterization of polar functional groups was done by Fourier-transform infrared (FTIR) on a Nicolet 6700 FTIR with a deuterated tri-glycine sulfate (DTGS) detector and a potassium bromide beamsplitter (KBr). The morphological features of the CNTs and the cells were characterized using a scanning electron microscope (Zeiss 1550VP field emission SEM) equipped with a secondary electron detector. X-ray photoelectron spectroscopy (XPS) experiments were carried out in an ultrahigh vacuum system (Thermo Scientific ESCALAB 250Xi) equipped with a 180° hemispherical electron analyzer. A monochromatic Al K α X-ray source (1486.7 eV; anode operating at 14.6 kV and 4.35 mA) was used as incident radiation in all XPS measurements. Charging effects were compensated by using a flooding electron gun and Ar ion gun. The XPS core level spectra were analyzed with a CASAXPS fitting routine, which can deconvolute each spectrum into mixed Lorentzian-Gaussian peaks after a Shirley background subtraction. The binding energies were calibrated based on the graphite C 1s peak at 284.4 eV. The standard deviation in XPS core level peak positions is $\sim \pm 0.06$ eV.

Electrochemical characterization- AC impedance spectra on the symmetric cells were collected using a Solartron 1260 Impedance/Gain-Phase Analyzer. The perturbation voltage was 40 mV and the frequency range was 5 mHz to 10 kHz. The cell was initially heated to 140 °C at 2 °C/min in air, then heated up to 250 °C under Ar humidified through a water bubbler held at 80 °C (saturation $p_{H_2O} = 0.4$ atm). At each condition, the cells were equilibrated for 10 minutes before collecting the impedance spectra.

4.4. Results and discussion

Precursor partial pressure and seed catalyst size- The effect of the partial pressure of the precursor gas, acetylene ($P_{C_2H_2}$), on resulting carbon nanotube nanostructure is shown in the SEM micrographs taken in **Figure 4.2**. The MWCNTs shown were grown with 80 ± 10 nm nickel (Ni) nanoparticles and at 800 °C. Structural defects were incorporated into the MWCNT nanostructure by changing the partial pressure of acetylene in the growth oven during growth from 0.016 atm (**Figure 4.2a**) to 0.060 atm (**Figure 4.2b**). Bright spots at the end of the MWCNTs in both images suggest a tip growth mechanism as illustrated in **Figure 4.1**. The MWCNTs in **Figure 4.2a** are ~ 10 μm in length and 90 ± 10 nm in diameter. MWCNTs in **Figure 4.2b** are generally shorter at 3-10 μm in length and thicker, with a diameter of 100 ± 15 nm.

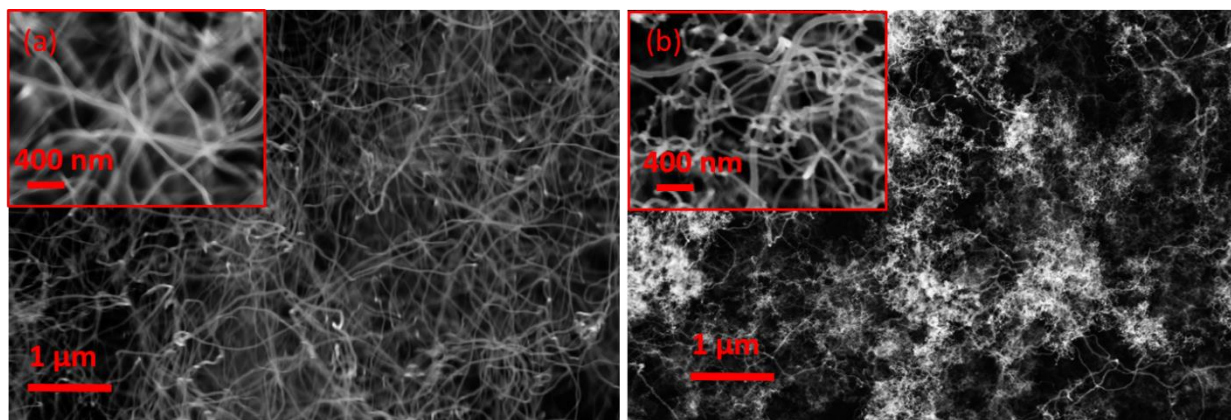


Figure 4.2. SEM micrographs of MWCNTs grown with 80 nm Ni seed catalyst and growth temperature 800 °C in; (a) $P_{C_2H_2} = 0.016$ atm: 16 sccm C_2H_2 , 750 sccm Ar, 250 sccm H_2 and (b) $P_{C_2H_2} = 0.060$ atm: 16 sccm C_2H_2 , 250 sccm H_2 . Inset is higher magnification.

The MWCNTs grown with lower $P_{C_2H_2}$ (**Figure 4.2a**) appear to have fewer bends and kinks along the MWCNT tube walls in comparison to MWCNTs grown at higher $P_{C_2H_2}$, shown in **Figure 4.2b**. Scanning tunneling electron microscopy images shown in **Figure 4.3** reveal that the MWCNTs grown by this CVD method are ‘bamboo’ like. The dashed lines in **Figure 4.3a** highlight the MWCNT structure from which the ‘bamboo’ name is derived. In bamboo variation MWCNTs, the graphite planes are formed at an angle to the axis of the tube, therefore these MWCNTs have a higher proportion of edge plane sites/defects than the *traditional* hollow MWCNTs.¹¹⁴ MWCNTs grown at higher $P_{C_2H_2}$, shown in **Figure 4.3b**, reveal amorphous carbon deposits (black spots) along the bends and kinks. It is suspected that the MWCNTs are ‘bamboo’ with more breaks along the side wall. The graphite planes are likely invisible as a result of amorphous carbon deposits along the side walls. This could also explain why these CNTs have a slightly larger diameter, despite being grown with the same Ni nanoparticle size.

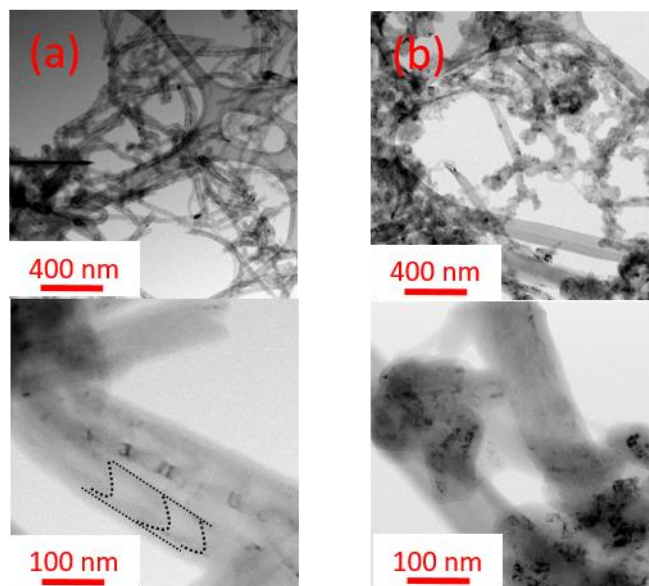


Figure 4.3. STEM images of MWCNTs grown with 80 nm Ni seed catalyst and growth temperature 800 °C in (a) $P_{C_2H_2} = 0.016$ atm. Dashed lines show the ‘bamboo’ like structure of the MWCNTs. (b) $P_{C_2H_2} = 0.060$ atm. Dark spots are amorphous carbon deposits.

The structural quality of the MWCNTs can be characterized quantitatively by Raman spectroscopy. Characteristic D ($w = 1350$ cm^{-1}), G ($w = 1585$ cm^{-1}), and D’ ($w = 1619$ cm^{-1}) peaks appear in the wavenumber region of 1150-2250 cm^{-1} as first order Raman modes.³⁸ The G band is a result of tangential in-plane stretching of C-C bonds in graphene sheets.^{50, 104} The D and D’

bands are double resonance Raman mode and can be attributed to MWCNT defects.³⁹ Therefore, the integrated intensity ratio (I_D/I_G or $I_{D'}/I_G$) is a measure of defect density in MWCNTs. Structural defect characterization of the MWCNTs by Raman spectroscopy is presented in **Figure 4.4**. As proposed by Mennella *et al.* the D and G band were fitted with Lorentzian curves and the D' band was fitted with a Gaussian (shown inset).⁵³ **Figure 4.4a** shows the Raman spectra for samples grown with 80 nm Ni seed catalyst for $P_{C_2H_2} = 0.06$ atm and $P_{C_2H_2} = 0.016$ atm. Inset is the integrated peak intensities (the standard deviation is for 3-5 samples each). **Figure 4.4b** shows the same characterization for MWCNTs grown with 40 nm Ni seed catalyst. SEM analysis of these MWCNTs (not shown) reveals that the MWCNT diameter decreases to 40 -50 nm and the length is relatively unchanged in comparison to those grown with 80 nm Ni. In **Figure 4.4a**, it is evident that the MWCNT structural defect density (I_D/I_G) increases from 0.96 ± 0.07 to 1.2 ± 0.05 with increase in $P_{C_2H_2}$. In **Figure 4.4b**, I_D/I_G increases from 1.2 ± 0.05 to 1.6 ± 0.05 .

These results support the model for defect formation introduced in **Figure 4.1**. The growth rate of the CNTs is directly related to the flux of carbon atoms through the catalyst. Following a model in the literature for CNT growth from ethylene,¹¹⁹ the CNT growth rate can be shown to be proportional to the consumption of acetylene and production of hydrogen as $\frac{dL}{dt} \sim e^{-\frac{E_a}{k_b T}} (P_{C_2H_2} - \frac{P_{H_2}}{K})$. Therefore, the carbon flux and consequently the growth rate is higher in the growth conditions with higher $P_{C_2H_2}$. It is known that for single walled CNTs, the migration energy of carbon atoms is much lower than the binding energy of carbon in the graphite plane. In the presence of surplus carbon, these interstitial carbon atoms agglomerate to form graphitic clusters or amorphous carbon. Interestingly, the activation barrier to form defects in the form of non-hexagonal rings (pentagons and hexagons) decreases from 5-8 eV to 3.5 eV in the presence of interstitial carbon.¹¹⁸ Therefore, the observation of amorphous and graphitic carbon deposits in the high acetylene growth regime, suggests lower activation barrier to defect formation. The increase in $P_{C_2H_2}$ increases the flux of the carbon species through the catalyst to the MWCNT walls during growth, causing increased defect formation, apparent in the SEM/STEM images, and supported by quantitative Raman characterization.

In addition, the results in **Figure 4.4** suggest that decreasing the Ni seed catalyst size (consequently the MWCNT diameter) increases the measured defect density. It is known that there is a correlation between seed catalyst size and MWCNT diameter, consequently influencing the

Raman peaks.^{52, 130} Antunes *et al.* and Bokova *et al.* found an increase in defect related Raman bands with decreasing diameter.^{52, 130} The I_D/I_G density is sensitive to MWCNT structural organization, particularly along the tube axis, and the decrease in tube curvature is likely the cause of the increase in D band intensity.⁵² Therefore, growing MWCNTs with smaller Ni seed catalyst does not necessarily increase the number of defects per nanotube. However, decreasing MWCNT diameter is expected to increase the mass normalized electro-active surface area, which should consequently affect electro-activity.

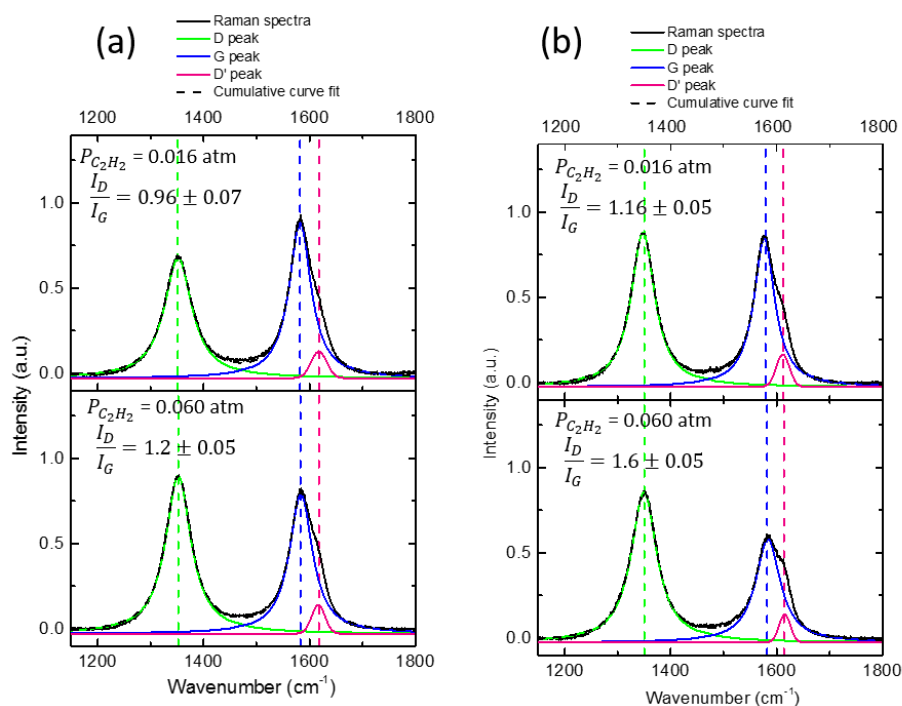


Figure 4.4. First order Raman spectra measured for MWCNTs grown with $P_{C_2H_2} = 0.016$ atm (top) and $P_{C_2H_2} = 0.060$ atm (bottom). (a) 80 nm Ni seed catalyst. (b) 40 nm Ni seed catalyst. The dashed lines indicate the peak position of the D band, G band and D' band. The defect density characterized as the ratio of the D band intensity to the G band intensity is shown inset. In all cases, the growth temperature is 800 °C.

Symmetric cell AC impedance measurements in humidified O₂, on the CNTs characterized in **Figure 4.2**, are presented in **Figure 4.5a**. In **Figure 4.5b**, I_D/I_G is plotted against the area normalized impedance from curve fitting the impedance spectra in **Figure 4.5a**. **Figure 4.5** shows a clear trend that an increase in defect density (I_D/I_G , characterized by Raman spectroscopy)

correlates with an increase in ORR electrochemical activity in the solid acid electrochemical system. Thus, for bamboo variation MWCNTs, the structural defects measured by Raman spectroscopy are active for the ORR. The improvement with decrease in MWCNT diameter is likely a result of the increase in electro-active surface area as hypothesized above.

Chemical oxidation of MWCNT- Figure 4.6 is a scanning tunneling electron microscope (STEM) image of HNO_3 treated MWCNTs grown with conditions $P_{\text{C}_2\text{H}_2} = 0.060 \text{ atm}$, growth temperature = $800 \text{ }^\circ\text{C}$, and 80 nm Ni seed catalyst in scanning mode (Figure 4.6a) and transmission mode (Figure 4.6b). Literature reports indicate that liquid phase acid treatments simultaneously remove amorphous carbon and metal impurities.^{108, 131, 132} After acid treatment, the MWCNT walls are visible in transmission mode in comparison to the image of untreated MWCNTs shown in Figure 4.3b. However, there appear to be regions with amorphous carbon deposits in the kinks (dark spots).

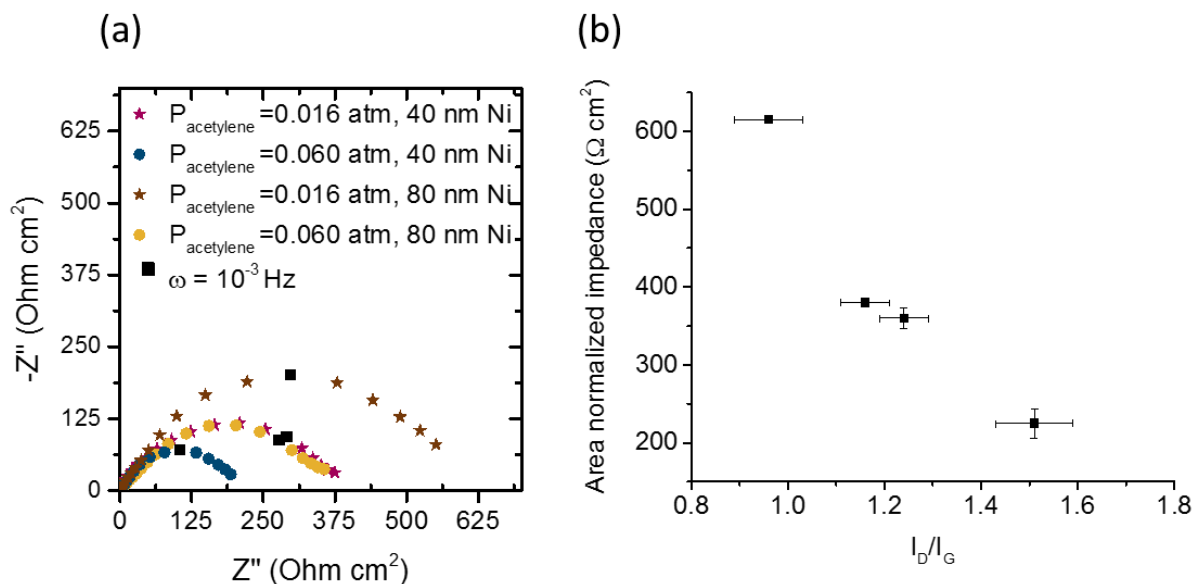


Figure 4.5. a) Comparison of symmetric cell impedance measurements of 50mg 1:1 CNT: CsH_2PO_4 composite electrodes (varied parameters shown inset and growth temperature is $800 \text{ }^\circ\text{C}$) in a Nyquist representation ($\omega = 10 \text{ KHz} - 5 \text{ mHz}$). Measurements collected at 250°C under humidified O_2 ($p_{\text{H}_2\text{O}} = 0.4 \text{ atm}$) flowing at 40 sccm. (b) Area normalized impedance versus I_D/I_G ratios from Raman characterization.

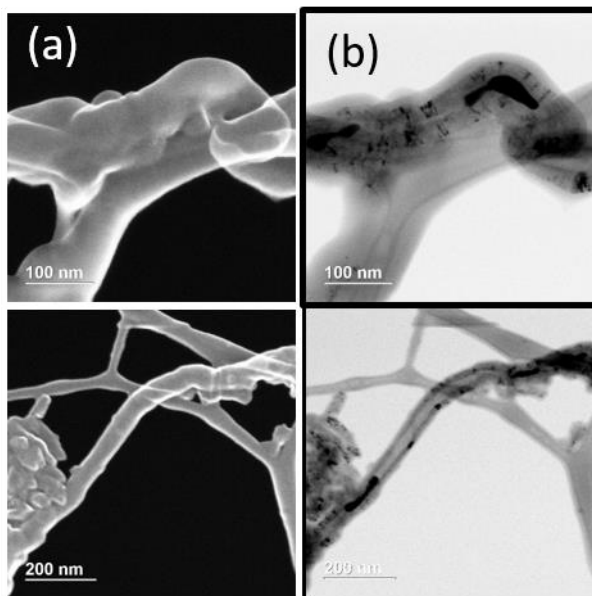


Figure 4.6. STEM microscopy images of MWCNTs grown at $P_{C_2H_2} = 0.060$ atm, growth temperature = 800 °C, and 80 nm Ni seed catalyst in (a) scanning mode and (b) transmission mode.

Fourier transform infrared (FTIR) spectroscopy can identify organic functional groups on the MWCNT surface by measuring characteristic vibrational modes. Surface functional groups of the MWCNTs before and after functionalization were characterized by FTIR spectroscopy. Acid-treated MWCNTs have characteristic carbonyl ($\omega = 1720$ cm^{-1}), hydroxyl ($\omega = 1575$ cm^{-1}), and carboxylic acid groups ($\omega = 1150$ cm^{-1}) consistent with literature reports.¹⁰¹ The elemental composition of the near surface region of the MWCNTs was quantitatively analyzed by XPS. C 1s peaks of the untreated and HNO₃ treated MWCNTs are presented in **Figure 4.8** and curve fitting results are summarized in **Table 4.2**. Deconvolution of the untreated and HNO₃ treated MWCNTs C1s spectra in **Figure 4.8** have a characteristic peak at 284.4 eV and ~290-292 eV. The peak at 284.4 eV is attributed to sp^2 hybridized graphitic carbon atoms, and the peak at 290-292 eV is the characteristic shakeup line of carbon in aromatic compounds (π - π^* transition loss).^{77, 109} The MWCNT C 1s peak at 285.4 eV is from sp^3 hybridized carbon atoms that are a result of structural defects at the surface of the graphitic sheet (amorphous carbon atoms in another state than typical graphitic sp^2 carbon atoms).¹⁰⁸⁻¹¹¹ In the HNO₃-treated MWCNT C 1s scan, this peak is shifted to 285.8 eV, representative of C-OH bonds. In addition, the HNO₃ treated MWCNTs C 1s spectra

have a peak at 288.4 eV assigned to carbon atoms in a double bond with oxygen (C=O bonds in carboxylic acid groups).^{77, 108}

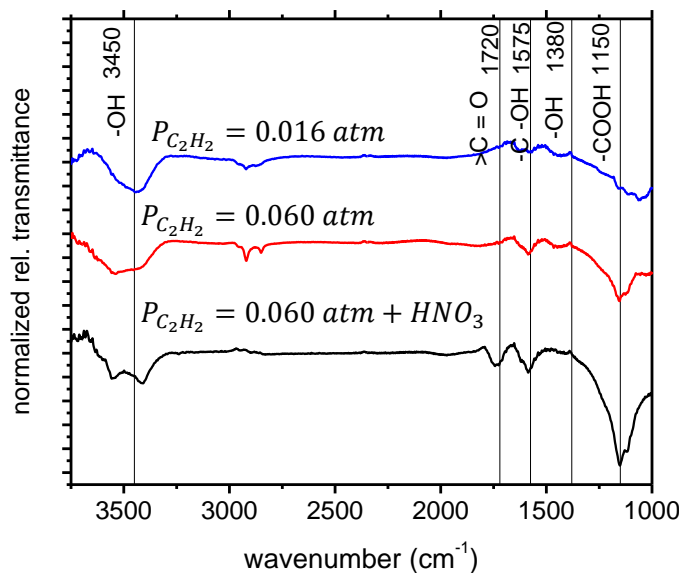


Figure 4.7. Normalized relative transmittance FTIR spectra of MWCNTs grown at 800 °C with 80 nm Ni seed catalyst. Solid lines indicate peaks corresponding to labelled functional groups.

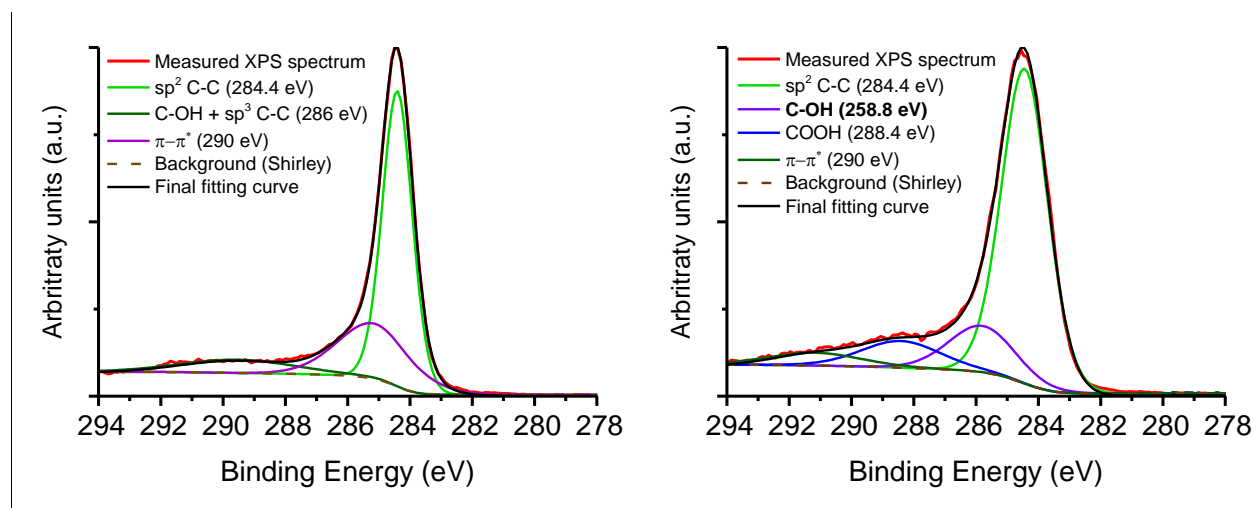


Figure 4.8. Deconvolution of the XPS C1s peak for MWCNTs grown at $P_{C_2H_2} = 0.060$ atm, growth temperature = 800 °C, and 80 nm Ni seed catalyst: (a) untreated MWCNTs (b) HNO_3 treated MWCNTs.

Table 4.2. Integrated elemental concentrations of MWCNTs grown at $P_{C_2H_2} = 0.060$ atm, growth temperature = 800 °C, and 80 nm Ni seed catalyst for untreated MWCNTs and HNO₃ treated MWCNTs.

		C 1s		C %	N 1s	N %	O 1s	O %	C/O		
Binding energy (eV)	290.0 π - π^*	285.4 C-OH + sp ³ -C-	284.4 sp ² -C-				532.2 C-O- C				
MWCNT	10	26	58	94	-	-	6	6	15		
Binding energy (eV)	291.2 π - π^*	288.4 COO H	285.8 C-OH + sp ³ -C-	284.4 sp ² -C-	405.2 -N-		532.2 C=O	530.7 C-O- C			
MWCNT (HNO₃)	2	4	42	25	73	1	1	9	17	26	3

The N 1s peaks at ~405 eV (**Table 4.2**) indicate the presence of chemisorbed nitrogen oxide species,^{107, 133} likely a result of HNO₃ refluxing. HNO₃ treated MWCNTs have higher oxygen content (26%) than untreated MWCNT (3%). The carbon to oxygen (C/O) ratio decreases from 15 for the untreated MWCNTs to 3 with HNO₃ acid treatment. The O1s peak at 532.2 eV is assigned to oxygen in a double bond with carbon atoms (C=O or O-C=O) and the peak at 530.7 eV is assigned to physically absorbed oxygen moieties.¹⁰⁸ It is clear from the FTIR and XPS analysis that oxygen functionalities - specifically -COOH functional groups - have been incorporated into the MWCNT surface chemistry.

Raman characterization before and after HNO₃ treatment is presented in **Figure 4.9**. There are conflicting reports in the literature on the effect of acid treatment on the structural defect density (characterized by I_D/I_G in MWCNTs); some authors report a decrease in I_D/I_G with acid treatment¹⁰⁸ that they attribute to the absence of amorphous carbon, and others report an increase in I_D/I_G as a result of additional *kinks* incorporated into the MWCNT structure.^{50, 106} In this case, it is evident that the D and D' peaks are more prominent in the acid treated MWCNT Raman spectra than untreated MWCNTs. This suggests that the dark spots visible in the STEM images in **Figure 4.4** are likely additional defect sites from the chemical oxidation process. In addition, the authors

that report the opposite finding used a weaker acid concentration, did not report the refluxing temperature and did not report a standard deviation in I_D/I_G . Hence, we conclude that the acid treatment incorporates additional defects that include the oxygen moieties incorporated into the MWCNT characterized by the increase in I_D/I_G and $I_{D'}/I_G$.

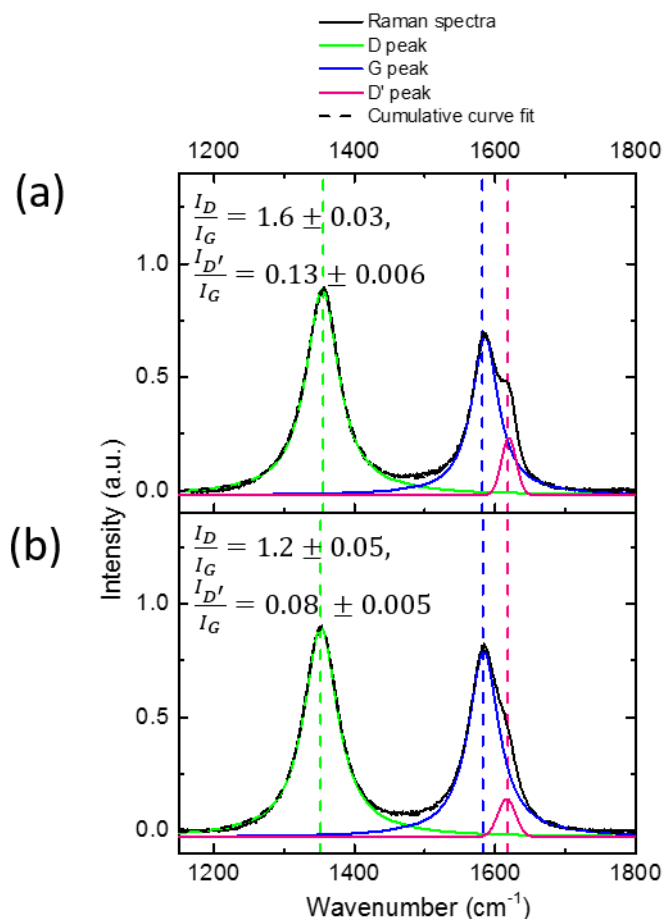


Figure 4.9. First order Raman spectra measured for MWCNTs grown with $P_{C_2H_2} = 0.60$ atm and 80 nm Ni seed, at 800 °C; (a) HNO₃ treated and (b) untreated MWCNTs. The dashed lines specify the peak position of the D band, G band and D' band. I_D/I_G and $I_{D'}/I_G$ is shown inset.

To investigate the effect of chemical functionalization on the electrocatalytic activity towards ORR, electrodes made from HNO₃ treated MWCNTs and untreated MWCNTs were characterized by symmetric cell AC impedance measurements (shown in **Figure 4.10**). The area normalized electrode impedance decreases from $360 \pm 13 \Omega \text{ cm}^2$ to $21 \pm 2 \Omega \text{ cm}^2$. This

demonstrates that oxygen functionalities result in order of magnitude improvement in ORR resistance in comparison to untreated MWCNTs in the solid acid electrochemical system.

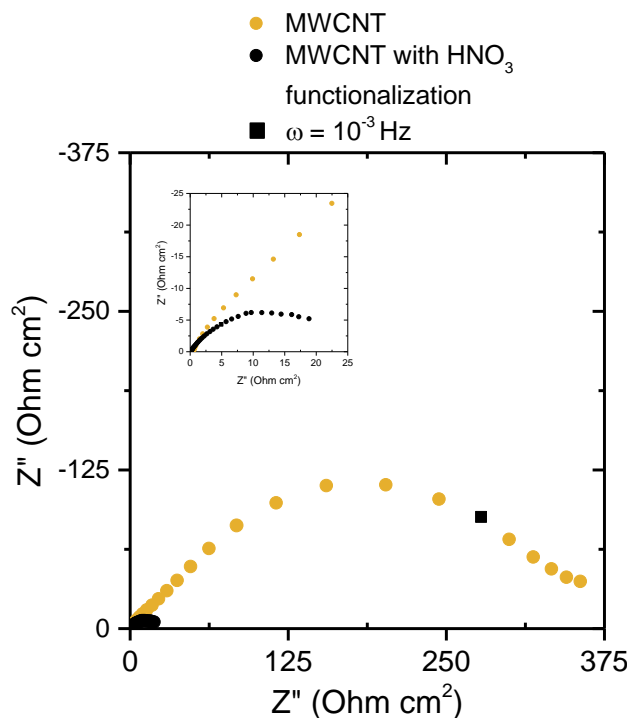


Figure 4.10. Comparison of symmetric cell impedance measurements of 50mg 1:1 MWCNT: CsH_2PO_4 composite electrodes in a Nyquist representation for untreated and HNO_3 treated MWCNTs. Measurements were collected at 250°C under humidified O_2 ($p_{\text{H}_2\text{O}} = 0.4\text{atm}$) flowing at 40 sccm in the 5mHz to 10KHz frequency range. Inset is higher magnification. MWCNTs grown in $P_{\text{C}_2\text{H}_2} = 0.060\text{ atm}$, growth temperature = 800°C , and 80 nm Ni seed catalyst.

MWCNT growth temperature - SEM images for MWCNTs grown in $P_{\text{C}_2\text{H}_2} = 0.16\text{ atm}$ with 80 nm Ni particles at varying substrate temperatures are shown in **Figure 4.11**. MWCNTs were grown at 600°C , 650°C , 700°C , and 800°C . It is clear that there is a difference in morphology of the MWCNTs with varying substrate temperature. The MWCNTs grown at lower temperatures appear to have twists in the MWCNT structure characteristic of ‘herringbone’ MWCNTs.¹¹⁴ Herringbone MWCNTs are known to have a higher number of edge plane-like defect sites than hollow tube MWCNTs. This is because the graphite sheet planes are at an angle to the axis of the tube, requiring a high number of the graphite sheets to be terminated at the surface of the tube.¹¹⁴

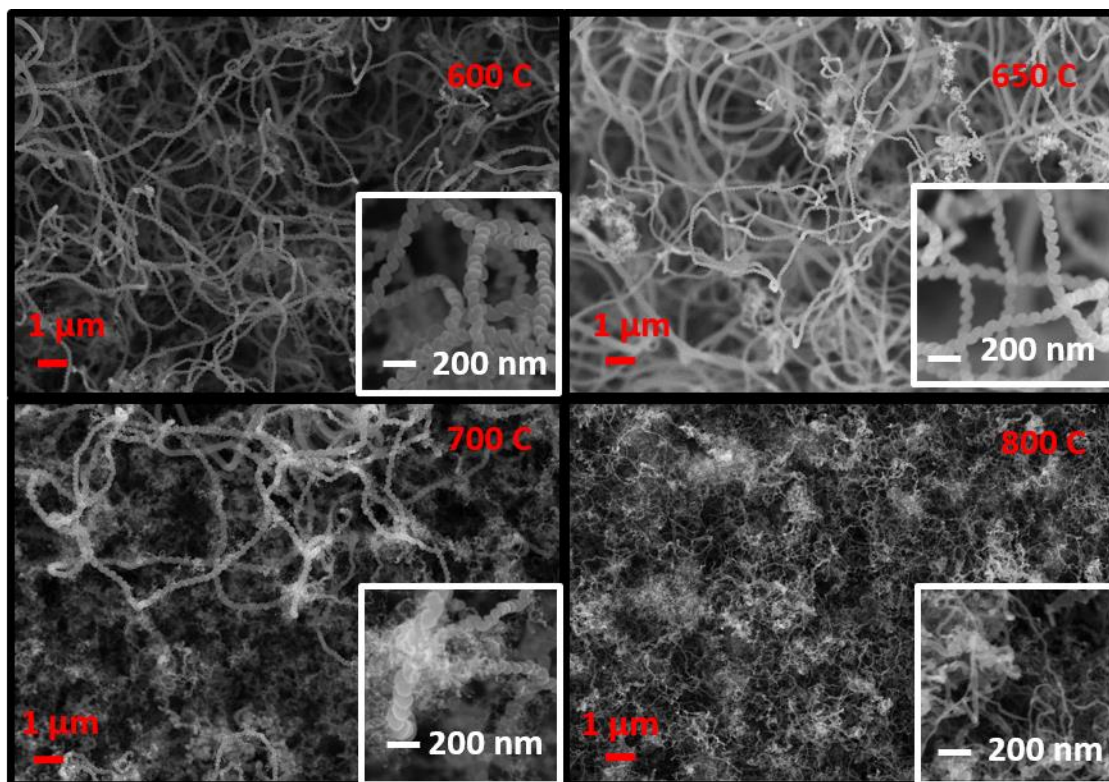


Figure 4. 11. SEM images of MWCNTs grown in $P_{C_2H_2} = 0.060$ atm with 80 nm Ni particles at 600 °C, 650 °C, 700 °C, and 800 °C. Inset is higher magnification

To study the influence of growth temperature on the defect density, elemental composition, and congruently the chemical functionalization process, MWCNTs grown at varying substrate temperatures (shown in **Figure 4.11**) were characterized by Raman Spectroscopy and XPS. In **Figure 4.12a** Raman spectra collected from all MWCNTs were fit with two Lorentzian curves and a Gaussian curve (as presented previously in **Figure 4.4** and **Figure 4.9**). This is the accepted way to fit MWCNT Raman that captures the non-dispersive behavior of the graphite (G) band. However, for the MWCNTs grown at 600 °C – 700 °C, G band shifts to ~ 1562 cm^{-1} . This means the curve fitting routine is incorrect because the G band is non-dispersive for all graphitic materials. This highlights the power of Raman spectroscopy in characterizing MWCNT structure. Raman characterization of ‘herringbone’ structures has not been reported extensively in the literature. For example, one literature reports Raman spectra fitting of ‘herringbone’ MWCNTs (or carbon nanofibers as the authors refer to this structure) with an additional ‘T₂’ band at ~ 1500 cm^{-1} .¹²¹ This captures the non-dispersive behavior of the G band but disallows the use of the I_D/I_G or I_D’/I_G as a measure of structural defects as a result of the influence of the T₂ band on the I_D/I_G or I_D’/I_G ratio.

The authors found that the G' (overtone of the D-band which is a result of an inelastic phonon emission process, and occurs usually around 2700 cm^{-1}) and full width half maximum (FWHM) of the D band were the better metric for quantifying crystallinity of carbon nanofibers. They report an increase in $I_{G'}/I_G$ and a decrease in FWHM (D) with increasing crystallinity. The latter observation is supported in the literature by Zickler *et al.*¹²⁰ who report that the FWHM (D) decreases with increasing crystallinity for samples with a small graphite crystal size, L_a . They conclude that for graphitic samples of low crystalline quality the relation found between L_a and $I_{D'}/I_G$ in the seminal paper by Tuinstra and Koenig¹⁰⁵ should be taken with caution.

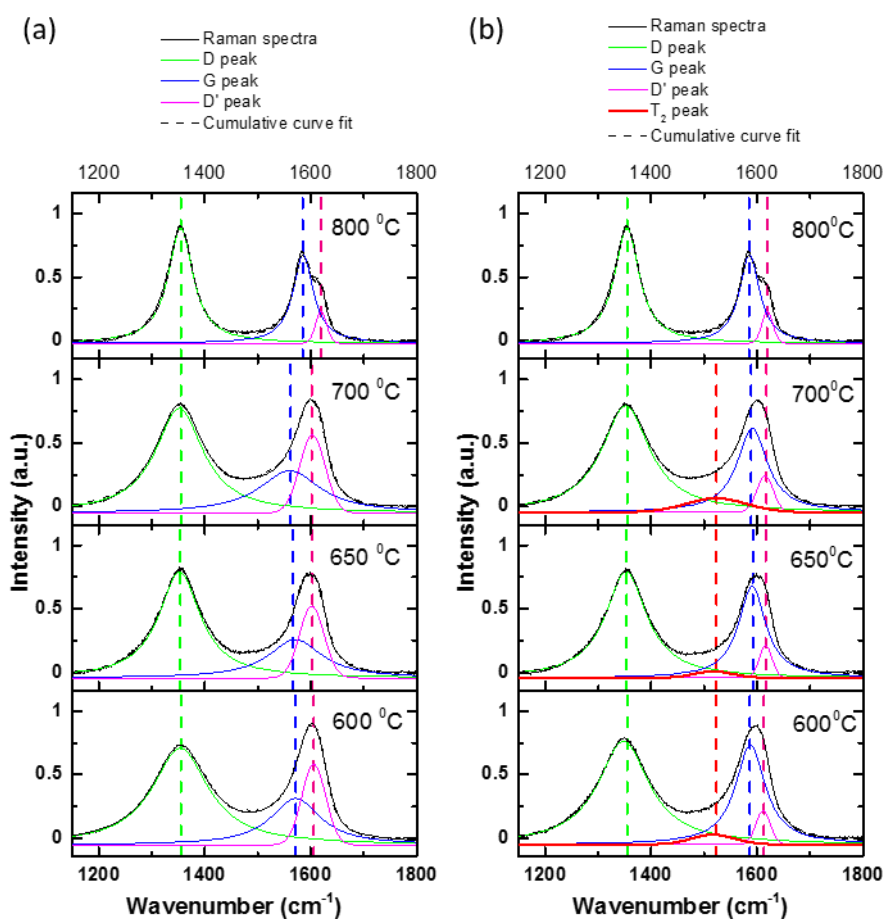


Figure 4.12. First order Raman spectra measured for HNO_3 -treated MWCNTs grown with $P_{\text{C}_2\text{H}_2} = 0.060\text{ atm}$ and 80 nm Ni seed catalyst; (a) fit with D band, G band and D' band (b) D band, G band D' band, and T_2 band. Growth temperature *is inset*.

In **Figure 4.12b** the MWCNTs grown at $600\text{ }^\circ\text{C} - 700\text{ }^\circ\text{C}$ were fit with an additional Gaussian T_2 band at $\sim 1520\text{ cm}^{-1}$ (MWCNTs grown at $800\text{ }^\circ\text{C}$ same fitting routine in **Figure 4.12a**

and **4.12b**).¹²¹ The FWHM of the D band from **Figure 4.12b** fitting is shown versus growth temperature in **Figure 4.13**.

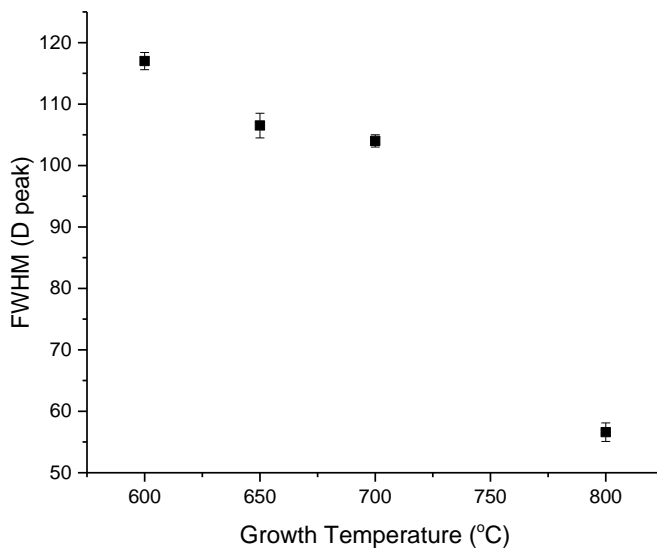


Figure 4.13. FWHM of the ‘D’ peak in Raman measurements versus growth temperature.

The FWHM of the D peak decreases with increasing growth temperature, suggesting that the samples grown at lower temperature have more structural defects (less crystalline quality).

To assess the surface functionalities on the acid treated MWCNTs, chemical composition was characterized by XPS. The XPS C 1s of untreated MWCNTs at varying substrate temperature is shown in **Figure 4.14**. XPS C 1s and N 1s spectra of the HNO₃ treated MWCNTs grown at varying substrate temperature are shown in **Figure 4.15** and **Figure 4.16**, respectively. All C 1s scans (HNO₃ treated and untreated) have the characteristic peaks observed previously at 284.4 eV and ~290-291 eV, attributed to sp² hybridized graphitic carbon atoms and the π-π* transition loss, respectively. In addition, the peak at 285.8 is a sum of contributions from sp³ hybridized carbon atoms that are a result of structural defects at the surface of the graphitic sheet (amorphous carbon atoms in another state than typical graphitic sp² carbon atoms) typically present at 285.5 eV, and C-OH species typically present at 285.9 eV.¹⁰⁸⁻¹¹¹ The HNO₃ treated MWCNTs C 1s spectra (at all growth temperatures) have a peak at 288.4 eV, assigned to COOH groups. However, for the HNO₃ treated MWCNTs, there is a distinct increase in the COOH peak at ~288.4 eV with decreasing

temperature. Therefore, the herringbone structures (grown at 700 °C- 600 °C) have a higher concentration of oxygen functionalities.

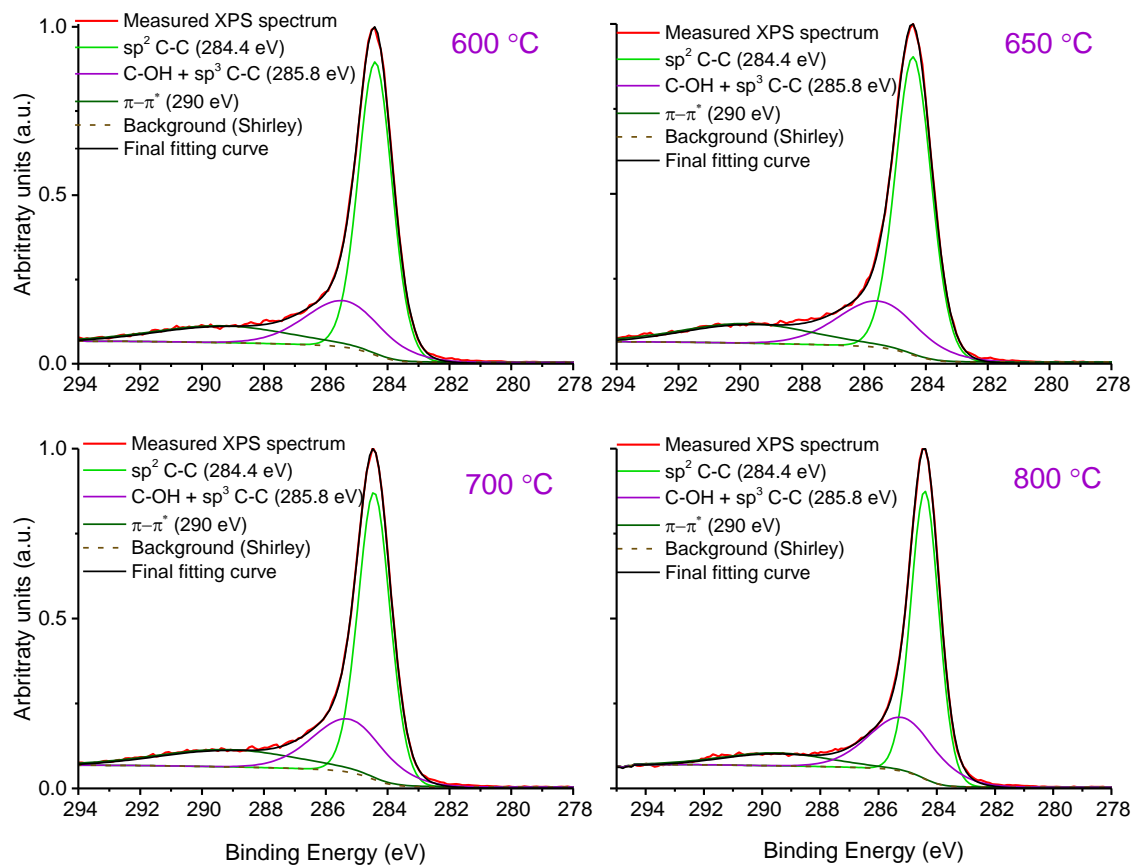


Figure 4.14. Deconvolution of the XPS C1s peak for MWCNTs grown at $P_{C_2H_2} = 0.060$ atm with 80 nm Ni seed catalyst at a growth temperature of (a) 600 °C, (b) 650 °C, (c) 700 °C, and (d) 800 °C

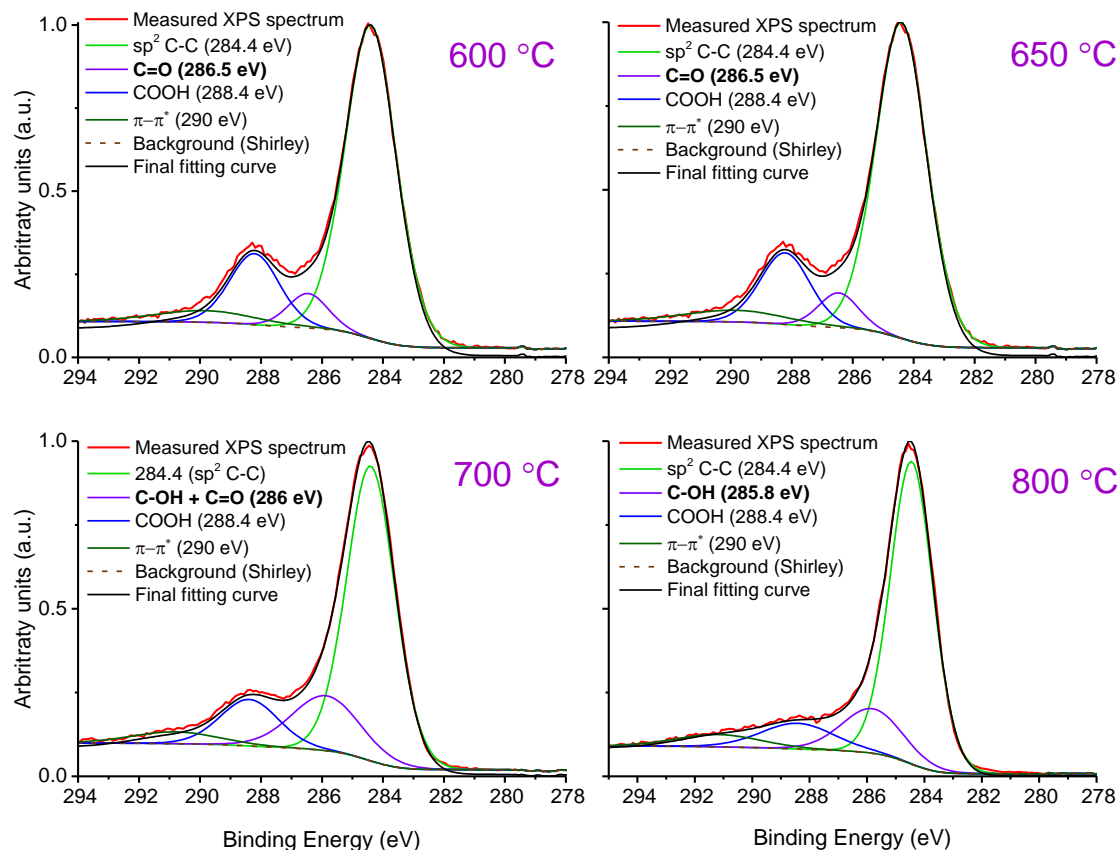


Figure 4.15. Deconvolution of the XPS C1s peak for HNO_3 treated MWCNTs grown at $P_{\text{C}_2\text{H}_2} = 0.060$ atm with 80 nm Ni seed catalyst at a growth temperature of (a) 600 °C, (b) 650 °C, (c) 700 °C, and (d) 800 °C.

In addition, there is a noticeable shift in binding energy of the peak at 285.8 eV, for the MWCNTs grown at 800 °C, to 286.5 eV for the MWCNTs grown at 600 °C (highlighted bold in **Figure 4.15**). That peak shifts from 285.5 eV at 600 °C, to 286.0 eV at 700 °C and 286.5 eV at 650-600 °C. This peak positions suggest carbon-oxygen covalent bond formation in the form of C-OH at 285.9 eV and C=O at 286.9 eV). This results indicate that there are more C=O groups, either in quinone form or in carboxylic acid form, in the MWCNTs grown at lower temperatures.

XPS N 1s scans reveal that the slight nitrogen incorporation observed for samples grown at 800 °C increase with decreasing growth temperature. The N1s peaks at 400.0 eV and 405.2 eV are indicative of pyrrol (N-H) groups on the MWCNT surface and chemisorbed NO_x species, respectively.

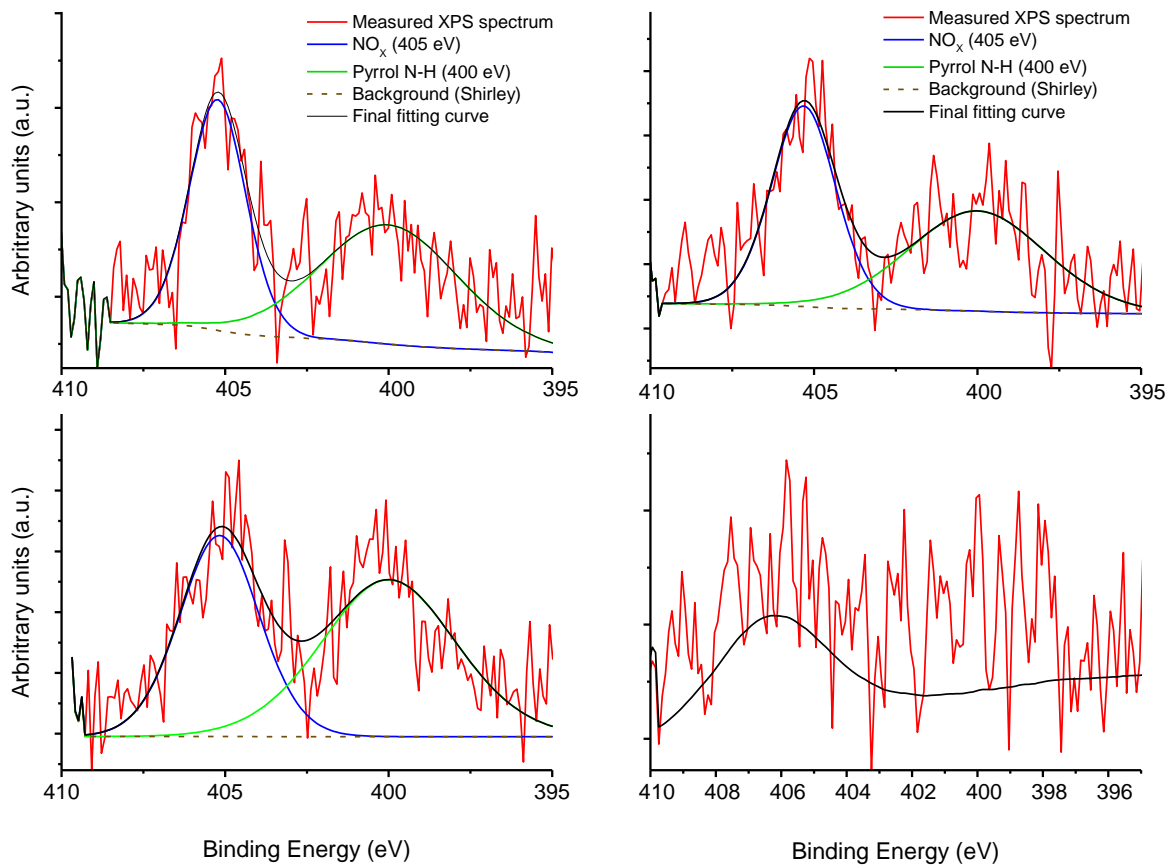


Figure 4.16. Deconvolution of the XPS N1s peak for MWCNTs grown at $P_{C_2H_2} = 0.060$ atm with 80 nm Ni seed catalyst at a growth temperature of (a) 600 °C, (b) 650 °C, (c) 700 °C, and (d) 800 °C (CPS refers to counts per second).

Integrated elemental compositions are presented in **Table 4.3** show that the nitrogen incorporation is fairly constant at 3% for the herringbone structures (700 °C- 600 °C). This is not untoward, as one reference on nitric acid treatments of MWCNTs, reports 2% nitrogen incorporation into the MWCNT structure as a result of HNO_3 treatment.⁷⁷ The nitrogen incorporation observed is likely due to the highly reactive defect sites in these structures. In addition, there is a significant increase in oxygen content with decreasing growth temperature. Therefore, the carbon to oxygen ratio (C/O) decreases with decreasing substrate temperature. It is expected that the nature and the density of these oxygen moieties observed will impact the oxygen reduction reaction activity of these MWCNTs.

					C1 %			N 1 %			O1 %	C/O
	290 π - π^*	288.4 COOH	286.5 C=O	284.4 sp ² -C		405.2 -N-	400.0 NO		532.2 C-O-C	530.7 C=O		
600- COOH	2.6	8.0	3.1	36.2	50	1.2	1.6	3	28.3	19.0	47	1.1
650- COOH	3.8	4.7	12.2	32.4	53	1.2	1.2	3	24.0	20.4	44	1.2
700- COOH	2.8	7.4	10.2	38.6	59	1.4	1.9	3	29.3	8.5	38	1.6
	291.6	288.4 COOH	285.8 C-OH sp ³ -C-									
800- COOH	2	3.7	41.5	25.1	73	1			18	8	26	3

Table 4.3. Integrated elemental concentrations of HNO₃ treated MWCNTs grown at P_{C₂H₂} = 0.016 atm, with 80 nm Ni seed catalyst.

ORR electrochemical reactivity of all four HNO₃ treated MWCNTs were assessed by symmetric cell impedance studies presented in **Figure 4.17**, alongside average area normalized impedance values for multiple samples grown at each temperature. There is an observed decrease in average area normalized impedance from $21 \pm 2 \Omega \text{ cm}^2$ (800 °C) to $8 \pm 1 \Omega \text{ cm}^2$ (700 °C), and further decrease to $7 \pm 1 \Omega \text{ cm}^2$ (650 °C). Surprisingly, the MWCNTs grown at 600 °C showed no activity, as is evident by the blocking electrode impedance response. It is important to note here that the mixing by conventional milling techniques, was more difficult for the herringbone structures grown at lower CVD growth temperatures (600- 650°C). The herringbone MWCNTs after HNO₃ treatment, although dispersive in aqueous solvents, were difficult to mix by mortar and pestle into an electrode matrix with the electrolyte, CsH₂PO₄. This suggests that the functionalization treatment has a strong influence on the nominally weak Van der Waals forces between the graphite layers. CsH₂PO₄ is water soluble and hygroscopic, hence, this presented a challenge in making the electrode with a solvent-based method. Electrospray has been demonstrated as a feasible method to fabricate solid acid electrodes from aqueous solutions

containing MWCNTs.^{7,8} However, electrospray deposition of the MWCNTs was not explored in this work but is a potential electrode fabrication method to circumvent this issue.

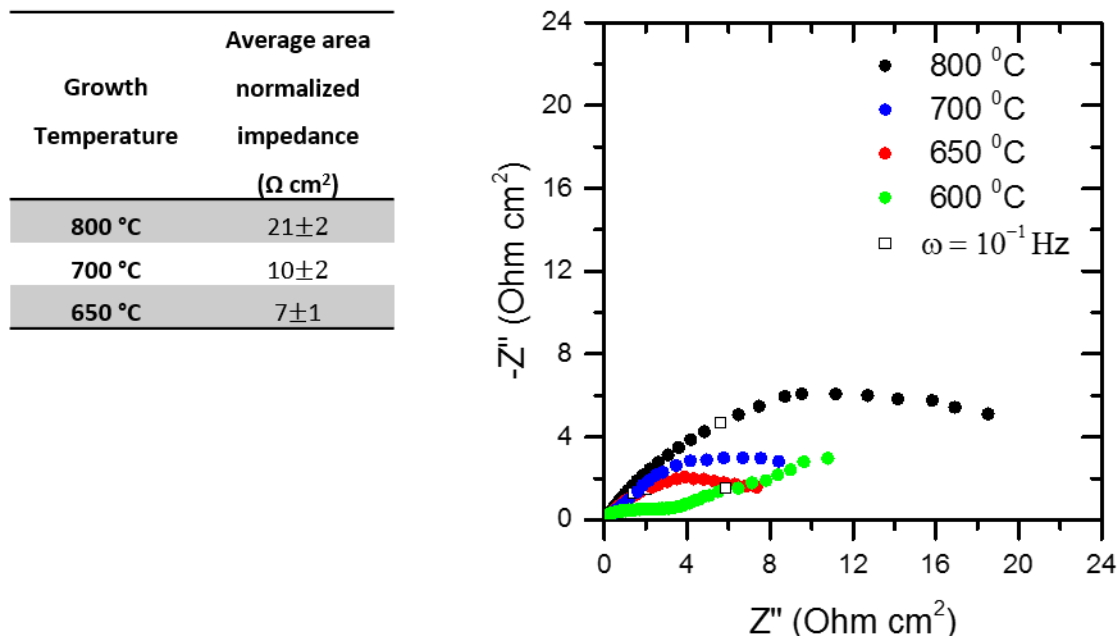


Figure 4.17. Comparison of symmetric cell impedance measurements of 50mg 1:1 MWCNT:CsH₂PO₄ composite electrodes in a Nyquist representation for HNO₃ treated MWCNTs. Measurements were collected at 250°C under humidified O₂ (pH₂O = 0.4atm) flowing at 40 sccm in the 5mHz to 10KHz frequency range. MWCNTs grown in P_{C₂H₂} = 0.060 atm with 80 nm Ni seed catalyst. The growth temperature is inset.

The increase in ORR activity observed can be correlated to the increase in oxygen content in the form of carbonyl and carboxylic acid functional groups in the MWCNTs. The HNO₃ treated MWCNTs grown at 650 °C show the highest concentration of the quinone (C=O) functional group. The catalytic ORR activity of carbon materials is generally attributed to quinone groups.¹¹⁵ Although, this mechanism has not been confirmed, glassy carbon electrodes modified with a variety of quinone compounds have shown enhanced catalytic activity towards oxygen reduction reaction via a 2 electron pathway.^{87, 134} In this case, an increase in the relative percent of oxygen in the form of (C=O in quinone and carboxylic form) causes an increase in ORR activity. Presented in **Figure 4.18** is the average ORR area normalized impedance versus the relative percent of oxygen in the MWCNT structure. The increased activity of MWCNTs with higher percentage of

C=O groups in quinone and carboxylic form gives experimental evidence that the proposed mechanism on carbon nanostructures extends to MWCNTs.

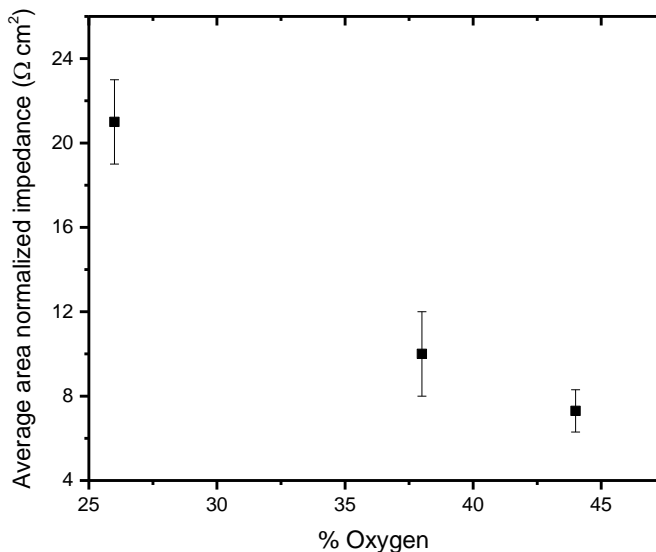


Figure 4.18. Average area normalized impedance values versus the % Oxygen from XPS analysis of HNO_3 treated MWCNTs grown with $P_{\text{C}_2\text{H}_2} = 0.16 \text{ atm}$ and 80 nm Ni seed catalyst

4.5. Conclusion

MWCNTS grown by chemical vapor deposition have been demonstrated as potential ORR catalysts in the solid acid electrochemical system. The structural defect density characterized by Raman spectroscopy can be correlated to the size of the Ni catalyst used in the growth (consequently MWCNT diameter), the partial pressure of the acetylene precursor, and the growth temperature. All of which can be used to control the density of ORR active sites. In addition, ORR activity is enhanced by two orders of magnitude with HNO_3 oxidation. This enhancement is as a result of increasing carbonyl functionalization in the MWCNTs. This experimental observation substantiates the Yeager model for ORR on carbon nanostructures.

4.6. Acknowledgement

Authors would like to acknowledge Dr. Nick Brunelli for the synthesis of the Ni nanoparticles used in this work. Authors would like to acknowledge Mike Bauer who helped with CNT synthesis (Ni = 40 nm). Finally, Authors would like to acknowledge Moritz Pfohl, whose parameter exploration on the CVD of carbon nanotubes was used as a starting point for CNT growth in this work.

CHAPTER 5

Oxygen reduction by TiO_x overlayers

Reproduced with permission from Hadi Tavassol, Vanessa Evoen, Sheel Sanghvi, and Sossina M. Haile

5.1. Introduction

In this chapter we evaluate titania (TiO_x) as potential ORR catalysts in solid acid fuel cell cathodes.

5.2. Experimental

Materials preparation - CsH_2PO_4 solid electrolyte was synthesized in house using the method explained previously.¹⁴ Commercial TiO_2 powders of rutile (Alfa Aesar) and anatase (Alfa Aesar) were used as received. An in-house synthesis method was used to grow TiO_x overlayers. The growth was performed by oxidizing Ti metal powder (325 mesh from Alfa Aesar) under 0.7% O_2 (balance Ar) at a flow rate of 250 sccm at selected temperatures between 600 °C and 900 °C for 30 min. The powder samples were brought to the growth temperature under pure Ar (250 sccm) at a rate of 15° per minute. Following the growth, the temperature was ramped down to the room temperature under Ar atmosphere. For the samples prepared at 600 °C, the growth time was varied between 15 min and 60 min.

Characterization - X-ray diffraction measurements were carried out using an X'pert MD (Panalytical) diffractometer. Peak refinement analysis was performed using the GSAS software. X-ray photoelectron spectroscopy measurements on powder samples were carried out on a Thermo-Scientific ESCALAB 250Xi instrument using a monochromatic Al $K\alpha$ (1486.6 eV) X-ray source. C 1s peak at 285 eV was used as reference for correcting the binding energy values.

Electrochemical testing - Cathode composites were made by mechanically mixing CsH_2PO_4 , Ti-based catalysts, and nanographitic powders as the primary electronic component (GS-2299,

Asbury Carbons, Asbury, NJ) in a 3:3:1 mass ratio, and 50 mg was used for each experiment. The Pt cathode data was acquired from a mechanically mixed CsH₂PO₄, Pt-black, and Pt/carbon black (40 weight % loading on carbon from Sigma Aldrich) in a 3:3:1 mass ratio, and 50 mg was used. The anode mixture was kept constant between all samples. Anode in all cases was a mixture of CsH₂PO₄ and Pt on carbon black (40% Pt/Carbon black, Sigma Aldrich) in a 3:1 mass ratio, and 30 mg was used. The cells were assembled by pressing 50 mg of cathode and anode composites against *ca.* 700 mg of CsH₂PO₄ powder in a 19 mm die at 69 MPa for 20 min. The thickness of the CsH₂PO₄ solid electrolyte was *ca.* 0.7 mm with *ca.* 90% of the theoretical density. Two stainless steel gas diffusion layers (McMaster-Carr, Type 316, mesh size 100 × 100) were placed on either side of the cells. The cells were wrapped in Teflon tape to ensure proper sealing before placing in the custom-built stainless steel anode and cathode cell compartments. Initially, the cell compartment was ramped up to 140 °C at 5 °C min⁻¹ in air. Then the temperature was increased to 240 °C at 5 °C min⁻¹, under humidified Ar (0.4 atm H₂O, 6 cm min⁻¹). At 240 °C, humidified hydrogen and oxygen (0.4 atm H₂O, 6 cm min⁻¹) were introduced to the anode and cathode compartments of the fuel cell. Gases were humidified by flowing through a water bubbler heated to 80 °C. Once at 240°C under humidified gases, polarization and impedance data were collected using an AutoLab PGSTAT20N instrument.

5.3. Results and discussion

Electrochemical activity and oxide phase- **Figure 5.1a** shows polarization curves of cathodes made from as-received rutile and anatase micropowders. For performance comparison, TiO_x samples were compared with a cathode made from 40% Pt on carbon. Interestingly, rutile TiO₂ shows an onset potential of *ca.* 0.70 V, which is higher than the onset potential of the as-received anatase powder at *ca.* 0.63 V. The cathode made with the rutile micropowder also exhibits higher voltage at all current values. This observation seems consistent with previously reported higher activity of mainly rutile oxide films grown on titanium metal substrates.¹³⁵ **Figure 5.1b** shows XRD spectra of as received micropowders, which reveals phase impurities of both rutile and anatase micropowders. Phase fraction analysis of powder samples confirms that the rutile and anatase titania powders are not phase pure.

The apparent correlation of oxygen reduction reaction (ORR) catalysis with the phase of the TiO₂ based electrodes led us to further investigate this material as an alternative catalyst in the

cathodes of the solid acid fuel cell. To this end, an in-house growth method was used to control the phase fraction of the oxide overlayers. Oxide films were grown on Ti metal powder substrates at selected growth temperatures and times under slightly oxidizing environment (0.7% O₂, balance Ar). **Figure 5.1a** shows the oxide phase fraction acquired from peak refinement of XRD patterns of different powder samples following the growth. The XRD analysis reveals that the phase fraction of the rutile TiO₂ increases with increasing growth temperature from 600 °C to 900 °C, while 800 °C and 900 °C shows similar phase distribution. Interestingly, anatase growth pattern with temperature is not monotonic. Initially anatase phase fraction increases from 600 °C to 700 °C. At 700 °C, the relative anatase amount is the highest of all growth temperatures studied here. At higher temperatures, *i.e.* 800 °C and 900 °C, the oxide overlayer is almost entirely rutile. In fact, at 900 °C, XRD peak refinement does not recognize any anatase pattern.

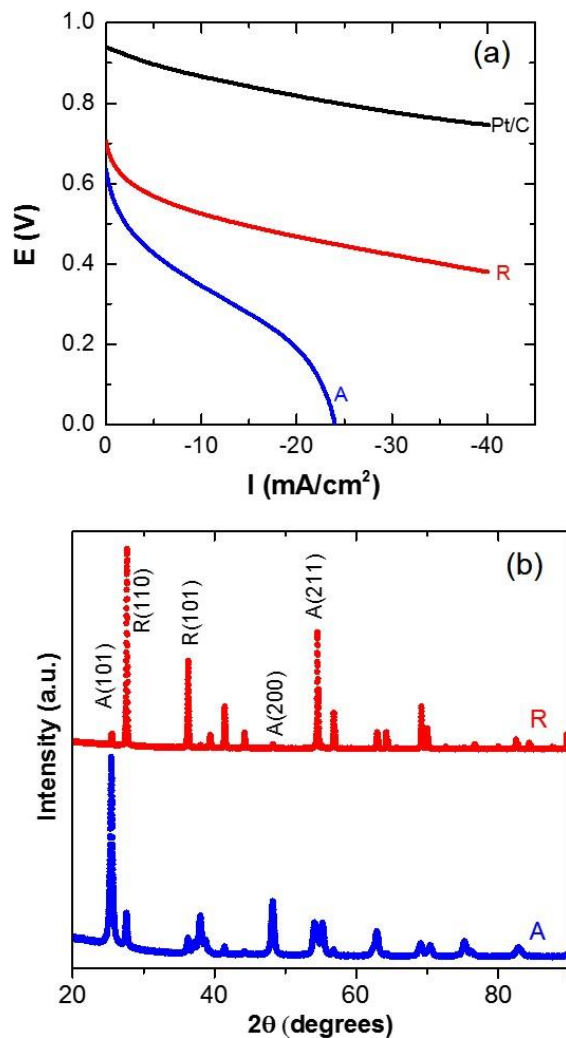


Figure 5.1. (a) Polarization behavior and (b) phase fraction of the as-received TiO_2 micropowders of rutile (R) and anatase (A).

Figure 5.2b shows polarization curves acquired from fuel cells assembled using cathodes made from oxide overlayer titanium powders, annealed between 600 °C and 900 °C under mentioned conditions for 30 min vs. Pt/carbon anodes. For comparison, polarization data from cathodes made from as-received rutile and anatase micropowders and Pt/carbon cathodes are also included. **Figure 5.2c** shows the cell voltage of the titania based cathodes at a current value of 5 mA cm^{-2} . Interestingly, the sample prepared at 600 °C, which showed the lowest amount of rutile phase in the XRD analysis (**Figure 5.2a**), outperforms the rest of the titanium oxide based

cathodes. This sample exhibits an onset voltage of *ca.* 0.72 V, while showing higher voltage at all current values. The activity of the remaining titanium oxide based cathodes correlates with the relative amount of rutile oxide phase present in the oxide overlayers, which agrees with what was observed in the as-received TiO₂ micropowders. The sample prepared at 700 °C, with *ca.* 5% of the oxide layer in the anatase form has the lowest activity of the in-house prepared samples.

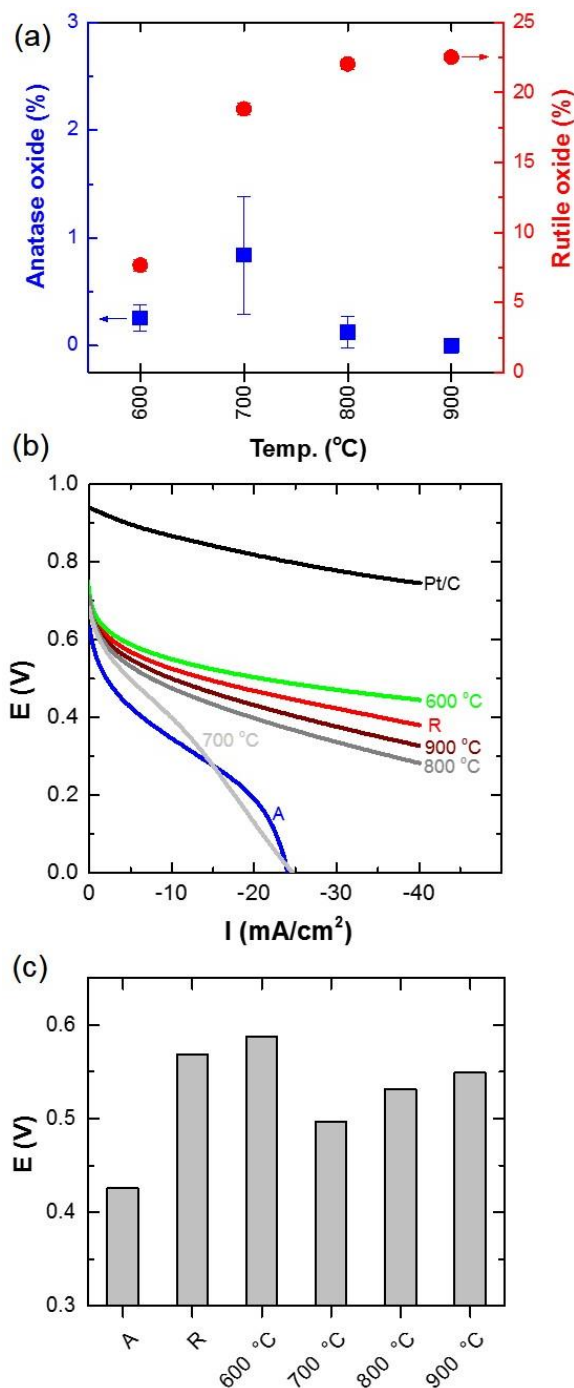


Figure 5.2. (a) Phase fraction of rutile and anatase TiO₂ in the oxide layers grown on Ti metal powders. (b) Polarization response of different Ti-based cathodes, and comparison with a Pt on carbon black cathode. R and A represents as received rutile and anatase micro-powders. Polarization curves represented are from Titanium micro-powders treated at shown temperatures for 30 min under 0.7% O₂ (Ar balance). (c) Cell voltage of the titania cathodes shown in part b at 5 mA cm⁻² of current.

Influence of oxidation state on electrochemical activity- In order to further investigate the observed higher activity as a result of annealing at 600 °C, we varied the annealing time at this temperature. **Figure 5.3** shows the cell voltage of cathodes made from samples annealed for different times at 600 °C. The cell voltage is shown at a current value of 5 mA cm⁻², although the trend remains the same for even higher current values. As evident from **Figure 5.3**, voltages of the cells made from powders annealed at this temperature are sensitive to the growth time. The highest voltages are evident at 25 and 30 minutes of annealing. Deviation from these annealing times, that is, annealing for longer and shorter times, results in a decrease of cell voltage. This indicates that the powders annealed for 25-30 minutes under slightly oxidizing environment at 600 °C contain some form of an active site for the reduction of O₂. Furthermore, we continued cycling the cells between 0.95 V and 0.0 V at a scan rate of 2.5 mV s⁻¹. After five electro-chemical cycles (gray bars in **Figure 5.3**), the most active samples, that is powders annealed for 25 and 30 min at 600 °C, show no loss of activity. The activity of the rest of the cells assembled with cathodes made from powders annealed at 600 °C decreases with cycling, as more negative potentials are required to achieve 5 mA cm⁻² current.

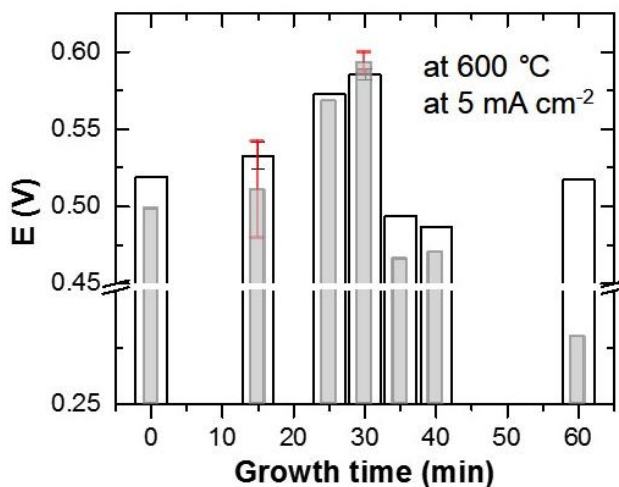


Figure 5.3. Cell voltage with cathodes made from titanium micropowders annealed at 600 °C, under 0.7% O₂ (balance Ar) for different growth times. Voltage is compared at 5 mA cm⁻² of current. Gray bars represent the cathodes following five electrochemical cycles between 0.95 V and 0V at a scan rate of 2.5 mV s⁻¹.

Interestingly the color of powder samples annealed at 600 °C changes as the treatment time was varied. **Figure 5.4** shows photographs of the starting titanium powder (**Figure 5.4a**) and powders following annealing at 600 °C for 15, 30 and 60 minutes (**Figure 5.4b-d**). While the titanium metal powder substrate is gray, annealing at 600 °C for 15 min results in a navy blue color. Annealing for longer times of 30 and 60 minutes results in dark and bright green colored powders respectively. The powders annealed at 800 and 900 °C for 30 minutes remain gray.

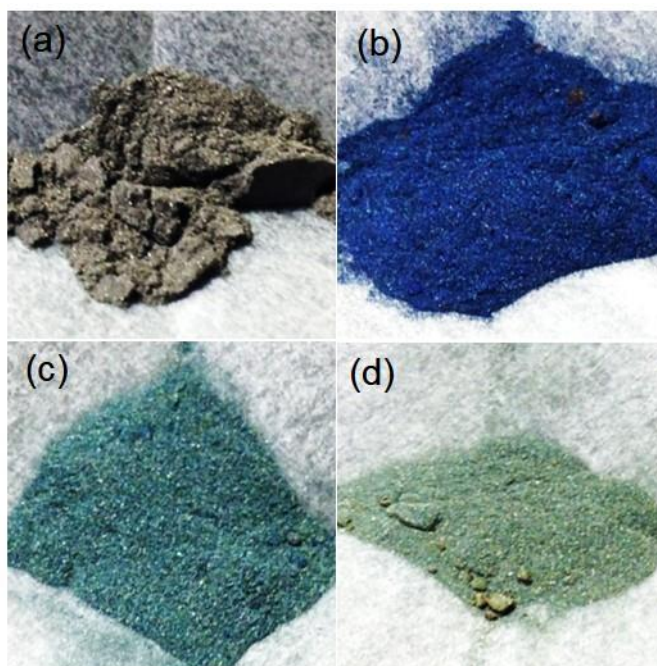


Figure 5.4. Samples prepared from titanium metal micropowder (a) before annealing; and after annealing at 600 °C in 0.7% O₂ (balance Ar) for (b) 15 min, (c) 30 min and (d) 60 min.

To identify the nature of the active sites on oxidized titanium samples, we further analyzed the powders annealed at 600 °C using XRD. Phase fraction of the samples prepared at 600°C acquired from XRD are shown in **Figure 5.5**. Annealing the titanium micropowder at 600 °C for 15 minutes under 0.7% O₂ (balance Ar) results in an oxide film (ca. 5.5%) entirely in rutile form. Annealing for 30 minutes under the same condition results in ca. 7.5% rutile and 0.3% anatase TiO₂. Annealing the powder under the same conditions for 60 minutes results in ca. 9.5% rutile and 6.1% anatase phase in the oxide overlayer. Hence, the growth behavior at 600 °C under these

conditions initially favors the rutile phase. With increasing annealing time, the phase fraction of the anatase form increases rapidly.

Although the presence of the rutile phase seems to be important in the activity toward oxygen reduction, phase distribution alone does not explain the higher activity of some powders annealed at 600 °C in a slightly oxidizing environment. In order to gain insight into the electronic properties of oxidized titanium powders, and their effect on catalysis, we performed XPS analysis. **Figure 5.6** shows XPS spectra of Ti 2p (**Figure 5.6a**) and O 1s (**Figure 5.6b**) regions of the Ti-based powders studied here. XPS analysis of the Ti 2p region of the starting titanium metal powder (labeled Ti, Bg) exhibits two distinct peaks at *ca.* 464.5 and 458.8 eV (with a separation of 5.5 eV), corresponding to 2p_{3/2} and 2p_{1/2} respectively. These values match the binding energies of the Ti 2p region of TiO₂¹³⁶. These peaks are assigned to the native oxide formed on Ti metal surfaces upon exposure to air as shown previously.¹³⁶ It has been also shown that the native oxide layer can be removed under inert atmosphere at elevated temperatures (*ca.* 600 °C).¹³⁶ Here, since Ti metal powders are brought up to the selected temperature (600 °C to 900 °C) under an Ar atmosphere (at a 15 ° min⁻¹ rate), the growth of crystalline oxide overlayers occurs on a mostly metallic titanium powder substrate, as the native oxide layer is removed. As expected, XPS analysis of a powder sample annealed at 600 °C for 30 min under Ar atmosphere results in no change in the Ti 2p region, as a TiO₂ native oxide is formed on the surface upon re-exposure to air. Interesting XPS spectra of the powder sample annealed at 600 °C under 0.7% O₂ (Ar balance) for 15, 30 and 60 min reveal a shift (*ca.* 0.1 eV) to smaller binding energies for the Ti 2p_{3/2} core-level electrons. Binding energy shifts indicate changes in the chemistry and electronic structure of materials; these are especially important in catalysis.¹³⁷ In this case, the observed shift to smaller binding energies indicates slightly reduced metal sites. The powder sample annealed at 700 °C also shows a slight shift to smaller binding energy values. However, the samples annealed at higher temperatures (800 °C and 900 °C) under the same gas environment do not show any shift in the binding energy of the Ti 2p region, and they show values consistent with a TiO₂ films. The O 1s region (**Figure 5.6b**) of the XPS spectra reveals a similar trend, as the samples annealed at 600 °C for 15, 30, and 60 min show a shift to lower (*ca.* 0.4 eV) binding energies. Samples annealed at 800 °C and 900 °C do not show such shifts in the binding energy of the O 1s region, consistent with a TiO₂ film.

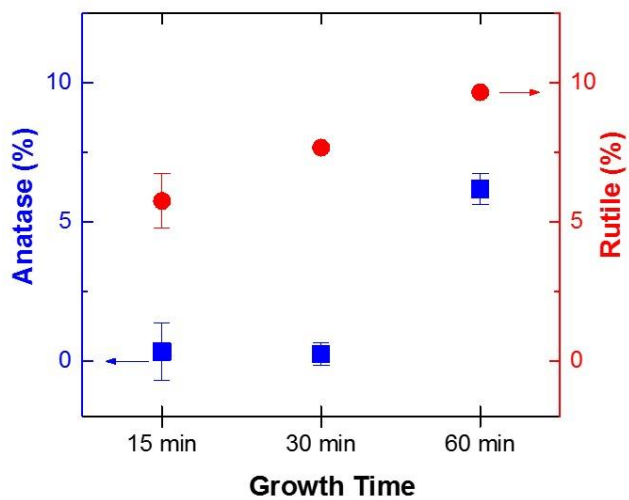


Figure 5.5. Rutile and anatase phase fractions of the powder samples following annealing at 600 °C for different times.

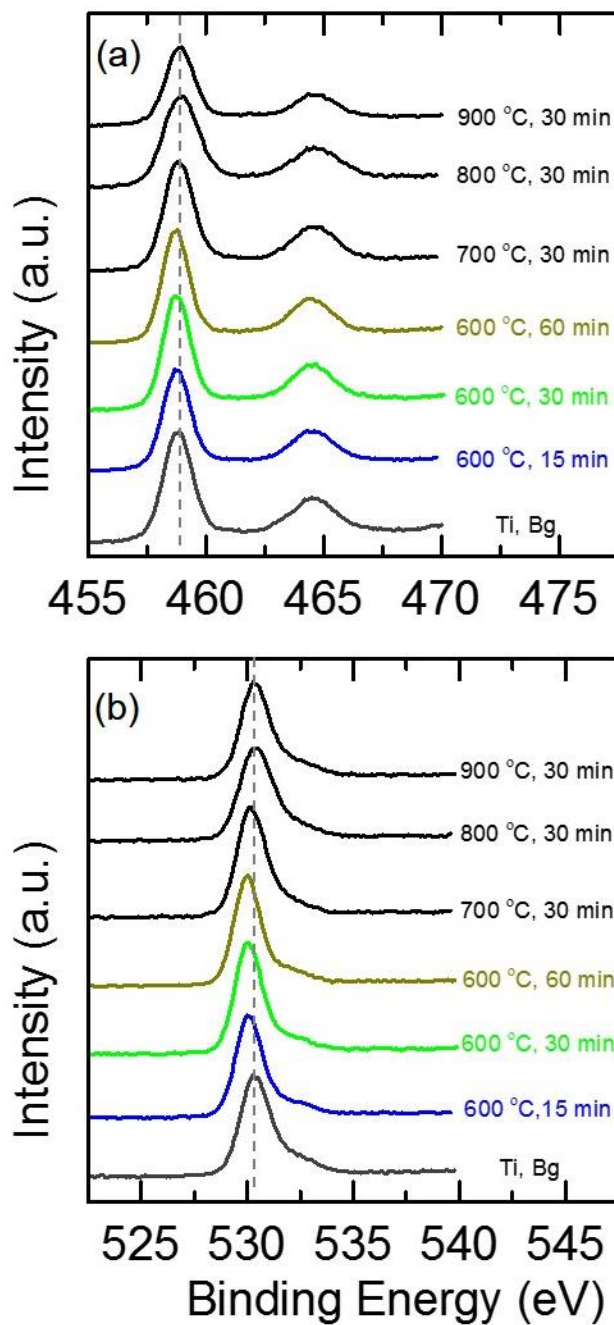


Figure 5.6. XPS spectra of (a) Ti 2P and (b) O 1S regions acquired from the different powder samples prepared.

The shift to lower binding energies in both Ti 2p and O 1s for some samples indicates that oxygen vacancies are generated under these conditions.^{138, 139} The presence of oxygen vacancies is consistent with the change in the color of powder samples following annealing at 600 °C under

0.7% O₂ (balance Ar). The change of the color is due to the partially reduced TiO₂.¹⁴⁰⁻¹⁴² It should be noted that these so-called self-doped structures remain stable at ambient conditions.

As evident in the Ti 2p and O 1s binding energies, all the samples annealed at 600 °C under 0.7% O₂ (balance Ar) exhibit the partially reduced structure as evident in the XPS spectra of the powders (**Figure 5.6**). However, only samples annealed for 25-30 min at this temperature show improved electrochemical activity toward oxygen reduction (**Figure 5.3**). The lower activity of the sample annealed at 600 °C for 15 min may be related to the growth of a discontinuous oxide film, and lower amount of oxide.

Interplay of phase distribution and oxidation state in oxygen reduction catalysis- Here we investigate the dependence of O₂ reduction reaction activity on phase distribution and oxidation state of oxidized Ti materials. As evident from XRD analysis (**Figure 5.2a** and **Figure 5.5**) annealing the powders under a low amount of oxygen results in the formation of fully crystalline oxide films. The crystalline nature of the oxide films is further confirmed from Raman spectra of the samples (**Figure 5.7**). The titanium metal powder shows no features in its Raman spectra, which is consistent with the presence of an amorphous native oxide layer. The powder samples annealed at different temperatures under low amount of oxygen show two distinct features. The bands located at *ca.* 447 and 612 cm⁻¹ are characteristic features of the rutile phase.^{142, 143} This result agrees with the higher weight fraction of rutile (acquired from XRD analysis) in all annealed samples (**Figure 5.2a** and **Figure 5.5**). Raman spectrum of an anatase micropowder (as-received sample) shows the characteristic bands of anatase phase located at 146, 197, 397, 516, 640 cm⁻¹.¹⁴⁴ Powders annealed at 600 °C for 60 min and at 700 °C for 30 min show broad features at *ca.* 437 and 613 cm⁻¹ which indicate the presence of a higher amount of anatase TiO₂, as also is evident from their XRD analyses. It should be noted that both these samples showed lower activity toward O₂ reduction even though their XPS analyses revealed partially reduced Ti sites. We propose that this observation could be related to their phase distribution and the presence of a higher amount of anatase phase in the oxide overlayer. Anatase surfaces are known to have a lower concentration of oxygen vacancies at their top-most layer surface, and are more difficult to reduce.^{145, 146} Oxygen vacancies are more stable at subsurface in anatase TiO₂. Surface concentration of oxygen vacancies is higher on rutile surfaces.¹⁴⁷⁻¹⁴⁹ The higher activity of the partially reduced TiO_x overlayers with higher rutile content may be explained by the higher concentration of oxygen

vacancies on these surfaces. As the amount of anatase increases, since defect sites are more stable at the subsurface, the partially reduced structures are not as active toward oxygen reduction.

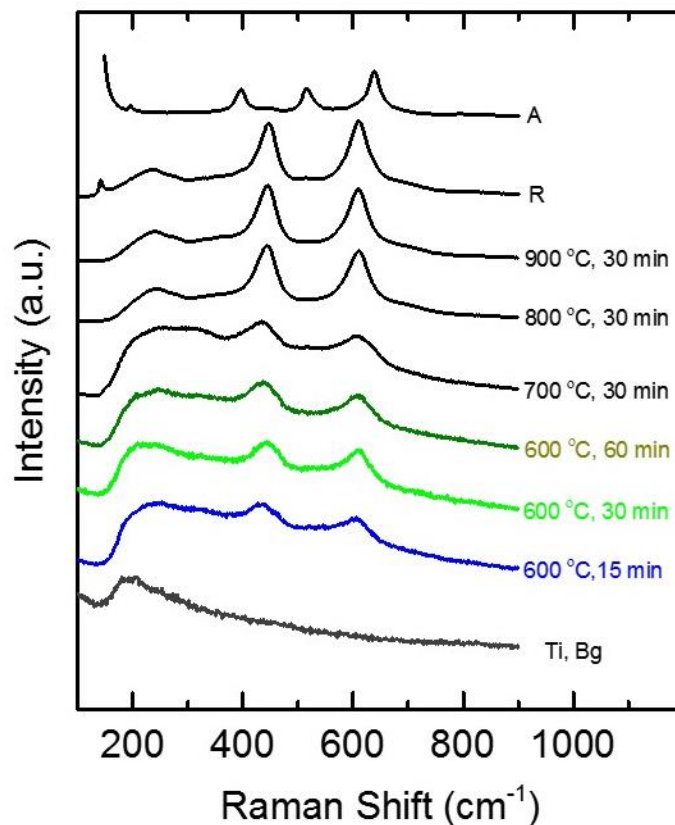


Figure 5.7. Raman spectra of the titanium metal powder (Ti, Bg), titanium powders following annealing at 600 °C under Ar for 30 min, and under 0,7% O₂ (balance Ar) for 15, 30 and 60 min, and at 700, 800 and 900 °C. For comparison, Raman spectra of as received TiO₂ rutile (R) and anatase (A) micropowders are also shown.

5.4. Conclusion

The activity of the titanium oxide is controlled by both the phase and the oxidation state of Ti in the oxide overlayers. The lowest amount of rutile phase titania in the XRD, XPS, and Raman analyses outperforms pure anatase, pure rutile and all other combinations of titanium oxide based cathodes. The effect of the Ti phase on ORR activity is attributed to differences in the availability of oxygen vacancies between rutile and anatase phases.

CHAPTER 6

Electrospray of nano-sized CsH_2PO_4 for SAFC electrodes

Section 6.1. *In situ* characterization of electrosprayed CsH_2PO_4 solid acid nanoparticles

Reproduced with permission from Áron Varga, Vanessa Evoen, Andrew J. Downard, Hyung Wan Do, Konstantinos P. Giapis, Richard C. Flagan², Sossina M. Haile.

6.1.1. Abstract

Nanometer-sized particles of the solid acid fuel cell electrolyte material CsH_2PO_4 have been prepared by electrospray synthesis. Using a differential mobility analyzer to provide real-time particle-size information, the role of electrospray parameters, such as precursor solution composition, surface tension, conductivity, sheath gas temperature and flow rate, and solution flow rate, were evaluated. The results are compared with particle sizes calculated using well-established scaling laws.

6.1.2. Introduction

Fuel cells have long held the promise of efficient, clean, and silent conversion of chemical to electrical energy. As such, they are positioned to play an important role in a sustainable energy future. Among the various types of fuel cells, solid acid fuel cells (SAFCs) are particularly attractive due to their intermediate temperature of operation ($\sim 240^\circ\text{C}$) and their incorporation of a truly solid electrolyte. These features engender fuel flexibility, enhance impurity tolerance, eliminate fuel cross-over and obviate challenges with catalyst flooding.¹⁵⁰ These advantages notwithstanding, state-of-the-art SAFCs deliver lower power densities than their solid oxide fuel cell (SOFC) and polymer electrolyte membrane (PEM) fuel cell counterparts, largely due to performance limitations at the cathode.¹⁴ This component is generally constructed as a composite of the electrolyte material, serving as the proton transport medium; nanoparticulate platinum supported on carbon, serving as the electrocatalyst; and graphitic carbon serving to create

additional electron transport pathways from the sites of electrocatalysis to the carbon paper current collector. To date, a peak power density of 415 mW cm^{-2} has been achieved with a platinum loading of 7.7 mg cm^{-2} .²⁶ Significantly, it has been shown that the electrode overpotentials scale with the size of the electrolyte particles in the electrode structure, a phenomenon that has been attributed to the increase in the density of electrocatalytically active triple phase boundaries between the catalyst, the electrolyte and a gas phase with decreasing electrolyte particle size.¹⁵¹ Such an observation motivates an effort to substantially decrease the particle size while maintaining an interconnected, porous structure. To this end, we recently applied the method of electrospray deposition for the fabrication of SAFC electrodes and attained a significant reduction in electrolyte particle size to about 100 nm. The achievement enabled a dramatic reduction in Pt loading without sacrifice in electrode activity.⁷

Despite this advance, Pt loadings in SAFCs remain too high for commercial viability in many applications. Thus, even greater reductions in electrode feature sizes, predicted to provide still greater activity, are desirable, motivating further refinements to the electrospray approach. A major challenge to the utilization and optimization of this method as currently implemented, however, is the long development time involved in the deposit-image-modify cycle. This long cycle time has hindered efforts to lower particle size beyond the $\sim 100 \text{ nm}$ size obtained in the first study. In addition, it is not known whether dry particles, semi-dry particles, or (supersaturated) solution droplets are deposited onto the substrate during the electrospraying process. For many systems, the morphology of the film can be used to deduce the nature of the species that has impacted the substrate. In the case of hygroscopic and low melting point materials as used here, however, uncertainty emerges because of possible differences between as-deposited and imaged structures. Thus, the feature sizes recorded post-deposition may not be reflective of the actual particle size achieved during synthesis.

In the present work, we address the challenges associated with post-deposition characterization through the implementation of *in situ* characterization capabilities. Specifically, we integrate a differential mobility particle sizer (DMPS) into the electrospray apparatus so as to gain immediate feedback connecting electrospray parameters and aerosol size. This integrated system enables rapid and systematic exploration of the parameter space for controlling the electrospray outcome. The experimentally measured sizes are compared with the scaling law expectations predicted from the analysis of Ganan-Calvo.⁷³

6.1.3. Electrospray background

Electrospray atomization is a process in which a liquid is supplied to a capillary that is held at a high voltage relative to a substrate or emitter placed some distance away from the capillary. The process can be utilized for the deposition of materials included as either dissolved solutes or suspended particles in the precursor liquid. It is of value to consider the droplet creation and evolution in order to understand the impact of process parameters on the final outcome.

Droplet formation- For low viscosity liquids, a stable cone-jet mode of droplet emission can be achieved in which the liquid adopts a geometry with conical cusp (the Taylor cone) and a thin jet of diameter d_j emerges from the cone tip. Varicose break-up of this emerging solution describes the situation in which a highly monodisperse distribution of droplets is emitted from an axially symmetric jet, in contrast, for example, to a whipping break-up in which the jet whips from side to side as droplets are emitted and provides the greatest opportunity for control over the spray characteristics.^{74, 152} There have been extensive studies in the literature, both theoretical and experimental, to understand the relationship between electrospray parameters and the size of the emitted droplets under the varicose break-up regime.^{73, 74, 153-156} A study by Ganan-Calvo presents an integrated analysis that unifies previous observations of different scaling laws under different experimental regimes.⁷³ Under conditions relevant to the present work ((i) inertial forces dominate the jet development over surface tension and viscous forces, and (ii) electrostatic suction dominates over polarization forces in cone-jet necking), the jet diameter is given as⁷³

$$d_j = \left(\frac{\rho \varepsilon_0}{\gamma K} \right)^{1/6} Q^{1/2}, \quad (6.1)$$

where ρ is the liquid density, K is the liquid electrical conductivity, Q is the liquid flow rate, γ is the gas-liquid surface tension, ε_0 is the permittivity of vacuum. Significantly, the viscosity of the liquid and its dielectric constant do not appear in Eq. (6.1) and hence do not influence the system behavior. The minimal influence of viscosity in this parametric regime, moreover/ results in emitted droplets with diameter d_d , comparable to those of the jet, and thus d_j can be evaluated as a

proxy for d_d .⁷⁴ For the range of solution parameters explored, the initial droplet size is on the order of several micrometers.

Droplet velocity and time- At the point of emission from the Taylor cone tip, the Coulombic force (qE) is balanced by the drag force on the droplet and gravity, hence establishing the initial droplet velocity (discussed in Chapter 2).⁷⁶ After emission, the electric field gradient (normally also the direction of gas flow) drives the droplets toward the substrate. In addition to the electrostatic force, during travel the droplets experience aerodynamic drag and rapidly approach a quasi-steady-state migration velocity. The characteristic time required to establish this steady-state is the aerodynamic relaxation time, given as⁷⁵

$$\tau = \frac{\rho d_d^2 C_c}{18\eta}, \quad (6.2)$$

where η is the gas viscosity. The Cunningham correction factor C_c accounts for the “slip” between the particle and the surrounding gas that develops in the transition from continuum to non-continuum flow. For micron-sized droplets in the continuum range, where $d_d \gg$ mean free path of the sheath gas molecules (60-75 nm), C_c is ~ 1 , but it can be as large as ~ 25 when d_d falls to ~ 10 nm, the diameter of the smallest particles observed in this work. The range of parameters encountered in this study implies, via Eq. (6.2), a range for the relaxation times from several milliseconds for a micron sized droplet to tens of milliseconds for a 10 nm dry CsH_2PO_4 . On the other hand, the total flight time for gas molecules to travel 2.5 cm (the tip-to-substrate distance employed in our earlier work)⁷ at a gas space velocity of $\sim 1.8 \text{ cm s}^{-1}$ (a typical value for this and the previous work) is $> 1 \text{ s}$, much longer than the relaxation time. Thus the total flight time, a key factor in determining whether residual liquid remains when the particle impacts the substrate, can be approximated as the flight time implied by the gas space velocity. In the present configuration the travel distance from the point of emission to the particle sizer is substantially longer (39 cm), justifying the use of the gas space velocity to estimate the travel time. However, as solvent evaporates, droplet size decreases causing non-continuum effects, which could possibly affect the value of the slip factor and consequently the relaxation time. Non-continuum effects are addressed in the Supplementary Material.

Solvent evaporation rate- During droplet travel to the counter-electrode, the droplet decreases in radius as solvent evaporates. Concomitant with the reduction in droplet volume is an increase in the surface charge density. Ultimately, the Columbic repulsion due to charge concentration overcomes surface tension forces (Rayleigh limit) causing the droplet to undergo a fission event. In accord with the charge residue model (CRM), multiple small secondary droplets, with sizes less than 5% of that of the parent, are emitted, whereas the loss of charge is much greater, on the order of 15 - 40%.^{157, 158 152 159} Thus, the fission has little influence on the parent droplet size, but increases the particle size distribution through the generation of progeny in a distribution which itself is less monodisperse than the original distribution.¹⁶⁰

Of particular importance to the synthesis of solid particles by the electrospray process is the question of whether solvent evaporation is complete by the time of impact with the substrate. Evaporation of multicomponent droplets has been studied experimentally and described with quasi-steady state evaporation models.^{161, 162}

An approximation for the evaporation rate of a droplet can be obtained using the simple expression derived in Seinfeld and Pandis. A conservative estimate of drying time at ambient room temperature and 99% relative humidity of a single, non-ideal CsH_2PO_4 solution droplet, was estimated as 90 ms. In **Figure 6.1**, the droplets travel 39 cm before reaching the Differential Mobility Analyzer (DMA). A gas space velocity of 1.8 cm/s corresponds to 22 seconds of particle flight time. In addition, using pure water as the solvent, the calculations for evaporation rate give the upper bound for the time required for complete evaporation of the electrosprayed droplet, since the presence of a significantly more volatile methanol component is expected to result in a faster evaporation rate. This suggests that in the parameter space explored in this experiment, the particles sizes reported are of dry CsH_2PO_4 nanoparticles.

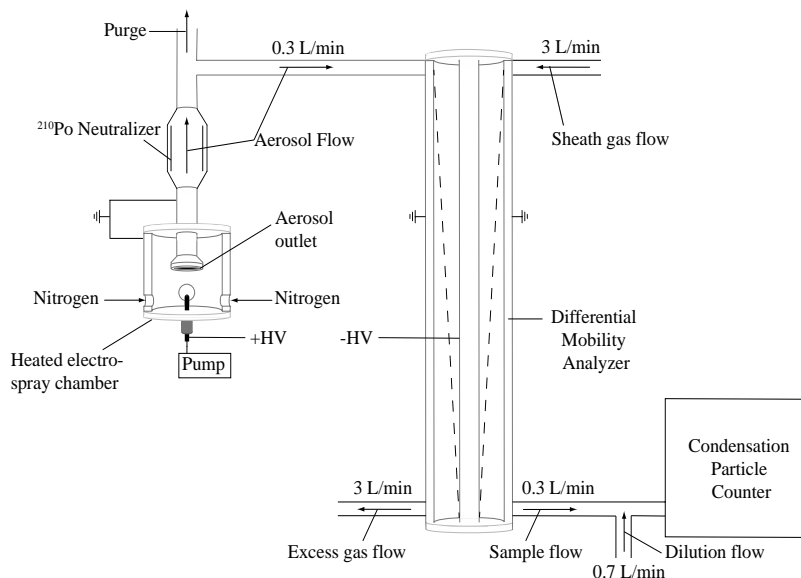


Figure 6.1. Schematic of the electro spray and differential mobility analyzer

It becomes evident from this overview that the particle size ultimately resulting from electro spray synthesis depends on both solution properties and process parameters.^{157 152, 154} Furthermore, while the Ganan-Calvo expression of Eq. (6.1), can provide guidance on these dependencies, the expression is unlikely to provide a quantitative prediction of the electro spray process outcome, which includes not only the step of initial droplet formation, but also the evolution of the charged droplet into a dry neutral particle deposited onto a conductive substrate. Integration of an *in situ* aerosol sizing tool to evaluate particle size prior to deposition, as implemented here, advances our ability to quantitatively understand the role of these various parameters by deconvoluting post-deposition microstructural evolution from the outcome of the droplet generation and particle creation steps.

6.1.4. Experimental procedures

Materials preparation and solution characterization - The electrolyte CsH_2PO_4 was synthesized from aqueous solution as described elsewhere.¹⁶³ In brief, stoichiometric quantities of CsCO_3 (Alfa Aesar, 99% metal basis, Stk# 12 887) and H_2PO_3 (Mallinckrodt Chemicals, 85%, Stk#2788-14) were dissolved in deionized water and the precipitation of the compound was induced by introduction of methanol (EMDMillipore, HPLC grade, Stk#67-56-1). Phase formation was confirmed by X-ray powder diffraction (X'Pert Pro, CuK α). Polyvinylpyrrolidone (PVP,

molecular weight 8000, purity), found in our previous work to be effective for morphological stabilization of the resulting structure¹⁵, was acquired from a commercial source (Alfa Aesar, Stk# 41626) and used without further purification. [Aqueous solutions of these compounds served as the electrospray liquid.

As indicated from the discussion above, several properties of the electrospray solution and process parameters influence the synthesis outcomes. The three properties of the greatest relevance, solubility of CsH_2PO_4 , electrical conductivity, and surface tension, were measured here. Solubility was determined using straightforward light scattering methods. Granulated CsH_2PO_4 was added incrementally to the solution of interest at room temperature under continuous stirring while observing the light scattering that resulted from shining a conventional laser light on the liquid. If scattering was observed beyond one hour of stirring, the solution was considered to be beyond the saturation limit. Electrical conductivity was measured using a digital conductivity meter (Omega CDH-7X, applied DC voltage: 10 mV) equipped with fixed stainless steel electrodes which were cleaned prior to each measurement. The surface tension of selected solutions was measured via the DuNuoy ring method, using a Cenco Interfacial Tensiometer (Precision direct reading model, Ser. No. 909) and a CSC Scientific Inc. platinum ring (Cat. No. 70542, mean circumference 5.992 cm).

Experimental apparatus - The electrospray apparatus constructed for the fabrication of nanoparticulate CsH_2PO_4 has been described previously.¹⁶⁴ Briefly, the system consists of a heated chamber into which the CsH_2PO_4 solution is supplied by mechanical pumping through an electrically biased stainless steel capillary positioned to electrospray upwards, as shown in Figure 6.1. For fabrication of fuel cell electrodes, a carbon paper substrate is placed 3 cm from the capillary tip and particles are directly deposited on this substrate. An example of the type of structure resulting from this deposition is shown in Figure 6.2, a scanning electron microscopy image (ZEISS 1550VP Field Emission SEM); the morphology is similar to what we have previously reported. To facilitate *in situ* particle sizing, the electrospray apparatus is modified by removing the grounded substrate holder for electrode deposition and replacing it with a grounded collection tube (ID 4.8 mm, OD 20 mm) exiting from the top of the chamber. A small flow of aerosol is extracted from the electrospray chamber through this orifice and directed to a differential

mobility particle size analyzer (DMPS). The benefits and challenges of combining electrospray atomization and particle sizing have been addressed in a handful of previous studies [Knutson & Whitby (1975)¹⁶⁵]; the system constructed here is described in some depth below.

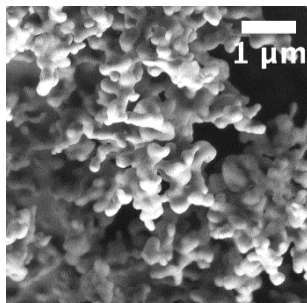


Figure 6.2. Scanning electron micrograph of deposited CsH_2PO_4 structure for feature size measurement.

The DMPS is comprised of three primary components: a ^{210}Po neutralizer, a cylindrical differential mobility analyzer (DMA, TSI Model 3081), and a butanol condensation particle counter (CPC, TSI Model 3010). The neutralizer is positioned upstream of the DMA and immediately after the sampling orifice. By exposing the particles to an electrically neutral cloud of positive and negative gas ions the neutralizer serves to reduce the charge per aerosol particle, as required for subsequent sizing. A ^{210}Po neutralizer was selected as it has the most efficient neutralizing properties for the initial charge distribution and flow rates resulting from the electrospray system utilized. Within the ^{210}Po neutralizer environment the aerosol attains a steady-state charge distribution in which a small but known fraction of the particles carries a single elementary unit of charge, i.e. $q = \pm e$. The positioning of the neutralizer is selected to minimize losses due to electrostatic repulsion and deposition on walls, which could, in turn, influence the measured particle size distribution.¹⁶⁶ After passing through the neutralizer (beyond which aerosol droplet size can decrease only via evaporation of any residual liquid), the polydisperse aerosol is introduced into the cylindrical DMA (flow rate of 0.3 l min^{-1}), the core component of the DMPS. A DMA-sheath gas (flow rate of 3 l min^{-1}) is also introduced at the inlet of the DMA, Figure 6.1. Charged particles entering the DMA are classified according to the velocities with which they migrate across the particle-free sheath-gas flow that is confined between coaxial cylindrical electrodes held at different voltages. Particles of different diameter are selected by adjusting the

electric field strength that is applied transverse to the flow, where the voltage range is bounded by the electrostatic breakdown at the high end and the onset of diffusional degradation at the low end. Because the drag force is a monotonic function of diameter, singly charged particles are differentially displaced by the electric field. Those particles whose transit time across the channel equals the residence time in the classification region are eluted in the classified flow. Their mean mobility, Z_p , is simply their velocity (obtained from the residence time and gas space velocity) divided by the electric field. The remainder particles are rejected in the excess flow or deposited on the walls of the classifier. The classified aerosol exiting the DMA at each voltage step is then directed to the condensation particle counter (CPC). Conducting polymer tubes were used as interconnections in order to avoid parasitic fields arising from charge buildup, which may cause severe aerosol losses and, hence, complicate the measurement of the particle size distribution. In the CPC the particles are grown to a sufficiently large size that they can be counted optically. The mobility distribution so determined was translated into a size distribution recognizing that the electrophoretic mobility, Z_p , of a spherical particle of diameter d_p and charge q is given by¹⁶⁷

$$Z_p = \frac{qC_c \left(\frac{2\lambda}{d_p} \right)}{3\pi\mu d_p}, \quad (6.3)$$

where C_c is the slip correction factor and λ the mean-free-path of the gas molecules. For small particles in the free molecular regime, $Z_p \propto \mu d_p^{-2}$. The charge on the particles is taken from the known distribution resulting from the ^{210}Po neutralizer. To establish whether the neutralization was sufficient, the residual charge carried by the aerosol particles was measured via a grounded probe and a picoammeter (Keithley 480) placed downstream of the ^{210}Po neutralizer.

The data were analyzed using the following standard methodology.¹⁶⁸ The DMA voltage measurement range was 84 V to 500 V, with step sizes linearly varying from 8.2 V to 17 V. At the operating flow rates, this corresponds to a particle size range from 10 to 100 nm. Periodically, a wider particle size range was scanned with voltages ranging from 84 V to 5.2 kV and step size varying linearly from 8.2 V to 40 V. The measurement time was 10 seconds at each step, with the concentration recorded every second, i.e. 10 measurements per step. The transients between the size steps were deleted and the concentration data for each size step averaged and adjusted for aerosol particle-size-dependent charging statistics described by Hoppel & Frick (1986)¹⁶⁹ and

manufacturer specified counting efficiency of the CPC. The raw data (counts vs. applied voltage) were inverted to obtain the size distribution for each electrospray condition using the methodology proposed by Stolzenburg & McMurry (2008)¹⁶⁸. The resulting distribution was subsequently fitted to a log-normal function - the standard distribution function for dilute nanometer sized aerosol particles - from which the geometric mean diameter, d_g , and standard deviation of the distribution were obtained, **Figure 6.3**. The standard deviations in the size distributions are shown as error bars in figures in which the mean sizes are reported. The system was calibrated using stock polymer spheres (21, 59, 82, 92, 105 nm diameter, Nanosphere Size Standards, Duke Scientific Corp.) dispersed in de-ionized water and aerosolized via a standard particle aerosolizer¹⁷⁰.

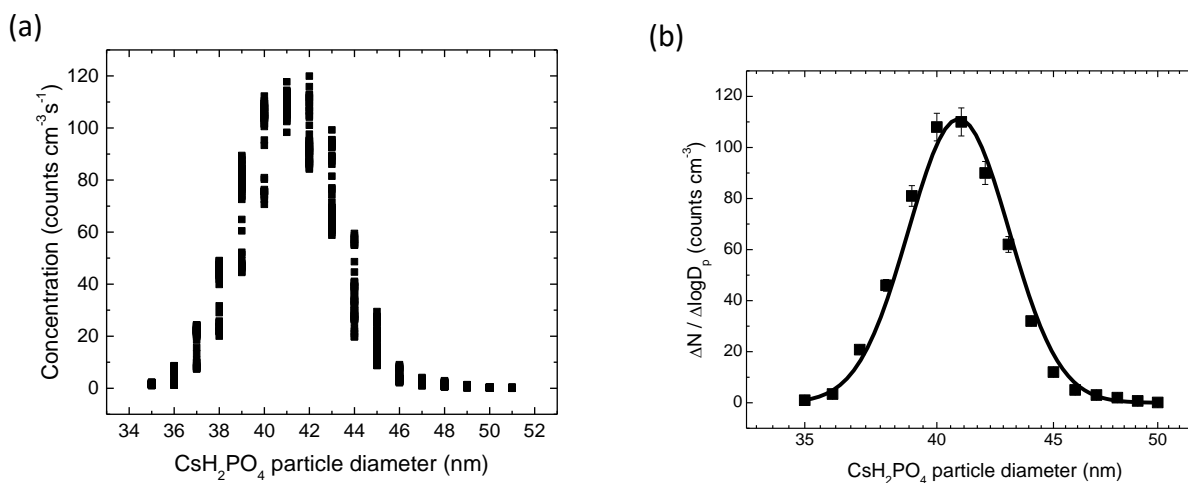


Figure 6.3. Example of particle size measurements and data analysis. (a) Counts ($\text{cm}^{-3} \text{s}^{-1}$) as a function of particle diameter, multiple measurements, as detected at discrete particle sizes; and (b) averaged values and fit to a log-normal distribution.

Parameter variations - Key parameters were varied to determine their impact on mean particle size and size distribution. Given the breadth of the parameter space, the problem was parsed by retaining a set of default parameters and changing only one variable at a time, **Table 6.1**. This default parameter set had been determined in a previous study to be adequate for deposition of porous solid acid fuel cell electrode structures.¹⁶⁴ Both solution properties (CsH_2PO_4 concentration, methanol to water ratio, and PVP concentration) and process parameters (voltage, temperature, nitrogen flow rate, and precursor solution flow rate) were varied in this study. The full particle size distribution was measured at least two times for a given set of parameters to

evaluate reproducibility and enable determination of experimental uncertainty. The range of parameter space accessible (in particular the voltage and precursor liquid flow rate), was limited to those conditions that yielded a stable Taylor cone-jet spraying mode. The stability of the spray was monitored by visual observation through the viewing port of the apparatus. Erratic fluctuations in the Taylor cone were interpreted as indications that other spraying modes, such as the multi-jet, pulsating, or dripping mode, had emerged,¹⁷¹ and such conditions were avoided. Instabilities in the Taylor cone were also reflected in increases in the breadth of the particle size distribution.¹⁷²

6.1.5. Results

Solution properties - The solubility limit for CsH_2PO_4 in water-methanol mixtures determined here is presented in **Figure 6.4**. The solubility decreases exponentially with increasing methanol content, from 137.9 g/L in 100% H_2O to 0.5 g/L in 90 wt% methanol, and undetectable solubility in 100% methanol. These values set the limit of the maximum CsH_2PO_4 concentration that can be employed in the electrospray solutions. Use of solutions with solute concentrations no higher than ~50 % of the solubility limit ensured that the electrospray nozzle would not clog during operation over long time periods (>1 hour). At the default methanol concentration of 53 wt% this process-imposed limit corresponds to a CsH_2PO_4 concentration of 5 g/L, in turn, corresponding to a volume per cent of solids of 0.16 %. Thus, the radius of the equivalent solid material contained in the droplet is smaller than that of the droplet by a factor of 8.5 for the default solution concentration.

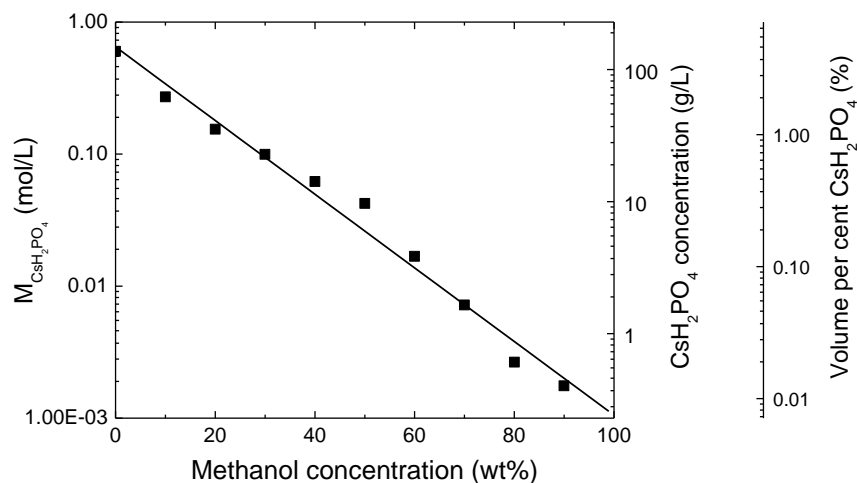


Figure 6.4. Solubility limit of CsH_2PO_4 in water-methanol mixtures

The impact of CsH_2PO_4 and methanol concentration on solution properties (conductivity and surface tension) are presented in **Figure 6.5**. Varying the CsH_2PO_4 concentration has a dramatic impact on the solution conductivity, but limited impact on the surface tension of the solution. For example, for a methanol concentration of 50 wt% (close to the default) the conductivity rises from negligible (< 0.1 mS/cm) in the absence of CDP to ~ 2 mS/cm at a CDP concentration of 10 g/L, whereas the surface tension is almost unchanged, rising from 31.6 to 33.8 over approximately the same CDP concentration range. Both results are in line with expectations for introducing ions into an aqueous solution. In contrast, the methanol concentration influences dramatically the surface tension but has a smaller effect on conductivity, the latter particularly at low CDP concentrations. The measured values for the surface tension of pure distilled water and pure methanol, with values of 73.4 mN/m and 22.5 mN/m, respectively, are in excellent agreement with the literature, as are the measured values for the mixtures thereof. Introduction of CDP has little effect on the dependence of surface tension on the solvent composition. In the case of conductivity, this property decreases linearly with increasing methanol concentration, for example, at a CDP concentration of 3 g/L the value drops from 1 to 0.42 mS/cm as the methanol content is increased from 16 to 60 wt%, and the sensitivity to methanol concentration increases with increasing electrolyte concentration. The additive PVP was found to have negligible effect on both the solution conductivity and surface tension, specifically over the concentration range from 0 to 10 g/L, for solutions with 50 wt% methanol and 3 g/L CDP (not shown).

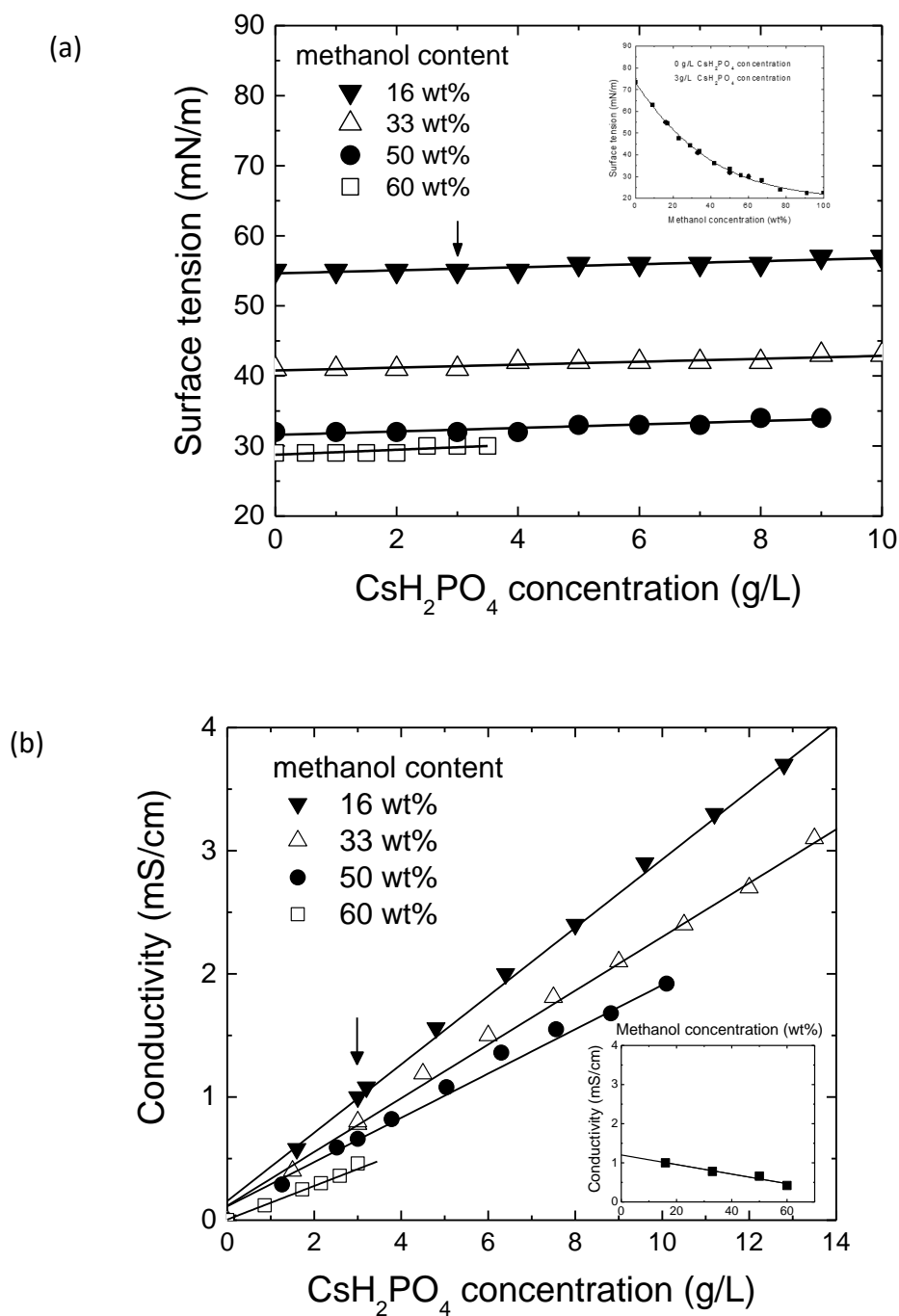


Figure 6.5. (a) Surface tension of precursor solutions with 16 wt %, 33 wt %, 50 wt%, and 60 wt% methanol in water vs. CsH_2PO_4 concentration. Inset is surface tension of precursor solutions vs. methanol concentration (3 g/L CsH_2PO_4 and no CsH_2PO_4 , respectively). (b) Conductivity of precursor solutions with 16 wt %, 33 wt %, 50 wt%, and 60 wt% methanol in water vs. CsH_2PO_4 concentration. Inset is conductivity versus methanol concentration.

These results suggest that, although the methanol content and CDP concentration have measurable impact on the important properties of conductivity and surface tension, because of the $-1/6$ power law dependence of d_j on γ and K , the impact on initial droplet size may, in fact, be slight.

Particle size trends - An initial exploration of the system behavior was carried out by varying the applied capillary voltage, the results of which are summarized in **Figure 6.6**. The current measured with and without the ^{210}Po neutralizer show, in the former case, a current that is nearly zero, and in the latter, a current that increases linearly with voltage, demonstrating the high efficiency of the neutralizer. As measured in the absence of the neutralizer, an increase in voltage resulted in an increase in current. However, counter to the behavior expected according to Eq. 6.3, this increased current did not necessitate an increase in the liquid flow rate to maintain the Taylor cone. This observation reveals the limitations of analyses of the electrospray process that ignore complexities such as capillary shape and surface tension between the liquid and capillary material. Nevertheless, it is apparent that, at the lower voltages within the range of this particular exploration, the spray becomes increasingly erratic, as reflected in the increase in the particle size distribution (reflected in the error bars). For each measurement of particle size distribution in the subsequent results, voltage was optimized within the range shown in **Figure 6.6a** so as to maximize Taylor cone stability.

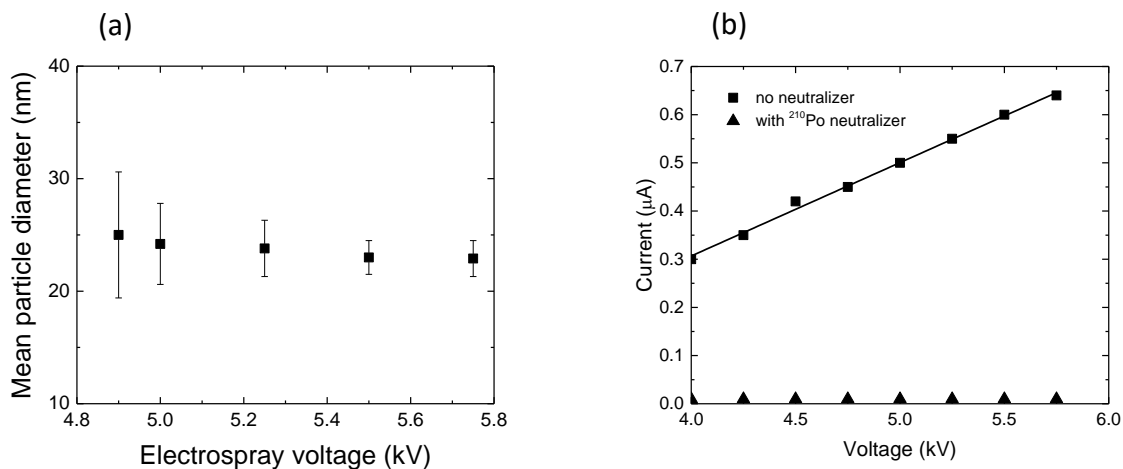


Figure 6.6. Influence of electro spray voltage on (a) mean particle size in the CDP aerosol, and (b) detected current, with and without the Po neutralizer. Solution and process parameters as given in **Table 6.1** (default values), with CDP concentration of 10 g/L.

Turning to the influence of parameters expressed in Eq. (6.1), the expected variation in initial droplet size and corresponding solid volume is shown in **Figure 6.7** as a function of methanol concentration, CDP concentration and liquid flow rate. Overall, an initial droplet size in the range of 1 to 3 μm is expected for the range of conditions explored, and the predicted particle sizes range from 100 to 350 nm. The latter values are substantially larger than the ~ 25 nm determined experimentally, for example in **Figure 6.6a**, a point to which we return below. Increasing the methanol concentration is predicted to cause the size of the initial droplet and accordingly that of the dry particle to increase slightly. This can be understood to result from the slight decrease in surface tension and in conductivity with increasing methanol concentration (**Figure 6.5**), in combination with the weak power law dependence of d_j on these two parameters in Eq. (6.1). Varying the CDP concentration has a noticeably more significant impact on initial droplet size, causing it to decrease by a factor of almost two over the range explored. This is largely a result of the substantial increase in solution conductivity with increasing solid acid concentration. However, because each droplet now carries a greater mass of CsH_2PO_4 , one expects that the ultimate particle size will increase with increasing CDP concentration. Liquid flow rate is predicted to be the most effective parameter for manipulated droplet and ultimately particle size. As given in Eq. (6.1), the power law exponent in this case is $\frac{1}{2}$, much larger than the $\frac{1}{6}$ exponent for the material's parameters.

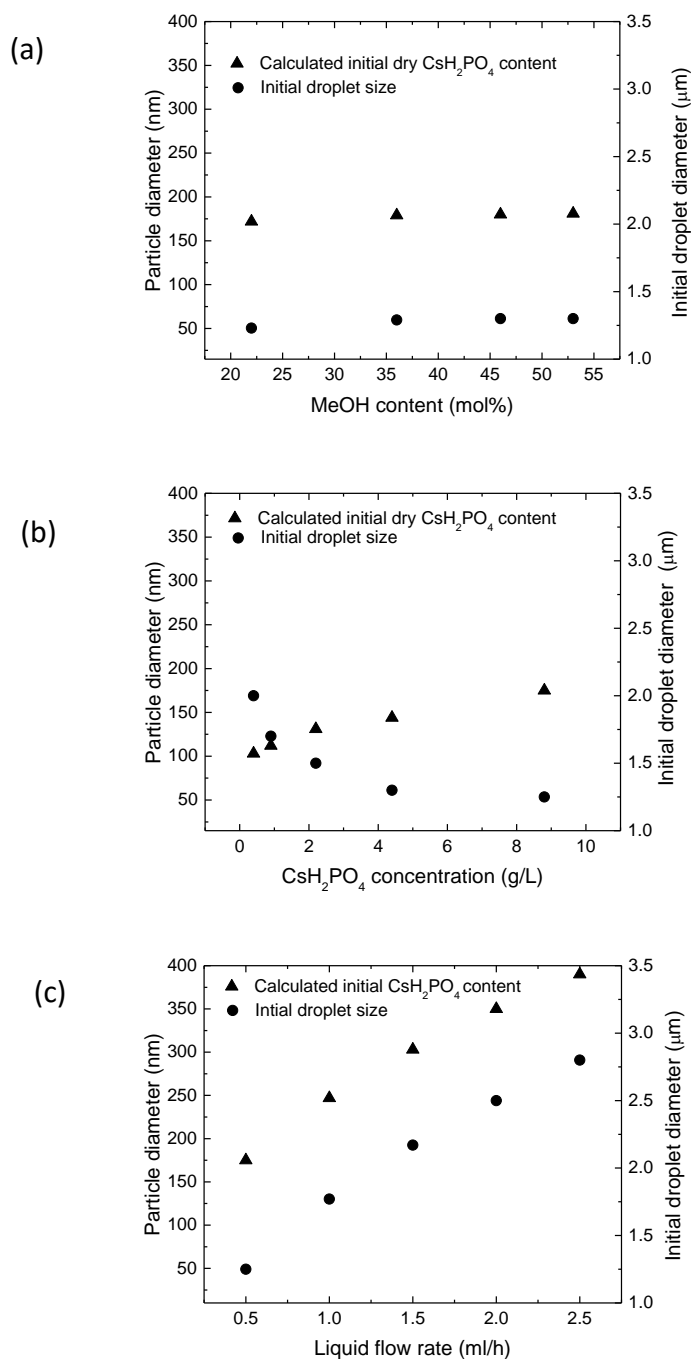


Figure 6.7. Expected variation in initial droplet size and corresponding expected variation in solid volume according to Eq. (6.1) as a result of varying solution and process parameters: (a) varied methanol concentration, (b) varied CsH_2PO_4 concentration, and (c) varied liquid flow rate. Where not varied, methanol content is 50 mol% (46 wt%), CDP is 10 g/L, and liquid flow is 0.5 mL/h.

Figure 6.8a summarizes the impact of methanol concentration on the mean particle size measured. In agreement with the theoretical prediction, methanol concentration has minimal impact on the final aerosol particle size. Here the CsH_2PO_4 concentration is fixed at 5 g/L and no other components are added to the solution. With increasing methanol concentration in the precursor solution, that is decreasing precursor solution surface tension the mean particle diameter decreases only slightly. At 22 wt% and 53 wt% methanol concentration, a less stable spraying mode (pulsating mode) was observed, corresponding to low particle concentrations and a broad particle size distribution. At 25 and 36 wt% methanol, we observe the narrowest particle size distribution and the highest measured concentration, respectively. Rather remarkably, increasing the CDP concentration causes a substantial decrease in particle size, **Figure 6.8b**. As noted, while a decrease in initial droplet size is to be expected, the size of the final dry particles is expected to increase. Clearly, this expectation is not met. Finally, the precursor solution flow rate can be varied within a range, controlled by the stability of the Taylor cone spraying mode.¹⁷² Increasing the liquid flow rate has the expected impact of increasing the particle size, **Figure 6.8c**. We observed both a reduction in CsH_2PO_4 particle size and a narrower particle size distribution with a decrease in precursor solution flow rate, **Figure 6.8c**. At flow rates higher than 2.5 ml/h, the dripping mode was observed. At flow rates lower than 0.5 ml/h, the Taylor cone disappeared periodically and clogging of the capillary tip occurred frequently. The particle size distribution is narrowest at 0.5 ml/h.

Figure 6.6a shows minimal variation in the mean particle size as the electrospray voltage is varied over the narrow range of 4.9 to 5.75 kV, limited by the stability of the Taylor cone spraying mode. More significant is the narrowing of the particle size distribution as voltage is increased. **Figure 6.6a**, shows a significantly broader particle size distribution at the lower bound of the applied voltage. At voltages higher than 5.75 kV, corona discharge and/or occasional dielectric breakdown is observed and is to be avoided.

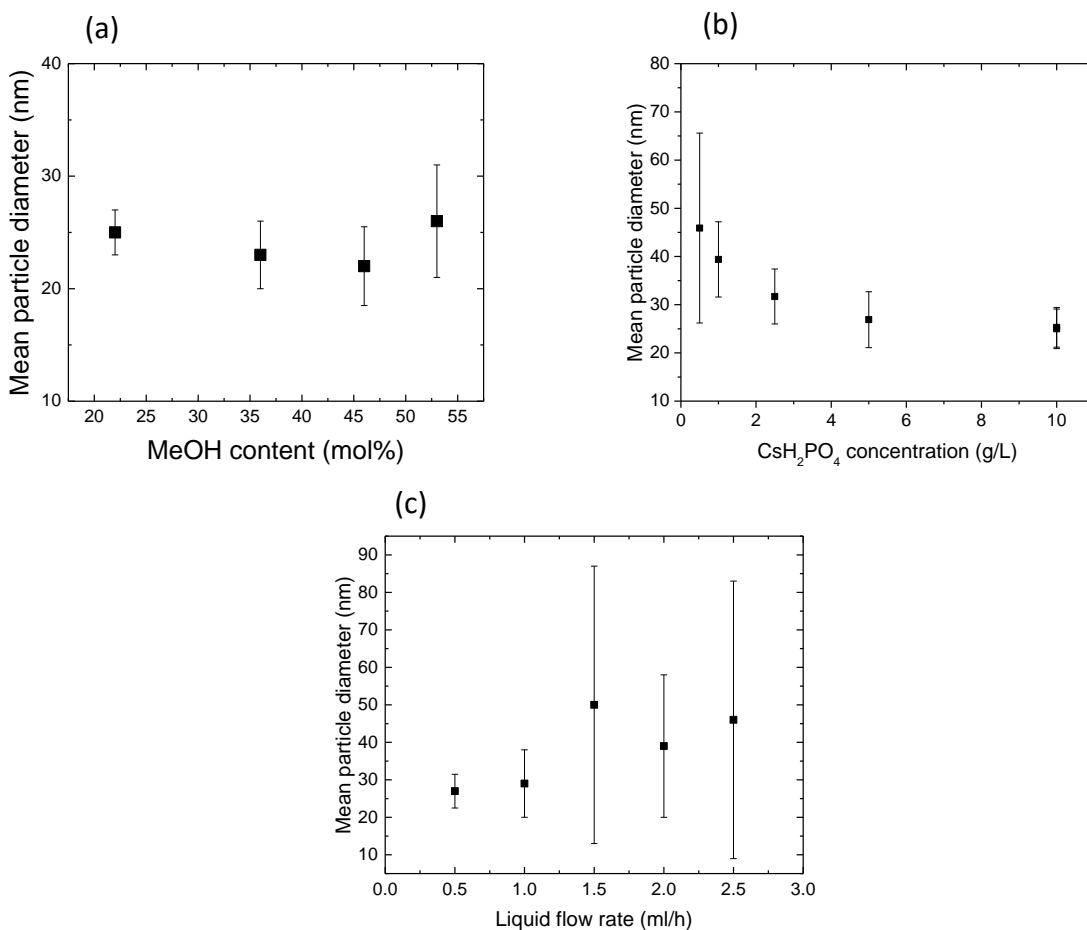


Figure 6.8. Mean particle size of aerosol vs. (a) MeOH concentration, (b) CsH₂PO₄ concentration, and (c) liquid flow rate through electrospray capillary with standard deviation of the distributions indicated.

When the surfactant PVP is added to the electrospray precursor solution, the mean particle diameter increases monotonically, see **Figure 6.9a**. We observe the narrowest particle size distribution with the highest peak concentration at 10 g/L, indicating a stable spraying mode. The particle size exhibits a broad minimum with electrospray temperature (heated gas lines, chamber, and substrate). Smaller electrolyte particles are seen at 60 and 100°C, with a significantly larger particle size and higher concentration at 120°C as shown in **Figure 6.9b**. The particle size distributions were significantly narrower at the intermediate temperature range. The final parameter giving a reduction of the electrolyte particle size is the nitrogen sheath gas flow rate. The increased nitrogen sheath gas flow rate results in a significant initial decrease in particle size and a narrower particle size distribution **Figure 6.9c**.

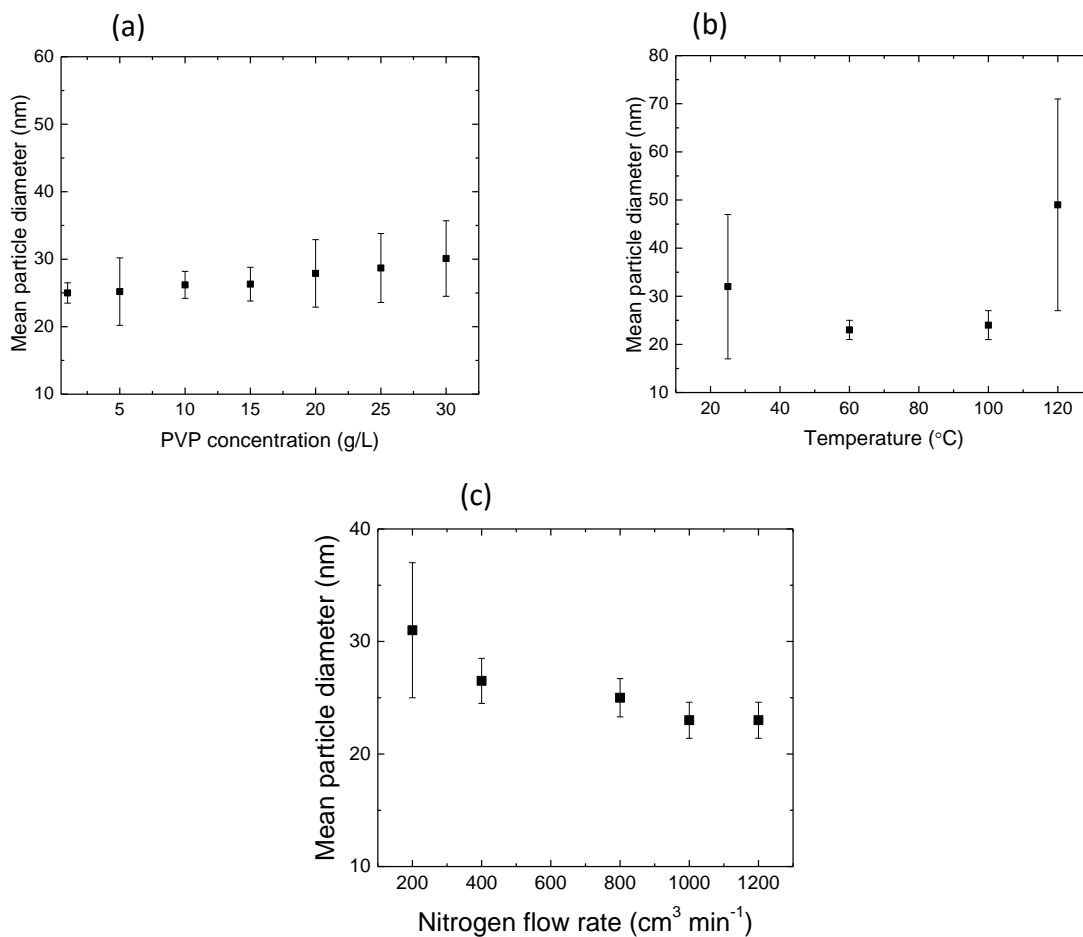


Figure 6.9. Mean particle size of aerosol vs. (a) PVP concentration, (b) electro spray chamber temperature, and (c) sheath nitrogen flow rate through electro spray capillary with standard deviation of the distributions indicated.

6.1.6. Discussion

Generally, the trends can be explained by applying current models for the initial droplet formation from the Taylor cone.^{153, 154, 173}, the evaporation-fission sequence^{75, 157, 158, 23, 24}, and solute precipitation^{174, 175, 176}. The dynamic equilibrium between surface tension and repulsive electrostatic forces at the tip of the electro spray capillary determine how the droplets are ejected at the tip of the Taylor cone. Coulombic repulsion ultimately has to exceed the surface tension of

the liquid before droplets form when the cone jet breaks up. The formation of aerosol droplets is more facile and occurs more frequently for high conductivity and low surface tension solutions, resulting in smaller initial droplet size.

Similarly, highly charged liquid aerosol droplets experience both repulsive Coulombic forces and stabilizing forces due to surface tension. As the solvent evaporates without carrying a significant amount of charge away from the primary droplet, the charge concentration increases up to the Rayleigh limit, when Coulomb fission or oscillatory instabilities occur according to the charge residue model. The Rayleigh limit is reached faster when the surface tension is lower and the droplet charge higher, leading to more frequent droplet fission events. Solvent evaporation rate is higher from smaller droplets, also favoring more frequent fission events. Fission events can occur multiple times during droplet flight, leading to significantly smaller aerosol droplets. When the aerosol droplets reach the neutralizer, the charge per droplet is reduced so that fission events become impossible. Beyond the neutralizer droplet size reduction can only occur via solvent evaporation. At this stage, the final electrolyte particle size is dependent on the droplet size and the solute concentration. As the solvent evaporates, the solute concentration of the droplets increases. The solute precipitates when critical supersaturation is reached, forming either solid particles or hollow shells, depending mainly on the solvent evaporation rate. Volume precipitation is favored at low evaporation rates, while surface precipitation is favored at high evaporation rates.

Considering the results of this paper, the decrease in the mean particle size with increasing CsH_2PO_4 concentration observed in Fig. 5 is consistent with the increased solution conductivity. A higher conductivity results in smaller initial aerosol droplets and a higher evaporation rate. In addition, higher solution conductivity permits more charge to be transferred on the aerosol droplets at the Taylor cone. Stronger repulsive Coulomb forces cause less stable aerosol droplets leading to more frequent disintegration events and, hence, smaller aerosol droplets. The leveling off of the particle size is plausibly a result of the higher amount of solute per droplet as the CsH_2PO_4 concentration continues to increase.

If we take this measured particle size to reflect solid rather than liquid particles, we can estimate, based on the solubility limit, the droplet sizes prior to solid precipitation. This provides an indication of the liquid content of the particles as they impinge onto the substrate. In the case of 25 nm and 45 nm solid CsH_2PO_4 particles, the droplet sizes, beyond which no further Coulomb fission events are possible, are 86 nm and 150 nm, respectively, in a 53 wt% methanol-water

solution. We also observe a decrease in the standard deviation, i.e., a more monodisperse particle size distribution with increasing CsH_2PO_4 concentration, consistent with a more stable Taylor cone. A CsH_2PO_4 concentration larger than 5 g/L leads to frequent clogging of the capillary and hence is not suitable for long-term operation (>1 hour).

The slight decrease of the mean particle diameter with increasing methanol concentration is consistent with the decreasing surface tension of the solution; however, the effect is moderated by the simultaneous drop in solution conductivity, which reduces the droplet charge. In addition to smaller size initial aerosol droplets due to lower surface tension, methanol has a lower boiling point than water. Decreasing the water-methanol ratio should allow faster evaporation of the solution and, with that, more frequent droplet disintegration events before the aerosol enters the neutralizer. This effect is less dramatic because of the decrease of the solution conductivity with increasing methanol concentration, so that the droplets are charged to a smaller fraction of the Rayleigh limit, driving fewer fission events.

Similarly, the slightly lower surface tension with increasing PVP content does not impact particle size. The added volume of the surfactant as a skin on the electrolyte particles probably influences the evaporation rate adversely to counter the surface tension effect.¹⁷⁶

When the applied capillary voltage is increased, the droplets are charged to a higher fraction of the Rayleigh limit, facilitating droplet disintegration.¹⁷⁷ Since the range of the voltage variation is very limited, the particle size reduction at the high end of the applied voltage range is also barely detectable.

When the electrospray temperature is varied, the reduction of the mean particle diameter can be explained by the higher evaporation rate of the solvent and the reduction of the surface tension. A higher solvent evaporation rate allows more frequent fission events leading to smaller electrolyte particles. At very high evaporation rates, hollow particles with larger diameters are generated as in other salt containing liquid systems, explaining the marked increase in the mean particle diameter and the width of the particle size distribution, without the increase of the solute supply rate.

Finally, an increase in the nitrogen flow rate effectively reduces the partial pressure of the solvents and hence increases the evaporation rate in addition to possible convective effects, leading to more frequent fission events and smaller electrolyte particles.

	Methanol (mol %)	CsH ₂ PO ₄ (g/L)	PVP (g/L)	Temperature (°C)	N ₂ flow rate (cm ³ /min)	Liq flow rate* (ml/h)	Voltage* (kV)
Range	22 – 53	0.5 - 10	1 – 30	22 – 120	200 - 1200	0.5 – 2.5	4.9 – 5.75
Default	53	5 or 10	1	100	1000	0.5	5

Table 6.1. Parameters varied in the electrospray deposition process. The sprayed solution consists of CsH₂PO₄ dissolved in a water-methanol mixture, in some cases with PVP added as a surfactant.

*The voltage and liquid flow rate settings cannot be varied entirely independently as they are restricted to values that yield a stable Taylor cone, and constant particle concentration.

6.1.7. Conclusions

In situ aerosol size measurement via a differential mobility particle sizer allowed the characterization of the electrospray parameter space, including the precursor solution composition, surface tension, conductivity, and flow rate; and the electrospray sheath gas temperature, flow rate, and electrospray voltage. The process established here yielded insights into the influence of certain parameters on the final particle size, and this process can be applied to similar systems for rapid, *in situ* exploration of the large parameter space that is common for nanoparticle synthesis methods. The most significant parameters influencing the final particle size are solute concentration, electrospray temperature, and nitrogen flow rate, each resulting in a decreased mean particle diameter as their value is increased.

It is interesting to note the size difference between the deposited CsH₂PO₄ nanoparticles with a ~100 nm feature size as observed with a scanning electron microscope¹⁶⁴ and the consistently smaller particle size of <50 nm as measured with the differential mobility particle sizer. The presented results provide two possible explanations for the size discrepancy. If fully dry nanoparticles are measured by the differential mobility particle sizer, then all else being equal, the process parameter nitrogen carrier gas flow rate should not have a significant impact on the particle size, as it only influences the speed at which the droplets go through the evaporation-Coulomb fission-evaporation sequence. But if the droplets entering the neutralizer still contain solvent, a further reduction in particle size due to Coulomb fission events is prevented, hence at low nitrogen carrier gas flow rates we observe larger particles than at high flow rates. The significantly larger feature size of ~100 nm of deposited CsH₂PO₄ can be explained by the presence of solvent in the droplet when deposited, which is not sufficient to re-dissolve the already deposited porous, fractal structure, but enough to prevent the crystallization of sub-100 nm particles. Increasing the capillary

to substrate distance may lead to smaller, dry particles depositing. Furthermore, the low melting temperature of 345°C, and the high hygroscopicity of CsH₂PO₄ explain fast agglomeration of the nanoparticles even at ambient conditions without a stabilizing agent.

Depending on the possibility of stabilizing the nanometer phases and allowing fully dry CsH₂PO₄ nanoparticles to deposit on a substrate, this result opens the opportunity for fabricating composite solid acid fuel electrodes that have the ideal structure consisting of percolating, porous networks of 12 nm CsH₂PO₄ particles. These structures hold the promise of much improved catalyst utilization allowing for significantly enhanced fuel cell power density values with equal platinum loading to traditional, mechanically milled electrodes.

Section 6.1. Supplementary material

6.1.1. Solvent evaporation of a single μm sized droplet

For an isothermal, quasi-steady state evaporation of a spherical droplet, Maxwell obtained the time rate of change of the droplet mass dm/dt , the equation ¹⁷⁸

$$\frac{dm}{dt} = \left(\frac{1}{2}\pi d_d^2\right) \rho \frac{dd_d}{dt} = 2\pi d_d D_v (c_{w,\infty} - c_{w,s}), \quad (6S.1)$$

where d_d is the diameter of the droplet, ρ is the droplet density, $c_{w,\infty}$ and $c_{w,s}$ is the concentration of water in the gas and surface of the droplet, respectively, and D_v is the diffusivity of water vapor in air as a function of temperature and pressure given as $D_v=(0.211/P)(T/273)^{1.94}$ in $\text{cm}^2 \text{s}^{-1}$. Evaporation of sub-micron droplets is in the Knudsen transition regime, hence, non-continuum effects should be included by introducing a modified diffusivity D_v' :

$$D_v' = \frac{D_v}{\left[1 + \frac{2D_v}{\alpha_c d_d} \left(\frac{2\pi M_w}{RT_a}\right)^{1/2}\right]}, \quad (6S.2)$$

where α_c is the water accommodation coefficient, M_w is the molar mass of droplet and R is the gas constant. **Equation 6S.1** is derived on the assumption that the interfacial concentration $c_{w,s}$ is constant (equivalent to assuming the interfacial temperature T_a is constant). When the initial temperature of the droplet is different from the surrounding continuum and a large heat of vaporization is involved, the interfacial temperature cannot be expected to be constant, especially during the short time after vaporization begins ¹⁷⁹. Therefore, the heat and mass transfer processes are coupled. The steady-state temperature distribution around a particle is governed by

$$u_r \frac{dT}{dr} = \alpha \frac{1}{r^2} \frac{d}{dr} \left(r^2 \frac{dT}{dr} \right), \quad (6S.3)$$

where $\alpha = k/\rho c_p$ is the thermal diffusivity of air and u_r is the mass average velocity. The first term is the convective term called Stefan flow, which can be neglected on the assumption that the bulk

flow of vapor is small compared with diffusional flux of vapor. Hence, an energy balance on the droplet can be written as

$$2\pi D_p k'_a (T_\infty - T_a) = -\Delta H_v \left(\frac{dm}{dt} \right). \quad (6S.4)$$

T_a is the surface temperature, T_∞ is the environment temperature, ΔH_v is the latent heat of vaporization and k'_a is the modified form for the thermal conductivity of air accounting for non-continuum effects and is given by

$$k'_a = \frac{k_a}{\left[1 + \frac{2k_a}{\alpha_T D_p \rho \bar{c}_p} \left(\frac{2\pi M_a}{RT} \right)^{1/2} \right]}, \quad (6S.5)$$

where $k_a = 10^{-3}(4.39 + 0.071T)$ in $\text{Jm}^{-1}\text{s}^{-1}\text{K}^{-1}$, and M_a , ρ and c_p are the air molar mass, density and heat capacity, respectively. α_T is the thermal accommodation coefficient, which is also uncertain and often set equal to the value of the mass accommodation coefficient α_c . **Equation 6S.4** simply states that at steady state the heat released during water condensation is equal to the heat released to the droplet surroundings¹⁸⁰.

There are two types of factors that affect the kinetics of droplet growth and evaporation given in **Equation 6S.1**; namely, those that provide resistance to heat and vapor flow and those that change the equilibrium vapor pressure of the droplet. The thermal and water accommodation coefficient belong to the first group representing resistance to heat and vapor flow. Two opposing factors belong to the second type - the Kelvin effect and the solute effect. The Kelvin effect of the droplet surface curvature tends to cause an increase in vapor pressure as the droplet decreases and the solute effect causes a decrease in vapor pressure as radius decreases. One or the other of these effects is dominant depending on the droplet radius and solute content of the drop. Substituting ideal gas law, **Equation 6S.1** can be written as

$$D_p \frac{dD_p}{dt} = \frac{4\pi D_p' M_w p^0(T_\infty)}{\rho R T_a} \left(\frac{p_{w,\infty}}{p^0(T_\infty)} - \frac{p_{w,s}}{p^0(T_\infty)} \right), \quad (6S.6)$$

where M_w is the molar mass of the solution, $p^0(T_\infty)$ is the vapor pressure at T , $p_{w,\infty}/p^0(T_\infty)$ is the environmental saturation ratio and is equal to unity (relative humidity is equal to 100%) when the partial pressure in the atmosphere $p_{w,\infty}$ is equal to saturation vapor pressure $p^0(T_\infty)$.

$$\frac{p_{w,s}}{p^0(T_\infty)} = \frac{p_{w,s}(D_p, T_a)}{p^0(T_a)} * \frac{p^0(T_a)}{p^0(T_\infty)} \quad (6S.7)$$

The first term in **Equation 6S.7** for a non-ideal solution of soluble and insoluble materials can be written as

$$\frac{p_{w,s}(D_p, T_a)}{p^0(T_a)} = \exp \left[\frac{4M_w \sigma_w}{\rho R T_a D_p} + \ln \gamma_w - \frac{6n_s \tilde{v}_w}{\pi(D_p^3 - d_u^3)} \right], \quad (6S.8)$$

where n_s is the number of moles of solute, σ_w is the droplet surface tension, γ_w is the activity coefficient, \tilde{v}_w is the partial molar volume of water and d_u is the diameter of insoluble particles in the droplet solution. γ_w was estimated with the Davies equation for a 10g/L cesium di-hydrogen phosphate solution in water as 0.8. The first two terms in **Equation 6S.8** are the Kelvin effect, giving the dependence of vapor pressure on surface tension and droplet diameter, the third term in **Equation 6S.8** accounts for the solute effect from Raoult's law.

The second term in **Equation 6S.7** is a ratio of water saturation pressures at T_a and T_∞ and is given by the Clausius-Clapeyron equation as

$$\frac{p^0(T_a)}{p^0(T_\infty)} = \exp \left[\frac{\Delta H_v M_w}{R} \left(\frac{T_a - T_\infty}{T_a T_\infty} \right) \right]. \quad (6S.9)$$

Substituting into **Equation 6S.6** we have the complete droplet evaporation given as

$$\frac{dD_p}{dt} = \frac{4\pi D_p' M_w p^0(T_\infty)}{\rho R T_a} \left[\frac{p_{w,\infty}}{p^0(T_\infty)} - \exp \left[\frac{4M_w \sigma_w}{\rho R T_a D_p} + \gamma_w - \frac{6n_s \tilde{v}_w}{\pi(D_p^3 - d_u^3)} + \frac{\Delta H_v M_w}{R} \left(\frac{T_a - T_\infty}{T_a T_\infty} \right) \right] \right]. \quad (6S.10)$$

Equation 6S.10 and **Equation 6S.4** are coupled and must be solved numerically to describe the evaporation rate of a single droplet. The set of parameters used to solve the evaporation are given as follows; $T_\infty = 373\text{K}$, and the concentration of the solute of choice (cesium di-hydrogen phosphate) is 10g/L . The solvent parameters molar mass, surface tension, density correspond to values for water. **Figure 6.S.1** shows the evolution of a single droplet of initial droplet size of $1\mu\text{m}$ to its dry solute size 100nm for varying relative humidity and ambient temperature and a water accommodation coefficients (α_c) and the thermal accommodation coefficient (α_T) of unity.

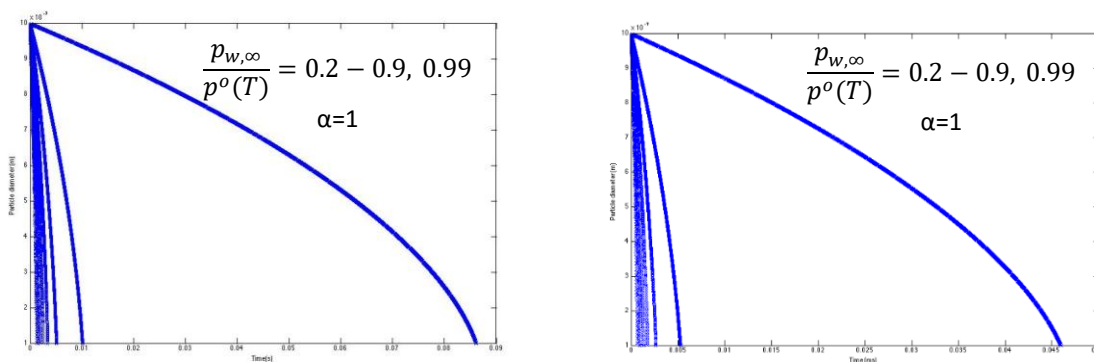


Figure 6.S.1. Evolution of a single $1\mu\text{m}$ droplet to 100nm dry CsH_2PO_4 particle in 20-99% relative humidity and ambient temperature of (a) 25°C and (b) 100°C .

The evaporation coefficient (α_c) is defined as the fraction of molecules that hit the liquid surface and condense. This is also called the sticking probability and corresponds to the water accommodation coefficient in the derivations above. Polar liquids like water vaporize at significantly lower rates than the maximum rate predicted by kinetic theory using the equilibrium value of vapor pressure, and therefore have a smaller value of evaporation coefficient than non-polar liquids. An increase in water accommodation coefficient (sticking probability of water to the droplet) decreases the modified diffusivity of the water molecule in air. On the other hand, increase in the thermal accommodation coefficient (transfer of vapor molecules across the interface) increases the modified thermal conductivity of air.

The magnitude of the non-continuum correction depends strongly on the value of the water accommodation coefficient (α_c) and the thermal accommodation coefficient (α_T). In **Figure 6.S. 1**, $\alpha_c = \alpha_T$. The value of α_c has been subject to be debate, a value of 0.045 was used by Pruppacher and Klett, while ambient measures suggest a value closer to unity^{180, 181}. Fukuta et al explain the

difference between thermal accommodation coefficient and evaporation coefficient (water accommodation coefficient) ¹⁸². They define the thermal accommodation coefficient as the transfer of heat energy by molecules arriving and leaving the interface between a gas and a condensed phase, and consider it to be related to the transfer of vapor molecules across the interface. Knudsen's definition of accommodation coefficient is ¹⁸²

$$\alpha_T = \frac{T'_2 - T_1}{T_2 - T_1}, \quad (6S.12)$$

where T_1 is the temperature of the gas molecule ($T_1=373\text{K}$), T_2 is the temperature of the condensed phase and T'_2 is the temperature of the gas molecule leaving the condensed phase. If we assume T_2 is the initial droplet temperature, 298K, and T'_2 is the geometric mean, 336K, this corresponds to a thermal accommodation coefficient (α_T) of 0.5.

The combined effect is shown in **Figure 6.S.2** where the change in droplet evolution time for constant relative humidity of 40% is shown for varying $\alpha_c = \alpha_T$. It is evident that, α_c and α_T do not have a significant effect on the overall prediction of evaporation rate in this setup.

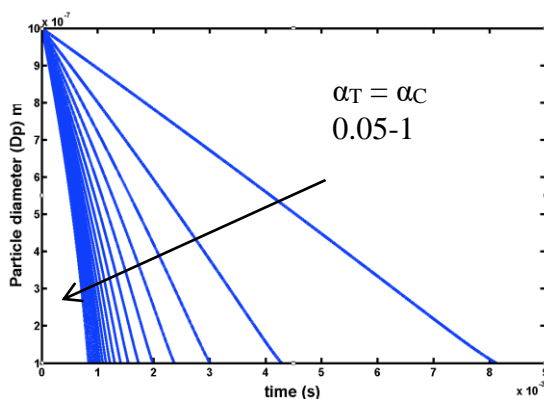


Figure 6.S.2. For $\alpha_T = \alpha_C$ ranging from 0.05-1, the evolution of a single droplet of initial droplet size $1\mu\text{m}$ at 40% relative humidity and $T=100\text{ }^\circ\text{C}$.

The results above indicate that the drying time of a micron sized droplet is in the millisecond range. Since the particles have a substantially long flight time to the analyzer (22sec), the particles sizes reported in Section 6.1. are of dry CsH_2PO_4 nanoparticles.

Section 6.2. Electrospray throughput

The main challenges of the electrospray process are its low throughput and the uniformity of the deposited film. The electrospray throughput is on the order of $10\mu\text{l/hr}$ in the cone-jet mode¹⁸³. Such low flow rates severely limit the use of a single electrospray emitter in industrial applications¹⁸³. Therefore, several studies have been done on scaling up the electrospray process^{71, 183-189}. Very sophisticated multi-electrospray arrays have been manufactured by micro-fabrication techniques for mass spectrometry applications^{185, 187, 188, 190}. These designs are aimed at mass spectrometric sensitivity rather than increasing the flow rate. Laser etching and MEMS techniques have been used for liquid fuel combustion^{186, 189}. Although these works are aimed at increasing throughput, they are not intended to deposit uniform overlapping films suitable for fuel cell electrodes. A common characteristic of the emitters in the works above is the conical shapes at the tip of the capillary to anchor the Taylor cone menisci. This is because the Taylor cone is less likely to be stable in a single cone-jet if the capillary tip is flat and sharp. In addition, it is unclear in most of these works if the emitters operated in the steady cone-jet mode necessary for nanostructure fabrication. There are some important issues addressed in the literature that are useful to the proposed multi-capillary electrospray process for fuel cells.

Rulison *et al.* found that the potential required to establish Taylor cones on each capillary increases with decreasing distance between capillaries in a linear array but the liquid flow rate per cone was independent of spacing⁷¹. In addition, they found that dummy capillaries must be placed at the ends of the array to reduce field distortions at the capillary tips. Without these capillaries, the Taylor cones located at the ends of the array are distorted and tilt away from the inner capillaries. Although this work does not report the uniformity of the deposition profile, unstable Taylor cones at the edges that are tilted away from the center could lead to non-uniform deposition.

Deng *et al.* fabricated a 90-microneedle injector in a hexagonal pattern on a silicon thin plate. This is the electrospray with the highest compactness built thus far at 250 emitters per square centimeter¹⁸⁵. They found that with such high compactness, an intermediate electrode called an extractor was required to lead the droplet from the cone tip to the ground electrode. The extractor is a metal plate with holes aligned with the emitter. Without an extractor, the space charge from the cloud of charged droplets is significantly high causing shielding of the electric field near the

surface of the Taylor cones located in the central part of the atomizer. These affected emitters lose the cone-jet shape, stop emitting mass and charge, or have fluctuating Taylor cones. The extractor also lowers the voltage difference required to form the Taylor cone. This is significant since increasing the number of emitters and decreasing the distance between the emitters increases this voltage. In addition, if the extractor to emitter distance is smaller than the distance between each Taylor cone, the electric field near a conical meniscus due to the extractor is larger than the effect of the neighboring Taylor cone. Therefore, each Taylor cone is electrically isolated from all the others¹⁸³.

Finally, Bocanegra, Barrero, Loscertales and Marquez reported that liquids could also be electrosprayed in a steady cone-jet mode without using capillaries or tips but through holes on a flat metallic surface^{183, 191-193}. The authors also found that, like Deng, an extractor plate with larger holes aligned with the emitting holes is required for stable Taylor cones. Unfortunately, the authors do not detail the uniformity of films deposited in these works but clearly increase throughput with high compactness of emitters. Most importantly, feeding holes through a reservoir versus multiple capillaries greatly simplifies fabrication.

Therefore, there are significant factors to be considered in the case of a multi-spray setup. Electrical shielding in the form of dummy capillaries or metal extractors will be crucial to forming multiple stable Taylor cones.

6.2.1. Experimental details

Simulations were done to gain insight on the electrospray system. COMSOL is a multi-physics simulation package used to calculate the trajectory and magnitude of the electric field lines emitted from a capillary. COMSOL simulations give insight to the behavior of the electric field with differing geometries. This is important because the electric field lines predict the particle flight path. This is because electrostatic forces on the charged particles are dominant, in comparison to drag force as a result of the sheath gas, and the gravitational pull on the charged particles. The electric field can be derived from the negative gradient of the scalar potential as shown in **Equation 6.2.1**. Taking the divergence of the electrostatic field we obtain Poisson's equation in **Equation 6.2.2**:

$$E = -\nabla\varphi, \quad (6.2.1)$$

$$\nabla^2\varphi = -\frac{\rho}{\varepsilon_0}, \quad (6.2.2)$$

where ρ is the space charge density and ε_0 is the permittivity of free space. In the electrospray model the space charge density is a function of distance and time. The charged droplets after emission from the Taylor cone experience a changing charge density as they move towards the substrate. This makes solving the Poisson's equation almost impossible. Some groups have developed models with intensive computing methods to simulate the electrospray space charge cloud^{184 185}. The COMSOL package can model the Laplace equation ($\nabla^2\varphi = 0$). Therefore, in these simulations it is assumed that the space charge density is zero. This is an assumption that the electric field information calculated by COMSOL represents the initial behavior of the droplet right after emission from the Taylor cone.

The electric field required to overcome the surface tension of a liquid and establish a Taylor cone is given as⁷¹

$$E_s = \left(\frac{2\gamma\cos\theta}{\varepsilon_0 r_c}\right)^{\frac{1}{2}}, \quad (6.2.3)$$

where r_c is the capillary radius, γ is the gas-liquid surface tension, θ is the cone semi vertex angle, and ε_0 is the permittivity of free space. The equilibrium cone semi-vertex is 49.3° , ignoring space charge effects⁷¹. The onset capillary voltage required to establish this electric field at the capillary tip is

$$V_s = 0.667 \left(\frac{2\gamma r_c \cos\theta}{\varepsilon_0}\right)^{\frac{1}{2}} \ln\left(\frac{4h}{r_c}\right), \quad (6.2.4)$$

where h is the distance between the capillary tip and the grounded substrate. The greater the distance between the capillary tip and substrate, the higher the voltage required to establish a Taylor cone.

From the calculated electric field at the capillary tip, it can determine if a Taylor cone will form on a capillary in a defined setup, and a specified set of parameters, with **Equation 6.2.3**. **Figure 6.2.1** is a map of the electric field at the tip of a capillary.

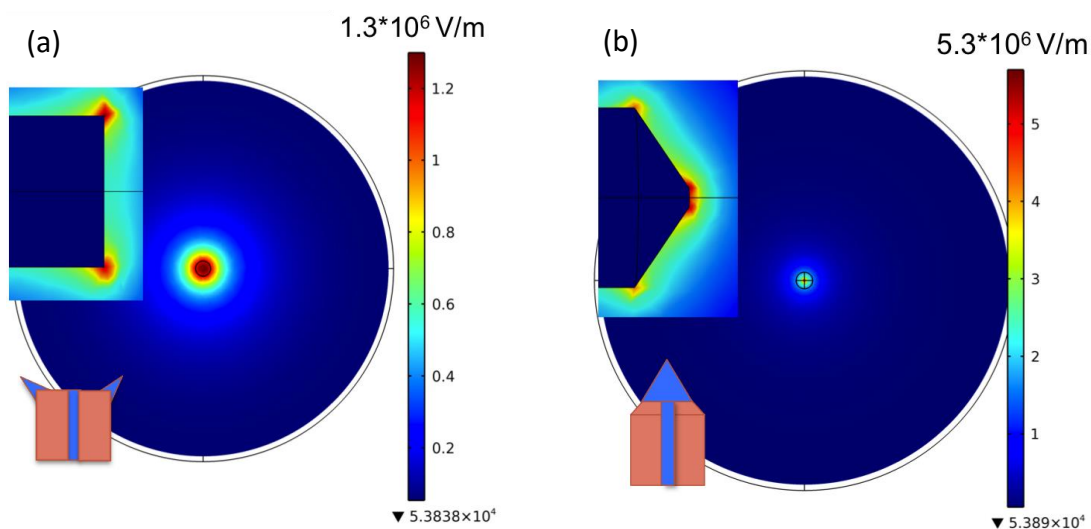


Figure 6.2.1. Electric field map showing top view and side view, to the right is the scale bar depicting red as the highest electric field value. A schematic of Taylor cone formation shown at bottom left. (a) Flat capillary (b) Frustum shaped capillary.

The side view shows that the electric field is highest at the sharp edges of the capillary. In addition, bottom left schematic shows where Taylor cones will form according to **Equation 6.2.3** (electric field $> 10^6$ V/m). This agrees with literature findings that the capillary tips must be sharpened to anchor the Taylor cone^{64, 71, 194, 195}. The angle at which the authors in the literature sharpened the tip is never really specified. Therefore, simulations were made to calculate the electric field above the tip of the capillary and at the corner of the capillaries to see if the tip angle has an effect on the electric field. **Figure 6.2.2** shows that the tip angle does not really affect the electric field above the capillary but the electric field at the sharp edges of the capillary increases with an increase in tip angle. A tip angle of zero corresponds to the flat capillary. On the other hand, there is a limit on the angle of a frustum for a given height. Hence, getting as close to this limit when sharpening the capillary tip is paramount. With this insight from COMSOL, an electro spray setup was constructed for testing.

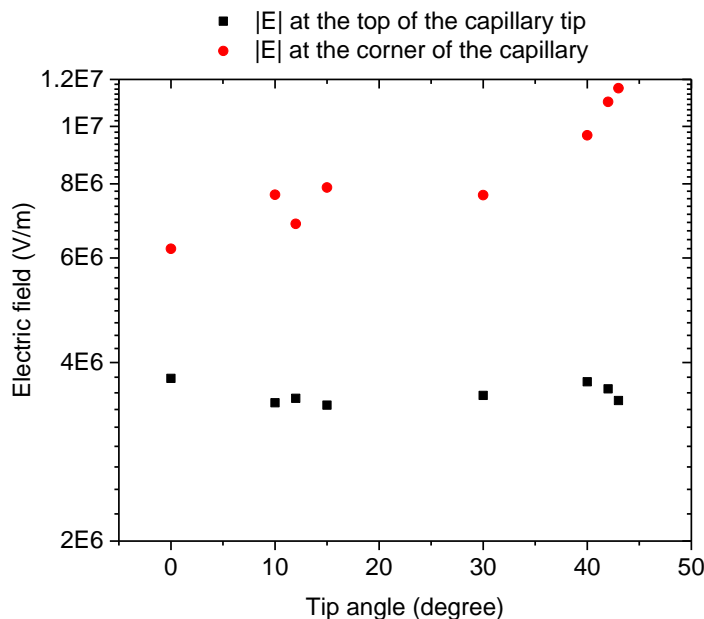


Figure 6.2.2. Plot of electric field versus the capillary tip angle

The aqueous solution electrosprayed was 10g/L of CsH_2PO_4 and 20g/L polyvinylpyrrolidone (PVP) dissolved in a 1 : 1 molar ratio of methanol : water mixture. This gives the optimized balance between conductivity and surface tension of the solution to maintain a steady cone-jet and deposit porous, fractal nanostructures⁷. The PVP serves as a surfactant that keeps the solute in solution and also prevents the nanostructures deposited from agglomerating. CsH_2PO_4 was prepared by precipitation from an aqueous solution of Cs_2CO_3 and H_3PO_4 . The solution enters the deposition chamber at a controlled flow rate by a syringe pump via a stainless steel capillary (ID $127\mu\text{m}$, OD 1.6mm, L 50mm) that has been sharpened to a frustum shape. The capillary tip is opposite an aluminum substrate holder. The spray geometry is upwards in order to avoid instabilities that can arise from dripping of excess droplets. A positive bias in the 4.5 kV – 8 kV range is applied to the capillary and the substrate is grounded. The chamber is an aluminum casing with insulating caps to electrically isolate the capillary from the substrate holder. The chamber walls are heated independently of the substrate. Two inlets on the side of the wall allow preheated N_2 gas to flow towards the outlets on the substrate holder. The N_2 gas serves as a drying gas for the charged wet particles moving towards the substrate. The current carried by the flux of charged particles to the substrate was measured using a Keithley 40 Digital 3.5 digit Bench Picoammeter connected in series between the ground wire and the substrate holder. Monitoring the current is an easier and

safer way to monitor the stability of the Taylor cone versus looking through the chamber windows at high proximity to high voltage wires. The parameters leading to the porous fractal structure ideal for an SAFC are summarized in **Table 6.2.1**.

6.2.2. Results and discussion

In general, the parameters to get a porous, fractal structure with different chambers/setups are similar. The discrepancy in voltage is likely because the chambers are different and the distance between capillary and substrate is about 1 cm longer in my chamber. Although the capillary flow rate is significantly lower, deposition rate is similar in both works (~ 5 mg/h).⁷ Therefore, the deposition rate is not necessarily solely determined by the flow rate through the capillary.

Parameter	Varga et al. ⁷	This work
Chamber and N ₂	140	100
Temperature/ ⁰ C		
Substrate Temperature/ ⁰ C	140	140
Voltage/kV	4.5	5
N ₂ gas flow rate	1000	1000
CsH ₂ PO ₄ concentration/g L ⁻¹	10	10
Capillary Flow rate /mL h ⁻¹	1	0.5

Table 6.2.1. *Electrospray parameters*

It was found that if the solution composition remains the same, the substrate temperature is above 100 ⁰C, and the spray is in cone jet mode (~ 5 kV). Changes to the chamber temperature, N₂ temperature and flow rate do not affect the outcome of the porous fractal structure. On the other hand, there are small, insignificant changes in deposition rate with changes in N₂ flow rate. This agrees with Chen and Perednis' suggestion that solution composition and substrate temperature are the most important factors that determine film morphology. The CsH₂PO₄ feature size

deposited in **Figure 6.2.3** is 300 nm. Changes to capillary flow rate, N₂ temperature and flow rate do not affect the particle size deposited on the substrate. Although the particle size emitted from the Taylor cone is determined by the flow rate through the capillary as shown in **Equation 6.1**, the droplets undergo subsequent coulumbic breakup and drying as they move towards the substrate. Intuitively, capillary flow rate, N₂ temperature and flow rate should affect the particle size deposited if dry nanoparticles are deposited directly on the substrate. The results above concur with Chen's observation that spreading and additional drying can occur on the substrate after the deposition on the substrate ⁷². A study has been done in the Haile group on how gas temperature, gas flow rate, capillary flow rate, solute composition and solvent composition affect the particle size in real time (before deposition). CsH₂PO₄ particle sizes as small as 12 nm were produced under optimized conditions. The CsH₂PO₄ size is significant because the smallest commercially available platinum catalyst size is about 10 nm. Hence, if CsH₂PO₄ co-deposited by electrospray is the same order of magnitude in size, the power density will be significantly increased as the number of TPBs increases.

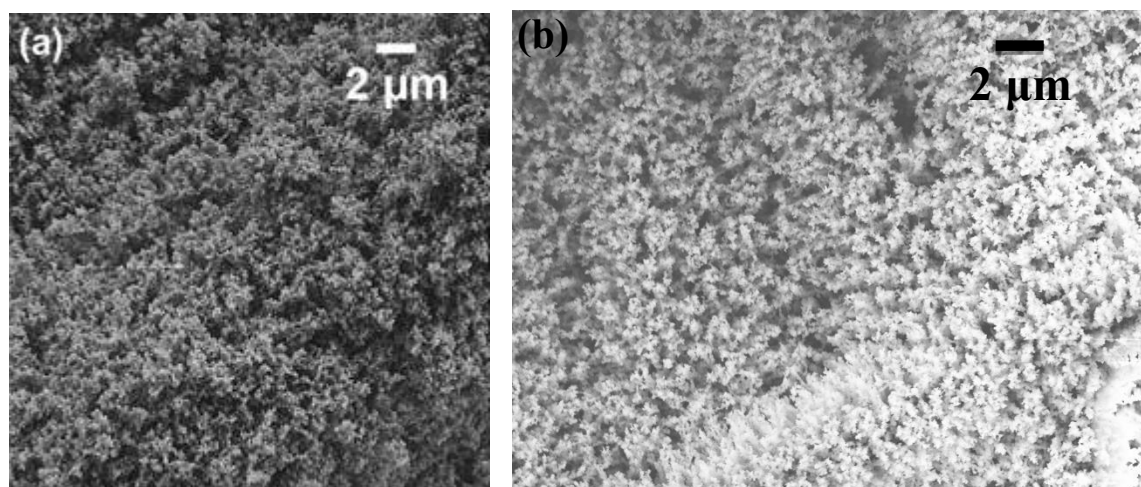


Figure 6.2.3. SEM micrograph of porous interconnected CsH₂PO₄ obtained by electrospray. (a) Published work by Varga *et al.*⁷ (b) This work.

Platinum and platinum black were co-sprayed with CsH₂PO₄ for electrochemical characterization. Incorporation of these electron-conducting and catalytic additives increases the solution conductivity, which in turn decreases the particle size emitted from the Taylor cone (Eqn. 3). Consequently, the particle size deposited is about 100 nm, significantly smaller than the 300nm

feature size of CsH_2PO_4 deposited.

Electrochemical characterization was done by symmetric cell measurement of the AC impedance. This is done by applying a sinusoidal voltage to both sides of a cell with identical electrodes, varying the frequency and measuring the resulting steady sinusoidal current. Each physical process responds to a certain frequency, based on the time constant of that process. AC impedance separates physical properties in the Nyquist plot. Symmetric electrochemical cells were fabricated using dense CsH_2PO_4 and identical, electrospayed carbon paper substrates were the electrodes. The carbon paper served as the current collector from the electrodes. CsH_2PO_4 powder was cold-pressed for 20 min under a uniaxial pressure of 34 MPa. Two porous stainless steel discs were placed on the electrospayed electrodes on either side of the electrolyte for uniform gas diffusion to the surface of the electrode. This ‘sandwich’ is placed in a compression holder that goes in to the testing chamber. Electrical data was collected under humidified hydrogen at 248 °C using an impedance analyzer (Eco Chemie Autolab PGstat302). The voltage amplitude of 10 mV is applied over frequencies ranging from 10 MHz to 1MHz. The H_2 flow rate was 30 sccm and it was humidified with water flowing through a bubbler at 80 °C. **Figure 6.2.4a** is a schematic of the components of the symmetric cell sandwich. **Figure 6.2.4b** is a picture of the symmetric cell in the compression holder that goes into the chamber for testing.

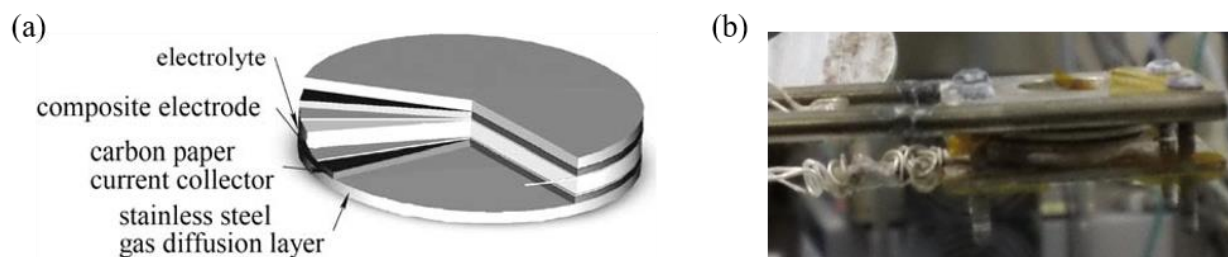


Figure 6.2.4. Schematic of symmetric cell assembly used for electrochemical characterization. (B) Picture of compression holder that holds the symmetric cell in the testing chamber.

Figure 6.2.5 is the impedance spectra in Nyquist form. In general, the Nyquist plot displays an arc in the 1MHz to 10 Hz frequency range. The offset along the real axis corresponds to the resistance of the electrolyte (thickness) and electrolyte conductivity. The span of the arc corresponds to the electrode resistance. The lower the electrode resistance the higher the electrode performance. The plot below shows the Nyquist plot for a mechanically milled and pressed

electrode with a 3:3:1 composition of platinum : CsH_2PO_4 : platinum on carbon and that for an electro sprayed electrode with a 2:1:1 composition of CsH_2PO_4 : platinum : platinum on carbon. The mechanically milled electrodes have a higher mass of 25mg each and higher platinum loading of about $10\text{mg}/\text{cm}^2$. The electro sprayed electrodes have a mass of 8mg each and platinum loading of about $0.3\text{ mg}/\text{cm}^2$. Platinum loading is based on the change in mass of the substrate before and after deposition, and is estimated at $0.3\text{ mg}/\text{cm}^2$. The impedance of the mechanically milled electrode is $0.07\ \Omega\ \text{cm}^2$ and the impedance of the electro sprayed electrode is about $0.7\ \Omega\ \text{cm}^2$. The mechanically milled electrode has lower electrode resistance as indicated by the impedance, but the platinum mass normalized activity is the same at $2.2\ \text{S}/\text{mg}$. The performance of these electro sprayed samples is comparable to the performance of the electro sprayed electrodes with the same composition published by Varga ($1.5\ \Omega\ \text{cm}^2$).⁷

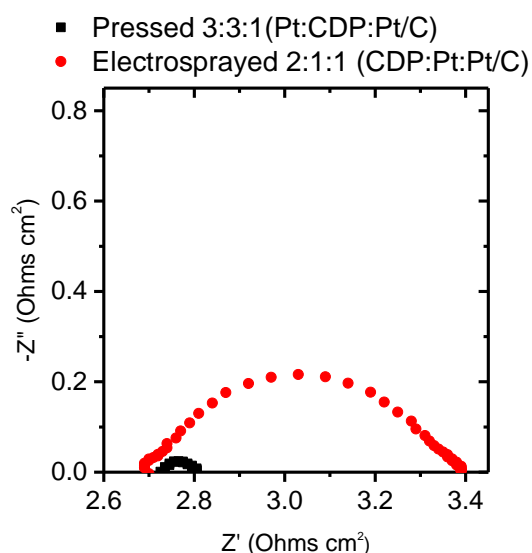


Figure 6.2.5. Impedance spectra of a representative CsH_2PO_4 (CDP) : platinum : platinum on carbon symmetric cell collected under humidified hydrogen with a water partial pressure of 0.4 atm at 248°C .

Although these results are promising there is room for improvement. There are three main challenges; the feature size deposited, the uniformity of the film deposited, and the deposition rate.

Reducing the CsH_2PO_4 feature size will increase the power density by increasing the triple phase boundaries. Back scattering images of the electro sprayed electrodes show well-dispersed bright spots believed to be the Pt nanoparticles. Platinum's high conductivity can cause rapid

discharge of the electrical current and repulsion of the particles from each other. The lack of interconnectivity between the catalyst nanoparticles suggests that the current measured by impedance is not the total output from every triple phase boundary in the electrode structure. Therefore, future work will be done on improving the electro spray electrode structure interconnectivity and reducing feature size.

Improving uniformity of the films deposited - **Figure 6.2.6a** shows SEM images of the cross-section of CsH_2PO_4 electro sprayed on carbon paper. **Figure 6.2.6b** is a top view. From both images, it is clear that the deposition area (~ 1.3 cm diameter) is non-uniform. The height varies from about $260\mu\text{m}$ (Carbon paper thickness) to $580\mu\text{m}$ at the center of the film. Consequently, this non-uniformity affects the electrochemical characterization, hence it is important that the film tested be fairly flat to maintain good contact with the electrolyte surface. Typically, after SEM inspection of an electro sprayed sample, a uniform area of the sample, usually about $0.3\text{-}0.7$ cm^2 , is cut out and used for electrochemical testing. For accurate comparison between samples, the impedance measured must be normalized by the area tested. To make this method useful for fuel cell electrodes, the uniformity of the films deposited must be improved. Increasing the area of deposition and throughput is unavailing if the electrode cannot make good contact with the electrolyte.

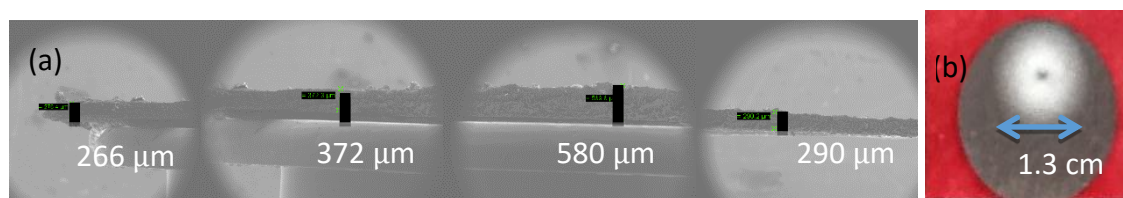


Figure 6.2.6. a) SEM micrographs of the cross section of an electro sprayed CsH_2PO_4 sample on carbon paper. (b) Picture showing the top view of CsH_2PO_4 .

To solve this problem of non-uniformity, the charged cloud of particles has to be spread out with a defocusing effect. A defocusing lens is an electrode used in beam physics to interfere with the path of a charged beam. COMSOL was used to predict how a metal electrode and corresponding bias would affect the electric field emitted from a capillary. **Figure 6.2.7a** shows electric field lines from a single capillary, biased at 5 kV, moving towards a grounded substrate.

Figure 6.2.7b-d show the electric field line behavior when there is a metal ring with no bias around the capillary. The capillary bias is 5 kV. The figure suggests that the smaller the ring the wider the field lines spread. In addition, the electric field at the tip of the capillary (top right) decreases with increase in ring diameter. Hence, a metal ring of small enough diameter can act as an extractor, reducing the onset voltage required to achieve a Taylor cone (electric field $>10^6$ V/m).

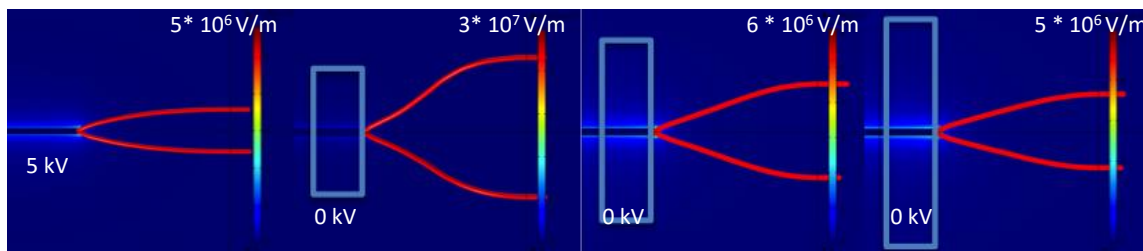


Figure 6.2.7. Side view of the electric field map, the electric field scale bar is on the right. The highest value of electric field (at the top right corner) corresponds to the electric field at the capillary tip (not visible). (a) Single capillary biased at 5kV. (b) Single capillary surrounded by a ring 1.9 cm in diameter. (c) Single capillary surrounded by a ring 2.8 cm in diameter. (d) Single capillary surrounded by a ring 5.7 cm in diameter

The influence of the ring bias on the electric field was also studied. **Figure 6.2.8** shows that increasing the bias above zero will cause the particles to reverse trajectory and deposit on the ring. From these simulations, I gather that there is a possibility of losing material to the ring.

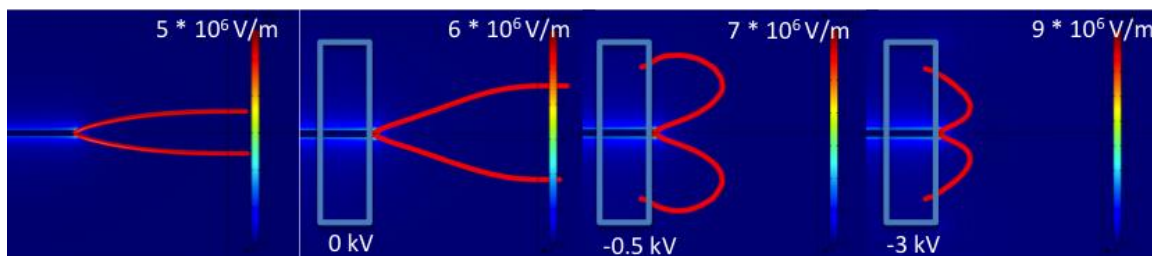


Figure 6.2.8. Side view of the electric field map, the electric field scale bar is on the right. The highest value of electric field (at the top right corner) corresponds to the electric field at the capillary tip (not visible). (a) Single capillary biased at 5kV. (b) Single capillary surrounded by a ring 1.9 cm in diameter with no bias. (c) Single capillary surrounded by a ring 1.9 cm in diameter with a bias of -0.5 kV. (d) Single capillary surrounded by a ring 1.9 cm in diameter with a bias of -3 kV

It is cumbersome and wasteful to build a chamber for each configuration above. So a testing station with a single capillary and a grounded plate was setup in a fume hood. In this open setup,

the deformation ring size can be easily exchanged and with varying voltage bias. The experimental results of this study are shown in **Figure 6.2.9**.

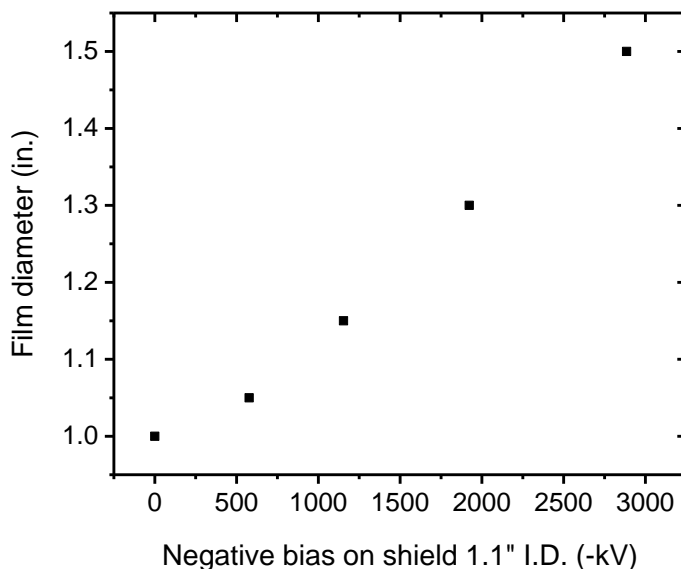


Figure 6.2.9. Plot of film diameter (in inches) versus the bias on the negative bias on the ring surrounding the capillary (-kV). Increasing the bias increases the defocusing effect.

Figure 6.2.9 is a plot of deposited film diameter versus the negative bias on a metal ring that is 2.8 cm (1.1"). For comparison, a single capillary without a metal ring deposits a film with a diameter of 1.3 cm (0.5"). Although COMSOL simulations predict that all field lines would go to the biased ring, it is clear that increasing the negative bias increases the diameter of the film deposited. COMSOL accurately predicts that there will be a spread in the space charge cloud with the presence of a metal ring. On the other hand, the COMSOL simulations do not account for the varying space charge density and the presence of N₂ gas sheath flow that can carry the charged particle upwards. Therefore, COMSOL simulations cannot accurately predict what the trend experiments show. -2.9 kV is the highest negative bias used in this experiment because it is the highest value that can be reached without breakdown between the capillary and the ring.

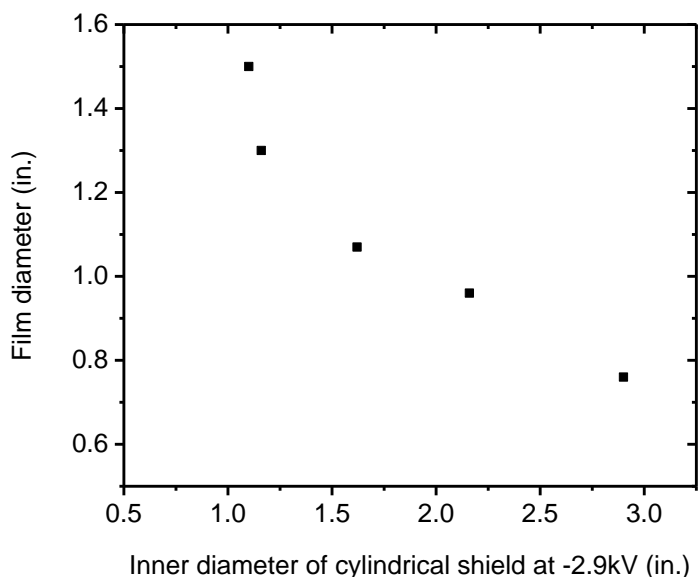


Figure 6.2.10. Plot of deposited film diameter (in inches) versus the internal diameter of the metal ring (in inches). Decreasing shield radius increases the defocusing effect.

Figure 6.2.10 is a plot of the deposited film diameter versus the inner diameter of the cylindrical shield. As predicted by the COMSOL simulations, the film diameter decreases as the inner diameter of the metal ring increases. The smallest inner diameter tested is the smallest possible without breakdown between the capillary and the ring. The experimental data in **Figure 6.2.9** and **Figure 6.2.10** show that the metal ring has a defocusing effect that attracts the charged particles, spreading the beam as they move toward the substrate. With this knowledge, we built an electro spray chamber that can accommodate a ring with a negative bias and deposit films with greater uniformity.

Figure 6.2.11 shows the SEM cross-section images of CsH_2PO_4 electro sprayed with a defocusing ring that is 2.8 cm (1.1”) in diameter. In comparison to the cross-section of the electro spray sample without the ring in Figure 11, the average height is uniform. The total mass deposited in both samples is the same. Hence, defocusing the beam improves the uniformity of the films deposited, allowing us to test larger areas of the electro sprayed samples.



Figure 6.2.11. SEM micrographs of the cross section of an electrospayed CsH_2PO_4 sample with a defocusing ring on carbon paper

Electrochemical characterization was done on samples with incorporated Pt and Pt on carbon. The impedance data for a uniform sample, of area $\sim 2.8 \text{ cm}^2$ (0.75" diameter), electrospayed with a defocusing ring, is shown in **Figure 6.2.12**.

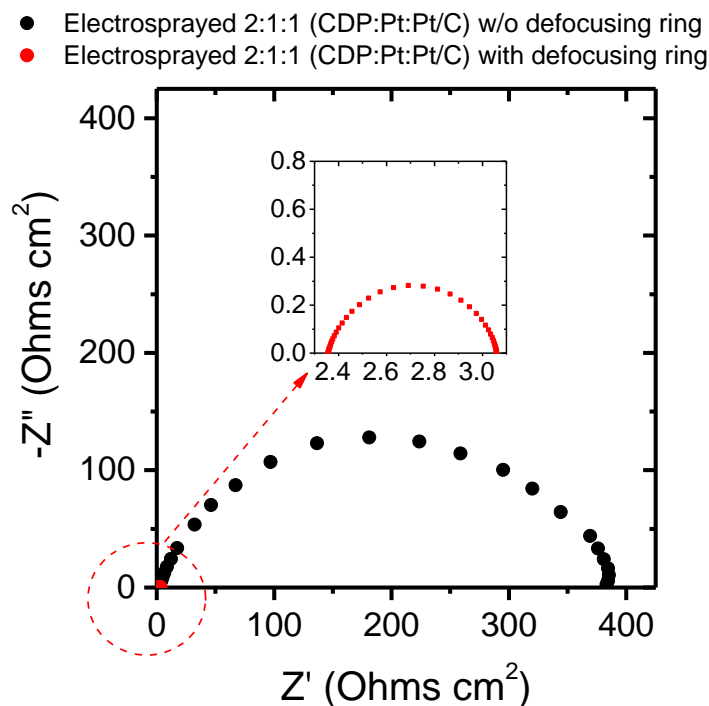


Figure 6.2.12. Impedance spectra for electrospayed 2:1:1 CsH_2PO_4 :Pt:Pt/C of equal area with and without a defocusing ring.

For comparison, the impedance of a non-uniform sample of equal area (electrospayed without ring) is also shown in **Figure 6.2.12**. The activity is drastically improved with an increase in uniformity from over $375 \Omega \text{ cm}^2$ to $0.8 \Omega \text{ cm}^2$. In addition, the area-normalized performance of

these uniform large area films is comparable to the performance of the electro sprayed electrodes of area $\sim 0.3 \text{ cm}^2$ published by Varga ($1.5 \Omega \text{ cm}^2$) and shown in **Figure 6.2.10** ($0.7 \Omega \text{ cm}^2$).

Increasing deposition rate with a multi-capillary electro spray setup - Increasing the throughput is definitely the most challenging issue facing electro spray. The deposition rate of CsH_2PO_4 with a single capillary is about 5 mg/hr , this decreases to $\sim 1 \text{ mg/hr}$ with a defocusing ring because of material lost to the ring as predicted by COMSOL. Fortunately, with incorporation of Pt and Pt/C, material lost to the ring is negligible. This is probably because the jump in conductivity of the solution causes preferential deposition of platinum on the substrate versus the stainless steel ring. Since we cannot increase the deposition rate of a single capillary, increasing the number of capillaries can increase total amount deposited at a time.

The scale-up goal is to increase the area of the film deposited from 1.3 cm^2 ($0.5''$ diameter) to 20 cm^2 ($2''$ diameter)- 200 cm^2 ($6''$ diameter). COMSOL simulations of a three capillary system and a seven capillary system were done to determine the optimum geometry for stable Taylor cones on each capillary. In the three-capillary system the influence of dummy capillaries (non-emitting capillaries) on the emitting capillaries was studied. The geometry studied is shown in **Figure 6.2.13**. The three central capillaries in the center are the emitters and the outer capillaries serve as the dummy capillaries.

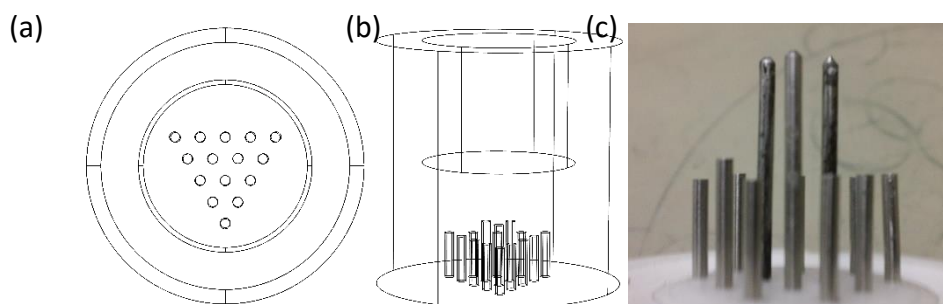


Figure 6.2.13. (a) Top view of the capillary arrangement. (b) Side view showing the central emitting capillaries and the dummy capillaries lower in height. (c) Picture of the capillaries used in the experiment.

From the COMSOL simulations, we found that without the dummy capillaries the electric field is non-uniform at the capillary tip. This agrees with Rullison's findings that the outer

capillaries experience end effects and need a dummy capillary to reduce this end effect.⁷¹ In addition, we found that if the dummy capillaries are the same height as the emitting capillaries, the electric field at the tip of the capillaries is too low to form a Taylor cone. The optimal geometry where the electric field at the emitting tip is uniform, and the electric field is high enough for a Taylor cone, is when the dummy capillary height is 75% of the emitting capillary height. This geometry is depicted above in **Figure 6.2.13c**. We built a three-capillary system to test these findings.

The experimental results are presented in **Figure 6.2.14**. The top row is the electric field map calculated by COMSOL for differing cases where blue is the lowest electric field magnitude and red is the highest. In all cases, all of the capillaries are biased at 5kV. Case A is three capillaries only, case B is three capillaries surrounded by dummy capillaries half the height of the emitting capillaries in the center, case C is three capillaries surrounded by dummy capillaries three quarters their height, and case D is three capillaries surrounded by dummy capillaries of the same height. The numbers below correspond to the electric field range at the emitting capillary tip. The corresponding experimental result is below the simulation. In case A, the electric field is highest at the outer corners of the capillary due to shielding from the other capillaries. This non-uniformity in electric field causes the formation of unstable Taylor cones and little or no deposition on the substrate. In case B, the electric field is more uniform at the capillary tip because of the stabilizing effect of the dummy capillaries, hence Taylor cones form. COMSOL predicts that the field lines move outwards because the charge clouds repel each other (not shown). This can be seen in the deposition profile. The particles repel each other such that there is deposition on the side of the substrate holder as shown in **Figure 6.2.14**. In case C, the dummy capillaries are higher, hence the field lines from the emitting capillaries are shielded inwards causing the deposition profile shown below. The electric field on the capillary tip is also more uniform and the Taylor cone is stable for longer periods of time than in case B. An important note is that although the three films are closer together, they do not overlap because the particles still repel each other as they move toward the substrate. In case D, the electric field is the most uniform at the capillary tip but the dummy capillaries shield the emitting capillaries such that the electric field is too low to form Taylor cones. The solution electrospayed is an aqueous solution electrospayed of 10g/L of CsH_2PO_4 and 20g/L polyvinylpyrrolidone (PVP) dissolved in a 1 : 1 molar ratio of methanol : water mixture.

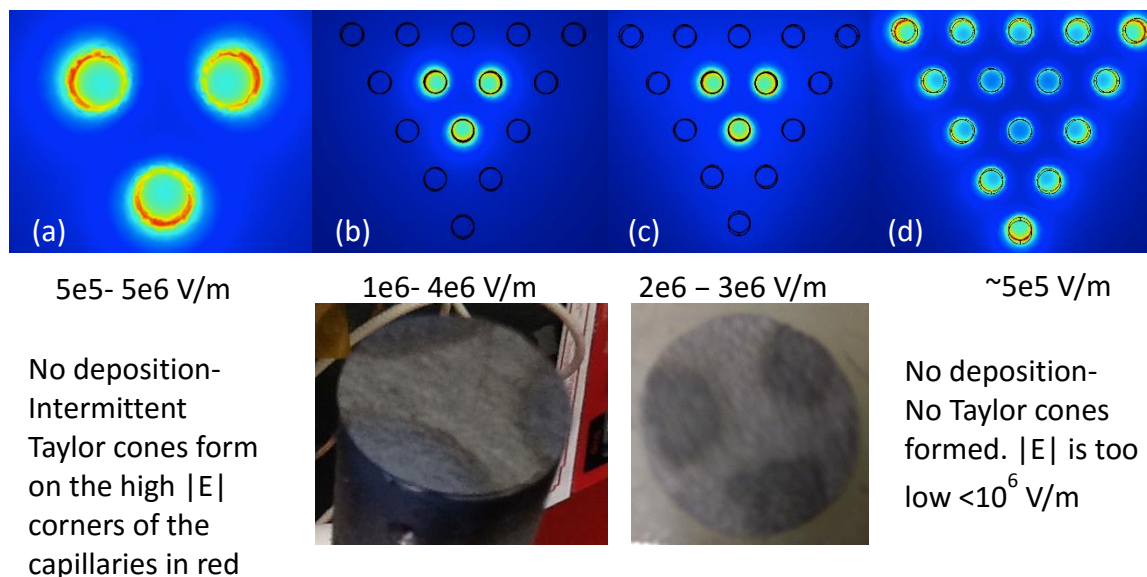


Figure 6.2.14. First row is the electric field map (red -highest electric field, blue-lowest), second row is the electric field range at the capillary tip, and the third row is the experimental result. (a) 3 capillaries only. (b) 3 capillaries surrounded by dummy capillaries half the height of the emitting capillaries in the center. (c) 3 capillaries surrounded by dummy capillaries three quarters their height. (d) 3 capillaries surrounded by dummy capillaries of the same height

COMSOL simulations were carried out to predict the behavior of a seven-capillary system. The dummy capillaries act as a shield in the experiments above so COMSOL results suggest that dummy capillaries as shown above can be replaced with a metal ring and the effect on the emitting capillaries is the same. This makes fabrication easier and less cumbersome because it is easier to work with a ring instead of the over 20 dummy capillaries needed to properly shield seven capillaries. **Figure 6.2.15a** is a schematic of the seven-capillary model and the corresponding systems built in **Figure 6.2.15b**.

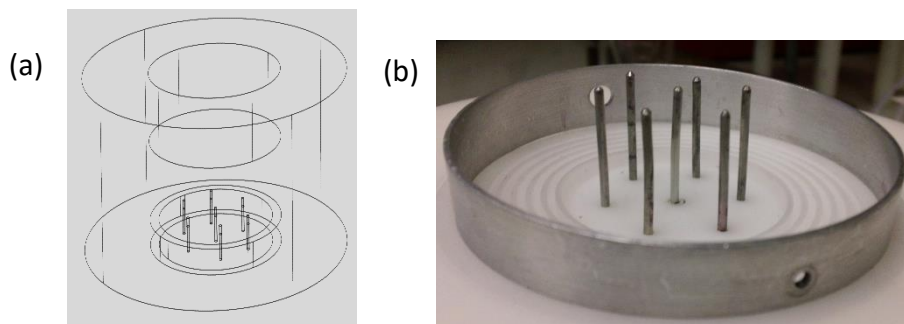


Figure 6.2.15. a) Schematic of the seven-capillary system with a metal ring. (b) Picture of apparatus.

Figure 6.2.16 shows the COMSOL simulations and the corresponding experimental results. The metal shield is 75% of the capillary height. In addition, the capillaries are biased at 8kV and the shield is at 3kV to attain a high enough electric field to form a Taylor cone at the capillary tips. The top row is the electric field map generated by COMSOL and the legend. Blue is the region of highest electric field and red is the region of lowest electric field. The second row is the corresponding picture of the capillaries. The third row is the spray deposition profile for each experiment. In case A, the seven capillaries are of equal height. Because of the shielding effect of the six surrounding capillaries the electric field is not high enough at the central capillary's tip to form a Taylor cone. Hence, there is relatively no deposition at the center of the substrate. Increasing the height of the central capillary by 0.3-0.5 cm increases the electric field at the tip and all seven capillaries electro spray onto the substrate. The results for the three-capillary and seven-capillary system are promising, however, to use these systems to electro spray fuel cell electrodes the deposited structures must overlap to form a continuous uniform film.

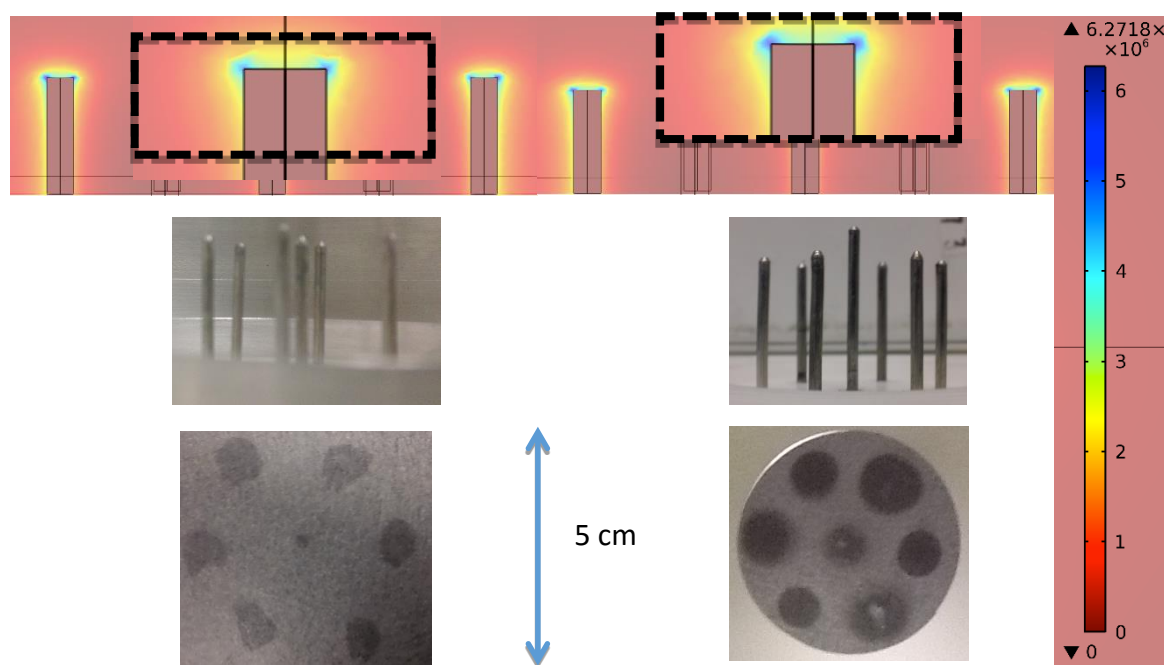


Figure 6.2.16. First row is the electric field map at the capillary tips, to the right is the electric field scale bar. Second row is a picture of the capillary arrangement. Third row is the CsH_2PO_4 deposition profile. (a) All seven capillaries are the same height. (b) The central capillary is ~ 0.3 cm above the surrounding capillaries.

These results suggest that if the particles are defocused at each capillary tip, they might have a greater chance at combining. This effect cannot be accurately predicted by COMSOL because the streamlines terminate at the negative shield because of the limitations in computation. To test this idea without building a cumbersome seven-capillary setup with seven defocusing rings, we tried the experiment with two and three capillary systems. The results are summarized in **Figure 6.2.17**. The top row is the COMSOL simulation result showing the electric field streamlines and the arrows are the potential vector plots depicting the magnitude and the direction of the electric field vector at that point. The second row is a picture of the capillaries in the configuration. The third row is a picture of the deposited film for the corresponding experiment. In case A, two capillaries about 1.3 cm apart are biased at 6 kV. COMSOL results show that the streamlines move outward away from each other. Accordingly, the field vectors move out towards the substrate. This is confirmed by the experimental result, which gives two distinct deposition profiles. In case B, metal rings 2.5 cm in diameter each surround two capillaries. The capillaries are biased at 4kV and the rings are biased at -3kV. COMSOL predicts that the field lines terminate at the rings. The vector plot is more informative showing that the defocusing ring changes the particle trajectory from its original path in case A. This defocusing effect causes an overlap in the deposition profile. This is also the case in case C, where three defocused capillaries equidistant from each other deposit a film about 28 cm² in area.

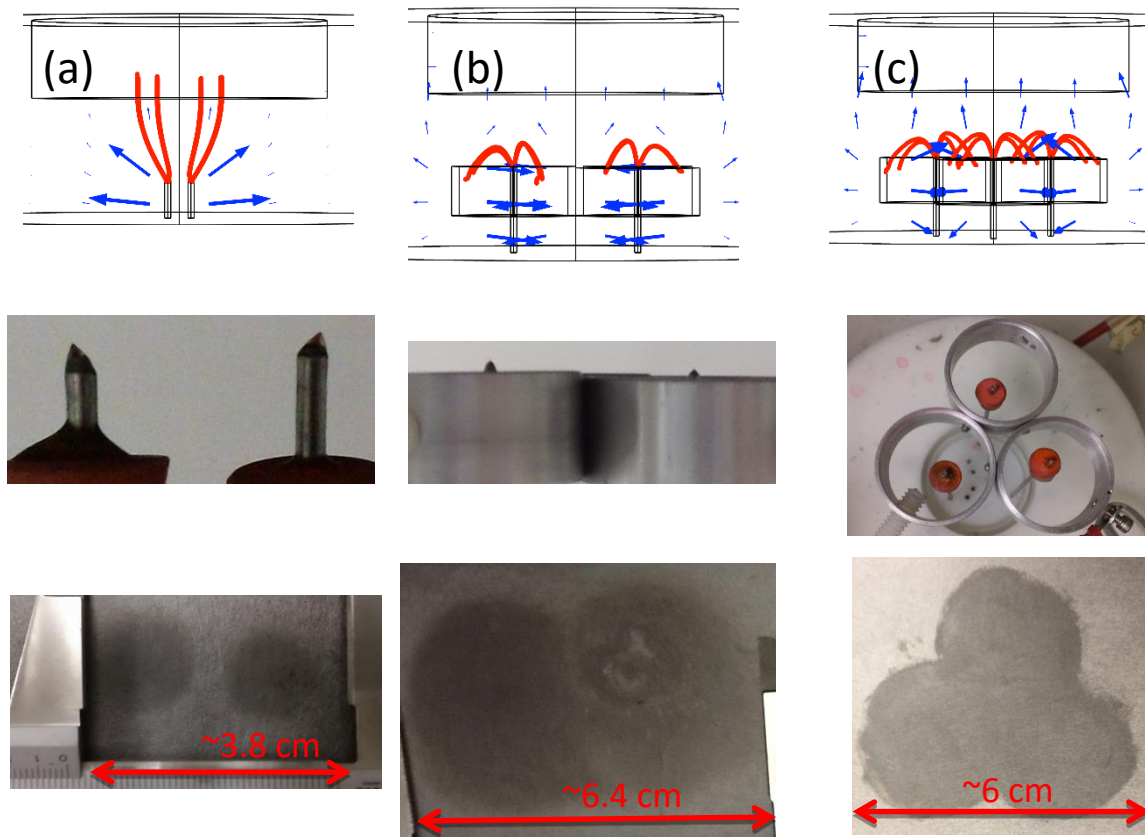


Figure 6.2.17. First row is COMSOL simulation showing the electric field lines and the potential vector plot. Second row is the picture of the apparatus. Third row is the resulting CsH_2PO_4 profile. (a) Two capillaries 1.3cm apart. (b) Two capillaries each surrounded by metal rings 2.8 cm in diameter biased at -3kV. (c) Three capillaries equidistant from each other surrounded by rings 2.8cm in diameter.

With this insight, an electrospay setup that can electrospay films with overlap and excellent uniformity can be realized. Defocusing the charged particles emitted at each capillary tip with oppositely charged electrodes allows for overlap in deposition from the capillaries. The ideal setup is shown in **Figure 6.2.18**.

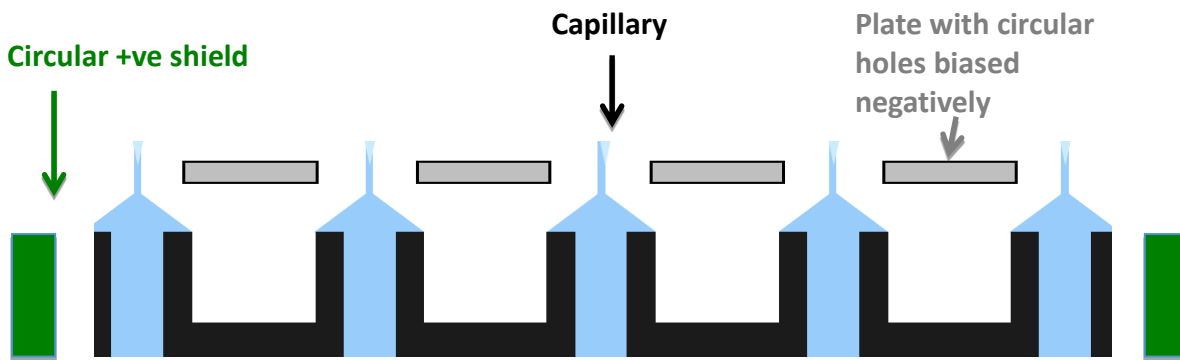


Figure 6.2.18. Schematic of proposed multi-capillary apparatus.

Simulations were carried out to compare the vector map of a seven-capillary system without a defocusing plate with a seven-capillary system with defocusing. **Figure 6.2.19a** is a seven-capillary system with a plate with holes bigger than the capillary radius. The plate is at -3kV . The capillaries are biased at $+8\text{kV}$. **Figure 6.2.19b** is a seven-capillary system without a defocusing plate. It is clear that the defocusing plate pulls apart the charged cloud from its ideal path.

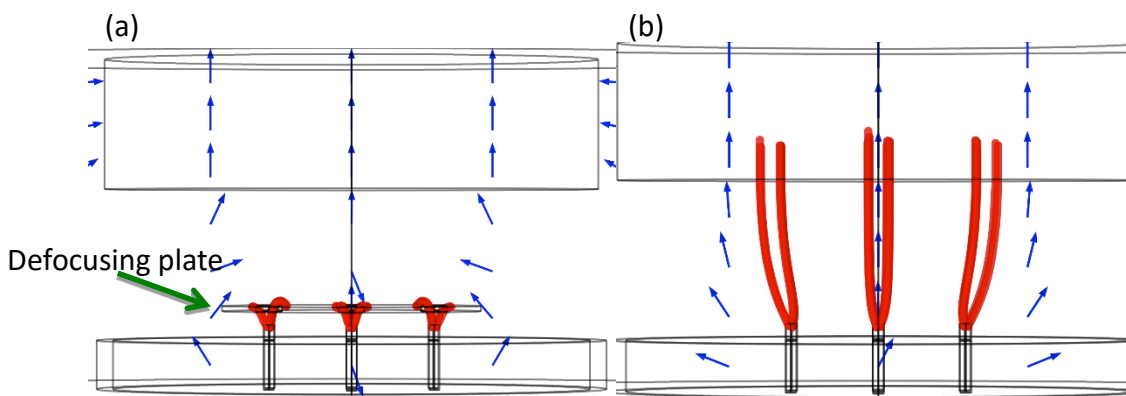


Figure 6.2.19. COMSOL simulations comparing the electric field lines and the potential gradient vector plot for a seven-capillary system (a) with a defocusing plate (b) without a defocusing plate.

6.2.3. Conclusion

With the objective of creating a porous, interconnected nanostructure electrode for solid acid fuel cells, with a uniform thickness and high deposition rate, electrospray deposition was

studied. I explored the electrospray parameter space to obtain a porous nanostructure of CsH_2PO_4 and platinum composite. Electrochemical measurements were made on electrodes to confirm good electro-catalytic activity. The interfacial impedance was $0.7 \Omega \text{ cm}^2$, this is similar to the performance of mechanically milled electrodes with a thirty-fold reduction in platinum loading. The three areas for improvement in these results are the feature size, uniformity and the deposition rate. Future work will be done on reducing the CsH_2PO_4 feature size from 100nm to the order of the platinum particle size (10nm). This will improve power density and ultimately performance. To address the issue of uniformity, the particles emitted were defocused with rings of opposite charge that caused the charged particles to spread out and uniformly deposit on the substrate. Multiple capillary approaches were used to address the low deposition rate issue. COMSOL simulations aided in making educated guesses on how to build a multi-spray setup. We built three-capillary and seven-capillary electrospray systems to scale up the electrospray. It was discovered that multi-cone jet regimes will not combine without a defocusing effect. This was demonstrated with two and three capillary systems. The next steps include building an electrospray setup with multiple capillaries with a negatively biased plate as the defocusing electrode. These findings demonstrate the viability of electrospray deposition as a scalable fabrication tool for widespread use of solid acid fuel cells.

IMPACTS AND INSIGHTS

In this thesis, we have demonstrated the efficacy of carbon nanostructures in the solid acid electrochemical system. We found that CNTs have high oxygen reduction reaction (ORR) activity, as well as high reactivity with steam in SAFC cathodes. The ORR activity is dependent on the oxygen functionalities in the MWCNT structure, as well as the structural defect density. We have demonstrated that these properties can be tuned by CNT growth parameters such as; the precursor partial pressure, seed catalyst size and growth temperature.

On the other hand, the reactivity with steam generates hydrogen at the cathode that lowers the open circuit potential and consequently, the operational power density. However, a solid acid(s) with suitable proton conductivity ($>10^{-2}$ S/cm) that does not have a humidity requirement for stability in the superprotonic phase, could mitigate this problem. Currently, the only solid acids that meet these criteria are S and Se containing solid acids that decompose in H_2 at the anode to form H_2S and H_2Se . These byproducts are poisonous to anode catalysts and unsuitable for widespread applications. Moreover, the humidity requirement for CsH_2PO_4 SAFCs reduces the efficiency of the fuel cell, by decreasing the concentration of the oxidant and fuel at the electrodes. Therefore, for the realization of Pt-free SAFC cathodes with carbon nanotubes, the humidity requirement must be mitigated.

The work on electrospray fabrication of nano-sized CsH_2PO_4 , presents a systematic way to fabricate high surface area SAFC electrodes with increased throughput, catalyst utilization and consequently, power density. Although CsH_2PO_4 nanoparticles as small as 13 nm (sized *in situ*) can be synthesized, the smallest feature size observable by SEM after deposition is ~50 - 100nm. Thus, the outstanding issue is stability of the nano-sized CsH_2PO_4 after synthesis. We recommend coating the synthesized nano-sized CsH_2PO_4 with few atomic layers of ion-permeable oxide (like ceria/titania) to inhibit CsH_2PO_4 agglomeration after electrospray synthesis. This has the potential to drastically increase SAFC electrode power density. In this work, the CsH_2PO_4 particles in the CNT/ CsH_2PO_4 electrodes studied, were μ m-sized. Therefore, there is room for orders of magnitude in improvement over the ORR activity reported in this work, solely by decreasing the CsH_2PO_4 nanoparticle size. Another issue with electrode fabrication is throughput. We have demonstrated that electrospray can be scaled up via multiple emitters and a defocusing plate. However, this is still not a particularly facile method to realize throughput of the scale of grams/hour necessary for widespread application. Therefore, we recommend research on other scalable solid acid nanoparticle fabrication methods.

BIBLIOGRAPHY

1. Chisholm, C. R. I.; Boysen, D. A.; Papandrew, A. B.; Zecevic, S.; Cha, S.; Sasaki, K. A.; Varga, A.; Giapis, K. P.; Haile, S. M. *The Electrochemical Society Interface* **2009**, Fall, 53-59.
2. Haile, S. M.; Chisholm, C. R.; Sasaki, K.; Boysen, D. A.; Uda, T. *Faraday Discussions* **2007**, 134, 17-39.
3. Louie, M. W. *Electrocatalysis in Solid Acid Fuel Cells*. California Institute of Technology, 2011.
4. Haile, S. M.; Chisholm, C. R. I.; Sasaki, K.; Boysen, D. A.; Uda, T. *Faraday Discussions* **2007**, 134, 17-39.
5. Taninouchi, Y.; Uda, T.; Awakura, Y. *Solid State Ionics* **2008**, 178, (31-32), 1648-1653.
6. Varga, A.; Pfohl, M.; Brunelli, N. A.; Schreier, M.; Giapis, K. P.; Haile, S. M. *Phys Chem Chem Phys* **2013**, 15, (37), 15470-15476.
7. Varga, A.; Brunelli, N. A.; Louie, M. W.; Giapis, K. P.; Haile, S. M. *Journal of Materials Chemistry* **2010**, 20, (30), 6309-6315.
8. Thoi, V. S.; Usiskin, R. E.; Haile, S. M. *Chem Sci* **2015**, 6, (2), 1570-1577.
9. Chisholm, C. R. I. *The Electrochemical Society Interface* **2009**, 53-59.
10. O'Hayre, R. P., *Fuel cell fundamentals*. 2nd ed.; John Wiley & Sons: Hoboken, N.J., 2009; p xxv, 546 p., 4 p. of plates.
11. Pelosato, R.; Cordaro, G.; Stucchi, D.; Cristiani, C.; Dotelli, G. *Journal of Power Sources* **2015**, 298, 46-67.
12. Liu, Y. F.; Lehnert, W.; Janssen, H.; Samsun, R. C.; Stolten, D. *Journal of Power Sources* **2016**, 311, 91-102.
13. Haile, S. M. *Acta Materialia* **2003**, 51, 5981-6000.
14. Haile, S. M.; Chisholm, C. R. I.; Sasaki, K.; Boysen, D. A.; Uda, T. *Faraday Discussions* **2007**, 134, 17.
15. Haile, S. M.; Boyse, D. A.; Chisholm, C. R. I.; Merle, R. B. *Nature* **2001**, 410, (6831), 910-913.
16. Baranov, A. I.; Shuvalov, L. A.; Shchagina, N. M. *Jetp Letters* **1982**, 36, (11), 459-462.
17. Pawlowski, A.; Pawlaczyk, C.; Hilczer, B. *Solid State Ionics* **1990**, 44, (1-2), 17-19.
18. Kirpichnikova, L.; Polomska, M.; Pietraszko, A.; Hilczer, B.; Szczesniak, L. *Ferroelectrics* **2003**, 290, 61-69.
19. Chisholm, C. R. I.; Haile, S. M. *Solid State Ionics* **2000**, 136, 229-241.
20. Haile, S. M.; Boysen, D. A.; Chisholm, C. R. I.; Merle, R. B. *Nature* **2001**, 410, (6831), 910-913.
21. Chisholm, C. R. I.; Haile, S. M. *Abstr Pap Am Chem S* **2011**, 241.
22. Merle, R. B.; Chisholm, C. R. I.; Boysen, D. A.; Haile, S. M. *Energ Fuel* **2003**, 17, (1), 210-215.
23. Taninouchi, Y.-k.; Uda, T.; Awakura, Y.; Ikeda, A.; Haile, S. M. *Journal of Materials Chemistry* **2007**, 17, (30), 3182.
24. Zhou, W. H.; Bondarenko, A. S.; Boukamp, B. A.; Bouwmeester, H. J. M. *Solid State Ionics* **2008**, 179, (11-12), 380-384.
25. Bondarenko, A. S.; Zhou, W.; Bouwmeester, H. J. M. *Journal of Power Sources* **2009**, 194, (2), 843-846.

26. Uda, T.; Haile, S. M. *Electrochemical and Solid-State Letters* **2005**, 8, (5), A245.
27. Uda, T. *Solid State Ionics* **2005**, 176, (1-2), 127-133.
28. Uda, T.; Boysen, D. A.; Chisholm, C. R. I.; Haile, S. M. *Electrochemical and Solid-State Letters* **2006**, 9, (6), A261.
29. Sasaki, K. *Electrochemical Characterization of Solid Acid Fuel Cell Electrodes*. California Institute of Technology, Pasadena, 2010.
30. Chisholm, C. R. I.; Haile, S. M. *Chemistry of Materials* **2007**, 19, (2), 270-279.
31. Louie, M. W.; Haile, S. M. *Energ Environ Sci* **2011**, 4, (10), 4230-4238.
32. Orazem, M. E.; Tribollet, B., *Electrochemical Impedance Spectroscopy* -. John Wiley & Sons: New York, 2011.
33. Barsoukov, E.; Macdonald, J. R., *Impedance Spectroscopy - Theory, Experiment, and Applications*. John Wiley & Sons: New York, 2005.
34. Uda, T.; Haile, S. M. *Electrochemical and Solid-State Letters* **2005**, 8, (5), A245-A246.
35. Barsoukov, E.; Macdonald, J. R., *Impedance spectroscopy : theory, experiment, and applications*. 2nd ed.; Wiley-Interscience: Hoboken, N.J., 2005; p xvii, 595 p.
36. Schrader, B., Bougeard, D. , *Infrared and Raman Spectroscopy - Methods and Applications* VCH Publishers, Inc. : New York, 1995.
37. Larkin, P., *Infrared and Raman spectroscopy : principles and spectral interpretation*. Elsevier: Amsterdam ; Boston, 2011; p x, 228 p.
38. Li, W. Z.; Zhang, H.; Wang, C. Y.; Zhang, Y.; Xu, L. W.; Zhu, K.; Xie, S. S. *Appl Phys Lett* **1997**, 70, (20), 2684-2686.
39. Dresselhaus, M. S. D., G. Saito, R. Jorio, A. . *Physics Reports* **2005**, 409, 47-99.
40. Collins, P. G., *Defects and disorder in carbon nanotubes*. Oxford university press: Oxford university, 2009.
41. Costa, S.; Borowiak-Palen, E.; Kruszynska, M.; Bachmatiuk, A.; Kalenczuk, R. J. *Mater Sci-Poland* **2008**, 26, (2), 433-441.
42. Wang, Y.; Alsmeyer, D. C.; McCreery, R. L. *Chemistry of Materials* **1990**, 2, (5), 557-563.
43. Saito, R.; Dresselhaus, G.; Dresselhaus, M. S., *Physical properties of carbon nanotubes*. Imperial College Press: London, 1998; p xii, 259 p.
44. Rao, R.; Reppert, J.; Podila, R.; Zhang, X. F.; Rao, A. M.; Talapatra, S.; Maruyama, B. *Carbon* **2011**, 49, (4), 1318-1325.
45. Antunes, E. F.; Lobo, A. O.; Corat, E. J.; Trava-Airoldi, V. J.; Martin, A. A.; Verissimo, C. *Carbon* **2006**, 44, (11), 2202-2211.
46. Behler, K.; Osswald, S.; Ye, H.; Dimovski, S.; Gogotsi, Y. *J Nanopart Res* **2006**, 8, (5), 615-625.
47. Dementev, N.; Osswald, S.; Gogotsi, Y.; Borguet, E. *Journal of Materials Chemistry* **2009**, 19, (42), 7904-7908.
48. Osswald, S.; Flahaut, E.; Gogotsi, Y. *Chemistry of Materials* **2006**, 18, (6), 1525-1533.
49. Osswald, S.; Flahaut, E.; Ye, H.; Gogotsi, Y. *Chem Phys Lett* **2005**, 402, (4-6), 422-427.
50. Osswald, S.; Havel, M.; Gogotsi, Y. *J Raman Spectrosc* **2007**, 38, (6), 728-736.
51. Rossi, M. P.; Gogotsi, Y.; Kornev, K. G. *Langmuir* **2009**, 25, (5), 2804-2810.
52. Antunes, E. F.; Lobo, A. O.; Corat, E. J.; Trava-Airoldi, V. J. *Carbon* **2007**, 45, (5), 913-921.
53. Mennella, V.; Monaco, G.; Colangeli, L.; Bussoletti, E. *Carbon* **1995**, 33, (2), 115-121.
54. Bailey. **1988**.

55. Chiarot, P. R.; Sullivan, P.; Ben Mrad, R. *J Microelectromech S* **2011**, 20, (6), 1241-1249.
56. Chen, C. H.; Kelder, E. M.; Schoonman, J. *J Eur Ceram Soc* **1998**, 18, (10), 1439-1443.
57. Chiarot, P. R.; Sullivan, P.; Ben Mrad, R. *Exp Therm Fluid Sci* **2012**, 37, 184-188.
58. Schug, K. *Lc Gc N Am* **2011**, 29, (3), 282-282.
59. Benitez, R.; Soler, J.; Daza, L. *Journal of Power Sources* **2005**, 151, 108-113.
60. Chen, C. H.; Kelder, E. M.; Schoonman, J. *J Mater Sci* **1996**, 31, (20), 5437-5442.
61. Chen, C. H.; Schoonman, J. *Nato Adv Sci I E-App* **2000**, 368, 295-321.
62. Choi, K. H.; Muhammad, N. M.; Dang, H. W.; Lee, A.; Hwang, J. S.; Nam, J. W.; Ryu, B. H. *Int J Mater Res* **2011**, 102, (10), 1252-1260.
63. Taniguchi, I. *Solid State Ionics* **2003**, 160, (3-4), 271-279.
64. Perednis, D.; Wilhelm, O.; Pratsinis, S. E.; Gauckler, L. J. *Thin Solid Films* **2005**, 474, (1-2), 84-95.
65. Jung, S.; Effelsberg, U.; Tallarek, U. *J Chromatogr A* **2011**, 1218, (12), 1611-1619.
66. Chen, C. H.; Schoonman, J. *J Ind Eng Chem* **2004**, 10, (7), 1114-1125.
67. Chen, C. H.; Kelder, E. M.; Schoonman, J. *Journal of Power Sources* **1997**, 68, (2), 377-380.
68. Chaparro, A. M.; Gallardo, B.; Folgado, M. A.; Martin, A. J.; Daza, L. *Catal Today* **2009**, 143, (3-4), 237-241.
69. Chaparro, A. M.; Folgado, M. A.; Ferreira-Aparicio, P.; Martin, A. J.; Alonso-Alvarez, I.; Daza, L. *Journal of The Electrochemical Society* **2010**, 157, (7), B993-B999.
70. Taylor, G. *Proc R Soc Lon Ser-A* **1964**, 280, (1380), 383-+.
71. Rulison, A. J.; Flagan, R. C. *Rev Sci Instrum* **1993**, 64, (3), 683-686.
72. Chen, C. H.; Kelder, E. M.; vanderPut, P. J. J. M.; Schoonman, J. *Journal of Materials Chemistry* **1996**, 6, (5), 765-771.
73. Ganan-Calvo, A. M. *J Fluid Mech* **2004**, 507, 203-212.
74. Cloupeau, M.; Prunetfoch, B. *Journal of Aerosol Science* **1994**, 25, (6), 1021-1036.
75. Seinfeld, J. H.; Pandis, S. N., *Atmospheric Chemistry and Physics*. John Wiley and Sons: New York, 1998.
76. Flagan, R. C.; Seinfeld, J. H., *Fundamentals of air pollution engineering*. Prentice Hall: Englewood Cliffs, N.J., 1988; p xiii, 542 p.
77. Kundu, S.; Wang, Y. M.; Xia, W.; Muhler, M. *J Phys Chem C* **2008**, 112, (43), 16869-16878.
78. Auer, E.; Freund, A.; Pietsch, J.; Tacke, T. *Appl Catal a-Gen* **1998**, 173, (2), 259-271.
79. Zhang, H. M.; Wang, X. B.; Wan, L. J.; Liu, Y. Q.; Bai, C. L. *Electrochimica Acta* **2004**, 49, (5), 715-719.
80. Hu, C. G.; Yuan, S.; Hu, S. S. *Electrochimica Acta* **2006**, 51, (15), 3013-3021.
81. Hembram, K. P. S. S.; Rao, G. M. *Mater Lett* **2012**, 72, 68-70.
82. Chen, Z.; Chen, Z. W. *Ecs Transactions* **2010**, 28, (21), 65-70.
83. Chen, Z.; Higgins, D.; Chen, Z. W. *Carbon* **2010**, 48, (11), 3057-3065.
84. Gong, K. P.; Du, F.; Xia, Z. H.; Durstock, M.; Dai, L. M. *Science* **2009**, 323, (5915), 760-764.
85. Li, J. C.; Zhao, S. Y.; Hou, P. X.; Fang, R. P.; Liu, C.; Liang, J.; Luan, J.; Shan, X. Y.; Cheng, H. M. *Nanoscale* **2015**, 7, (45), 19201-19206.
86. Zhang, M. N.; Yan, Y. M.; Gong, K. P.; Mao, L. Q.; Guo, Z. X.; Chen, Y. *Langmuir* **2004**, 20, (20), 8781-8785.

87. Jurmann, G.; Tammeveski, K. *J Electroanal Chem* **2006**, 597, (2), 119-126.
88. Kruusenberg, I.; Marandi, M.; Sammelselg, V.; Tammeveski, K. *Electrochem Solid St* **2009**, 12, (11), F31-F34.
89. Nagaiah, T. C.; Kundu, S.; Bron, M.; Muhler, M.; Schuhmann, W. *Electrochem Commun* **2010**, 12, (3), 338-341.
90. Ratso, S.; Kruusenberg, I.; Vikkisk, M.; Joost, U.; Shulga, E.; Kink, I.; Kallio, T.; Tammeveski, K. *Carbon* **2014**, 73, 361-370.
91. Vikkisk, M.; Kruusenberg, I.; Joost, U.; Shulga, E.; Tammeveski, K. *Electrochimica Acta* **2013**, 87, 709-716.
92. Li, W. Q.; Yang, D. G.; Chen, H. B.; Gao, Y.; Li, H. M. *Electrochimica Acta* **2015**, 165, 191-197.
93. Vikkisk, M.; Kruusenberg, I.; Ratso, S.; Joost, U.; Shulga, E.; Kink, I.; Rauwel, P.; Tammeveski, K. *Rsc Adv* **2015**, 5, (73), 59495-59505.
94. Alexeyeva, N.; Tammeveski, K. *Electrochem Solid St* **2007**, 10, (5), F18-F21.
95. Shanmugam, S.; Gedanken, A. *The Journal of Physical Chemistry B* **2006**, 110, (5), 2037-2044.
96. Matsubara, K.; Waki, K. *Electrochimica Acta* **2010**, 55, (28), 9166-9173.
97. Matsubara, K.; Waki, K. *Ecs Transactions* **2010**, 28, (21), 35-46.
98. Li, Y. H.; Zhong, G. Y.; Yu, H.; Wang, H. J.; Peng, F. *Phys Chem Chem Phys* **2015**, 17, (34), 21950-21959.
99. Tang, H.; Qi, Z. G.; Ramani, M.; Elter, J. F. *Journal of Power Sources* **2006**, 158, (2), 1306-1312.
100. Maass, S.; Finsterwalder, F.; Frank, G.; Hartmann, R.; Merten, C. *Journal of Power Sources* **2008**, 176, (2), 444-451.
101. Tuci, G.; Zafferoni, C.; Rossin, A.; Milella, A.; Luconi, L.; Innocenti, M.; Truong Phuoc, L.; Duong-Viet, C.; Pham-Huu, C.; Giambastiani, G. *Chemistry of Materials* **2014**, 26, (11), 3460-3470.
102. Jimeno, A.; Goyanes, S.; Eceiza, A.; Kortaberria, G.; Mondragon, I.; Corcuera, M. A. *J Nanosci Nanotechno* **2009**, 9, (10), 6222-6227.
103. Pillai, S. K.; Ramontja, J.; Ray, S. S. *Ceram Eng Sci Proc* **2011**, 32, (7), 43-51.
104. Dresselhaus, M. S.; Dresselhaus, G.; Avouris, P., Carbon nanotubes synthesis, structure, properties, and applications. In *Topics in applied physics v 80*, Springer, Berlin ; New York, 2001; pp xvi, 448 p.
105. Tuinstra, F.; Koenig, J. L. *The Journal of Chemical Physics* **1970**, 53, (3), 1126-1130.
106. Lau, C. H.; Cervini, R.; Clarke, S. R.; Markovic, M. G.; Matisons, J. G.; Hawkins, S. C.; Huynh, C. P.; Simon, G. P. *J Nanopart Res* **2008**, 10, 77-88.
107. Kundu, S.; Nagaiah, T. C.; Xia, W.; Wang, Y. M.; Van Dommele, S.; Bitter, J. H.; Santa, M.; Grundmeier, G.; Bron, M.; Schuhmann, W.; Muhler, M. *J Phys Chem C* **2009**, 113, (32), 14302-14310.
108. Datsyuk, V.; Kalyva, M.; Papagelis, K.; Parthenios, J.; Tasis, D.; Siokou, A.; Kallitsis, I.; Galiotis, C. *Carbon* **2008**, 46, (6), 833-840.
109. Ago, H.; Kugler, T.; Cacialli, F.; Salaneck, W. R.; Shaffer, M. S. P.; Windle, A. H.; Friend, R. H. *J Phys Chem B* **1999**, 103, (38), 8116-8121.
110. Zhang, N. Y.; Me, J.; Varadan, V. K. *Smart Mater Struct* **2002**, 11, (6), 962-965.
111. Datsyuk, V.; Guerret-Piecourt, C.; Dagevou, S.; Billon, L.; Dupin, J. C.; Flahaut, E.; Peigney, A.; Laurent, C. *Carbon* **2005**, 43, (4), 873-876.

112. Osorio, A. G.; Silveira, I. C. L.; Bueno, V. L.; Bergmann, C. P. *Appl Surf Sci* **2008**, 255, (5), 2485-2489.
113. Makharia, R.; Mathias, M. F.; Baker, D. R. *Journal of the Electrochemical Society* **2005**, 152, (5), A970-A977.
114. Banks, C. E.; Compton, R. G. *Analyst* **2006**, 131, (1), 15-21.
115. Yeager, E. *J Mol Catal* **1986**, 38, (1-2), 5-25.
116. Zhang, H. J.; Li, H. L.; Deng, C. C.; Zhao, B.; Yang, J. H. *Ecs Electrochem Lett* **2015**, 4, (8).
117. Morcos, I.; Yeager, E. *Electrochimica Acta* **1970**, 15, (6), 953-&.
118. Charlier, J. C. *Accounts Chem Res* **2002**, 35, (12), 1063-1069.
119. Stadermann, M.; Sherlock, S. P.; In, J. B.; Fornasiero, F.; Park, H. G.; Artyukhin, A. B.; Wang, Y. M.; De Yoreo, J. J.; Grigoropoulos, C. P.; Bakajin, O.; Chernov, A. A.; Noy, A. *Nano Lett* **2009**, 9, (2), 738-744.
120. Zickler, G. A.; Smarsly, B.; Gierlinger, N.; Peterlik, H.; Paris, O. *Carbon* **2006**, 44, (15), 3239-3246.
121. Vollebregt, S.; Ishihara, R.; Tichelaar, F. D.; Hou, Y.; Beenakker, C. I. M. *Carbon* **2012**, 50, (10), 3542-3554.
122. Zhang, H. J.; Li, H. L.; Li, X. T.; Zhao, B.; Yang, J. H. *Int J Hydrogen Energ* **2014**, 39, (30), 16964-16975.
123. Wang, X.; Ouyang, C. B.; Dou, S.; Liu, D. D.; Wang, S. Y. *Rsc Adv* **2015**, 5, (52), 41901-41904.
124. Hu, I. F.; Karweik, D. H.; Kuwana, T. *J Electroanal Chem* **1985**, 188, (1-2), 59-72.
125. Maruyama, J.; Abe, I. *J Electroanal Chem* **2002**, 527, (1-2), 65-70.
126. Toebes, M. L.; van Heeswijk, E. M. P.; Bitter, J. H.; van Dillen, A. J.; de Jong, K. P. *Carbon* **2004**, 42, (2), 307-315.
127. Lakshminarayanan, P. V.; Toghiani, H.; Pittman, C. U. *Carbon* **2004**, 42, (12-13), 2433-2442.
128. Metin, O.; Mazumder, V.; Ozkar, S.; Sun, S. S. *J Am Chem Soc* **2010**, 132, (5), 1468-+.
129. Tsang, S. C.; Chen, Y. K.; Harris, P. J. F.; Green, M. L. H. *Nature* **1994**, 372, (6502), 159-162.
130. Bokova, S. N.; Obraztsova, E. D.; Grebenyukov, V. V.; Elumeeva, K. V.; Ishchenko, A. V.; Kuznetsov, V. L. *Phys Status Solidi B* **2010**, 247, (11-12), 2827-2830.
131. Hou, P. X.; Liu, C.; Cheng, H. M. *Carbon* **2008**, 46, (15), 2003-2025.
132. Yu, R. Q.; Chen, L. W.; Liu, Q. P.; Lin, J. Y.; Tan, K. L.; Ng, S. C.; Chan, H. S. O.; Xu, G. Q.; Hor, T. S. A. *Chemistry of Materials* **1998**, 10, (3), 718-722.
133. Pietrzak, R.; Wachowska, H.; Nowicki, P. *Energ Fuel* **2006**, 20, (3), 1275-1280.
134. Tammeveski, K.; Kontturi, K.; Nichols, R. J.; Potter, R. J.; Schiffrin, D. J. *J Electroanal Chem* **2001**, 515, (1-2), 101-112.
135. Kim, J.-H.; Ishihara, A.; Mitsushima, S.; Kamiya, N.; Ota, K.-I. *Electrochimica Acta* **2007**, 52, (7), 2492-2497.
136. Lu, G.; Bernasek, S. L.; Schwartz, J. *Surface Science* **2000**, 458, (1-3), 80-90.
137. Corcoran, C. J.; Tavassol, H.; Rigsby, M. A.; Bagus, P. S.; Wieckowski, A. *Journal of Power Sources* **2010**, 195, (24), 7856-7879.
138. Lin, H.; Rumaiz, A. K.; Schulz, M.; Wang, D.; Rock, R.; Huang, C. P.; Shah, S. I. *Materials Science and Engineering: B* **2008**, 151, (2), 133-139.

139. Park, S.-J.; Lee, J.-P.; Jang, J. S.; Rhu, H.; Yu, H.; You, B. Y.; Kim, C. S.; Kim, K. J.; Cho, Y. J.; Baik, S.; Lee, W. *Nanotechnology* **2013**, 24, (29), 295202.
140. Hauf, C.; Kniep, R.; Pfaff, G. *J Mater Sci* **1999**, 34, (6), 1287-1292.
141. Li, M.; Hebenstreit, W.; Diebold, U.; Tyryshkin, A. M.; Bowman, M. K.; Dunham, G. G.; Henderson, M. A. *The Journal of Physical Chemistry B* **2000**, 104, (20), 4944-4950.
142. Strunk, J.; Vining, W. C.; Bell, A. T. *J. Phys. Chem. C* **2010**, 114, (40), 16937-16945.
143. Katiyar, R. S.; Krishnan, R. S. *Physics Letters A* **1967**, 25, (7), 525-526.
144. Ohsaka, T.; Izumi, F.; Fujiki, Y. *J Raman Spectrosc* **1978**, 7, (6), 321-324.
145. Cheng, H.; Selloni, A. *Physical Review B* **2009**, 79, (9), 092101.
146. Setvín, M.; Aschauer, U.; Scheiber, P.; Li, Y.-F.; Hou, W.; Schmid, M.; Selloni, A.; Diebold, U. *Science* **2013**, 341, (6149), 988-991.
147. Diebold, U. *Surface Science Reports* **2003**, 48, (5-8), 53-229.
148. Matsunaga, K.; Tanaka, Y.; Toyoura, K.; Nakamura, A.; Ikuhara, Y.; Shibata, N. *Physical Review B* **2014**, 90, (19), 195303.
149. Pang, C. L.; Lindsay, R.; Thornton, G. *Chem Rev* **2013**, 113, (6), 3887-3948.
150. Boysen, D. A.; Uda, T.; Chisholm, C. R. I.; Haile, S. M. *Science* **2004**, 303, (5654), 68-70.
151. C.R.I. Chisholm, D. A. B., A.B. Papandrew, S. Zezevic, S. Cha, K. Sasaki, A. Varga, K.P. Giapis, S.M.Haile. *Interface Magazine* **2009**, 18, 53-59.
152. Hartman, R. P. A.; Brunner, D. J.; Camelot, D. M. A.; Marijnissen, J. C. M.; Scarlett, B. *Journal of Aerosol Science* **2000**, 31, (1), 65-95.
153. Ganan-Calvo, A. M.; Davila, J.; Barrero, A. *Journal of Aerosol Science* **1997**, 28, (2), 249-275.
154. Pantano, C.; Ganan-Calvo, A.; Barrero, A. *Journal of Aerosol Science* **1994**, 25, (6), 1065-1077.
155. Cloupeau, M.; Prunetfoch, B. *J Electrostat* **1989**, 22, (2), 135-159.
156. Cloupeau, M.; Prunetfoch, B. *J Electrostat* **1990**, 25, (2), 165-184.
157. Dole, M.; Marck, L.; Hines, R.; Mobley, R.; Ferguson, L.; MB, A. *The Journal of Chemical Physics* **1968**, 49, (5), 2240.
158. Gu, W.; Heil, P. E.; Choi, H.; Kim, K. *Appl Phys Lett* **2007**, 91, (6), 064104.
159. Smith, J. N.; Flagan, R. C.; Beauchamp, J. L. *J Phys Chem A* **2002**, 106, (42), 9957-9967.
160. Gomez, A.; Tang, K. *Phys Fluids* **1994**, 6, (1), 404.
161. Grimm, R. L.; Beauchamp, J. *Anal Chem* **2002**, 74, 6291-6297.
162. Hopkins, R. J.; Reid, J. P. *J Phys Chem-Us* **2006**, 110, 3239-3249.
163. Louie, M. W.; Sasaki, K.; Haile, S. M. *Electrochemical Society Transactions* **2008**, 13, (28), 57-62.
164. Varga, Á.; Brunelli, N. A.; Louie, M. W.; Giapis, K. P.; Haile, S. M. *Journal of Materials Chemistry* **2010**, 20, (30), 6309.
165. Knutson, E.; Whitby, K. *Journal of Aerosol Science* **1975**, 6, 453-460.
166. Fu, H.; Patel, A. C.; Holtzman, M. J.; Chen, D. R. *Aerosol science and technology : the journal of the American Association for Aerosol Research* **2011**, 45, (10), 1176-1183.
167. Flagan, R. C. *Aerosol Sci Tech* **1999**, 30, (6), 556-570.
168. Stolzenburg, M. R.; McMurry, P. H. *Aerosol Sci Tech* **2008**, 42, (6), 421-432.
169. Hoppel, W. A.; Frick, G. M. *Aerosol Sci Tech* **1986**, 5, (1), 1-21.
170. Liu, B.; KW, L. *American Industrial Hygiene Association* **1975**, 36, 861-865.

171. Jaworek, A.; Krupota, A. *Journal of Aerosol Science* **1999**, 30, (7), 873-893.
172. Chen, D.; Pui, D.; Kaufman, S. *Journal of Aerosol Science* **1995**, 26, (6), 963-977.
173. Fernandez de la Mora, J.; Loscertales, I. G. *J Fluid Mech* **1994**, 260, 155-184.
174. Jayanthi, G. V.; Zhang, S. C.; Messing, G. L. *Aerosol Sci Tech* **1993**, 19, (4), 478-490.
175. Charlesworth, D. H.; Marshall Jr., W. R. *Aiche J* **1957**, 6, (1), 9-23.
176. Park, C. H.; Lee, J. *J Appl Polym Sci* **2009**, 114, (1), 430-437.
177. Wilm, M. S.; Mann, M. *International Journal of Mass Spectrometry and Ion Processes* **1994**, 136, 167-180.
178. Chang, R.; Davis, E. J. *J Colloid Interf Sci* **1976**, 54, (3), 352-363.
179. Chang, R.; Davis, E. J. *J Colloid Interf Sci* **1974**, 47, (1), 65-76.
180. John Seinfeld, S. P., *Atmospheric Chemistry and Physics*. John Wiley & Sons: United States, 1997; Vol. 1, p 97-7638.
181. Leaitch, W. R.; Strapp, J. W.; Wiebe, H. A.; Anlauf, K. G.; Isaac, G. A. *J Geophys Res-Atmos* **1986**, 91, (D11), 1821-1831.
182. Fukuta, N.; Walter, L. A. *J Atmos Sci* **1970**, 27, (8), 1160-&.
183. Bocanegra, R.; Galán, D.; Márquez, M.; Loscertales, I. G.; Barrero, A. *Journal of Aerosol Science* **2005**, 36, (12), 1387-1399.
184. Almekinders, J. C.; Jones, C. *Journal of Aerosol Science* **1999**, 30, (7), 969-971.
185. Deng, W. W.; Klemic, J. F.; Li, X. H.; Reed, M. A.; Gomez, A. *Journal of Aerosol Science* **2006**, 37, (6), 696-714.
186. Deng, W. W.; Klemic, J. F.; Li, X. H.; Reed, M. A.; Gomez, A. *P Combust Inst* **2007**, 31, 2239-2246.
187. J.C., A. *Journal of Aerosol Science* **1999**, 30, (7), 969-971.
188. Tatemoto, Y.; Ishikawa, R.; Takeuchi, M.; Takeshita, T.; Noda, K.; Okazaki, T. *Chemical Engineering & Technology* **2007**, 30, (9), 1274-1279.
189. Waits, C. M.; Hanrahan, B.; Lee, I. *J Micromech Microeng* **2010**, 20, (10).
190. Tang, K. Q.; Lin, Y. H.; Matson, D. W.; Kim, T.; Smith, R. D. *Anal Chem* **2001**, 73, (8), 1658-1663.
191. Barrero, A.; Lopez-Herrera, J. M.; Boucard, A.; Loscertales, I. G.; Marquez, M. *J Colloid Interf Sci* **2004**, 272, (1), 104-108.
192. Loscertales, I. G.; Barrero, A.; Guerrero, I.; Cortijo, R.; Marquez, M.; Ganan-Calvo, A. *M. Science* **2002**, 295, (5560), 1695-1698.
193. Lopez-Herrera, J. M.; Barrero, A.; Lopez, A.; Loscertales, I. G.; Marquez, M. *Journal of Aerosol Science* **2003**, 34, (5), 535-552.
194. Barrero, A.; Loscertales, I. G. *Annu Rev Fluid Mech* **2007**, 39, 89-106.
195. Marin, A. G.; Loscertales, I. G.; Barrero, A. *Phys Fluids* **2008**, 20, (4).